Universiteit Antwerpen

Faculteit Wetenschappen
Departement Fysica

Study of the underlying event at forward rapidity in pp collisions at $\sqrt{s} = 0.9$, 2.76 and 7 TeV

Studie van de Underlying Event activiteit bij voorwaartse rapiditeit in pp botsingen met $\sqrt{s} = 0.9$, 2.76 en 7 TeV

Proefschrift voorgelegd tot het behalen van de graad van
doctor in de wetenschappen aan de Universiteit Antwerpen
te verdedigen door
Hans VAN HAEVERMAET

Promotor: Prof. Dr. Pierre Van Mechelen

Antwerpen, 2013

Preface

The primary goal of particle physics is to study the fundamental building blocks of the universe. It has the quest to understand which sets of elementary particles and interactions are needed to construct all matter and explain all processes observed in nature. Our current knowledge is contained in the Standard Model, a theory that provides a unified description of the interactions (with the exception of gravity) between the known elementary particles. Despite its success in explaining experimental results with high precision, many details still need to be fully understood and the puzzle of nature is not yet complete.

Particle accelerators provide the ideal environment to study particle physics. These machines accelerate particles up to very high energies and then collide them. From the debris of the collisions one can then study the behaviour and properties of the involved particles and interactions. The new energy domains that can be explored at such accelerators enable us to study the validity of the Standard Model and to search for missing pieces of the puzzle, e.g. new particles and interactions. The latest and most powerful particle accelerator currently available is the Large Hadron Collider (LHC) at CERN (Geneva). It provides proton-proton, and heavy ion, collisions in energy domains never accessed before.

The LHC is a true discovery machine, its high energy proton-proton collisions provide the ideal conditions to find particles such as the famous Higgs boson, but it is also the ideal machine to study the proton-proton collisions itself. The theory that describes the strong interactions between protons is called Quantum Chromodynamics (QCD), and is the topic of this thesis. Although it is part of the Standard Model, the description of proton-proton collisions, or more general hadron-hadron collisions, is far from trivial and still subject to a lot of research as many things yet have to be completely understood. Improving our knowledge about QCD is not only important for conducting precision measurements of the Standard Model, but also for the search for new physics. How else can one make precise discoveries when the default (background) processes of proton-proton collisions are not fully understood?

Within the framework of QCD, hadron collisions are described in terms of short distance (high energy transfer) and long distance (low energy transfer) processes. The former can be well described within perturbative QCD theory, while the latter cannot, due to the nature of the strong interactions, and as such their description relies on QCD inspired phenomenological models that use free parameters. These long distance interactions, or so called soft processes, are however important since they dominate the

cross section of hadron collisions. They are the origin of the additional activity, called the underlying event, that is present next to the perturbative hard scattering in the collision and can alter the total scattered energy quite significantly.

Since a universal theoretical framework to describe the underlying event activity is missing, a lot of research and experimental measurements have been, and still are conducted to improve the available phenomenological models by tuning their free parameters to the data. These analyses are done at different energy domains, and different regions of (geometrical) phase space to construct a complete picture of the underlying event. In this thesis we will present a novel and complementary measurement of the underlying event, conducted at the Compact Muon Solenoid (CMS) experiment at the LHC. Here, the underlying event activity at angles very close to the colliding proton-proton beams is studied with the CASTOR calorimeter. It is the first analysis ever to feature data from this calorimeter and region of phase space. This yields a different sensitivity to the various components of the underlying event than the currently available results. A significant part of the research conducted in this thesis was devoted to the commissioning and validation of the CASTOR detector, in order to understand its response and to develop the necessary software tools to perform the analysis.

The measurement is conducted at three different proton-proton centre-of-mass energies, namely 0.9, 2.76 and 7 TeV, where the results at 2.76 TeV are the first ever presented at this scale in the context of the underlying event. Furthermore, the underlying event activity is studied with a novel observable. While the existing studies usually measure absolute values of particle multiplicities or energy densities, we look at the ratio of the forward energy density for events with a hard scattering to the forward energy density for inclusive events. This forward energy density ratio is then measured as a function of the hard scale of the event at the three different centre-of-mass energies. This approach, in which we study the relative response, does not only minimises the systematic uncertainties, but also yields a direct sensitivity to the most significant component of the underlying event: the amount of multiple parton interactions, by factoring out the average energy per parton interaction. In addition, the evolution of the forward energy density with centre-of-mass energy is studied in inclusive events and in events with a hard scale present. The results are compared to phenomenological models for proton-proton collisions and are discussed in terms of the underlying event. Whereas the dependence of the forward energy density ratio on the hard scale of the event at each centre-of-mass energy separately can be well reproduced by some models, all models fail to simultaneously describe the increase of the forward energy density with centre-of-mass energy in both inclusive events and in events with a hard scale present.

The thesis is organised in three parts. The first theoretical part gives a review of QCD and the description hadron collisions within this framework. The second part introduces the experimental setup at which the measurements are conducted, with an emphasis on the CASTOR calorimeter as it is used to measure the energy densities. The third part starts with a brief overview of existing underlying event measurements conducted at the LHC experiments, to then fully describe the novel analysis and results presented in this thesis.

The results presented in this thesis are published in the following paper:
CMS Collaboration, *Study of the underlying event at forward rapidity in pp collisions at* $\sqrt{s}$ *= 0.9, 2.76, and 7 TeV*, JHEP **1304** (2013) 072, DOI: 10.1007/JHEP04(2013)072, e-Print: arXiv:1302.2394 [hep-ex].

Contents

"Physics is really nothing more than a search for ultimate simplicity, but so far all we have is a kind of elegant messiness."

— Bill Bryson

Part I.

Review of Quantum Chromodynamics and the description of hadron collisions

Chapter 1.

Introduction

1.1. The Standard Model

All experimental data currently available in particle physics are described by the *Standard Model* of particles and interactions. According to this model, which is illustrated in figure 1.1, all matter can be built from a small number of elementary spin $\frac{1}{2}$ particles, called *fermions*. There are two types: *quarks* and *leptons*, which are both present in three generations. They each have a specific mass and charge. All leptons have an integral electric charge: for the well known electron (e) and its two heavier unstable versions, the muon (μ) and tau (τ), it is -1, while their neutrino versions have no electrical charge and are known to have a very small mass, < 2.2 eV/c^2 for the electron neutrino. [1]

The quarks carry a fractional electrical charge of $+\frac{2}{3}|e|$ or $-\frac{1}{3}|e|$ and they are grouped into pairs differing by one unit of charge. There are 6 *flavours* of quarks. The up (u) and down (d) quarks are the lightest, most stable ones, and each have two heavy unstable versions called the charm (c), strange (s), top (t) and bottom (b) quarks. As we shall see later, one needs to introduce an extra degree of freedom for the quarks, called *colour*. Each flavour of quark then comes in three different colours: red, green and blue. A direct consequence of this extra property is that *hadrons*, particles that are made out of constituent quarks, can only exist in two configurations. First, one has the *baryons* that consist out of three quarks, and second, the *mesons* that contain a quark and anti-quark combination. The basic requirement here is that hadrons are colour neutral particles. Two famous examples of such baryon particles are the proton (uud) and neutron (udd). This implies that all common material of the present universe, i.e. the stable particles, can be made with only three fundamental particles: the up quark, down quark and electron. A common example of a meson is the *pion* (π), which can exist in three compositions: π^+ ($u\bar{d}$), π^- ($d\bar{u}$) and π^0, which is actually either a $u\bar{u}$ or $d\bar{d}$ combination. [1]

The Standard Model also describes the interactions, with the exception of gravity, the elementary particles can have. These interactions are mediated through the exchange of gauge *bosons*, which are particles of integral spin, between the fermions. The *Weak* interactions are e.g. responsible for the well known slow nuclear β-decay process, and are mediated by the massive $W^{\pm}$ and Z^0 bosons. The *electromagnetic* interactions are much stronger and are mediated through the exchange of massless *photons*. They are

responsible for virtually any phenomenon one can see in everyday life, i.e. the existence of atoms, molecules and their forces in liquids and solids. The last and strongest type of interactions are conveniently called the *Strong* interactions. They bind the quarks in proton and neutrons, and in turn bind protons and neutrons in nuclei. It thus describes the interactions between all hadrons and it is this type of interaction that is subject of the thesis. It is mediated through the exchange of a massless particle called the *gluon*. To indicate the relative magnitudes of these fundamental interactions, the comparative strengths of the force between two protons, when just in contact, are roughly as [1]:

strong	electromagnetic	weak
1	10^{-2}	10^{-7}

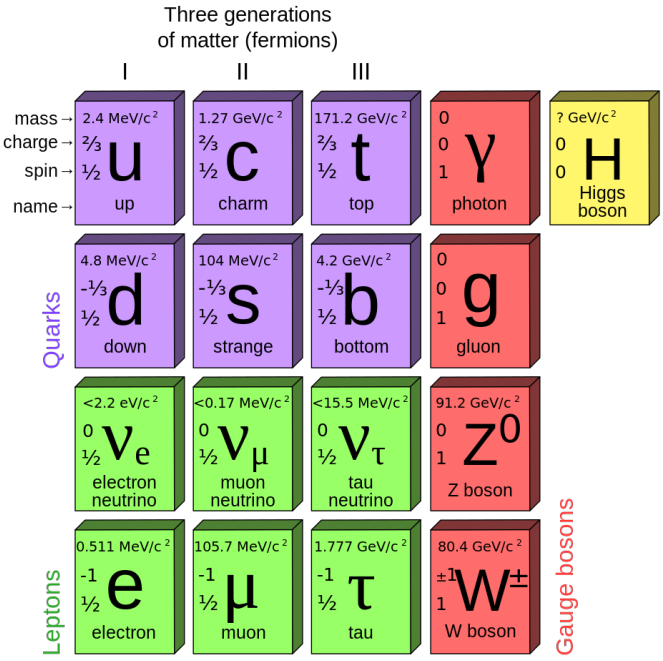

Figure 1.1.: A schematic view of the Standard Model of elementary particles, grouped according to type and generation. Their known mass, charge and spin properties are indicated in the table.

The combination of the electromagnetic and weak interactions by Glashow [2] into a unified electro-weak theory, which was soon extended in 1967 by Weinberg [3] and Salam [4] to incorporate the electro-weak symmetry breaking mechanism [5, 6, 7], which is responsible for the generation of the masses of the fermions and W,Z gauge bosons, formed the basis for the Standard Model. After that, the theory of the strong interactions, which we will describe onwards, was added to the existing electro-weak gauge symmetries into a $SU(3) \times SU(2) \times U(1)$ group. The recent discovery in July 2012 [8, 9] of a new scalar boson could be compatible with a Standard Model *Brout-Englert-Higgs* boson that arises from the proposed electro-weak symmetry breaking.

1.2. Quantum Chromodynamics

Quantum Chromodynamics (QCD) is the theory of strong interactions between hadrons. It is a self-consistent relativistic quantum field theory, based on a non-abelian SU(3) gauge symmetry (Yang-Mills theory) [10] [11]. The fields then represent the quarks and gluons that we introduced before, and the gauge group acts on the colour indices. The introduction of the extra colour degree of freedom was a resolution to the dilemma of the observed spectra of low mass mesons and baryons and the requirement of Fermi-Dirac statistics that the wave function obeys a total antisymmetry. In this view only colour singlet states are allowed, which are precisely the mesons and baryons.

Just as in Quantum Electrodynamics (QED), we can define QCD by a Lagrangian density from which the Feynman rules can be derived that describe the basic interactions between quarks and gluons. These Feynman rules are then used to perform a perturbative analysis of QCD processes. The expression for the classical Lagrangian density is:

$$\mathcal{L}_{\text{classical}} = -\frac{1}{4} F^A_{\alpha\beta} F^{\alpha\beta}_A + \sum_{\text{flavours}} \bar{q}_a \left(i \not{D} - m \right)_{ab} q_b. \tag{1.1}$$

This describes the interaction of spin-$\frac{1}{2}$ quarks, which are the Dirac fields q_a (a = 1, 2, 3) in the colour triplet representation, of mass m and massless spin-1 gluons. Here $\not{D} = \gamma_\mu D^\mu$ is the covariant derivative that acts on a general field ψ as:

$$D_\mu \psi = \left(\partial_\mu + i g t^A \mathcal{A}^A_\mu \right) \psi, \tag{1.2}$$

with g a coupling constant that determines the strength between the interacting coloured quanta and t^A the standard generating matrices of the SU(3) group, acting on the colour indices (A) of ψ. The gluon field $\mathcal{A}^A_\mu$ and coupling g are also present in the Lagrangian's field strength tensor:

$$F^A_{\alpha\beta} = \partial_\alpha \mathcal{A}^A_\beta - \partial_\beta \mathcal{A}^A_\alpha - g f^{ABC} \mathcal{A}^B_\alpha \mathcal{A}^C_\beta, \tag{1.3}$$

where the indices A,B,C run over the eight colour degrees of freedom of the gluon field. Here f^{ABC} are the structure constants of the SU(3) gauge group, defined such that $\left[t^A, t^B\right] = i f^{ABC} t^C$. The third non-Abelian term in the expression of the field strength tensor $F^A_{\alpha\beta}$ is what makes QCD different from QED. It is this term that gives rise to triplet and quartic gluon self-interactions as they actually carry a colour charge. This will lead to the specific behaviour of the strong coupling constant that we will discuss next. The main property of the Lagrangian defined above is that it is invariant under local gauge transformations. This means that one can perform an arbitrary redefinition of the quark fields at every space-time point without changing the physics of the theory.

The theory of QCD has two crucial properties: *confinement* and *asymptotic freedom*. The confinement of hadrons states that it is not possible for isolated quarks and gluons to appear, as it is experimentally validated. Asymptotic freedom means that the effective

coupling of QCD goes to zero at a zero interaction distance. Both of these effects are a direct consequence of the running of the strong coupling constant α_S.

In QED it is proven [12] that the divergencies, which appear through the vacuum polarisation diagrams when one wants to include higher orders in α in the perturbative analysis, can be avoided by a *renormalisation*. This procedure hides these divergencies by a redefinition of the charge, mass or wave function of the electron. One can then e.g. absorb the divergent part of a e^-e^+ loop in a photon propagator into the physical, measurable, charge e_R that is a function of the bare charge e_0, which corresponds to a electron-photon coupling in a Feynman diagram. The relation between e_R and e_0 has to be specified at a particular value of the virtual photon's momentum and due to this a free parameter μ enters the theory. Different choices of μ, usually called the *renormalisation scale*, will then lead to different expansions of e.g. the invariant amplitude $\mathfrak{M}$. But $|\mathfrak{M}|^2$ is a physical observable, hence it must be independent on the value of μ. This requirement leads to the renormalisation group equation:

$$\mu \frac{d\mathfrak{M}}{d\mu} = \left(\mu \left. \frac{\partial}{\partial \mu} \right|_e + \mu \frac{\partial e}{\partial \mu} \frac{\partial}{\partial e} \right) \mathfrak{M} = 0. \tag{1.4}$$

Here the dependence of the invariant amplitude on μ must be cancelled by the dependence of the charge e on μ. Hence the charge measured in an experiment depends on the energy scale Q^2 of that particular measurement, and the coupling constant $\alpha\left(Q^2\right) = e^2\left(Q^2\right)/4\pi$ is then a *running coupling constant*:

$$\alpha\left(Q^2\right) = \frac{\alpha\left(\mu^2\right)}{1 - \frac{\alpha(\mu^2)}{3\pi} \log\left(\frac{Q^2}{\mu^2}\right)}. \tag{1.5}$$

In QED the running of the coupling describes how the effective charge depends on the separation of two charged particles. By summing a part of all orders in α of perturbation theory, a charge screening actually happens. That is, when the separation of the particles increases the effective coupling decreases since the vacuum polarisation diagrams screen the charge seen by the other particle. When the distance decreases however, the coupling increases as the particles can feel each others charge much better.

The calculations performed above also apply on the strong coupling constant α_S in QCD. The behaviour of the running will be completely different however. This is due to the extra terms that arise in the α_S expansion from the self-coupling of the colour charged gluons. These extra terms change the coefficient of $\log\left(Q^2/\mu^2\right)$ such that the expression for $\alpha_S\left(Q^2\right)$ becomes:

$$\alpha_S\left(Q^2\right) = \frac{\alpha_S\left(\mu^2\right)}{1 + \frac{\alpha_S(\mu^2)}{12\pi}\left(33 - 2n_f\right) \log\left(\frac{Q^2}{\mu^2}\right)}, \tag{1.6}$$

where n_f equals the number of active quark flavours. Since there are only 6 known quark flavours, the coefficient of $\log\left(Q^2/\mu^2\right)$ is positive, which leads to a opposite behaviour

of the coupling in QCD than the one in QED. Indeed, when the scale Q^2 increases, the strong coupling α_S will decrease and at sufficiently high values of Q^2 the quarks will act as quasi-free particles, which is the *asymptotic freedom* property of QCD. On the other hand, when the energy scale decreases, the coupling will increase rapidly leading to the *confinement* of hadrons. It is customary to express the Q^2 scale at which this happens as Λ^2, which also absorbs the free parameter μ that is a relic of the renormalisation:

$$\Lambda^2 = \mu^2 \exp\left[\frac{-12\pi}{(33-2n_f)\,\alpha_S\,(\mu^2)}\right], \tag{1.7}$$

from which the expression of α_S can be rewritten as:

$$\alpha_S\left(Q^2\right) = \frac{12\pi}{(33-2n_f)\log\left(Q^2/\Lambda^2\right)}. \tag{1.8}$$

This peculiar behaviour of the strong coupling constant in QCD has the following key consequences:

- Short distance processes, characterised by a high Q^2, can be calculated correctly by perturbation theory due to the sufficient small coupling α_S.
- Long distance processes, characterised by a low Q^2, can not be calculated by means of perturbation theory since the coupling is too high. This means that many primary phenomena such as the simple bound states of quarks into protons or pions are not amenable to direct calculation, but are instead very difficult and non-perturbative.

This situation leads to the introduction of the *hard-scattering factorisation*: when calculating an observable, e.g. the cross section of a process, one will factorize the perturbative calculation of the hard scatter cross section from the non-perturbative part that can not be calculated, but can measured from experiment. The convolution of these two elements then enables one to calculate the final observable.

Experimental measurements of the running of the coupling constant α_S provide a beautiful confirmation of the above calculated predictions in the QCD framework. Figure 1.2 shows the latest result of the CMS experiment of a α_S measurement [13], compared with previous measurements conducted at lower energies. One can clearly see the asymptotic behaviour as predicted in the theory, which has a good agreement with all data. The CMS experiment measured the value of α_S at the scale $Q = 764$ GeV, and then used the renormalisation group equations to evolve this as a function of Q. The coupling at the mass of the Z boson is then found to be $\alpha_S\left(M_Z\right) = 0.1148^{+0.0055}_{-0.0023}$. The results show that, already at scales of the order of a few GeV, the coupling is small enough to perform perturbative calculations.

In the next chapters we shall elaborate more on the description of hadron scatterings in the framework of QCD. To do this we will first review the structure of those particles and describe how this lead to the widely accepted collinear factorisation ansatz, with its

corresponding limitations. Next we will introduce the phenomenology of the underlying event and how this can be integrated in Monte Carlo models.

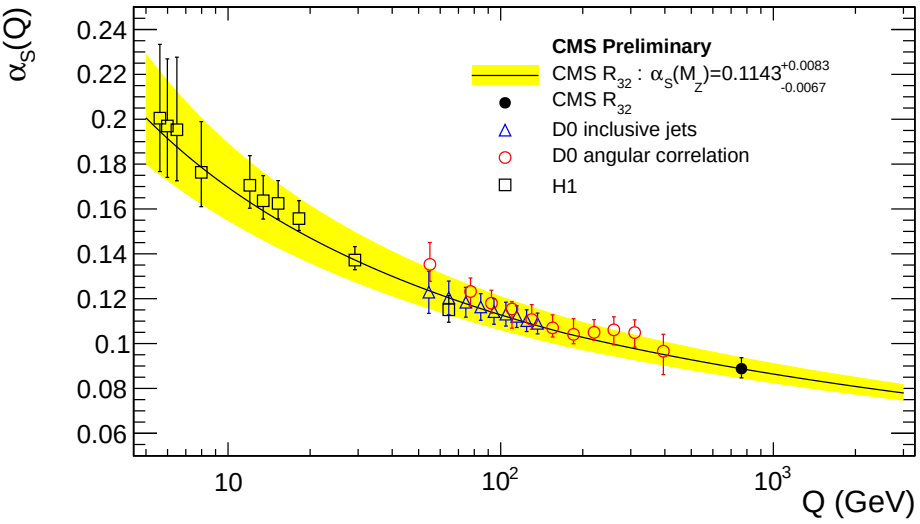

Figure 1.2.: The strong coupling $\alpha_S(Q)$ (black line) and its total uncertainty (yellow band) evolved from the CMS determination at $Q = 764$ GeV. Using the renormalisation group equations the value of α_S at M_Z has been determined: $\alpha_S(M_Z) = 0.1148^{+0.0055}_{-0.0023}$. The measurement is shown together with results from the H1 and D0 experiments at the HERA and Tevatron colliders. [13]

1.3. Kinematics and cross sections

Before we start it is interesting to review the most commonly used expressions and observables in the kinematical treatment of fundamental particle interactions. These definitions will be used throughout the thesis, and to avoid the need to introduce them with each equation, a summary is presented here, which the reader can use as an internal reference.

Let us look at a basic $2 \to 2$ process, shown in figure 1.3, in which two incoming particles with four-momenta p_1, p_2 scatter and produce a final state of two particles with four-momenta p_3, p_4.

We can then define the *centre-of-mass system* in which

$$\mathbf{p}_1 + \mathbf{p}_2 = 0. \tag{1.9}$$

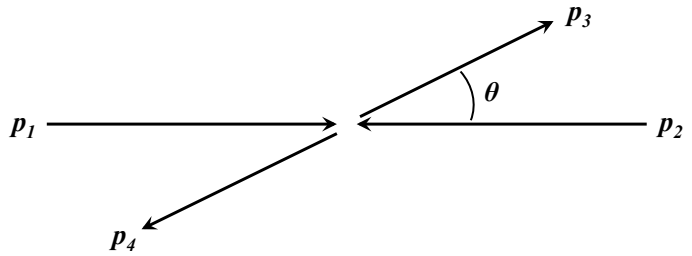

Figure 1.3.: The centre-of-mass system.

Assigning a right handed coordinate system to the interaction, with the convention that particle p_1 moves in the $+z$ direction, we can write:

$$\begin{aligned} p_1 &= (E_1, \mathbf{p}) = (E_1, 0, 0, p_z) && (1.10)\\ p_2 &= (E_2, -\mathbf{p}) = (E_2, 0, 0, -p_z) && (1.11)\\ p_3 &= (E_3, \mathbf{p}') = (E_3, \mathbf{p}_T, p_z') && (1.12)\\ p_4 &= (E_4, -\mathbf{p}') = (E_4, -\mathbf{p}_T, -p_z'), && (1.13) \end{aligned}$$

in which we have used (1.9) and the conservation of three-momentum. We have introduced the *transverse momentum* $\mathbf{p}_T$ of a particle that can be written as

$$|\mathbf{p}_T| = |\mathbf{p}'| \sin\theta = \sqrt{p_x^2 + p_y^2}, \tag{1.14}$$

with θ the angle with respect to the z axis. It is furthermore customary to introduce the *Mandelstam variables*:

$$\begin{aligned} s &= (p_1 + p_2)^2 = (p_3 + p_4)^2 && (1.15)\\ t &= (p_1 - p_3)^2 = (p_2 - p_4)^2 && (1.16)\\ u &= (p_1 - p_4)^2 = (p_2 - p_3)^2, && (1.17) \end{aligned}$$

which obey the identity:

$$s + t + u = \sum_{i=1}^{4} m_i^2, \tag{1.18}$$

with m_i the masses of the particles. If we have the process $p_1 + p_2 \to p_3 + p_4$, the Mandelstam variable s equals the *centre-of-mass energy* squared, and t is the *momentum transfer* squared. Such interactions are called *s-channel* processes. Analogously one can define *t-channel* and *u-channel* processes in which t and u are the centre-of-mass energy squared respectively. In the high energy limit ($E \simeq |\mathbf{p}|$) the masses can be neglected and in the centre-of-mass system one can then write:

$$E_1 + E_2 = E_3 + E_4 = \sqrt{s}, \tag{1.19}$$

with $\sqrt{s}$ the available centre-of-mass energy in a particle collision. Another frequently used kinematic variable is the *rapidity* of a particle. In the same coordinate system as above it is defined as

$$y = \frac{1}{2} \ln \frac{E + p_z}{E - p_z}, \tag{1.20}$$

which in the high energy limit, or for massless particles, can be directly related to the angle θ:

$$\eta \equiv y|_{m=0} = -\ln \tan \frac{\theta}{2}, \tag{1.21}$$

where we have defined the *pseudorapidity* η of a particle. A very useful property of the rapidity is that it transforms additively under a Lorentz boost along z, and hence any rapidity difference is invariant under such longitudinal boosts. Particles that are produced at high, or large, rapidities have a very small angle θ and are said to be produced in the *forward* region of the phase space. In experiments this usually means that they are very close to the beampipes of the accelerator.

One of the most basic observables used in high energy particle physics that characterises any fundamental interaction is the *cross section* σ. It can in general be expressed as follows:

$$d\sigma = \frac{1}{\Phi} \cdot d\text{Lips} \cdot \left|\mathfrak{M}\right|^2, \tag{1.22}$$

with $|\mathfrak{M}|^2$ the squared *matrix element* or invariant amplitude that contains the underlying physics, i.e. it includes the coupling constants and Feynman propagator terms. The cross section is inversely proportional to the flux Φ of the incoming particles, which is written as

$$\Phi = 4\sqrt{(p_1 \cdot p_2)^2 - m_1^2 m_2^2}, \tag{1.23}$$

in the case of two incoming particles that undergo a collinear collision, i.e. in any frame where $\mathbf{p}_1$ is parallel to $\mathbf{p}_2$. The factor $d\text{Lips}$ is the *Lorentz invariant phase space* and is defined as

$$d\text{Lips} = (2\pi)^4 \delta^4 \left(-p_1 - p_2 + \sum_i p_i \right) \prod_{i>2} \frac{d^3 p_i}{(2\pi)^3 2E_i}, \tag{1.24}$$

where the sum i runs over all final state particles. The differential cross section, as a function of the momentum transfer t, for a basic $2 \to 2$ process with $p_1 + p_2 \to p_3 + p_4$ (s-channel) can then be written as

$$\frac{d\sigma}{dt} = \frac{1}{16\pi s^2} \left|\mathfrak{M}\right|^2, \tag{1.25}$$

where we assumed that we are working in the large s limit and masses can be neglected. The *total* cross section of a process, e.g. a proton-proton collision, exists out of different components that correspond to different types of scattering. The first two physically distinguishable types are *elastic* and *inelastic* scattering:

$$\sigma_{tot}(s) = \sigma_{el}(s) + \sigma_{inel}(s). \tag{1.26}$$

Elastic scatterings consist of all interactions of the type $A(p_A) + B(p_B) \to A(p'_A) + B(p'_B)$. The only exchanged quantity is thus momentum, and the particles do not break up. Inelastic scatterings cover everything else: $A + B \to X$ where $X \neq AB$ can be anything. The particles thus break up, exchange one or more quantum numbers and produce a system X. If A and B are made out of constituent particles (e.g. protons), inelastic scatterings can in turn be divided into different types:

$$\sigma_{inel}(s) = \sigma_{sd}(s) + \sigma_{dd}(s) + \sigma_{cd}(s) + \sigma_{nd}(s). \tag{1.27}$$

Here σ_{sd}, σ_{dd} and σ_{cd} are the cross sections of *diffractive* topologies. This is a qualitative classification that is usually based on whether the final state resembles the decay of an excitation of the incoming particles, or upon the presence of a large *rapidity gap* (Δy) in the final state that is a region in phase space where no particles are produced, and would thus separate such excitations. In addition, there are several types of diffractive events: a) *single diffractive dissociation* (SD) in which only one incoming particle gets excited and the other survives, b) *double diffractive dissociation* (DD) where both incoming particles get excited and do not survive the interaction, and c) *central diffraction* (CD) where both incoming particles survive, but leave an excited system in the central region between them. The latter type is sometimes called *central exclusive production*. The last type, σ_{nd}, represents the *nondiffractive inelastic scatterings* in which the incoming particles do not survive the interaction, and produce a final state in which no large rapidity gaps are present. This latter type of events will be subject to the measurement performed in this work. A last type of classification made distinguishes between *inclusive* and *exclusive* cross sections (or events). The inclusive cross section takes all the possible final states of a particle collision into account, while an exclusive cross section only represents the production of a specific final state that one is interested in (e.g. production of a Higgs boson).

More detailed information about the kinematics and cross sections of fundamental interactions can be found in the used references [12, 14, 15].

Chapter 2.

Description of hadron collisions

We start the discussion in this chapter by looking at the scattering of an electron on a proton, which is commonly referred to as a *deep inelastic scattering* (DIS) process $ep \to eX$. This process has been used quite extensively throughout history to study and probe the structure of hadrons, even long before the actual foundations of QCD were made. It is thus ideal to introduce the now widely accepted methods that one uses to describe a scattering that involves hadrons. We will then see how this can be generalised and ported to hadron-hadron collisions, which are the type of scatterings studied in this work. We will conclude by stating the apparent limitations, and briefly provide alternative approaches.

2.1. Deep inelastic scattering

In physics it is common practice to scatter photons or electrons on a target to study its structure. If the wavelength λ of the probe has approximately the same length as the size d of the target, one can study its shape and properties by analysing the angular distribution of the scattered particles. However, if one wants to study the internal structure, the wavelength of the probe has to be smaller than the size of the target. That is, a smaller wavelength corresponds to a higher energy of the probe, which can then break up the target. The scatter is then called *deep* (a high energetic photon penetrates deep into the target) and *inelastic* (the target breaks up).

2.1.1. Structure functions

Before we can calculate the cross section of a deep inelastic $ep \to eX$ scattering, one needs to introduce the process more rigorously and define its specific kinematics. Figure 2.1 shows the lowest order Feynman diagram of such a scatter. An incident electron with four-momentum k emits a virtual photon with four-momentum $q = k - k'$, with k' the four-momentum of the outgoing electron. The incident proton with four-momentum p, illustrated as the circle (to emphasise our ignorance about its sub-structure), interacts somehow with the virtual photon and breaks up in different fragments (1,..,N). The four-

momentum of the hadronic final state is then defined as the sum of the two four-momenta q and p. The DIS process is characterised by following two independent variables [12]:

$$Q^2 \equiv -q^2 \qquad\qquad \nu \equiv \frac{p \cdot q}{M}, \tag{2.1}$$

with M the mass of the proton and $\nu = E - E'$ in the proton rest frame, with E en E' the initial and final electron energy respectively. Above variables can also be expressed in a dimensionless form [12]:

$$x = \frac{-q^2}{2p \cdot q} = \frac{-q^2}{2M\nu} = \frac{Q^2}{2M\nu} \qquad\qquad y = \frac{p \cdot q}{p \cdot k}. \tag{2.2}$$

Using this notation the allowed kinematic region then has the following ranges: $0 \leq x \leq 1$ and $0 \leq y \leq 1$. With this variables one can express the invariant mass W as follows [12]:

$$W^2 = (p+q)^2 = p^2 + 2p \cdot q + q^2 = M^2 + 2M\nu + q^2 = M^2 + \frac{Q^2}{x} - Q^2. \tag{2.3}$$

Deep inelastic scatterings are then processes in which $Q^2 \gg M^2$ and $W^2 \gg M^2$.

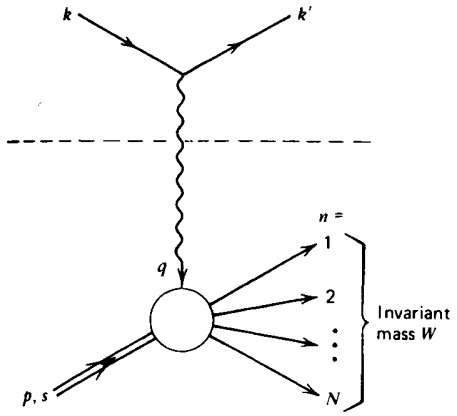

Figure 2.1.: Lowest order Feynman diagram of a deep inelastic $ep \to eX$ scattering. [12]

After the introduction of the relevant kinematics one can now perform a calculation of the cross section. If the process would have been elastic, one could simply use the results of a calculation for the $e^-\mu^- \to e^-\mu^-$ process by replacing the muon with a proton. This is possible since one can change the lepton current $j^\mu \sim \bar{u}\gamma^\mu u$ (with $u, \bar{u}$ Dirac spinors and γ^μ the gamma matrices) by a proton current J^μ that contained specific form factors to take into account the unknown structure of the proton (see [12]). This is however not possible for inelastic scatterings, since the final state of the proton can not be described as one fermion. Hence, to calculate the cross section (σ) one needs to express it as a product of a leptonic tensor ($L^e_{\mu\nu}$) and a hadronic tensor ($W^{\mu\nu}$) [12]:

$$d\sigma \sim L^e_{\mu\nu} W^{\mu\nu}. \tag{2.4}$$

The leptonic tensor represents what happens in the upper part of figure 2.1 and is exactly the same as in $e^-\mu^- \to e^-\mu^-$ scatterings [12]:

$$L^e_{\mu\nu} = \frac{1}{2} Tr\left(\left(\not{k}' + m\right)\gamma_\mu\left(\not{k} + m\right)\gamma_\nu\right), \tag{2.5}$$

in which we used the notation $\not{k} = \gamma^\mu k_\mu$. The hadronic tensor represents the bottom part of the diagram in figure 2.1 and describes what happens at the end of the photon propagator. Since we don't know anything about the internal structure of the proton, we have to start by expressing it in its most general form possible. We can do this by using the metric tensor $g^{\mu\nu}$ and the independent momenta p en q [12]:

$$W^{\mu\nu} = W_1(\nu, q^2)\left(-g^{\mu\nu} + \frac{q^\mu q^\nu}{q^2}\right) + \frac{W_2(\nu, q^2)}{M^2}\left(p^\mu - \frac{p\cdot q}{q^2}q^\mu\right)\left(p^\nu - \frac{p\cdot q}{q^2}q^\nu\right), \tag{2.6}$$

where we neglected ep interactions through the exchange of a Z boson, by assuming an energy scale $Q^2 \ll M_Z^2$ that facilitates the dominance of virtual photon exchange. The introduction of the two independent factors $W_i(\nu, q^2)$, which we will call *structure functions*, is our very first encounter with the idea that we can factorize the elements we do not know into $W_i(\nu, q^2)$ functions, and separate it from what we do know (the momenta p and q). The interesting thing about the introduction of the $W_i(\nu, q^2)$ functions is that now we can use the cross section of $e^-\mu^- \to e^-\mu^-$ processes to calculate the one for $ep \to eX$. Simply because all the unknown features that arise when going from a muon to a proton scattering are now absorbed in the structure functions. Hence it is sufficient to replace the original muon tensor $L^{muon}_{\mu\nu}$ with the above introduced $W^{\mu\nu}$ tensor. We can then derive the $ep \to eX$ cross section [12]:

$$\frac{d\sigma}{dE' d\Omega} = \frac{4\alpha^2 E'^2}{q^4}\left(W_2\left(\nu, q^2\right)\cos^2\frac{\theta}{2} + 2W_1\left(\nu, q^2\right)\sin^2\frac{\theta}{2}\right), \tag{2.7}$$

with E' and θ respectively the energy and angle of the final state electron.

As mentioned before, if the virtual photon is able to penetrate deep enough into the proton, it can see the point-like quark constituents that we assume to be quasi-free Dirac particles. Thus at sufficiently large Q^2 values we can then describe the inelastic electron-proton interaction as an elastic electron-quark interaction. We can use this analogy and express the structure functions in a dimensionless form (see [12]) so they only depend on the ratio $Q^2/2m\nu$ (with m the mass of the proton constituent), and not on Q^2 and ν separately. As a consequence the mass m only acts as a scaling variable for the Q^2 and ν momenta. In the limit of high momentum transfers $Q^2 \gg M^2, m^2$ we can introduce following more common notation for the structure functions [12]:

$$MW_1(\nu, Q^2) \overset{\text{high } Q^2}{\longrightarrow} F_1(x) \tag{2.8}$$

$$\nu W_2(\nu, Q^2) \overset{\text{high } Q^2}{\longrightarrow} F_2(x), \tag{2.9}$$

in which x is the defined DIS kinematic variable from 2.2. Hence if the proton exists out of quasi-free point-like particles, on which the photon elastically scatters, the introduced structure functions have to be independent of Q^2 for a certain value of x. This behaviour, which is called *Bjorken scaling*, was indeed confirmed at very early DIS measurements with the Stanford Linear Accelerator [12]. These seem to validate the picture we have drawn above.

2.1.2. The parton model

In parallel to the developments made during the direct study of DIS processes, Feynman introduced a general model to describe the structure of hadrons, and how they interact. This *parton model* existed long before the invention of QCD and combines motivations coming from field theory, combined with phenomenology from hadronic interactions. The basic assumption is that interactions of hadrons are due to the interactions of their *partons*, which can either be quarks or gluons, that each carry a fraction x of the hadron's momentum. Note however that the momentum fraction x, as defined in the parton model, *does not necessarily* need to coincide with the variable x from the DIS process.

The structure of a hadron is then described by an instantaneous distribution of partons. To achieve this so called *parton distribution functions* $f_i(x)$ were introduced: they represent the probability that a parton i carries a fraction x of the total hadron's momentum p. Since the sum of all fractions must be equal to the total hadron momentum one gets following relation [12]:

$$\sum_i \int dx f_i(x) x = 1. \tag{2.10}$$

With the introduction of the parton distribution functions, we can now rewrite the DIS F_1 and F_2 structure functions in terms of $f_i(x)$ [12]:

$$F_2(x) = \sum_i e_i^2 f_i(x) x \tag{2.11}$$

$$F_1(x) = \frac{1}{2x} F_2(x), \tag{2.12}$$

with the assumption that the momentum, energy and mass (m) of the parton can be expressed as xp, xE en xM with p, E and M the momentum, energy and mass of the proton. At this point e_i^2 represents the charge of parton i. For the DIS process the parton momentum fraction x is then [12]:

$$x = \frac{Q^2}{2M\nu}. \tag{2.13}$$

Thus also the parton distribution functions are independent of the energy scale Q^2 and obey the Bjorken scaling. In this particular model they only depend on the momentum

fraction x of the probed parton. The expression $2xF_1 = F_2$ is called the *Callan-Gross* relation and enables us to calculate one function if the other is known.

At this point however, it is interesting to state all the approximations and assumptions one intrinsically made to come at this stage in the parton model. The key point is to stress that all above kinematics and derivations are only valid when we are working in the proton's *infinite momentum frame*. In this frame, where the proton is moving with an infinite momentum, all the masses of the partons (m) and proton (M) can be neglected: $|\vec{p}| \gg m, M$. Only then the above used kinematical expressions are justified, including the fact that we implicitly assumed the partons to move parallel with the proton ($p_T = 0$). In addition, this frame also justifies our claim that the partons can be treated as quasi-free particles: due to the relativistic time dilation the interaction of the virtual photon with the parton happens at a much shorter time scale than the interaction of the partons with one another inside the proton. We can thus argue that in a *hard* scattering, i.e. a scattering with a high momentum transfer Q^2, the parton recoils as if it was free, which enables us to calculate the $ep \to eX$ cross section. The use of the infinite momentum frame to calculate a DIS cross section is justified since this type of process exactly demands $Q^2 \gg M^2$ and $W^2 \gg M^2$. [12]

2.1.3. Experimental measurements

In the previous sections we conveniently put all the incalculable elements into the factors $F(x)$ to derive an expression for the cross section. It is then of course necessary to measure these structure functions in DIS experiments at different regions in phase space. As mentioned before, early measurements seemed to confirm the predicted Bjorken scaling behaviour, which justified our quasi-free particle picture of the proton. However, more recent measurements of the proton structure functions at the HERA accelerator have revealed that the Bjorken scaling is violated. That is, when one goes to lower or higher values of the fraction x the measured structure functions actually depend on Q^2. One of the latest measurements of the $F_2(x, Q^2)$ function is presented in figure 2.2 and shows that at very low values of x the structure function increases with Q^2, while at very high x the structure function decreases with Q^2.

From the measurement of the structure functions, one can then also derive the parton distribution functions by using (2.11). Figure 2.3 shows such distributions, as a function of x at a fixed value $Q^2 = 10$ GeV^2, derived from the $F_2(x, Q^2)$ measurement. At high values of $x \approx 0.2 - 0.3$ one can clearly see the peak of the valence u and d quarks, which is in agreement with the uud picture of a low energy confined proton introduced in the first chapter. The distributions of the gluons (xg) and so called *sea quarks* (xS) however are small at high values of x, but rise very strong with decreasing x (they are scaled down in the figure by a factor 20 with respect to the valence quark contributions). This last feature is again something we would not expect to see in our naive parton model. Another feature that could become visible when going to even lower x values, is *parton*

saturation: taking into account that the proton has a finite size, one expects that the strong rise of the parton densities will be tamed at very small values of x.

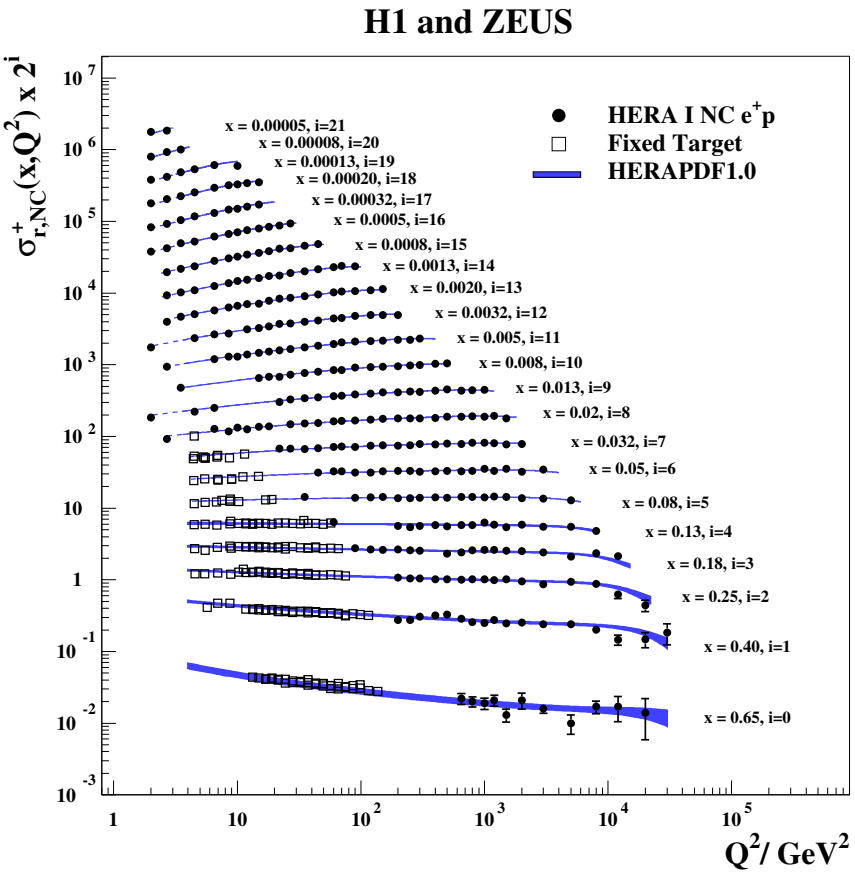

Figure 2.2.: The structure function $F_2(x, Q^2)$ as a function of Q^2, measured at different values of x in DIS scattering at the HERA accelerator. [16]

2.2. QCD corrections to the parton model

The reason for the violation of the Bjorken scaling, and the strong rise of the parton densities at low x values, is that the naive parton model does not take into account the necessary (Quantum Chromo)*dynamics*. Indeed, if we recall our description of the QCD field theory in chapter 1, the picture of an instantaneous distribution of quasi-free partons inside a proton is not correct. We saw that the non-abelian terms in the Lagrangian give rise to self-couplings of colour charged gluons and that, just as in QED, also vacuum polarisation diagrams (creation of $q\bar{q}$ pairs in this case) have to be taken into account. That was the origin of the renormalisation and the peculiar running of the coupling constant as a consequence. However the diagrams of the DIS process we considered until

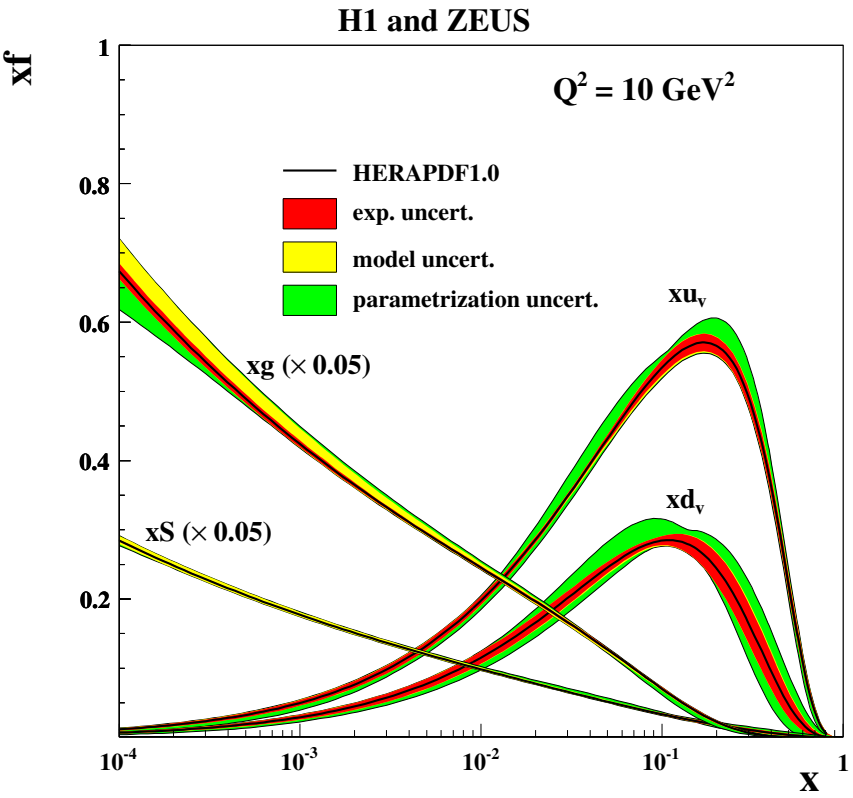

Figure 2.3.: The parton distribution functions $f_i(x)$ as a function of x at a momentum transfer $Q^2 = 10$ GeV as obtained from the measured $F_2(x, Q^2)$ structure functions. The contributions of the gluons (xg) and sea quarks (xS) are scaled down by a factor 20. [16]

now, only represented the lowest order coupling. Thus we have to extend the parton model and take these quark-gluon interactions into account, and include higher orders into our perturbative calculation.

The first type of such interaction one has to take into account is the *QCD-Compton* (QCDC) process, in which a quark radiates a gluon. From the DIS point of view the initial state $\gamma^* q$ then results in a final state qg: $\gamma^* q \to qg$. This is shown in figure 2.4 in which two contributions are present, as the gluon can be emitted before or after the interaction with the virtual photon. The second interaction is the quark pair production of a gluon and is called *Boson-Gluon Fusion* (BGF). This $\gamma^* g \to q\bar{q}$ process is shown in figure 2.5. In this situation the virtual photon will then interact with one of the quarks produced by gluon constituent of the proton. The inclusion of these interactions means that we will expand our $O(\alpha)$ calculation of the DIS process to $O(\alpha\alpha_S)$, since the quarks and gluons interact with one another through the strong coupling constant α_S. [12]

To include the above introduced interactions into the cross section and structure functions we will use a new notation for the momentum fractions of the partons in the

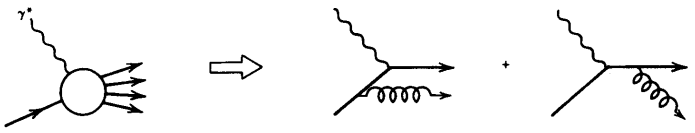

Figure 2.4.: $\gamma^* q \to qg$ contributions to the inclusive $ep \to eX$ process. [12]

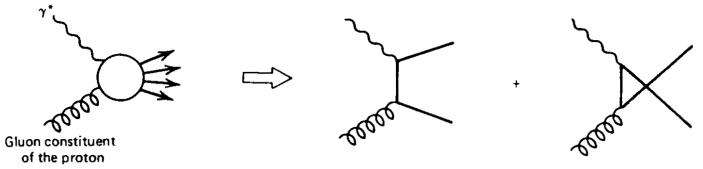

Figure 2.5.: $\gamma^* g \to q\bar{q}$ contributions to the inclusive $ep \to eX$ process. [12]

proton that is shown in figure 2.6. In the naive parton model, x represented the parton's momentum fraction of the total proton momentum. However, since the parton can emit a gluon we can define the momentum fraction before the emission as $p_i = yp$, and the remaining momentum fraction afterwards as zp_i. We then have $zp_i = zyp$ and thus $x = yz$.

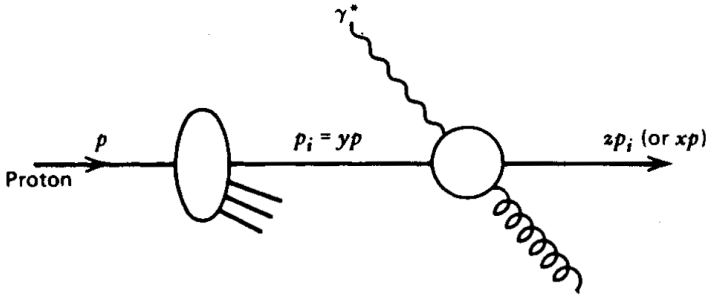

Figure 2.6.: Definition of the different momentum fractions after the inclusion of a $\gamma^* q \to qg$ process. [12]

With this new notation we can then rewrite expression (2.11) of the F_2 structure function in the parton model to [12]:

$$\frac{F_2(x,Q^2)}{x} = \sum_i e_i^2 f_i(x) = \sum_i e_i^2 \int_x^1 \frac{dy}{y} f_i(y) \delta\left(1 - \frac{x}{y}\right). \tag{2.14}$$

If we now want to include the $\gamma^* q \to qg$ and $\gamma^* g \to q\bar{q}$ processes, one needs to calculate their cross sections, which have the following form in leading order (see [12] and [17]):

$$\sigma \sim \frac{\alpha_s}{2\pi} P(z) \log \frac{Q^2}{\kappa^2}, \tag{2.15}$$

where we have introduced the *splitting functions* $P(z)$:

$$\gamma^* q \to qg \quad : \quad P_{qq}(z) = \frac{4}{3}\left(\frac{1+z^2}{1-z}\right) \tag{2.16}$$

$$\gamma^* g \to q\bar{q} \quad : \quad P_{qg}(z) = \frac{1}{2}\left(z^2 + (1-z)^2\right). \tag{2.17}$$

$P_{qq}(z)$ then represents the probability that a quark can emit a gluon at momentum fraction z, and P_{qg} the probability that a gluon produces a $q\bar{q}$ pair with the quark having a momentum fraction z. The introduction of the parameter κ in the cross sections is the consequence of the fact that the quarks and gluons get a transverse recoil k_T when they either emit a gluon or create a $q\bar{q}$ pair. To calculate the total cross section one has to integrate over all possible values of k_T: $\int (1/k_T^2) dk_T^2$. However as $k_T \to 0$ this integral diverges, and hence we have to introduce an artificial cut-off κ. To get rid of this we can apply a similar trick as the one we used to renormalise QCD: we can define scale (μ) dependent parton densities and absorb the collinear divergence into the bare, unmeasurable parton densities. We then have an expression for the structure function F_2 [12, 17]:

$$\begin{aligned}\frac{F_2(x,Q^2)}{x} &= \sum_q e_q^2 \int_x^1 \frac{dy}{y} q(y,\mu^2)\left(\delta\left(1-\frac{x}{y}\right) + \frac{\alpha_s}{2\pi} P_{qq}\left(\frac{x}{y}\right)\log\frac{Q^2}{\mu^2}\right) \\ &+ \sum_q e_q^2 \int_x^1 \frac{dy}{y} g(y,\mu^2)\frac{\alpha_s}{2\pi} P_{qg}\left(\frac{x}{y}\right)\log\frac{Q^2}{\mu^2},\end{aligned} \tag{2.18}$$

in which $q(y,\mu^2)$ and $g(y,\mu^2)$ represent the scale dependent quark and gluon densities respectively. However as the structure function is an observable, it must be independent from the arbitrary scale μ, i.e. $\partial F_2/\partial\mu^2 = 0$, and we can derive a set of renormalisation group equations [12, 17]:

$$\frac{dq_i(x,\mu^2)}{d\log\mu^2} = \frac{\alpha_s}{2\pi}\int_x^1 \frac{dy}{y}\left(q_i(y,\mu^2)P_{qq}\left(\frac{x}{y}\right) + g(y,\mu^2)P_{qg}\left(\frac{x}{y}\right)\right) \tag{2.19}$$

$$\frac{dg(x,\mu^2)}{d\log\mu^2} = \frac{\alpha_s}{2\pi}\int_x^1 \frac{dy}{y}\left(\sum_i q_i(y,\mu^2)P_{gq}\left(\frac{x}{y}\right) + g(y,\mu^2)P_{gg}\left(\frac{x}{y}\right)\right), \tag{2.20}$$

where the sum i runs over all quark flavours. The second line contains contributions from processes in which a colour charged gluon can produce a gluon pair (ggg vertex), and a gluon can radiate a quark. Their corresponding splitting functions are given below [12]:

$$P_{gq}(z) = \frac{4}{3}\left(\frac{1+(1-z)^2}{z}\right) \tag{2.21}$$

$$P_{gg}(z) = 6\left(\frac{1-z}{z} + \frac{z}{1-z} + z(1-z)\right). \tag{2.22}$$

The equations (2.19) and (2.20) are commonly referred to as the *Dokshitzer-Gribov-Lipatov-Altarelli-Parisi* (DGLAP) *evolution equations* in leading order of α_S. They describe the evolution of the parton densities with the scale μ and allow us to predict the parton densities at any scale, once they are determined at another initial scale. We also see that the inclusion of the quark-gluon interactions results in an explicit dependence of the structure function F_2 to the momentum transfer Q^2 (equation 2.18), which is in agreement with the experimental data recorded at the HERA accelerator. In fact, figure 2.2 shows the prediction of the DGLAP evolution (named HERAPDF1.0) that agrees remarkably well with the data over several orders of magnitude. When we include the QCD dynamics into the parton model, more and more fluctuations can be resolved with the increasingly shorter wavelength of the virtual photon, $\lambda = 1/Q$. Thus with Q^2 increasing we have a depletion of quarks at large x, and a growth at low x values. This explains both the behaviour seen in the structure function F_2 at lower x and the growth of the parton distributions shown in figure 2.3. At sufficiently large Q^2 the sea quarks, which we mentioned before and arise from the $g \to q\bar{q}$ processes, will dominate the low x region together with the gluons. [17, 18]

2.3. Collinear factorisation

2.3.1. The ansatz

The procedure we followed in this chapter is commonly referred to as *collinear factorisation*. This implies that the collinear singularities are factorized into process independent parton distributions and separated from the perturbatively calculable, process dependent, hard scattering cross section. One can express the cross section for an electron-proton scattering in the general form:

$$\sigma_{ep} = \sum_i f_{i,p}(\mu_F^2) \otimes \sigma_{ei}(\mu_F^2, \mu_R^2). \tag{2.23}$$

Here $f_{i,p}(\mu_F^2)$ represent the parton distribution functions of parton i in the proton that are dependent of the introduced *factorisation scale* μ_F needed to absorb the collinear divergence into the bare parton densities (see eq. 2.18). $\sigma_{ei}(\mu_F^2, \mu_R^2)$ is the hard scattering cross section that describes the interaction of the virtual photon and the parton i. It is infrared safe and can be calculated in perturbative QCD. It also depends on the factorisation scale μ_F, and in addition also on the renormalisation scale μ_R. The cross section σ_{ei}, sometimes called the *partonic* cross section, then corresponds to the short distance, high energy interactions in QCD that can be perturbatively calculated due to a small coupling, while the parton distribution functions $f_{i,p}$ correspond to the long-distance, low energy interactions in QCD that contain all the infrared sensitivity, and are non-perturbative due to the high value of the coupling. The strength of this factorisation ansatz is that the parton distribution functions are independent of the hard scattering. Once they are measured for a specific hadron, they can be used to calculate

any interaction involving this type of hadron. Although the parton distribution functions can not be calculated from first principles, their evolution with the scale can be calculated perturbatively with the DGLAP equations.

The factorisation scale μ_F defines the scale at which the long and short distance parts are separated and thus which elements of the cross section are factorized in the parton density functions. Different so called *factorisation schemes* are available, and once a scheme has been chosen, it has to be used for both the parton density function and the cross section calculation to get consistent results. Two common schemes are: a) the DIS scheme in which the relation between the structure function F_2 and the parton density is given by (2.11), but where the gluons only enter through the evolution of the quark densities (so $f_i = q_i$). This formula is required to hold at all orders in α_S and is obtained by choosing $\mu_F^2 = Q^2$. b) the modified minimal subtraction ($\overline{MS}$) scheme in which only the divergent parts are absorbed into the quark and gluon densities, which appear separately in the structure function.

The factorisation theorem is only proven for a few processes, i.e. (diffractive) deep inelastic scattering and single particle inclusive spectra. For all other processes it is assumed that one can apply the proposed factorisation. More detailed information about factorisation in QCD can be found in references [11, 17, 19, 20].

2.3.2. Hadron-hadron interactions

The introduced *factorisation theorem* for the DIS process can be extended to certain processes in hadron-hadron collisions. This was first proven during the study of the Drell-Yan process, illustrated in figure 2.7a, in which a lepton pair l^+l^- with a large invariant mass $M^2 = (p_{l+} + p_{l-})^2 \gg 1$ GeV^2 is produced through $q\bar{q}$ annihilation. The quarks are then partons from the incoming hadrons with momenta P_1 and P_2 and carry a momentum fraction x_1P_1 and x_2P_2 respectively.

Applying the factorisation concept one can express the the cross section as:

$$\sigma_{AB} = \sum_q \int dx_1 dx_2 f_q(x_1, M^2) f_{\bar{q}}(x_2, M^2) \hat{\sigma}_{q\bar{q}\to l^+l^-}, \tag{2.24}$$

in which $f_i(x_i, M^2)$ represent the scale dependent (anti-)quark parton distribution functions of the incoming hadrons. The scale μ^2 is set to the invariant mass M^2 of the lepton pair. This expression is valid in the same kinematic region as the one used in DIS ($Q^2, \nu \to \infty$), i.e. $M^2 \to \infty$. In fact it has been found that all the calculations done in the previous sections to describe the DIS cross section, lead to similar results for Drell-Yan process in hadron-hadron collisions. That is, one can start from the naive parton model picture and construct a cross section using factorisation. The parton model is then extended to include perturbative QCD corrections and just as in DIS one can absorb the collinear singularities into the bare parton distribution functions by introducing scale dependent ones. This renormalisation procedure will again lead to the

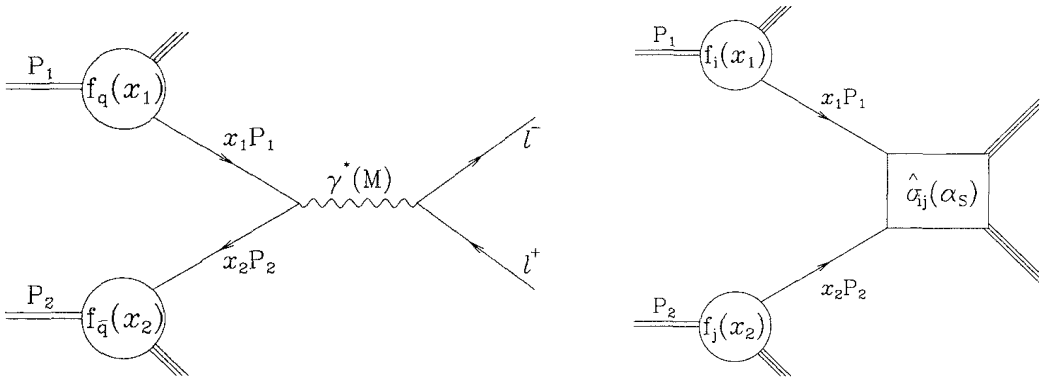

(a) **(b)**

Figure 2.7.: (a) Lepton pair production in the Drell-Yan process through a hard scattering of two partons (x_1P_1 and x_2P_2) from the incoming hadrons. (b) The parton model description for a general hard scattering process ($\hat{\sigma}_{ij}(\alpha_S)$) [11]

DGLAP evolution equations with exactly the same splitting functions. The observation of Drell-Yan lepton pairs with a net transverse momentum p_T was in fact one of the first pieces of evidence that the naive parton model was incomplete, and that the dynamics of QCD had to be added. It indicated that the quarks in the hard scatter can emit gluons with a significant transverse momentum.

The key point is that *all* the collinear divergencies appearing in the Drell-Yan corrections can be factorized into renormalised parton distributions, just as it was in DIS. Factorisation theorems can show that this is a general feature of inclusive hard-scattering processes in hadron-hadron collisions. This is one of the most important results of the QCD parton model: the parton densities, including the renormalisation of the bare parton densities, are the same in DIS lepton-proton scattering and in hadron-hadron scattering. Hence in general one assumes the cross section for a hard scattering process initiated by two hadrons, illustrated in figure 2.7b, can be written as

$$\sigma(P_1, P_2) = \sum_{i,j} \int dx_1 dx_2 f_i(x_1, \mu^2) f_j(x_2, \mu^2) \hat{\sigma}_{ij}(p_1, p_2, \alpha_S(\mu^2), Q^2/\mu^2), \tag{2.25}$$

in which $p_1 = x_1P_1$ and $p_2 = x_2P_2$ are the momenta of the partons that participate in the hard interaction. The scale of the hard scattering is Q^2, and $\hat{\sigma}_{ij}$ is the short distance cross section for the scattering of partons i and j. For simplicity the factorisation and renormalisation scales are set to a single scale $\mu = \mu_F = \mu_R$. [11, 17]

2.3.3. Limitations

Although the collinear factorisation theorem is widely accepted and used, it is only proven for a limited number of processes and significant approximations were made in

the derivation. Nevertheless it is performing very well, as we shall see later, but at some point we expect it to fail.

The first significant approximation concerns the treatment of the transverse momenta of the partons. When discussing the DIS process we systematically neglected the masses and transverse momenta in the kinematics of the initial state. But after the introduction of perturbative QCD corrections to the parton model, this picture is not consistent anymore. Due to the parton evolution, an initial state parton can have a significant transverse momentum: e.g. if a collinear gluon produces a $q\bar{q}$ pair, the quarks must have opposite transverse momenta. Thus evolving a parton from scale μ_0^2 to a larger scale μ^2 should automatically include their transverse momenta from the start.

The next limitation of the factorisation theorem comes into the game when we look closer to hadron-hadron collisions. In this case one can make following observations:

- In the general expression for the cross section (2.25) the parton distribution functions $f_i(x_1, \mu^2)$ and $f_j(x_2, \mu^2)$ are assumed to be independent from each other. However one has to assess whether the partons in hadron P_1 change the distribution of partons in hadron P_2 before the actual hard scattering. This can be due to the influence of their colour fields, especially soft gluons that can be emitted long before the collision could have a significant effect. It can be shown [11] however that the force experienced by a charge in hadron P_2, generated by the passage of a fast moving charge (hadron P_1), decreases as m^4/s^2 with s the centre-of-mass energy squared. Hence a breakdown of factorisation at order $1/s^2$ is expected in perturbation theory.

- In the factorisation theorems discussed until now, a hadron-hadron collision is governed by a single parton exchange, which produces the hard scattering, and all the non-perturbative elements are absorbed into the parton densities. However in high energy hadron-hadron collisions, which are characterised by high parton densities, it is possible that multiple partons effectively scatter with each other. These can be either hard or soft. At very high energies and densities one can e.g. expect to have two hard partons scatterings, a so called *double parton scattering*, which both have a perturbatively calculable cross section. Most parton scatterings in hadron collisions are however soft (or semi-hard), which makes their non-perturbative description much more difficult. As we shall see in the next chapter, this will lead to the need of phenomenological models that are tuned to experimental data by studying the behaviour of the so called *underlying event*. In addition we will see that all recent measurements indicate that it is mandatory to complement the collinear factorisation with the concept of *multiple parton interactions* (MPI).

2.4. Alternatives

2.4.1. High energy factorisation

An alternative factorisation theorem that takes the transverse momentum of the partons into account is called *high energy* or k_T *factorisation* [21]. This approach uses k_T dependent parton densities from the start, which will lead to a different set of evolution equations. The cross section can then be k_T-factorized:

$$\sigma = \int dx_1 dx_2 d^2k_{T,1} d^2k_{T,2} f(x_1, k_{T,1}) \hat{\sigma}(x_1, x_2, k_{T,1}, k_{T,2}) f(x_2, k_{T,2}), \tag{2.26}$$

in which we simplified the notation by hiding the scale dependencies and the sum over the parton flavours. The partonic cross section $\hat{\sigma}$ is now off-mass shell and depends also on the transverse momentum k_T of the partons. The functions $f(x, k_T)$ are the k_T-unintegrated parton density functions. If one does perform a k_T integration, a form fully consistent with the collinear factorisation approach can be obtained. The simplest evolution equations within the high energy factorisation theorem that can describe the evolution of the unintegrated parton densities as a function of x are the BFKL [22, 23] equations. At leading order in $\ln(1/x)$ they are (following the notation of [18]):

$$\frac{\partial f(x, k_T^2)}{\partial \ln(1/x)} = \frac{3\alpha_s}{\pi} k_T^2 \int_0^\infty \frac{dk_T'^2}{k_T'^2} \left(\frac{f(x, k_T'^2) - f(x, k_T^2)}{\left| k_T'^2 - k_T^2 \right|} + \frac{f(x, k_T^2)}{\sqrt{4k_T'^4 + k_T^4}} \right), \tag{2.27}$$

where $f(x, k_T^2)$ can be used to calculate the conventional, k_T integrated, parton densities:

$$x f(x, Q^2) = \int_0^{Q^2} \frac{dk_T^2}{k_T^2} f(x, k_T^2). \tag{2.28}$$

This evolution equation predicts a strong rise of the gluon density at small x values. A more advanced set of evolution equations, called CCFM [24, 25, 26], describe the parton evolution with the assumption that subsequent gluon emissions are ordered in an emission angle. One of its main advantages is that it combines information from both BFKL and DGLAP approximations and reduces to each of them in the appropriate limits. [27]

It is expected that the effects of finite transverse momenta of the partons becomes increasingly significant towards higher energies, i.e. smaller x values, since the evolution of the parton densities proceeds over a large region in rapidity: $\Delta y \sim \log(1/x)$. This is also the kinematical region in which the approximations done to derive the DGLAP equations are not entirely valid anymore. In those equations only the leading terms containing $\log(Q^2)$ were taken into account since we assumed $Q^2 \gg k_T$, and terms containing contributions of $\log(1/x)$ were implicitly neglected since we assumed that x was sufficiently big. However in the high energy limit ($x \to 0$) the latter terms become large and need to be taken into account. A perturbative treatment of these large logarithms to all orders may then be applicable. One thus expects a breakdown of

collinear factorisation and the DGLAP evolution equations in the small x limit where it is expected that k_T factorisation holds and the parton densities evolve according to the BFKL or CCFM equations. Indeed measurements [28, 29, 30] performed at the HERA accelerator that studied the DIS process indicated a deviation from the collinear factorisation with its DGLAP approximations in such kinematical region, where high energy factorisation is favoured. One should however be careful with its application since it is shown that k_T factorisation is violated in the production of high-p_T particles in hadron-hadron collisions [31].

2.4.2. Regge theory

This pre-QCD approach introduced to describe hadronic interactions is developed in the S-matrix framework and uses its properties, such as general analyticity and crossing properties, to construct scattering amplitudes. The optical theorem, which follows from the unitarity of the S-matrix, then allows the calculation of the total cross section. The idea of Regge [32] was that in this framework, the relativistic partial wave amplitude $A_\ell(t)$ can be analytically continued to complex values of the angular momentum ℓ in a unique way. This is a crucial tool in Regge theory, and it emerges rather naturally when one wants to establish the convergence domain of the scattering amplitude to allow a correct analytic continuation to arbitrary large energies. The resulting function $A(\ell, t)$ of the partial wave amplitude then contains simple poles at locations $\ell = \alpha(t)$ in the complex plane. Such poles are called *Regge trajectories*, and each pole corresponds to a family of bound states or resonances. Each pole then contributes to the scattering amplitude, which behaves asymptotically as:

$$A(s,t) \underset{s\to\infty}{\sim} s^{\alpha(t)}. \tag{2.29}$$

Thus the leading singularity in the t-channel determines the asymptotic behaviour of the scattering amplitude in the s-channel. If the values of t are real and positive, Regge poles represent resonances and bound states of increasing angular momentum ℓ, i.e. spin, and the Regge trajectory actually interpolates such resonances. Hence different processes will receive contributions from different trajectories. A common way to visualise Regge trajectories is to expand $\alpha(t)$ in power series around $t = 0$. For small t values we can then write:

$$\alpha(t) = \alpha(0) + \alpha' t, \tag{2.30}$$

with $\alpha(0)$ the *intercept* and α' the *slope* of the trajectory. [14]

The strong interaction in Regge theory is not due to the exchange of particles with a definite spin, but to the exchange of one or more Regge trajectories. In the language of particle physics, Regge trajectories are therefore often called *reggeons* ($\mathbb{R}$). Consider for example a two-body scattering process $1 + 2 \to 3 + 4$ in the large s limit. The amplitude

for this process in the simple case of just a single reggeon exchange is:

$$A(s,t) = \beta(t)\eta(t)s^{\alpha(t)}, \tag{2.31}$$

with $\beta(t)$ the *residue* and $\eta(t)$ the *signature* factor as defined in [14]. This power law behaviour of the scattering amplitude turns out to be a very successful feature of Regge theory. [14]

The previous discussed Regge trajectories have intercepts smaller than 0.5, their exchange thus leads to a decreasing cross section with higher energies. It is however experimentally known that the hadronic total cross section flattens, to then rise with increasing energy. This is shown in figure 2.8. In order to account for this behaviour a Regge trajectory was introduced that can have an intercept larger than 1. This reggeon is named the *pomeron* ($\mathbb{P}$) and corresponds to the rightmost singularity in the complex angular momentum plane. Its trajectory does not correspond to any known particle, but it is expected to result from a complicated exchange of gluons. The pomeron has the vacuum quantum numbers, and thus carries no electrical and no colour charge. Hence it is expected to be the dominant trajectory in the elastic and diffractive processes, which are known to proceed via the exchange of vacuum quantum numbers, which result in the large rapidity gaps. With the addition of the pomeron to Regge theory, it was possible to fit the total hadronic cross sections, as shown in figure 2.8, to high values of $\sqrt{s}$. The pomeron intercept can be written as $\alpha_{\mathbb{P}}(0) = 1 + \epsilon_1$, from the fit one then gets following values for the pomeron parameters:

$$\epsilon_1 = 0.0808, \quad \alpha'_{\mathbb{P}} = 0.25\,\mathrm{GeV}^{-2}, \quad \beta_{\mathbb{P}} = 1.87\,\mathrm{GeV}^{-1}. \tag{2.32}$$

These parameters are traditionally associated to the *soft pomeron*. [14, 33]

This simple ansatz however failed when it was applied to semi-hard diffractive reactions. To describe the DIS structure functions a second pomeron had to be introduced [34], which is called the *hard pomeron*, and it was found to have a much higher intercept: $\alpha_{\mathbb{P}}(0)_{hard} = 1.44$.

Since the advent of QCD a lot of research has been devoted on how to give a perturbative QCD content to the notion of a pomeron exchange between hadrons. In the original Regge theory, hadronic interactions were governed by the exchange of Regge trajectories, like the pomeron (figure 2.9 (b)), but how can one interpret this in the QCD parton model, where hadronic interactions are governed by the exchanges of quarks and gluons. The first proposal was to model the pomeron exchange as a perturbative two-gluon exchange [35, 36] (figure 2.9 (c)), which can reproduce the pomeron quantum numbers. However this approach did not take the gluon interaction into account, and the model was soon followed by a picture in which not one or two gluons are exchanged, but several gluon ladders (figure 2.9 (d)) in which the gluons are "reggeised". These are

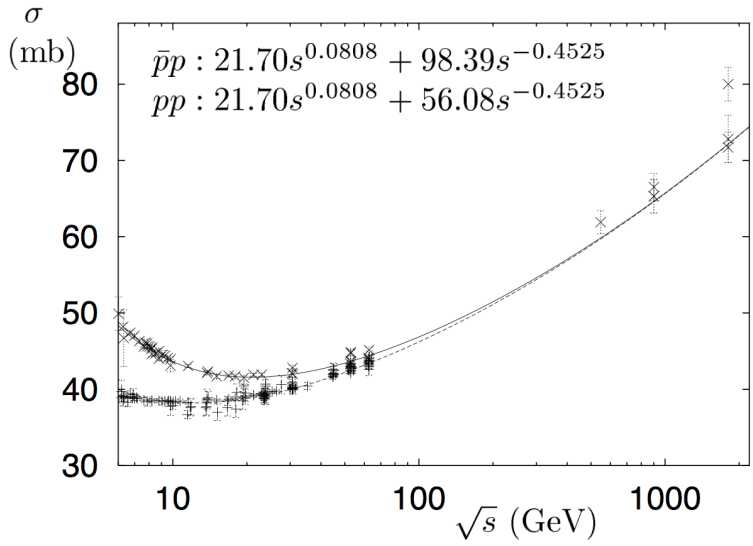

Figure 2.8.: Total pp and $p\bar{p}$ cross sections as a function of $\sqrt{s}$. The experimental measurements (points) are fitted with the Regge theory scattering amplitude function. The resulting parameters are shown in the figure. The first term represents the leading Regge exchange (pomeron), the second term takes non-leading contributions into account. [33]

gluons with a modified propagator:

$$D_{\mu\nu}(s, q^2) = -i\frac{g_{\mu\nu}}{q^2}\left(\frac{s}{s_0}\right)^{\alpha_g(q^2)-1}, \tag{2.33}$$

where $\alpha_g(q^2) = 1 + \epsilon(q^2)$ is the perturbatively calculable Regge trajectory of the gluon. This reggeisation is proven to all orders in perturbation theory, when keeping the leading $\ln s$ terms at each order. In this BFKL approach [22, 23], a perturbative pomeron in QCD thus represents a summation of an infinite number of diagrams in perturbation theory. Gribov then formulated reggeon field theory (RFT) [37, 38], which is a perturbative framework for analysing reggeon exchange and calculating the corresponding reggeon diagrams.

The soft pomeron can be seen as a non-perturbative object in QCD, in this approach hadrons then scatter at small values of t since the quarks only sense the non-perturbative fluctuations of the gluons fields in the vacuum (figure 2.9 (e)). [33]

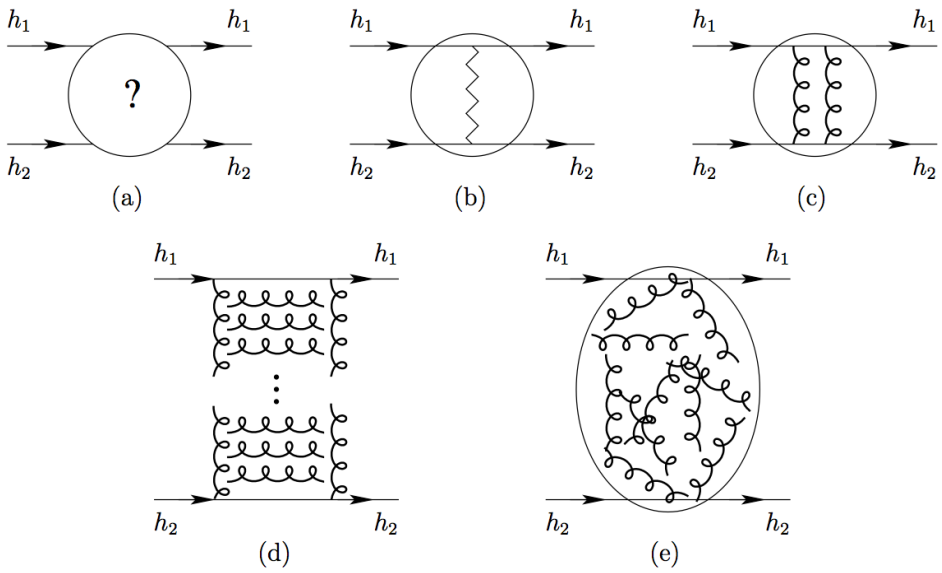

Figure 2.9.: Schematic presentation of a hadron-hadron scattering. (a) What happens during the interaction? (b) In Regge theory a phenomenological pomeron is exchanged, (c) in the framework of QCD this corresponds to a two gluon exchange in the simplest picture, (d) this needs to be extended to the exchange of a reggeised gluon ladder, (e) a fluctuating vacuum gluon field representation of the soft pomeron. [33]

Chapter 3.

Underlying event phenomenology

In the previous chapter we have seen how we can describe hadron collisions from a theoretical point of view. We introduced factorisation theorems and ended with stating the limitations and alternatives. In this chapter we will introduce phenomenological models that are needed to describe the experimental data and complement the factorisation approach. For this, one segments hadron-hadron collisions usually in different components that each describe a certain stage in the QCD dynamics of the collision. This is shown in figure 3.1.

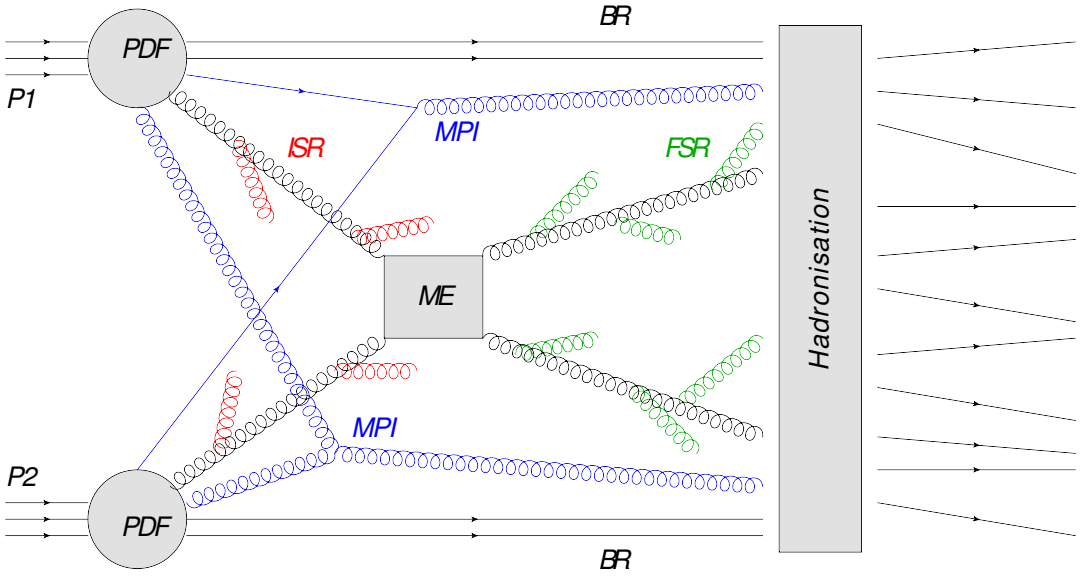

Figure 3.1.: Schematic view of a hadron-hadron collision with its different components indicated. It represents the evolution of an initial state (left) to the final state (right) with all its (non-)perturbative dynamics, which are explained in the text.

One important component of a hadron collision, is its *Underlying Event* (UE) structure. The UE is defined as *everything except the perturbative hard scattering* (ME in the figure), i.e. it represents all the possible additional activity that is not directly associated with that interaction. Unfortunately there is some ambiguity in the literature about what is "associated" with the hard interaction. Especially the so called initial (ISR) and final (FSR) state radiation, which will be explained later, is sometimes not regarded as a

component of the UE. One consequence of the underlying activity is the *jet pedestal effect* in which the final state of the hard scattering sits on top of a higher than average "pedestal" of additional soft activity. This can be understood if one characterises hadron-hadron collisions with an impact parameter b. At non-zero values of b, a hard scattering can only take place inside a small overlapping region between the two hadrons, thus it will have a low probability to happen and only a few rather soft interactions will occur. If one then imposes a hard scatter selection cut, the collision sample is statistically biased towards more central collisions that will also have more underlying activity.

A crucial component of the UE structure, which was introduced to account for all the underlying activity in hadron collisions, is the possibility to have *multiple parton interactions* (MPI), a feature that is neglected in the factorisation theorems. In the available phenomenological models there is a priori no limit on the hardness of such additional parton interactions and therefore they predict the possibility to have e.g. two hard parton scatterings in one collision, called *double parton scattering* (DPS), and in fact first evidence for such multiple scatterings is already found [39, 40]. However since the cross section scales with $1/Q^2$, where Q^2 represents the momentum transfer squared, the fraction of additional interactions that have a hard scale is quite small, and multiple soft parton interactions are much more abundant. These soft interactions don't produce additional high energy/momentum final state objects but can significantly alter the colour flow and total scattered energy of the event. This manifests itself by increased particle multiplicities and summed transverse energies in the measured final state [15]. Indeed we will see later that all recent measurements performed at high energy proton-proton collisions indicate that it is mandatory to include MPI effects to describe the final state.

A good understanding of the UE structure in hadron collisions is crucial for precision measurements of Standard Model processes and the search for new physics at high energies. Such processes, e.g. the production of a heavy Higgs boson out of a hard parton scattering, are hidden among a huge bulk of underlying QCD background processes that take place during a hadron-hadron collision. Hence a proper description of all this underlying activity is necessary to improve the selection, isolation and identification criteria that can enhance the reconstruction efficiency and discovery potential. Although the UE can contain perturbative interactions, it is most of the time of a non-perturbative nature, which implies the need of phenomenological models to describe the final state. These models are however based on different kinds of assumptions and have free parameters that need to be tuned to experimental data. Therefore the UE structure is subject to experimental measurements, such as the one presented in this thesis, with the purpose to rule out faulty phenomenological models, and improve the successful ones by tuning their parameters.

In the next sections we will describe all the different components of a hadron-hadron collision (indicated in figure 3.1) that contribute to the underlying event activity, with the focus on the modelling of multi-parton interactions. In the last section we review a list of available Monte Carlo models that are used in this work.

3.1. Parton showers

3.1.1. The parton distribution functions and matrix element

The Parton Distribution Functions (PDF) and the Matrix Element (ME) are in fact what we already have in the (collinear) factorisation expression (2.25). The PDF thus represent the probability to find a parton i with longitudinal momentum fraction x inside a hadron at a certain scale μ. These non-perturbative elements characterise the structure of the hadrons and can not be calculated from first principles. Their evolution with the scale can be calculated however, by using the evolution equations. This advantage of the factorisation theorem makes it possible to measure the PDF for a certain process and scale, evolve them and then apply them to a different process and scale.

The ME is exactly the partonic, or short distance, cross section we introduced before. It represents the perturbative calculation of the hard parton-parton scattering at a certain order in α_S, where the higher order corrections are due to the QCD parton dynamics. In the DIS example, which we used in section 2.2 to introduce the QCDC and BGF processes that give rise to the higher order corrections, we only considered such processes to happen once. But in reality this is not the case, once a gluon produced a $q\bar{q}$ pair it is possible that those quarks radiate multiple gluons themselves. Thus we have to take all possible contributions into account, and in principle calculate the cross section to all orders. This situation is illustrated in figure 3.2: one has to sum all possible gluon radiations, quark pair productions, gluon vertices, etc..., and all their combinations into the cross section. Each time an additional strong interaction is added, the order of the cross section is increased with α_s and a term proportional to $\left(\log \frac{Q^2}{\mu^2}\right)$ is added (recall eq. (2.15)). In the end, a series of $\left(\log \frac{Q^2}{\mu^2}\right)^n$ with $n \to \infty$ is needed to calculate the exact cross section. At this point however, for DIS processes, only the so called *Leading Order* ($O(\alpha_s)$), *Next-to-Leading Order* ($O(\alpha_s^2)$) and *Next-to-Next-to-Leading Order* ($O(\alpha_s^3)$) cross sections can be calculated, since the inclusion of higher orders become increasingly difficult and challenging. [18]

3.1.2. Initial and final state radiation

To cope with the limitation of the ME calculations, it is then common to do the following: one calculates the cross section (ME) until a certain order, and then add *parton showers* that are used to approximate the contributions of the higher orders. This leads to the definition of the *Initial State Radiation* (ISR) and *Final State Radiation* (FSR), shown in figure 3.1. Although the separation of ISR and FSR is completely arbitrary, one can picture it as follows: before a parton from hadron P_1 scatters with the parton from hadron P_2, it can radiate gluons and produce a shower of partons in the initial state (ISR). After the hard scattering, they can again radiate gluons and produce an avalanche of partons in the final state (FSR). Note that if it would be possible to calculate the

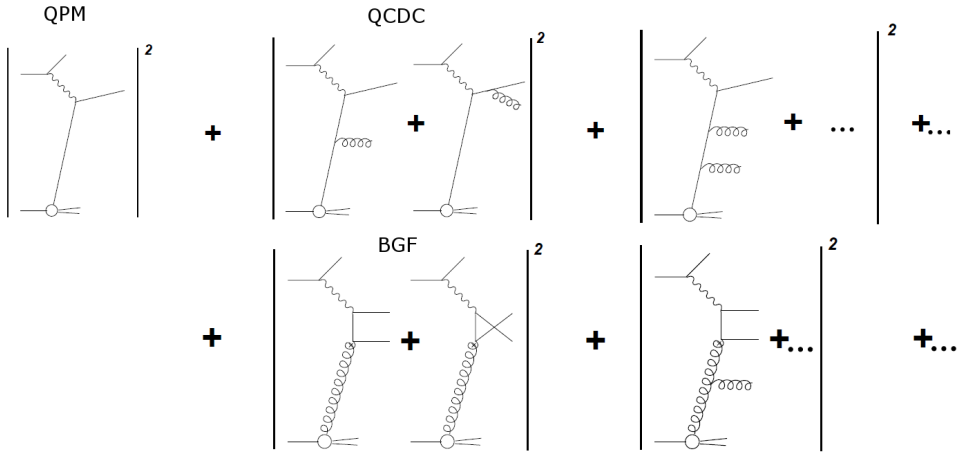

Figure 3.2.: Illustration of the naive parton model (QPM) extension to include all higher order QCD corrections in α_S in the perturbative cross section calculation.[18]

exact perturbative cross section, which takes *all* higher order corrections into account, the ISR and FSR would be completely absorbed in the ME.

The parton showers in the ISR and FSR can be modelled by using the evolution equations. In the case one uses the DGLAP equations in the collinear factorisation scheme, a parton ladder in which the transverse momenta k_{Ti} of the evolved partons are strongly ordered, $Q_0^2 \ll k_{Ti}^2 \ll k_{Ti+1}^2 \ll Q^2$, is created. This concept is illustrated in figure 3.3 in which a parton evolves from a scale Q_0^2 and longitudinal momentum fraction x_0 to a scale Q^2 and fraction x. At each branch the parton gains a transverse momentum k_T after the emission of a parton with transverse momentum p_T and longitudinal momentum fraction ξ. The probability to produce such a parton is then exactly given by the DGLAP splitting functions, i.e. (2.16), (2.17), (2.21), (2.22). [18]

This approach makes it possible to integrate over all contributions in the ladder diagram, which corresponds to a resummation of the terms $\left(\alpha_s \log \frac{Q^2}{Q_0^2}\right)^n$, needed for the calculation of the cross section. The approximation is called to be *Leading Log* (LL) since the coupling α_s and the logarithmic factor have the same power. The DGLAP evolution equations used in this example, are however only valid at high Q^2 values and not too small values of x since we implicitly assumed during the derivation that the following is true:

$$\alpha_s(Q^2) \ln \frac{1}{x} \ll \alpha_s(Q^2) \ln \frac{Q^2}{Q_0^2} < 1. \tag{3.1}$$

A more advanced solution would be the *Double Leading Log(DLL)* approximation that does not only order the transverse momenta k_T, but also the longitudinal momentum fraction x: $x \ll x_{i+1} \ll x_i \ll x_0$. One then gets a resummation of terms $\left(\alpha_s \ln \frac{Q^2}{Q_0^2} \ln \frac{1}{x}\right)^n$. This approximation is valid if the aforementioned terms are bigger than the separate

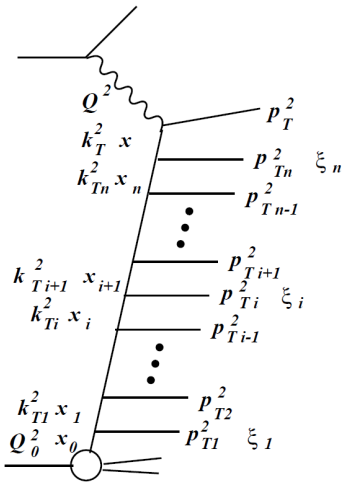

Figure 3.3.: Graphical presentation of a parton shower ladder diagram in a DIS process. The kinematics are explained in the text. [18]

$\ln Q^2$ and $\ln(1/x)$ contributions. This is the case in a kinematical region where Q^2 is high, and x small. [18]

When x becomes very small, but at lower values Q^2, the approximations needed for the DGLAP equations are not valid anymore, and one needs to use the alternative BFKL equations that are used in the high energy factorisation. In this region one sums all the diagrams ordered in x ($x \ll x_{i+1} \ll x_i \ll x_0$), without any ordering in k_T. We then get a LL series of terms $\propto \left(\alpha_s \ln \frac{1}{x}\right)^n$ that are valid if following conditions are true:

$$\alpha_s(Q^2) \ln \frac{Q^2}{Q_0^2} \ll \alpha_s(Q^2) \ln \frac{1}{x} < 1. \tag{3.2}$$

For completeness, figure 3.4 shows an overview of the kinematic regions in which the different evolution equations are valid [18]. It is important to note that both parton evolution approximations need a lower cut-off (Q_0 and $k_{T,0}$) to avoid going to the non-perturbative region. Thus when a parton-parton cross section is complemented with ISR and FSR parton showers, there's always a dependence on kinematical parameters that define the window in which parton showers are calculated. Hence the parton shower approach will always be an approximate result that has to be merged with the exact ME calculation. Different evolution equations will result in different parton showers, and hence, to a different final state. The (un-)ordered showers in k_T for the (BFKL)DGLAP evolution will obviously result in different energy deposits in a region of phase space, the unordered k_T parton showers of BFKL will predict a higher activity at a region far away from the hard scattering. One major consequence of ISR and FSR is that it can fill gaps with (soft) particles that should not be there if the parton showering was not possible. Hence the study of the energy deposit in a large region of phase space can test all the available parton shower models.

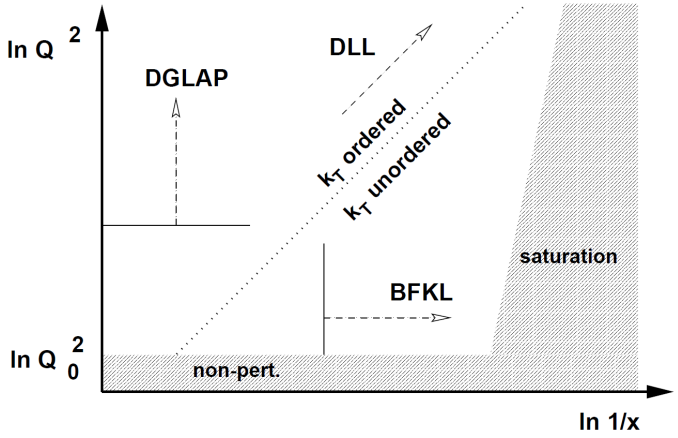

Figure 3.4.: Schematic presentation of the kinematic regions in the $(\ln(1/x), \ln(Q^2))$ phase space in which the different evolution equations are valid. In addition, the region where saturation of the parton densities is expected is included. [18]

3.2. Hadronisation

3.2.1. String fragmentation

This is the last stage in figure 3.1 needed to produce the final state, and it is a direct consequence of the behaviour of the strong coupling constant α_S. In chapter 1 we saw this lead to the property of confinement: at very large distances, and thus low energies, the effective coupling becomes very strong such that the coloured partons can not exist independently and have to form colour neutral hadrons. This process is called *hadronisation*. It has yet to be understood from first principles, starting from the QCD Lagrangian, and this led to the need and development of several phenomenological models.

One such model, the *Lund string model* [41, 42], uses the concept of string fragmentation to form hadrons out of a collection of partons. Although this is certainly not the only and latest model available, it is still widely used and interesting to illustrate the idea of hadronisation. String fragmentation can be understood from the behaviour of the QCD potential [1]:

$$V = -\frac{4\alpha_S}{3r} + kr, \tag{3.3}$$

where the first Coulomb term describes the interactions at small distances, while the second term describes interactions at larger distances where the potential must increase indefinitely to confine the partons inside a hadron. Thus the energy stored in the colour dipole field between a charge and anti-charge increases linearly with the separation between the charges. This assumption of linear confinement is the starting point of the string model. Let us imagine two partons, a quark q and anti-quark $\bar{q}$ that move away

from their production vertex. As they move apart, a colour flux tube is being stretched between the pair and the stored energy inside this tube increases linearly. At some point the energy stored is so high that the string may break and form a new $q'\bar{q}'$ pair. The resulting system will then consist out of two colour singlet states $q\bar{q}'$ and $q'\bar{q}$. Then, if the invariant mass of these new states is still large enough, further string breaks may occur and produce subsequent colour neutral states until all the energy is used and only on-mass shell hadrons remain. It is obvious to see how such mechanism can easily produce a series of mesons, but also baryons can be produced as such. In the simplest approach one could treat a diquark in a colour anti-triplet state as an ordinary anti-quark. This way a string can either break into a quark, anti-quark or diquark, anti-diquark pair. From hadron spectroscopy one can deduce a value for the string constant k, which represents the amount of energy per unit length, to be $k \approx 1$ GeV/fm. [42]

The picture described above is however a very simple one. One has not only to take into account the colour flow (charge, anti-charge), but also the flavour and momentum correlations. Finally it is also important to treat the possible decay of unstable particles. The applied phenomenological models will thus have a much more complicated and realistic hadronisation, though the basic concept stays the same. Note that the hadronisation process acts on all the elements in the final state of a hadron-hadron collision, as can be seen in figure 3.1. That means that not only the hard scattered partons from the ME and the radiated partons from ISR/FSR are fragmented into hadrons, but also the remaining items that we will discuss in the next sections.

3.2.2. Beam remnant

The *beam remnant* (see figure 3.1) is what remains after a parton with a momentum fraction x leaves the hadron to undergo the hard scattering. In a proton beam the u quark parton would then leave behind a ud diquark remnant that has an anti-triplet colour charge. The beam remnant is thus not colour neutral anymore, and therefore colour connected to the hard scattering and the other elements in the collision, which all go into the hadronisation. The remnant is often more complicated than the above example, especially at high energies, since a gluon initiator parton can then leave behind a uud remnant in a colour octet state. This could be divided into a colour triplet quark and a colour anti-triplet diquark, but the energy sharing and relative transverse momentum between the objects introduces additional degrees of freedom that are in fact not understood yet from first principles. The lack of a finite transverse momentum in the initial state in the collinear factorisation scheme needs to be compensated by adding a *primordial* k_T to the initial partons in the phenomenological models based on it. This takes the motion of quarks inside the original hadron into account as required by the uncertainty principle by the proton size, which can be augmented by unresolved soft shower activity. The primordial k_T can be selected according to a suitable distribution after which the recoil is taken by the beam remnant object. [43, 44, 42]

3.2.3. Jets

One major consequence of the confinement and hadronisation in QCD is that a high energy parton coming from a hard scattering will not be detected as one high energy hadron, but as a collimated, localised group of high energy hadrons, which is called a *jet*. As such, it are in fact jet objects that are used to study QCD and the interaction of hadrons from an experimental point of view. Therefore we will now briefly review the possible *algorithms* to reconstruct such objects.

To get an unambiguous picture of what is collimated or localised, one needs to use consistent algorithms that combine the available objects into jets by using their energy or momentum and position in phase space. Furthermore, these algorithms need to be universal in the sense that they can be applied to a theoretical collection of hadrons in a final state, but also on measured signals (tracks, energy deposits) in particle detectors. The choice for a specific algorithm is then driven by its theoretical properties and its phenomenological/experimental performance. To get such consistent results, a jet algorithm is required to have two important properties: it needs to be ultraviolet and infrared safe, i.e. the result of the algorithm should not depend on arbitrarily soft and/or collinear emissions. It is also necessary that the algorithm is as transparent as possible to hadronisation corrections, i.e. only small energy scale corrections are needed to compare theoretical predictions with experimental results. And finally, from a practical point of view, it needs to be efficient to limit the precious CPU time available in contemporary experiments.

There are two types of algorithms commonly used: *cone* algorithms, such as SISCone [45], and *sequential recombination* algorithms such as (anti-)k_T [46]. Inside the cone class of algorithms another division can be made into *Seeded* and *Seedless* versions. Here a seeded cone algorithm will reconstruct a jet by looking for a particle with the highest energy above some threshold (the seed) to then combine all nearby particles, which are required to be inside a cone with radius $\Delta R = \sqrt{(\eta_{\text{seed}} - \eta_j)^2 + (\phi_{\text{seed}} - \phi_j)^2}$ with η the pseudorapidity and ϕ the azimuthal angle. This procedure is iterated until no seeds can be found anymore. Although seeded cone algorithms are very fast, they are not ultraviolet and infrared safe. This is different for seedless cone algorithms (e.g. SISCone) that do have the two key properties. They do not work with seeds, but simply iterate over all particles in the collection, and check whether a jet within a ΔR cone can be created.

In this work we will use the (anti)-k_T recombination algorithm, which is ultraviolet and infrared safe, and has a short processing time. It yields robust jet collections and is flexible to implement in different situations. One common form of the algorithm used in hadron-hadron collisions is the following [46]:

1. The algorithm starts by assuming that each object in the input collection has the potential to be a jet without the need for any recombination at all, as such all objects are called *proto-jets*. If indeed no recombination seems possible given the algorithm's parameters, all objects are finally stored as jets.

2. For every object i, $d_i = p_{T,i}^{2p}$ is calculated, together with $d_{ij} = \min(p_{T,i}^{2p}, p_{T,j}^{2p})\frac{\Delta_{ij}^2}{R^2}$ for each pair of objects in the collection for which $i \neq j$ and $\Delta_{ij}^2 = (\eta_i - \eta_j)^2 + (\phi_i - \phi_j)^2$. R is a free radius parameter chosen to have the best jet reconstruction performance. The parameter p determines the relative power of the energy versus geometrical scales, and is different for each version of the algorithm. If $p = 1$ we call this the k_T algorithm, if $p = -1$ one gets the anti-k_T version.

3. Calculate the global minimum of all d_i and d_{ij} values.

4. If $d_{\min} = d_{ij,\min}$, i.e. $d_{ij,\min} < d_{i,\min}$, then objects i and j are combined into a new proto-jet object by adding their momenta. The used input objects i and j are removed from the collection and the algorithm goes back to step 1. If the above combination condition is not satisfied, proto-jet i is stored as a jet, it is removed from the input collection and the algorithm goes back to step 1.

5. This iterative procedure continues until all input objects are processed, in the end a complete collection of jets is returned to the user.

One of the main advantages of the anti-k_T algorithm is the resilience of its jet boundaries with respect to soft radiation [46]. The usage of the inverse transverse momentum, $d_{ij} = \min(1/p_{T,i}^2, 1/p_{T,j}^2)\Delta_{ij}^2/R^2$, implies that soft particles in the event will tend to combine with hard ones long before they combine among themselves. In the case a hard particle has no hard neighbours within a distance $2R$ it will simply accumulate all the surrounding soft particles within a radius R.

3.3. Multiple parton interactions

As stated in the introduction of this chapter, multiple parton interactions account for a significant contribution to the UE activity and are mandatory to describe the measured final states. Despite its importance and a lot of research efforts, the theoretical picture of MPI is not complete and a uniform, coherent description in both soft and hard regions has not been reached yet. The lack of such a theoretical framework lead to a lot of developed phenomenological models that implement multiple parton interactions. As we will see later it appears that such models can describe the experimental data quite well, despite the need of free parameters that need to be tuned to data. In this section we will explain one of the first proposed models that implemented MPI [47], and is nowadays still widely used and accepted.

3.3.1. Basic concepts

The notion of MPI can be understood from the following basic concept. Consider the cross section for a hard $2 \to 2$ QCD process as a function of the p_T^2 scale [44]:

$$\frac{d\sigma_{int}}{dp_T^2} = \sum_{i,j,k} \int dx_1 \int dx_2 \int dt f_i\left(x_1, Q^2\right) f_j\left(x_2, Q^2\right) \frac{d\hat{\sigma}_{ij\to kl}}{d\hat{t}} \delta\left(p_T^2 - \frac{tu}{s}\right), \tag{3.4}$$

in which we used the Mandelstam variables s, t, u (section 1.3), and where in fact σ_{int} represents the interaction cross section that corresponds to a single parton-parton scattering $\hat{\sigma}_{ij\to kl}$. As an example we can relate this to the total jet cross section as $\sigma_{jet} = 2\sigma_{int}$ since each $2 \to 2$ parton interaction will give rise to two jets. If we assume the hard scale of the process to be given by the p_T scale: $Q^2 = p_T^2$ and that $|t| \ll s$ so that $p_T^2 = tu/s \approx |t|$ we can approximately write

$$\frac{d\sigma_{int}}{dp_T^2} \approx \int\int \frac{dx_1}{x_1}\frac{dx_2}{x_2} F\left(x_1, p_T^2\right) F\left(x_2, p_T^2\right) \frac{d\hat{\sigma}}{p_T^2}, \tag{3.5}$$

in which the partonic cross section can be expressed as

$$\frac{d\hat{\sigma}}{dp_T^2} = \frac{8\pi\alpha_S^2\left(p_T^2\right)}{9p_T^4}, \tag{3.6}$$

and the parton density functions were replaced by the structure functions F. If we then take α_S constant and neglect the integrals over x it appears that the integrated cross section above some $p_{T,min}$ becomes divergent in the limit $p_{T,min} \to 0$ since we have:

$$\sigma_{int}\left(p_{T,min}\right) = \int_{p_{T,min}}^{\sqrt{s}/2} \frac{d\sigma}{dp_T} dp_T \propto \frac{1}{p_{T,min}^2}. \tag{3.7}$$

This divergence is illustrated in figure 3.5, which compares the total expected cross sections at the Tevatron ($p\bar{p}$ collisions at $\sqrt{s} = 1.8$ TeV) and LHC (pp collisions at $\sqrt{s} = 14$ TeV) accelerators with the integrated interaction cross section σ_{int} above some $p_{T,min}$. We clearly see that at the order of a few GeV the interaction cross section exceeds the total $p\bar{p}$ and pp cross sections. Since this is well above the scale Λ_{QCD}, a breakdown of perturbation theory cannot be held responsible for this anomaly. One can however find a resolution by introducing the concept of multiple interactions.

The first point to realise is that the interaction cross section introduced above is an inclusive number, i.e. if an event contains two interactions it counts twice in the interaction cross section σ_{int} but only once in the total cross section σ_{tot}. We can therefore identify the following relation:

$$\langle n \rangle \left(p_{T,min}\right) = \frac{\sigma_{int}(p_{T,min})}{\sigma_{tot}}, \tag{3.8}$$

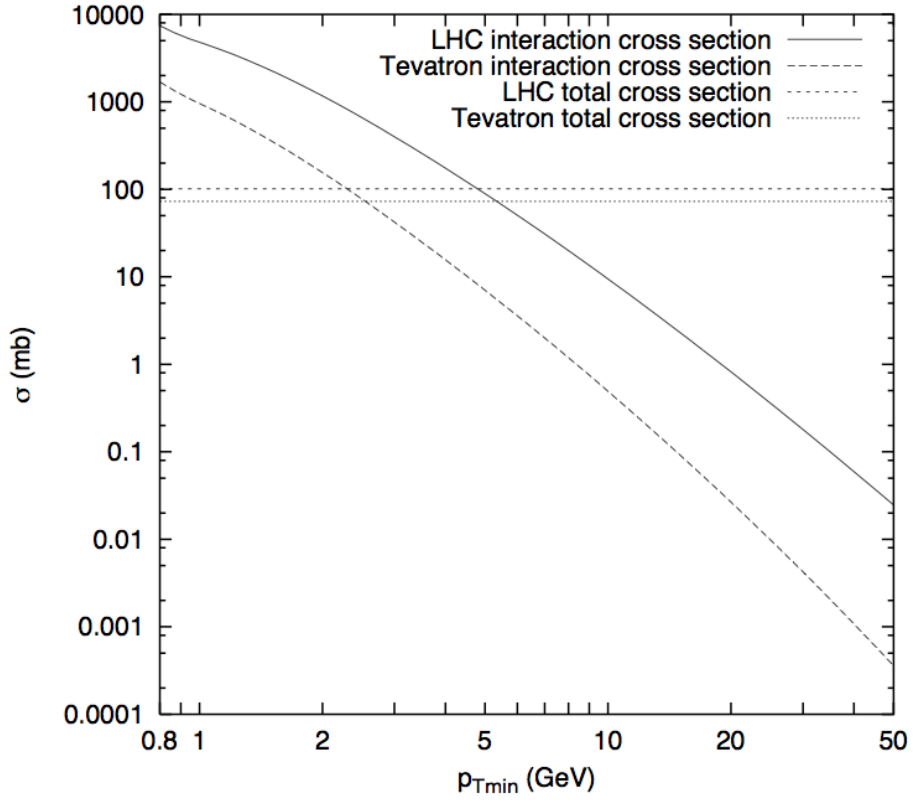

Figure 3.5.: The integrated interaction cross section σ_{int} above $p_{T,min}$ for the Tevatron and LHC accelerators with centre-of-mass energies $\sqrt{s} = 1.8$ TeV and $\sqrt{s} = 14$ TeV respectively. For comparison, the flat lines represent the respective total cross section. [44]

in which $\langle n \rangle (p_{T,min})$ represents the average number of interactions above $p_{T,min}$ per collision. Thus as the $p_{T,min}$ decreases in the integral of the cross section we are able to resolve more and more (soft) parton interactions. This cut-off introduced to avoid the divergence is also needed to tame the rise of $\langle n \rangle (p_{T,min})$ and can be justified additionally as follows: since the incoming hadrons are colour singlet objects an exchanged gluon with a very small p_T and corresponding large transverse wavelength can no longer resolve the individual colour charges such that the effective coupling is decreased and the cross section suppressed. A simple estimate of this effective cut-off could be

$$p_{T,min} \simeq \frac{\hbar}{r_p} \approx \frac{0.2\text{GeV} \cdot \text{fm}}{0.7\text{fm}} \approx 0.3\text{GeV} \simeq \Lambda_{QCD}, \tag{3.9}$$

but this is certainly too low as it is of the same order of Λ_{QCD}. This can be solved by replacing the proton radius r_p with the typical colour screening distance d, but this number is not known from first principles, and thus one has to keep this lower cut-off as a free parameter in the model that needs to be tuned to experimental data. This parameter $p_{T,0}$ can then be used to smoothly regularise the divergencies in the cross

section by rewriting it as follows:

$$\frac{d\hat{\sigma}}{dp_T^2} = \frac{8\pi\alpha_S^2\left(p_{T,0}^2 + p_T^2\right)}{9\left(p_{T,0}^2 + p_T^2\right)^2}. \tag{3.10}$$

Higher energies allow the parton densities to be probed at lower values of x where the number of partons rapidly increases and thus they become more closely packed, which results in a decreasing colour screening distance d. Hence, just as the small-x rise of the parton densities goes like a power of x, one can therefore expect the same kind of energy dependence for the $p_{T,0}$ cut-off parameter:

$$p_{T,0}\left(\sqrt{s}\right) = p_{T,0}\left(\sqrt{s_0}\right)\left(\frac{\sqrt{s}}{\sqrt{s_0}}\right)^{\epsilon}. \tag{3.11}$$

Here the power exponent ϵ is then another free parameter that can be tuned to describe the energy dependence starting from a value $p_{T,0}\left(\sqrt{s_0}\right)$, which is a tuned cut-off value at a certain centre-of-mass energy $\sqrt{s_0}$. [43, 44, 42]

3.3.2. A simple model implementation

A naive phenomenological model, for nondiffractive inelastic events, which implements the concept of multiple interactions calculates the probability to have n interactions per event by using a Poisson distribution with mean $\langle n\rangle$:

$$\mathcal{P}_n = \langle n\rangle^n \frac{e^{-\langle n\rangle}}{n!}, \tag{3.12}$$

where it is assumed that all hadron collisions are completely equivalent, and that the different parton interactions are independent of each other. One approach could then be to just pick the actual number of interactions for each event according to the Poissonian distribution and select the n p_T values independently according to (3.4). However this method doesn't take any correlations into account, such as the basic energy-momentum conservation requirement. A convenient way is then to impose an ordering in p_T on the multiple interactions, in which the first interaction is regarded as the hardest one (highest p_T), after which the second, third, etc. are successively softer interactions. The generation of such a sequence $\sqrt{s}/2 > p_{T,1} > p_{T,2} > ... > p_{T,n} > p_{T,min}$ can then be done according to the probability distribution

$$\frac{d\mathcal{P}}{dp_{T,i}} = \frac{1}{\sigma_{nd}}\frac{d\sigma}{dp_T}\exp\left[-\int_{p_T}^{p_{T,i-1}}\frac{1}{\sigma_{nd}}\frac{d\sigma}{dp_T'}dp_T'\right], \tag{3.13}$$

which determines $p_{T,i}$ from a known $p_{T,i-1}$. In this case the number of possible interactions n is then reached when the iterative procedure terminates. At each step the cross section $d\sigma/dp_T$ is modified according to the previous generated interactions, and as such a correlation between the harder and softer interactions is introduced. The parton

distribution functions are then not evaluated at x_i for the i'th scattered parton from a hadron, but at the rescaled value

$$x_i' = \frac{x_i}{1 - \sum_{j=1}^{i-1} x_j}, \tag{3.14}$$

which makes it impossible now to scatter more energy than initially available in the incoming beam. [43, 44, 42]

3.3.3. Impact parameter dependence

Until now we always assumed the same initial state for all events in our simple model, more realistically however one should include the possibility that each collision can be characterised by a varying impact parameter b [47], as illustrated in figure 3.6. A small value of b then corresponds to a large overlap between the two hadrons (central collisions) and hence one can expect an increased probability to have multiple parton interactions. For large impact parameters however, the overlap is rather small (peripheral collisions) and there's a large probability that no parton interactions take place at all.

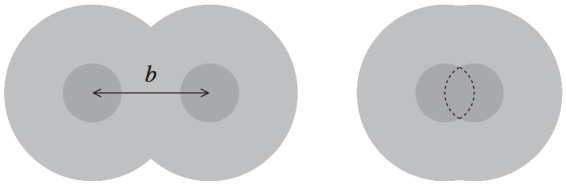

Figure 3.6.: Schematic view of peripheral collisions (left) and central collisions (right) with large and small impact parameters b respectively. The larger overlap between the two hadrons in central collisions implies an increased probability to have multiple parton interactions. [48]

One distribution that can quantify such hadronic matter overlap is a symmetric double Gaussian:

$$\rho(r) \propto \frac{1-\beta}{a_1^3} \exp\left(-\frac{r^2}{a_1^2}\right) + \frac{\beta}{a_2^3} \exp\left(-\frac{r^2}{a_2^2}\right). \tag{3.15}$$

This corresponds to a distribution with a small core region of radius a_2 that contains a fraction β of the total hadronic matter, embedded in a larger hadron region of radius a_1. This ansatz can be related to the physical picture of a hard hadronic core that is surrounded by a cloud of pions. The time-integrated overlap $\mathcal{O}(b)$ between the matter

distributions of the colliding hadrons with impact parameter b is then given by:

$$\begin{aligned}\mathcal{O}(b) &\propto \int dt \int d^3x \rho(x,y,z)\rho(x+b,y,z+t) \\ &\propto \frac{(1-\beta)^2}{2a_1^2}\exp\left(-\frac{b^2}{2a_1^2}\right) + \frac{2\beta(1-\beta)}{a_1^2+a_2^2}\exp\left(-\frac{b^2}{a_1^2+a_2^2}\right) + \frac{\beta^2}{2a_2^2}\exp\left(-\frac{b^2}{2a_2^2}\right).\end{aligned} \tag{3.16}$$

As stated before, the larger the overlap $\mathcal{O}(b)$ between the hadrons, the more likely it is to have multiple interactions, and thus in this approximation one expects again a linear relationship:

$$\langle n(b)\rangle = k\mathcal{O}(b), \tag{3.17}$$

in which n represents the number of interactions that happen when two hadrons pass each other with an impact parameter b, and where k is simply a constant of proportionality. Then, for each impact parameter value one can assume that the number of interactions is again distributed according to a Poissonian (3.12), before energy-momentum and other constraints are added. To generate an event with a specific number of interactions in a sequence of $p_{T,i}$ one has to generalise equation (3.13) to include the impact parameter b dependence:

$$\frac{d\mathcal{P}}{dp_{T,1}d^2b} = \frac{\mathcal{O}(b)}{\langle\mathcal{O}\rangle}\frac{1}{\sigma_{nd}}\frac{d\sigma}{dp_T}\exp\left[-\frac{\mathcal{O}(b)}{\langle\mathcal{O}\rangle}\int_{p_T}^{\sqrt{s}/2}\frac{1}{\sigma_{nd}}\frac{d\sigma}{dp_T'}dp_T'\right], \tag{3.18}$$

with $\langle\mathcal{O}\rangle$ the average hadronic overlap. The subsequent interactions can then be generated sequentially in decreasing p_T as before, with the only difference that the cross section $d\sigma/dp_T^2$ is multiplied with an extra factor $\mathcal{O}(b)/\langle\mathcal{O}\rangle$. [43, 44, 42]

3.3.4. Correlations and interleaving parton showers

To come to a more realistic MPI model it is obvious that all kinds of momentum, flavour, colour and parton density correlations need to be taken into account, together with the interplay between all parton interactions and their ISR. If a hadron undergoes multiple interactions, it should be described by multi-parton densities. These give the joint probability of simultaneously finding n partons with flavours $f_1, f_2, ..., f_n$ that carry longitudinal momentum fractions $x_1, x_2, ..., x_n$ inside the hadron, probed at interaction scales $Q_1^2, Q_2^2, ..., Q_n^2$. There are however no experimental data available to determine such distributions and hence one has to modify the standard one-parton densities in the phenomenological models.

The first observation is that each interaction i removes a momentum fraction x_i from the hadron remnant, this loss can be taken into account by applying a simple scaling to the parton distributions, which is in fact already present in the model through equation (3.14) that introduced a rescaled momentum fraction to evaluate the default parton

densities. But in addition one should also make sure that the valence distribution of a flavour f after n parton interactions, $q_{fvn}(x, Q^2)$, integrates to the number of valence quarks with flavour f that remain in the hadron remnant. This can be enforced by an extra down scaling of the original distribution by a ratio of the remaining to original valence quarks N_{fvn}/N_{fv0}. Furthermore in case a sea quark is knocked out of the hadron, a corresponding anti-sea quark must be left behind in the beam remnant, since they are produced through gluon branching $g \to q\bar{q}$ in the perturbative approximation. One can then also obtain a parton distribution for these anti-sea quarks, also called companion quarks q_c, from the probability that a sea quark q_s with momentum fraction x_s is produced by the branching of a gluon with momentum fraction y:

$$q_c(x, x_s) \propto \int_0^1 g(y) P_{g \to q_s q_c}(z) \delta(x_s - zy) dz, \tag{3.19}$$

in which $P_{g \to q_s q_c}$ are the well known DGLAP gluon splitting functions introduced before. The reduction of the valence distribution and the introduction of companion quark distributions would however result in a violation of the total momentum sum rule, thus in order to make sure that it is still respected, one assumes that the sea and gluon normalisations go up when a valence distribution is reduced, and down when a companion distribution is added.

Although it is not drawn in figure 3.1, for clarity, it is obvious that each multiple interaction can have its own ISR and FSR. Since the FSR does not modify the total amount of energy carried by the perturbatively defined partons, but only performs a redistribution of the energy among the partons, it can be treated rather separately. The addition of further ISR branching and the addition of more parton interactions however implies more energy that is taken from the limited beam remnant, and hence the two mechanisms are in direct competition with each other. In a convenient model both the MPI and ISR can then be ordered in decreasing p_T, and starting from a hard interaction, a common sequence of subsequent evolution steps of interactions and branchings can be generated. If the last step had a $p_{T,i-1}$ scale, the maximum for the continued evolution can be set to $p_{T,max} = p_{T,i-1}$. This can then be either a new interaction, or a new ISR branching. With this interleaving, the probability distribution for a certain $p_T = p_{T,i}$ is then extended to:

$$\frac{d\mathcal{P}}{dp_T} = \left(\frac{d\mathcal{P}_{MI}}{dp_T} + \sum \frac{d\mathcal{P}_{ISR}}{dp_T} \right) \exp\left(- \int_{p_T}^{p_{T,i-1}} \left(\frac{d\mathcal{P}_{MI}}{dp'_T} + \sum \frac{d\mathcal{P}_{ISR}}{dp'_T} \right) dp'_T \right). \tag{3.20}$$

The whole process of parallel MPI and ISR generation is then again iterated until a lower cut-off is reached, specified by the model. Figure 3.7 shows what one can expect in the end, after all possible MPI and ISR effects are taken into account. It shows a schematic of multiple partons (3) that go out of the incoming hadron, and produce 4 interactions, each with their associated ISR. The hardest interaction happens "first" at a scale of $p_{T,1}$, and the others at a lower scale, as illustrated in the figure. The interleaving of ISR with multiple interactions implies that, in this particular example, the second parton from the hadron can produce two parton interactions through its ISR branching. [43, 44, 42]

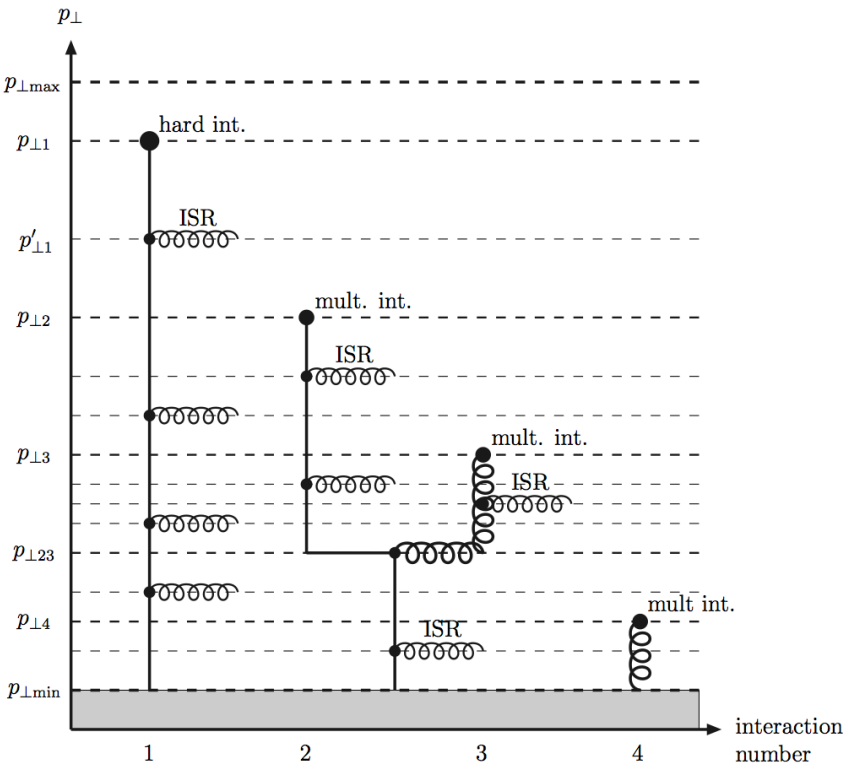

Figure 3.7.: Schematic figure illustrating an event with an incoming hadron that has a hard parton interaction at $p_{T,1}$ and three further parton interactions at successively lower p_T scales. With each interaction associated ISR can be generated, and two interacting partons (e.g. 2 and 3) can have a common ancestor in the parton showers. [43]

3.4. Monte Carlo model implementations

In this section we will briefly describe all the Monte Carlo [49] models that are used for the analysis in this work. These are computer programs that give us the ability to generate samples of hadron-hadron collisions according to a specific theoretical approach and/or phenomenological model. Based on the principle of random number generation, they create an initial state and calculate a complete final state, in accordance to a chosen model. Their results can then be compared to experimental data and hence one has the ability to test available theories and models. Since most of these are phenomenological and need free parameters to be tuned, the experimental data can be seen as input to further improve the model, or to rule it out completely.

3.4.1. Collinear factorisation based models

PYTHIA

One of the most widely used, successful and longstanding models is Pythia[42, 50], which is in fact the model we described in the previous sections throughout this chapter. It is thus based on the collinear factorisation theorem (section 2.3) to describe hadron-hadron collisions, uses the DGLAP evolution equations to calculate the parton dynamics, takes into account ISR/FSR (section 3.1.2), adds MPI (section 3.3), treats the beam remnants (section 3.2.2) and performs the hadronisation with the Lund string fragmentation model (section 3.2.1).

HERWIG

Herwig [51] is also based on the collinear factorisation theorem and DGLAP evolution, but uses different methods to take MPI into account and has a different hadronisation model, the cluster fragmentation. Also the parton shower construction is a bit different, as the parton emissions are angular ordered to take colour coherence effects into account.

The MPI framework in Herwig is based on an eikonal model, and starts from the assumption that at a fixed impact parameter b, partons can undergo n independent scatterings. The mean number is then given by (following the notation of [52]):

$$\begin{aligned}\langle n(b=|\mathbf{b}|,s)\rangle &= \int d^2\mathbf{b}' \int_{p_{T,min}^2} dp_T^2 \sum_{ij} \frac{1}{1+\delta_{ij}} \frac{d\hat{\sigma_{ij}}(x_1\sqrt{s}, x_2\sqrt{s}, p_T^2)}{dp_T^2} \\ &\otimes \; G_{i/h_1}(x_1, \mathbf{b}-\mathbf{b}', \mu^2) \otimes G_{j/h_2}(x_2, \mathbf{b}', \mu^2), \end{aligned} \tag{3.21}$$

with $\hat{\sigma}$ the partonic cross section for $2 \to 2$ QCD processes and $G(x, \mathbf{b}, \mu^2)$ the parton density functions at momentum fraction x, transverse coordinate $\mathbf{b}$ and factorisation scale μ^2. If we assume that the x and $\mathbf{b}$ dependencies can be factorized: $G(x, \mathbf{b}, \mu^2) = f(x, \mu^2) \cdot S(\mathbf{b})$ with $f(x, \mu^2)$ the usual parton densities, we can rewrite the previous equation as

$$\langle n(b,s)\rangle = A(b) \cdot \sigma^{inc}(s, p_{T,min}), \tag{3.22}$$

in which σ^{inc} represents the inclusive cross section for the production of a pair of jets (from the partons) with a $p_T > p_{T,min}$ and $A(b)$ is a function that describes the overlap of the partons in the colliding hadrons. It is expressed as $A(b) = \int d^2\mathbf{b}' S_{h_1}(\mathbf{b}') S_{h_2}(\mathbf{b}-\mathbf{b}')$, with $S(\mathbf{b})$ the impact parameter dependence of the partons in hadrons, which is modelled by the electromagnetic form factor:

$$S(\mathbf{b}) = \int \frac{d^2\mathbf{k}}{(2\pi)^2} \frac{e^{i\mathbf{k}\cdot\mathbf{b}}}{(1+\mathbf{k}^2/r_{had}^2)^2}. \tag{3.23}$$

Also in HERWIG the assumption is made that the multiple scatterings are independent, and hence their number is Poisson distributed (see eq. (3.12)). The probability of having n scatters in an event, with at least one interaction, is then:

$$P_{n\geq 1}(\sigma^{inc}) = \frac{\int d^2b \mathcal{P}_n(A(b)\cdot\sigma^{inc})}{\int d^2b \sum_{k=1}^{\infty}\mathcal{P}_k(A(b)\cdot\sigma^{inc})} = \frac{\sigma_n(\sigma^{inc})}{\sigma_{hard}(\sigma^{inc})}. \tag{3.24}$$

The number of additional scatters is then sampled according to standard QCD $2 \to 2$ process matrix elements with the same parton densities that were used for the hard process. The additional hard processes are thus generated according to the inclusive perturbative cross section, with no change for the fact that they are additional (softer) scatterings. All these interactions are then extended with parton showers [52]. In the region $0 < p_T < p_{T,min}$ additional soft scatters are generated with a Gaussian p_T distribution that has an integral given by the soft parton-parton cross section, and is matched with the perturbative contributions at $p_T = p_{T,min}$. The momentum fraction x of the soft partons is taken to be a flat distribution, and the spatial distribution of soft colour charges is specified by the parameter μ^2_{soft}. This parameter and the soft cross section are fixed from measurements or parametrisations of the total cross section and the elastic slope parameter [15].

In the end everything is passed onwards to the hadronisation process, which uses a *cluster fragmentation* model. The main difference with the string model, introduced in section 3.2.1, is that it employs an intermediate stage of cluster objects, which have a typical mass scale of a few GeV. Such a cluster model is based on the pre-confinement property of parton showers, which leads to colour singlet clusters with a universal mass distribution at low scales. The hadronisation then starts with a non-perturbative splitting of gluon into a $q\bar{q}$ (and possibly diquark-antidiquark) pair. Intermediate clusters are then formed from colour connected pairs, after which they undergo a quasi-two-body sequential phase-space decay. The limited mass spectrum in this model however, leads to limited transverse momenta and suppresses heavy flavour, strangeness and baryon production. Finally, when combined with angular ordered parton showers, the cluster model gives a good overall description of high-energy collider data. Although it performs slightly less than the string model, it has the big advantage of having less parameters. [15]

3.4.2. k_T factorisation based models

CASCADE

CASCADE [53, 54] is based on the high energy factorisation approach (section 2.4.1) and uses the CCFM evolution equations to describe the initial state parton branching, supplemented with off-shell matrix elements for the hard scattering. One major difference with the previous discussed models is that MPI are not implemented in CASCADE. In the CCFM approximation, the probability to find a gluon in a hadron depends on three variables: the momentum fraction x, the transverse momentum k_T and the scale

$\bar{q} = x_n\sqrt{s\Xi}$, with Ξ the maximum allowed angle for any gluon emission. This leads to the usage of unintegrated parton densities $\mathcal{A}(x, k_T, \bar{q})$ that can be evolved from one scale to another by using the CCFM equations. Given such unintegrated parton densities, a full hadron-hadron collisions is then generated in three steps:

- Generation of the hard scattering process, based on the k_T factorisation formula:

$$\sigma = \int dk_{T,1}^2 dk_{T,2}^2 dx_1 dx_2 \mathcal{A}(x_1, k_{T,1}, \bar{q})\mathcal{A}(x_2, k_{T,2}, \bar{q})\hat{\sigma}(k_1 + k_2 \to X), \tag{3.25}$$

  with $k_{1,2}$ the momenta of the incoming partons to the hard scattering that is described by $\hat{\sigma}$.

- The ISR is added to the event according to the CCFM evolution equations.

- In the end hadronisation is performed using the Lund string fragmentation model, as described in section 3.2.1.

DIPSY

The DIPSY [55] generator is somewhat different, it is based on Mueller's dipole cascade model [56, 57, 58], which is a formulation of the LL BFKL evolution in transverse coordinate, i.e. impact parameter, space. In this picture, gluon radiation that arises from the colour charge in a parent parton is screened by the accompanying anti-charge in the colour dipole. This feature suppresses emissions at large transverse separation, which corresponds to the suppression of small k_T values in the BFKL approximation. For a given dipole at a transverse position $(\mathbf{x}, \mathbf{y})$, the probability per unit of rapidity (y) for the emission of a gluon at a transverse position $\mathbf{z}$ is given by [55]:

$$\frac{d\mathcal{P}}{dy} = \frac{3\alpha_S}{2\pi^2} d^2\mathbf{z} \frac{(\mathbf{x}-\mathbf{y})^2}{(\mathbf{x}-\mathbf{z})^2(\mathbf{z}-\mathbf{y})^2}. \tag{3.26}$$

An emission corresponds to a dipole that is split into two new dipoles, which can in turn emit new gluons independently. This reproduces the BFKL evolution, with the number of dipoles growing exponentially with rapidity. Two cascades can then collide and interact through gluon, i.e. colour, exchange, and as such a BFKL ladder is formed between the two hadrons. Multiple interactions (MPI) and saturation effects represent multiple pomeron exchanges and pomeron loops. Mueller's model includes multiple dipole interactions, with free parameters that need to be tuned to data. In the present implementation however, quarks are not included in the evolution. The treatment of the proton remnant and valence quark structure is therefore simplistic.

In summary the generation of a final state in the DIPSY model is as follows [55]:

- Creation of two dipole cascades, from the incoming hadrons, according to the BFKL evolution and saturation.

- Determine which pairs of partons from the two hadrons interact. The emission of gluons in the BFKL approach is a Poissonian process, and the interaction probability is calculated in the eikonal approximation.
- Extract the primary k_T changing gluons and check that they have the correct weight in the generation process. These gluons then form the colour connected chains between the two colliding hadrons, including their branchings and loops. In addition the energy-momentum conservation is restored and branches in the cascade that do not interact are removed.
- Final state radiation is added in relevant parts of phase space. As a result one gets chains of colour connected gluons.
- In the last step, the hadronisation is performed using the Lund string fragmentation model (section 3.2.1).

3.4.3. Cosmic ray physics generators

These Monte Carlo models were originally developed to be used in high energy cosmic ray physics. Because of the extremely low flux of such high-energetic particles, they can not be detected directly, and one needs to infer their properties from the extensive air showers that they generate in the atmosphere. These originate from hadron-nucleus (or nucleus-nucleus) interactions and hence the understanding of such processes is of crucial importance. To improve the Monte Carlo treatment in this field, a series of models was designed that are able to describe general inelastic hadronic collisions.

These models are developed in the framework of Gribov's reggeon field theory (recall section 2.4.2) and describe the soft non-perturbative component in terms of the exchange of virtual quasi-particle states, the pomeron, with multi-pomeron exchanges accounting for MPI effects. At higher energies and scales, the interaction is described by perturbative QCD with the DGLAP evolution. These models also include non-linear parton effects, either by including pomeron-pomeron interactions, as in QGSJET [59] and EPOS [60], or by means of a parton saturation approach, as in SIBYLL [61].

QGSJET

The QGSJET model describes multiple scatterings (MPI) in hadronic processes as multiple exchanges of pomerons, which correspond to independent parton cascades. For the soft cascades, a phenomenological "soft" pomeron amplitude is used, while the semi-hard scattering processes are described by the exchange of "semi-hard" pomerons, which are composed of a DGLAP QCD parton ladder that is sandwiched between two soft pomerons, as illustrated in figure 3.8. A principal feature of QGSJET is the ability to take non-linear parton effects into account that are described by pomeron-pomeron interactions. The

basic assumption here is that these couplings are dominated by non-perturbative parton processes, and can as such be described by phenomenological multi-pomeron vertices.

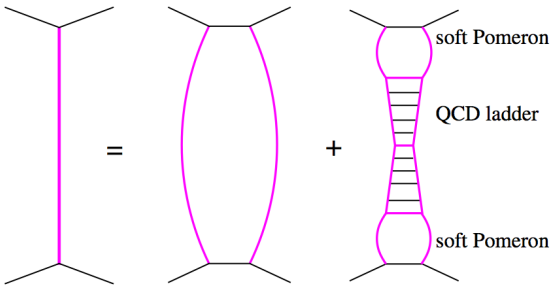

Figure 3.8.: Schematic representation of a general pomeron contribution (left hand side). It consists of a soft and semi-hard pomeron respectively. [59]

As such the elastic scattering amplitude between hadron a and d is defined as

$$f_{ad}(s,b) = i \sum_{j,k} C_{j/a} C_{k/d} \left[1 - e^{-(1/2)\Omega_{ad(jk)}(s,b)}\right], \tag{3.27}$$

with s the centre-of-mass energy squared, and b the impact parameter for the interaction. The $C_{j/a}$ and $C_{k/d}$ define the partial weights for hadrons a and d in their elastic scattering eigenstates. Furthermore we have:

$$\Omega_{ad(jk)}(s,b) = 2\chi^{\mathbb{P}}_{ad(jk)}(s,b) + 2\chi^{enh}_{ad(jk)}(s,b). \tag{3.28}$$

Here $\chi^{\mathbb{P}}_{ad(jk)}$ and $\chi^{enh}_{ad(jk)}$ are the eikonals that correspond to pomeron exchanges and irreducible enhanced pomeron-pomeron interactions respectively. The general pomeron eikonal is then given by contributions of the soft and semi-hard pomerons (figure 3.8):

$$\chi^{\mathbb{P}}_{ad(jk)}(s,b) = \chi^{\mathbb{P}_{soft}}_{ad(jk)}(s,b) + \chi^{\mathbb{P}_{sh}}_{ad(jk)}(s,b), \tag{3.29}$$

in which the soft pomeron eikonal is expressed via its emission vertices and the pomeron propagator, which is described by the pomeron Regge trajectory. $\chi^{\mathbb{P}_{sh}}_{ad(jk)}$ then contains the semi-hard contributions in which the collinear factorisation enters, with its parton densities, DGLAP evolution and perturbative QCD cross sections. The enhanced eikonal $\chi^{enh}_{ad(jk)}$ takes into account the saturation effects through possible pomeron-pomeron interactions, which in turn can contain soft and semi-hard processes. It is presently the most advanced model for the description of peripheral hadronic interactions, but for more central collisions sizeable corrections are expected from dedicated hard pomeron-pomeron couplings that are neglected in QGSJET. [59, 62]

SIBYLL

The SIBYLL generator is based on the dual parton model (DPM) picture in which a nucleon consists of a quark q (colour triplet) and a diquark qq (colour anti-triplet). In this model, soft gluons are exchanged in an interaction, during which the colour field gets reorganised. The quark (diquark) then combines with the diquark (quark) from the other hadron and two strings are formed, which each fragment separately according to the Lund string model. The fractional energies x of the quarks are then chosen from the following distribution:

$$f_q(x) = \frac{(1-x)^\alpha}{(x^2 + \mu^2/s)^{(1/4)}}, \tag{3.30}$$

with $\alpha = 3.0$ and $\mu = 0.35$ GeV, the effective quark mass. The diquark energy fractions are then chosen from: $f_{qq}(x) = 1 - f_q(x)$. However, the DPM picture, in which just two strings interact, can not explain the observed high multiplicities and high p_T jets that arise from hard perturbative interactions that are not originally included. To circumvent this, the SIBYLL model uses the collinear factorisation framework to determine the cross section $\sigma_{QCD}(s, p_{T,min})$, in which the parton density functions and perturbative partonic cross section enters. The average number of hard and soft interactions (MPI) that occur at a given s and b can be expressed as:

$$n_{\rm hard}(b,s) = A(b)\sigma_{\rm QCD}(s) \tag{3.31}$$

$$n_{\rm soft}(b,s) = A_{\rm soft}(b)\sigma_{\rm soft}(s), \tag{3.32}$$

which enter in the total inelastic cross section through the eikonals:

$$\sigma_{\rm inel} = \int d^2b \left[1 - e^{-2\chi(b,s)}\right] \tag{3.33}$$

$$\chi(b,s) = \chi_{\rm hard}(b,s) + \chi_{\rm soft}(b,s) \tag{3.34}$$

$$= \frac{1}{2} n_{\rm hard}(b,s) + \frac{1}{2} n_{\rm soft}(b,s). \tag{3.35}$$

The introduced factors $A(b)$ are the profile functions that characterise hadron-hadron collisions in terms of impact parameter b. The profile function of the soft processes $A_{\rm soft}(b)$ is different from the hard ones to take the energy dependent increase of the soft interaction region into account (see [61]). To describe the soft cross section, and allow multiple soft interactions, the Regge theory approach is adopted and the energy dependence of $\sigma_{\rm soft}$ is taken as a sum of two power laws, one for the pomeron exchange (Δ_{eff}) and another for additional reggeon exchange ($-\epsilon$):

$$\sigma_{\rm soft}(s) = X\left(\frac{s}{s_0}\right)^{\Delta_{eff}} + Y\left(\frac{s}{s_0}\right)^{-\epsilon}. \tag{3.36}$$

All the parameters $(X, Y, \Delta_{eff}, \epsilon)$ are then determined by fitting measured total, elastic and inelastic cross sections for pp and $p\bar{p}$ interactions. To generate the events, the number

of soft and hard interactions are again sampled using a Poisson distribution (eq. (3.12)). One of the multiple interactions always involves a valence quark, for which the momentum fraction is then sampled from distribution (3.30).

SIBYLL thus uses the same pomeron formalism to describe the soft processes as in QGSJET, and the semi-hard ones are treated in a slightly different framework, which is however qualitatively similar. Non-linear parton effects are also taken into account, but are based on a parton saturation approach, where it is assumed that semi-hard processes result in the production of partons with transverse momenta larger than an effective energy dependent saturation scale $Q_0^2 = Q_{\text{sat}}^2(s)$, for which the double leading-log ansatz is used. These non-linear effects are however neglected for the soft interactions component. [61, 62]

EPOS

The EPOS model employs the above discussed soft and semi-hard pomeron phenomenology and in addition it takes energy-momentum correlations between multiple re-scatterings into account, a feature that is missing in the previous described cosmic ray physics event generators. The description of non-linear parton effects is based on an effective treatment of the lowest order pomeron-pomeron interaction graphs.

The core of the EPOS approach is reflected in its name [60]:

- **E**nergy conserving quantum mechanical multiple scattering, based on:
- **P**artons, and parton ladders
- **O**ff-shell remnants
- **S**plitting of parton ladders

A parton ladder contains two parts: the hard one, which includes the hard scattering with its attached parton showers, and a soft one, which is purely a phenomenological object, described using the Regge theory approach. In the event there are then three colour neutral objects that participate in the interactions: two off-shell beam remnants, and the parton ladders between the two active partons on either side. In this picture one can refer to the inner contributions, coming from the parton ladders, and outer contributions from the beam remnants. This reflects the fact that remnants produce a lot of activity at large rapidities, while the parton ladders populate the phase space at central rapidities.

A key point in the EPOS model is that to come to a consistent quantum mechanical energy conserving multiple scattering treatment, one does not only need to take open parton ladders into account, but also so called closed ladders that represent elastic scatterings. The closed ladders do not contribute to particle production in the final state, but they are crucial since they can substantially affect the calculation of partial cross sections. Free parameters characterise the behaviour of soft interactions, and are

essentially fixed to have a correct pp cross section. In addition, parameters that regulate the perturbative QCD part in the event generation are fixed to provide reasonable parton distribution functions that are in fact calculated, and not given as input to the model. [60, 62]

Part II.

Experimental setup

Chapter 4.

The Large Hadron Collider

To study and test the theories described in the previous part, one needs to analyse the outcome of such proton-proton collisions. These measurements can be done using particle accelerators: machines that are able to accelerate and collide protons head-on at very high centre-of-mass energies. The result of the scattering can then be recorded with appropriate detectors placed around the interaction point.

The world's newest and most powerful particle accelerator is the Large Hadron Collider (LHC) at CERN[1] in Geneva, Switzerland. It is designed to search for answers to unresolved key questions in particle physics that might be hidden in the TeV energy scale domain and its unprecedented energy makes it thus ideal to study the QCD and Underlying Event physics in phase spaces that were never accessible before.

4.1. General design

The LHC is a circular superconducting hadron accelerator and collider installed in the existing LEP [63] tunnel, which has a circumference of 27 km and is located between 45 m and 170 m underground the Swiss - French border. It consists of 2 rings in which counter rotating beams of protons can be accelerated to energies of 7 TeV and can thus deliver proton-proton collisions with $\sqrt{s} = 14$ TeV. Additionally, the LHC can also accelerate Pb ions ($^{208}Pb^{82+}$) up to energies of 2.76 TeV/nucleon resulting in heavy ion collisions with a total $\sqrt{s}$ of 1.15 PeV [64]. In the proton-proton configuration peak luminosities of $L = 10^{34}$ cm^{-2} s^{-1} can be reached that are, together with the high centre-off-mass energy, a key feature for the search for new physics phenomena. Bunches containing 1.15×10^{11} protons with an energy of 450 GeV are injected using the SPS accelerator [65]. A maximum of 2808 bunches can be injected per beam with a minimal time of 25 ns between two bunches leading to a peak crossing rate of 40 MHz. When the beams are completely filled and accelerated they have a circulating beam current of 0.582 A and the total energy stored per beam equals 362 MJ. To keep the accelerated protons on track the LHC needs superconducting magnets that use state-of-the-art technology. With

[1] Conseil Européen pour la Recherche Nucléaire.

superfluid helium the used NbTi Rutherford cables are cooled down to a temperature below 2 K enabling fields of 8 T needed for 7 TeV operation.

The vacuum beampipes containing the counter rotating proton beams cross each other in 4 interaction points as can be seen in figure 4.1. Around these, 6 collaborations built particle detectors that have the capability to measure the proton-proton collisions very precisely. Two of these experiments, ATLAS [66] and CMS [67], are multi-purpose detectors that consist of several sub-detector systems that are each capable of measuring certain particle properties in a specific phase space. The detectors are completely built around the proton-proton interaction point and when the information from all subsystems is combined, one can reconstruct a complete picture of the proton-proton scattering. Both experiments have a very broad physics program and are designed to search for new physics phenomena such as the Higgs mechanism (electroweak symmetry breaking), super-symmetric particles and extra-dimensions. But the design also allows a thorough study of the Standard Model physics. Furthermore, both detectors have an heavy ion physics program. The very high energies and luminosities at the LHC make the design, construction and operation of such detectors very challenging. They have to cope with high radiation levels, high collision rates and must be able to conduct very precise measurements if one wants to find traces of new physics hidden in very rare processes. The work presented in this thesis is conducted at the CMS experiment, which will be more described in detail in the next chapter.

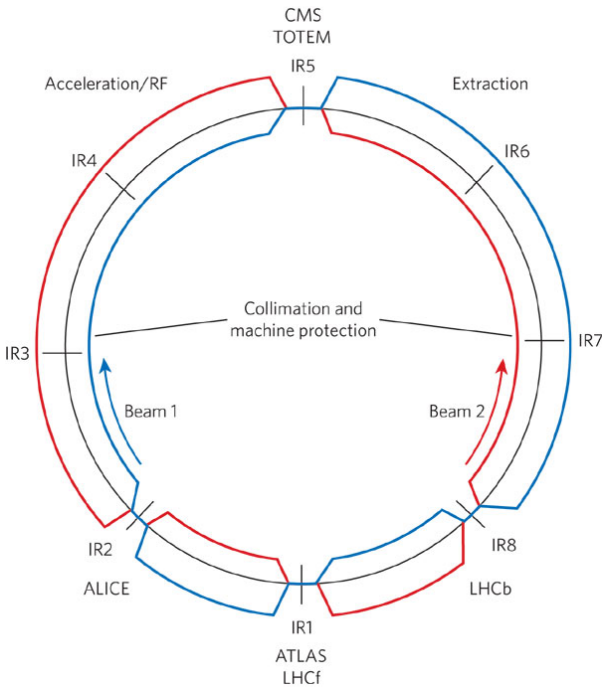

Figure 4.1.: Schematic layout of the LHC: the two proton beams rotate in opposite directions and cross each other at the designated interaction regions (IR) that contain the various experiments. In addition, the position of the radio-frequency (RF) acceleration equipment, collimation and machine protecting systems, and beam abort (extraction) systems are indicated on the figure. [68]

The LHCb [69] and ALICE [70] detectors have a rather different physics program. The LHCb experiment is a single-arm spectrometer with excellent forward angular coverage dedicated to the study of heavy flavour physics: its primary goal is to look for indirect evidence of new physics in CP violation and rare decays of beauty and charm hadrons. ALICE is a general-purpose heavy-ion detector designed to study the physics of strongly interacting matter (QCD) and the quark-gluon plasma at extreme energy densities and temperatures in nucleus-nucleus collisions. Finally, TOTEM [71] and LHCf [72] are small special purpose experiments that share the CMS and ATLAS interaction points respectively. The TOTEM experiment is dedicated to the measurement of the total cross section, and the study of elastic scattering and diffractive processes at the LHC. The LHCf experiment is dedicated to the measurement of neutral particles emitted in the very forward region of LHC collisions to study cosmic ray physics.

4.2. Run periods

Although the LHC has a design centre-of-mass energy $\sqrt{s} = 14$ TeV and luminosity $L = 10^{34}$ cm^{-2} s^{-1}, it did not run with these parameters yet. The main reason for this is an incident that happened right after the first beam injection and circulation in September 2008. A faulty electrical connection triggered a massive liquid helium leak causing several superconducting magnets to heat up. This quenching resulted in substantial damage to the accelerator magnets and their infrastructure. As a result, the LHC was down for more than a year in order to repair the damaged systems and to install additional safety systems to prevent such incidents in the future. Despite a lot of improvements were done, it was decided to run the LHC the next 3 years at substantial lower energies and luminosities to minimise the risks. In November 2009, at last proton beams were injected and circulated again to soon provide the first proton-proton collisions in the LHC ever[2]. These had a centre-of-mass energy of $\sqrt{s} = 900$ GeV, which means that the injected protons from the SPS (at 450 GeV) were not additionally accelerated by the LHC at that time.

In March 2010 the first ever proton-proton collisions with $\sqrt{s} = 7$ TeV took place, marking another milestone in particle physics history. Notwithstanding that the proton beams were only accelerated to 3.5 TeV, half the design energy, it is still the highest energy ever reached since the previous state-of-the-art hadron collider, the Tevatron, which provided proton-anti proton collisions with $\sqrt{s} = 1.96$ TeV [73]. This was the start of 3 long run periods where most of the data taking in 2010 and 2011 happened with $\sqrt{s} = 7$ TeV while it was decided, due to preliminary Higgs search results, to crank up the beam energies in 2012 to have collisions at $\sqrt{s} = 8$ TeV. Currently the LHC entered its first long shut down period and is being prepared to start up again in 2014 and provide proton-proton collisions at $\sqrt{s} = 13$ TeV.

[2] I was in fact in the CMS Centre at the CERN Meyrin site doing data quality monitoring shifts at that time. It was truly remarkable and unforgettable to witness such great achievement!

The first data taking period from February to November 2010 started quite modest. The first beams had only 2 to 13 low intensity bunches but afterwards the performance quickly increased by pushing the number of bunches up to 50. In the end the machine worked with bunch trains of 150 ns spacing containing up to 368 bunches. The luminosity increased gradually over the year from 8×10^{26} cm^{-2} s^{-1} to 2×10^{32} cm^{-2} s^{-1} at the end. The performance increased very quickly in the 2011 and 2012 run periods. Using beams containing a maximum of 1380 bunches with 50 ns spacing very high peak luminosities of 0.4×10^{34} cm^{-2} s^{-1} in 2011 and 0.7×10^{34} cm^{-2} s^{-1} in 2012 were reached [74] [75]. The total integrated luminosities recorded by the CMS experiment are shown in figure 4.2 and are 44.2 pb^{-1} in 2010, 6.1 fb^{-1} in 2011 and 23.3 fb^{-1} in 2012.

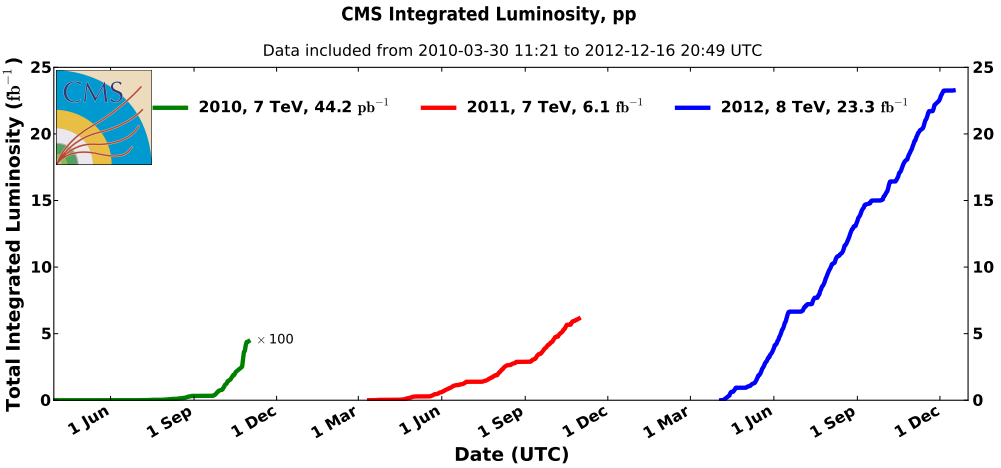

Figure 4.2.: Cumulative luminosity versus time delivered to CMS for p-p collisions. Shown for 2010 (green), 2011 (red) and 2012 (blue) data-taking periods. The integrated luminosity of 2010 is multiplied with a factor 100 for comparison.

However the fact that the LHC started at low energies and luminosities is very beneficiary to study the Underlying Event in proton-proton collisions. Despite not shown in figure 4.2, proton-proton collisions with $\sqrt{s} = 0.9$ TeV were recorded at the start of the 2010 run, while at the start of the 2011 run data was taken with $\sqrt{s} = 2.76$ TeV. This gives us the unique possibility to measure the Underlying Event activity at 3 different centre-of-mass energies. More important though is the very low luminosity of these proton-proton collisions: when the LHC runs at its design luminosity the beam intensities are so high that when they cross each other at the interaction point the probability to have more than 1 proton-proton collision increases significantly. This effect, called *pile-up*, caused a maximum of 35 measured interactions per bunch crossing during 2012 data taking. Since our study of interest concerns the underlying behaviour of a single proton-proton interaction we need to avoid the situation where detectors measure mixed signals originating from multiple proton-proton interactions at the same time. Hence we are interested in beam conditions that only provide 1 proton-proton interaction on average, and the low luminosity runs conducted during LHC startup periods give us exactly that.

Chapter 5.

The Compact Muon Solenoid

5.1. Introduction

The Compact Muon Solenoid (CMS) detector, introduced in the previous chapter as one of the 4 major LHC experiments, is used to collect the data analysed in this work. It is installed at the LHC point 5, in a huge underground cavern, 100 m below the French village of Cessy. Since it is a multi-purpose experiment it actually consists of many sub-detectors constructed within an onion-like design. Each layer registers certain types of particles using a specific detection mechanism. When the information from each layer is combined, one can completely reconstruct the outcome of an LHC bunch crossing. The detector has a length of 21.6 m, a diameter of 14.6 m and a total weight of 12 500 t. [67]

To cope with the extreme LHC conditions, a lot of experimental challenges have to be met. The very high centre-of-mass energies and beam intensities at the design luminosity of the accelerator imply that on average 20 collisions will take place during each beam crossing. This means that every 25 ns around 1000 charged particles emerge from the interaction point. Hence, the detection mechanisms, read-out electronics and online event selection process must be able to digest all the information within this time frame. Furthermore, the large flux of particles results in high radiation levels requiring hardware that can withstand this environment. In addition, to meet the LHC physics goals it is mandatory to have a high detector resolution.

From a general physics point of view the detector requirements for CMS can be summarised into following demands: [67]

- Good muon identification and momentum resolution over the whole phase space.
- Good charged-particle momentum resolution and trajectory reconstruction efficiency close to the interaction vertex.
- Good electromagnetic energy resolution and high calorimeter granularity
- Good missing-transverse-energy (E_T^{miss} or MET) detection efficiency, requiring a complete hermetic geometric coverage.

In the next sections the sub-systems most important for the analysis conducted in this work will be described in more detail and the above requirements will be stated more specifically.

Figure 5.1 shows a complete overview of the CMS detector and all its sub-components. At the heart of the experiment, closest to the interaction point of the proton-proton collisions, are the pixel detector and silicon tracker that reconstruct the trajectories of charged particles originating from the interaction. The next layer contains the electromagnetic calorimeter, which measures the energy deposited by particles that initiate electromagnetic showers when they interact with matter, such as electrons and photons. After that, remaining particles enter the hadron calorimeter that can measure the energy deposited by particles that initiate hadronic showers when they interact with matter, such as e.g. protons, neutrons and pions. All the sub-systems mentioned above are inside the field of the superconducting solenoid. This is one of the main features of CMS and generates a 3.8 T magnetic field that bends the trajectories of charged particles, to allow the measurement of their momentum using the tracker information. Outside the solenoid are muon detectors that take care of the muon charge and momentum reconstruction. In addition, CMS is complemented with calorimeters at both ends very close to the beampipe. These so called *forward detectors* can measure the energy deposited by particles that have a small angle with respect to the beampipe, and thus escape the other *central* sub-systems. Despite only one such detector, the Very Forward Calorimeter or Hadronic Forward calorimeter, is shown in figure 5.1, there are additional forward calorimeters installed, such as CASTOR, ZDC [76] and FSC [77], with each a specific range and purpose. The Centauro And Strange Object Research (CASTOR) detector will be described in a separate chapter given its importance for this work. [67]

It is important to note that the design and placement of the various sub-detectors is optimised to allow a complete and successive measurement of all kind of particles. The tracking system is located closest to the interaction point since it is used to reconstruct (see section 7.2) the interaction vertices and corresponding particle tracks without destroying any of them. In contrary, the electromagnetic and hadronic calorimeters measure the energy of particles in a destructive way. First particles such as electrons and photons will be absorbed in the electromagnetic section, while e.g. protons, neutrons and pions penetrate this and are absorbed in the hadronic section. Muons finally, which are minimum ionising particles, survive all this and leave their tracks in the large muon chambers at the outside of the CMS detector.

To make the detector description more rigorous a coordinate system has to be defined. The CMS experiment uses a right-handed coordinate system, with the origin at the nominal interaction point, the x-axis pointing to the centre of the LHC ring, the y-axis pointing up (perpendicular to the plane of the LHC ring), and the z-axis along the anticlockwise-beam direction. The polar angle θ is measured from the positive z-axis and the azimuthal angle ϕ is measured in the $x - y$ plane. Pseudorapidity is defined with respect to the polar angle θ as: $\eta = -\ln\tan(\theta/2)$. When the information from all sub-systems described above is combined, CMS covers the pseudorapidity range $-6.6 < \eta < +5.2$. [67]

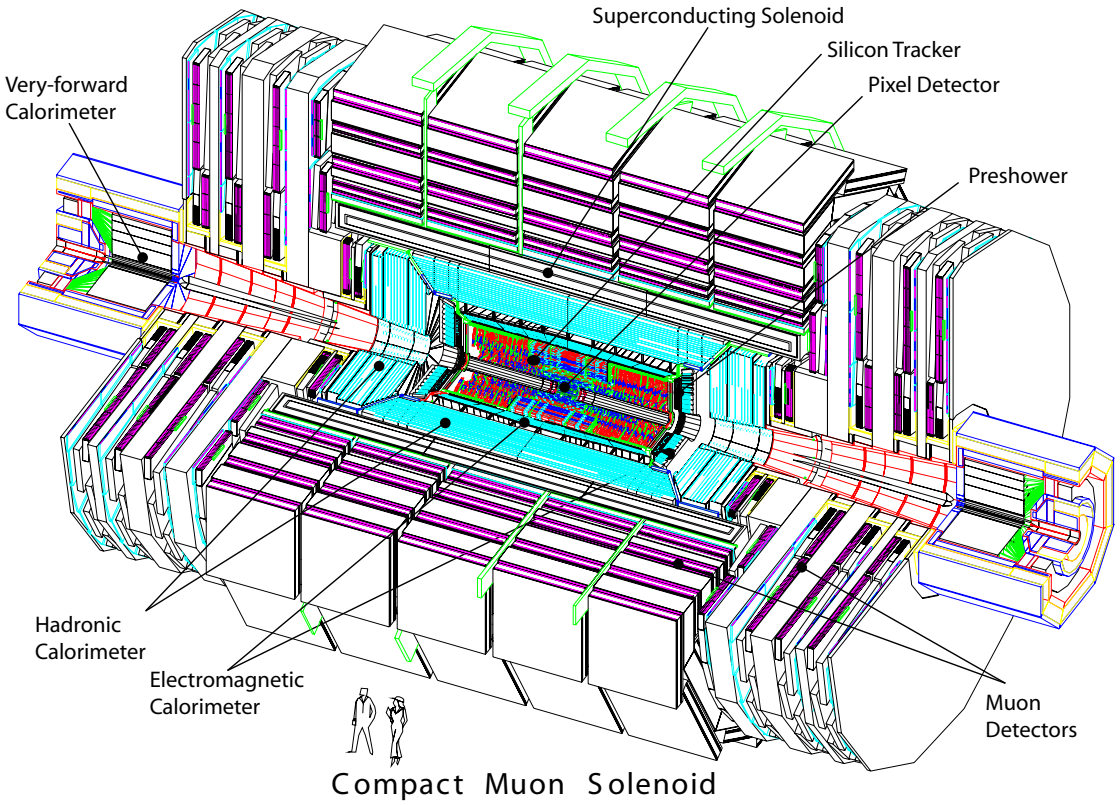

Figure 5.1.: Perspective view of the CMS detector with its sub-components. [67]

5.2. Tracking system

The CMS tracking system is designed to measure the trajectories of charged particles, emerging from the collisions at the interaction point, with great precision and efficiency for transverse momenta above 1 GeV/c in a pseudorapidity range of $|\eta| < 2.5$. In addition, a good reconstruction of secondary interaction vertices is mandatory to identify decays of long lived heavy particles, produced in many interesting physics channels, and to distinguish multiple independent collisions in case of *pile-up* conditions. It has a total length of 5.8 m, a diameter of 2.5 m and is completely embedded in the 3.8 T magnetic field of the solenoid. [67]

At the LHC design luminosity of 10^{34} cm^{-2} s^{-1} the tracker volume will be traversed by an average of 1000 particles every 25 ns, which results in a hit rate density of 1 MHz/mm^2 at a radius of 4 cm from the interaction point. This implies that detector technologies providing high granularity and fast response are required. As a consequence, a high density of read-out electronics is needed that require cooling. However one has to minimise the amount of material used, since this can introduce additional interactions that in turn produce charged particles that contaminate the original track collection. On top of that, the tracking system has to withstand severe radiation caused by the intense

particle flux, and aim for an expected lifetime of 10 years. All above requirements lead to a design entirely based on silicon detector technology. [67]

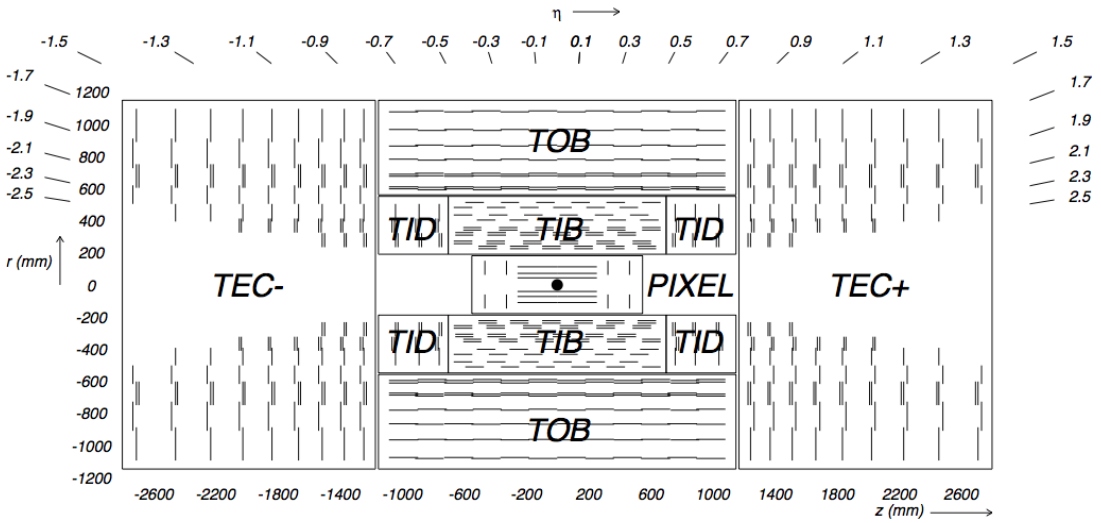

Figure 5.2.: Schematic cross section of the CMS tracking system. Each line represents a detector module. The acronyms are explained in the text. [67]

The tracking system is composed of two sub-systems, its layout is shown in figure 5.2. The first, most inner one, is the *pixel detector* (PIXEL). To keep the detector occupancy at maximum 1% and to meet the desired impact parameter resolution, a pixelated design with a pixel size of 100×150 μm^2 has to be used for a radius smaller than 10 cm. It consists of 3 cylindrical barrel layers with radii between 4.4 cm and 10.2 cm that surround the interaction point and are complemented by 2 disks of pixel modules at each side, called the endcaps. With this design, the pixel detector can deliver 3 high precision space points to measure the charged particle trajectories. It contains 66 million pixels distributed in modules over a total area of 1 m^2. [67]

The second part is the *silicon strip tracker*. At larger radii (20 cm $<$ r $<$ 55 cm) the reduced particle flux allows the use of silicon micro-strip detectors with cell sizes starting at 10 cm $\times$ 80 μm, which results in occupancies of 2-3% per strip in the inner tracker region. In the outer section of the tracker (55 cm $<$ r $<$ 110 cm) the strip size can be further increased to 25 cm $\times$ 180 μm leading to occupancies of 1%. An additional advantage of the increase in cell size is that the number of read-out channels can be limited. However since the electronics noise is a linear function of the strip length, thicker silicon sensors have to be used in the outer regions to maintain a good signal to noise ratio well above 10. Hence the outer tracker uses 500 μm thick sensors whereas the inner tracker uses sensors with a thickness of 320 μm. [67]

The inner tracker region introduced above, shown as TIB/TID in figure 5.2, consists of 4 barrel layers and 3 disks at each end. It delivers up to 4 $r - \phi$ measurements on a particle trajectory and the strip sizes lead to single point resolutions of $23 - 35\mu$m. The outer tracker region, shown as TOB/TEC+/TEC- in figure 5.2, consists of 6 barrel layers

(TOB) and provides 6 additional $r - \phi$ measurements with resolutions of $35 - 53\mu$m. Beyond the TOB z-range (± 118 cm) the tracker endcaps (TEC+ and TEC-) cover the region 124 cm $< |z| <$ 282 cm and 22.5 cm $< |r| <$ 113.5 cm. Each TEC is composed of 9 disks, and thus provides 9 additional ϕ measurements. The modules in the first two layers of TIB, TID, TOB and rings 1, 2 and 5 of each TEC carry a second micro-strip module mounted back-to-back to the first one with a stereo angle of 100 mrad in order to provide the measurement of a second coordinate (z in the barrel layers and r in the endcap disks). This layout ensures at least 9 hits in the full range of $|\eta| < 2.4$, where 4 of them are two-dimensional. In total, the CMS silicon strip tracker contains 9.3 million strips. [67]

The overall design results in a total pseudorapidity coverage of $|\eta| < 2.5$ for which about 200 m^2 of active silicon is used spread over 1440 pixel and 15 148 strip modules, making it the largest silicon based tracker ever built. To optimise the performance of the hardware the whole tracker volume will be operated around temperatures of -10°C. The total power consumption rises to 60 kW. [67]

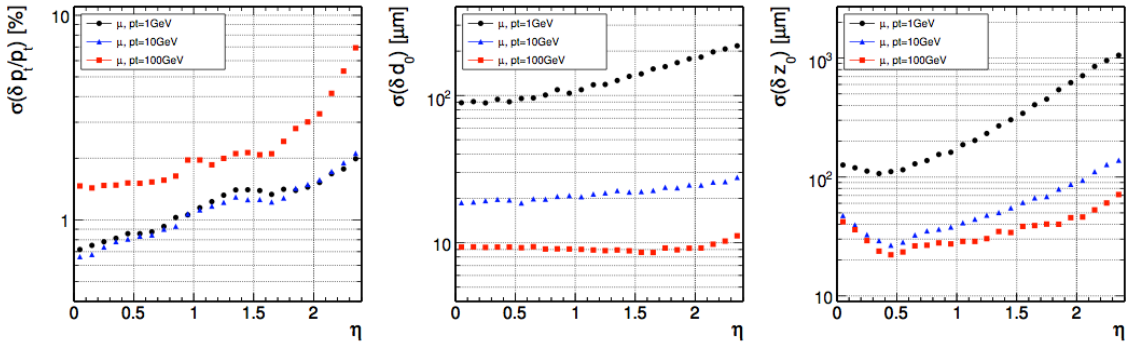

Figure 5.3.: Track parameter resolutions for single muons with a p_T of 1, 10, and 100 GeV: transverse momentum (left), transverse impact parameter (middle) and longitudinal impact parameter (right). [67]

The excellent tracker performance is illustrated in figure 5.3 for single muons with transverse momenta, p_T, of 1, 10 and 100 GeV. The expected resolutions of transverse momentum (left), transverse impact parameter (middle) and longitudinal impact parameter (right) are shown. For 100 GeV muon tracks, a p_T resolution of $1 - 2\%$ up to $|\eta| \approx 1.6$ can be reached. The transverse impact parameter resolution reaches a precision of 10 μm for high-p_T tracks while the longitudinal impact parameter measurement can reach a precision of 20 μm at $\eta \approx 0.5$, although it increases to 70 μm at the edge of the tracker volume ($|\eta| \approx 2.5$). [67]

The real power of the CMS tracking system becomes visible when one looks at figure 5.4. This picture shows an event display of an LHC bunch crossing taken during a very high pile-up test run, number 198609, in July 2012 [78]. Due to the extremely high beam intensities a huge amount of proton-proton collisions took place during this one bunch crossing, and the CMS tracking system was able to reconstruct 78 interaction vertices,

demonstrating its excellent performance. Figure 5.4a shows an overview of the tracker and calorimeter response, while 5.4b is a zoom into the inner tracker region. This example illustrates the general importance of the tracker since it is the only instrument that can quantify these pile-up effects and provide detailed particle trajectory measurements.

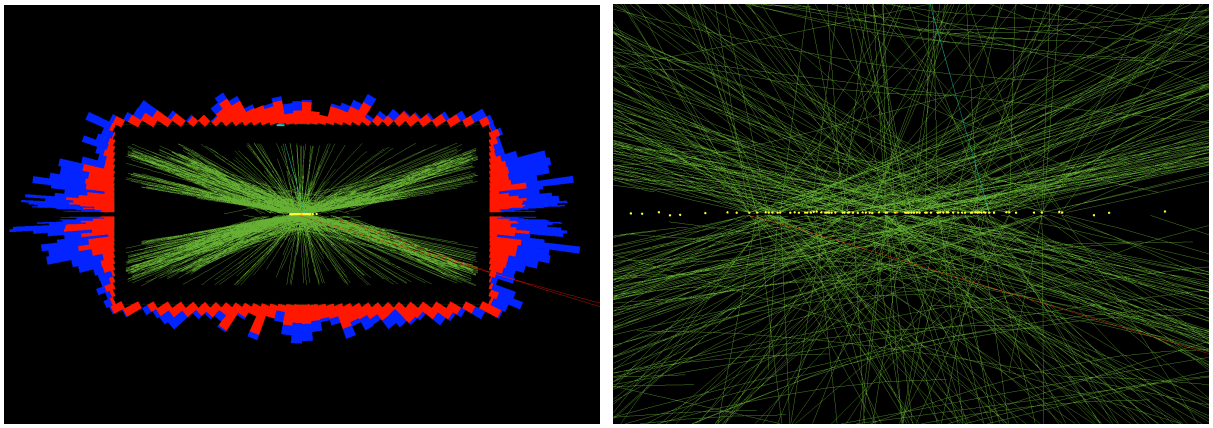

(a) (b)

Figure 5.4.: A CMS event display of an LHC bunch crossing, from high pile-up run 198609, with 78 reconstructed vertices. The vertices are indicated with yellow dots, reconstructed tracks are shown in green. An overview of the tracker, electromagnetic (red) and hadronic (blue) calorimeter response is shown in (a), while (b) shows a zoom of the inner tracker region. [78]

5.3. Central calorimetry

After the tracking system, particles enter the calorimetric part of CMS. First they will meet the electromagnetic calorimeter, and the ones that survive enter the hadronic calorimeter directly after.

5.3.1. Electromagnetic (ECAL)

The CMS electromagnetic calorimeter is an hermetic homogeneous calorimeter made of 61200 lead tungstate ($PbWO_4$) crystals in the central barrel and extended by 7324 crystals in each of the 2 endcaps. The scintillation light produced in the crystals is collected by highly efficient photodetectors placed at the rear. The requirement to have a fast, radiation resistant detector with a high granularity lead to the usage of these high density crystals. One of the main criteria in the design was the potential to detect the decay of the postulated Higgs boson to 2 photons. [67]

The scintillation decay time is of the same order of magnitude as the LHC bunch crossing time: in 25 ns about 80% of the light is emitted. However the light output,

blue-green scintillation light with a maximum around 420-430 nm, is rather low leading to a collection of 4.5 photoelectrons per MeV at a temperature of 18°C. This nominal operation temperature has to be maintained with a very high precision (± 0.05°C) to preserve the energy resolution, since the number of scintillation photons emitted by the crystals and the amplification of the photodetectors are both temperature dependent. The ECAL barrel covers the pseudorapidity range $|\eta| < 1.479$ and has a 360-fold granularity in ϕ and (2×85)-fold in η, which corresponds to a crystal area of 0.0174×0.0174 in $\eta - \phi$ or 22×22 mm^2 at the front face. The length equals 230 mm, which corresponds to a radiation length (X_0) of 25.8. The barrel volume is 8.14 m^3 and weighs 67.4 t. [67]

The endcaps cover the pseudorapidity range $1.479 < |\eta| < 3.0$ and are positioned at a longitudinal distance of 315.4 cm from the interaction point. Each endcap is divided into 2 halves, which each hold 3662 crystals grouped in mechanical units of 5×5 crystals. Their front face area is 28.62×28.62 mm^2 and they have a length of 220 mm (24.7 X_0). The endcaps have a total volume of 2.90 m^3 and a weight of 24.0 t. In front of the endcaps an additional preshower detector is installed with the purpose to identify neutral pions, through their $\pi^0 \rightarrow \gamma\gamma$ decay, within $1.653 < |\eta| < 2.6$. It also improves the identification of electrons against minimum ionising particles, and enhances the position determination of electrons and photons. [67]

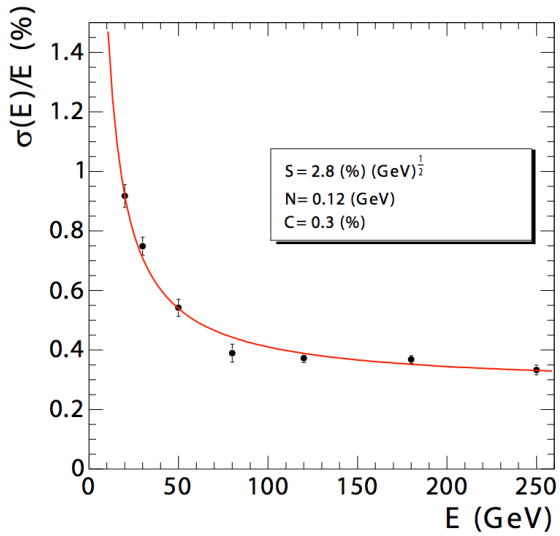

Figure 5.5.: ECAL energy resolution as a function of electron energy as measured from a beam test. The energy was measured in an array of 3 × 3 crystals with an electron impacting the central crystal. The stochastic (S), noise (N), and constant (C) terms of the fit are given. They are explained in more detail in section 6.3. [67]

The performance of the ECAL detector is illustrated in figure 5.5, which shows the electron energy resolution as a function of the initial electron energy. This measurement was conducted with specific beam tests during detector commissioning. To test and map the system one shoots beams of electrons with a known energy onto the surface of the calorimeter, at a certain $\eta - \phi$ position. In this case, the output is measured of

an array of 3×3 crystals where the electron hits the central one. At each energy the relative spread in the output distribution is calculated. In the end one can fit the energy dependence to get an average value of the stochastic and noise contributions. One can see that the electron energy resolution is below 1% at all energies, going from $\approx 0.9\%$ at low energies (≈ 20 GeV) to less than 0.4% at higher energies. [67]

5.3.2. Hadronic (HCAL)

The hadron calorimeters absorb the particles that survive the ECAL material and are particularly important for the measurement of jets. Its hermetic energy absorption is also essential to measure neutrinos or other exotic particles that are in fact detected by missing transverse energy. The design is like ECAL composed of a barrel section extended by endcaps. The barrel ranges from the outer radius of ECAL ($R = 1.77$ m) to the inner radius of the magnet coil ($R = 2.95$ m). [67]

The barrel design is a sampling calorimeter covering the pseudorapidity range $|\eta| < 1.3$. It consists of 36 identical azimuthal wedges that are constructed out of brass absorber plates aligned parallel to the beam axis. In addition, each wedge is divided into 4 ϕ sectors. The plastic scintillator between the absorber plates is segmented in 16 η sectors, which leads to a granularity of $(\Delta\eta, \Delta\phi) = (0.087, 0.087)$. The absorber consists of 8 brass plates with 50.5 mm thickness and 6 brass plates with a thickness of 56.5 mm enclosed in steel plates. This configuration corresponds to 5.82 nuclear interaction lengths (λ_I) at a 90°angle and to 10.6 λ_I at $|\eta| = 1.3$. If one takes the crystals from ECAL into account, 1.1 λ_I has to be added to the total. [67]

The endcaps cover the pseudorapidity region $1.3 < |\eta| < 3.0$ and use C26000 cartridge brass plates as absorber volume. Due to the overall CMS design, the hadron endcaps are attached to the muon endcap systems and the ECAL endcaps are in turn attached to the HCAL ones. The brass plates have a thickness of 79 mm with 9 mm gaps to accommodate the scintillators. The total length of the endcap hadron calorimeter is about 10 λ_I with the ECAL crystals included. [67]

The combined stopping power of the electromagnetic and hadronic calorimeters does not provide a sufficient containment for hadron showers in the central pseudorapidity region. To have a proper sampling depth within $|\eta| < 1.3$ the HCAL system is extended with the outer hadron calorimeter (HO) that uses the coil of the solenoid as an additional absorber. This extends the total depth of the CMS calorimeter system to minimum 11.8 λ_I. The layout and positioning of the scintillator tiles maps the layers of the HCAL barrel section in order to match the energy deposits. Studies [67] have shown that the mean fraction of energy deposited in HO can increase up to 4.3% for 300 GeV pions. [67]

Figure 5.6 illustrates the HCAL performance by looking at the resolution of the reconstructed jet transverse energy. The resolution is plotted for the barrel ($|\eta| < 1.4$) and endcap regions ($1.4 < |\eta| < 3.0$) separately. An iterative cone algorithm with a

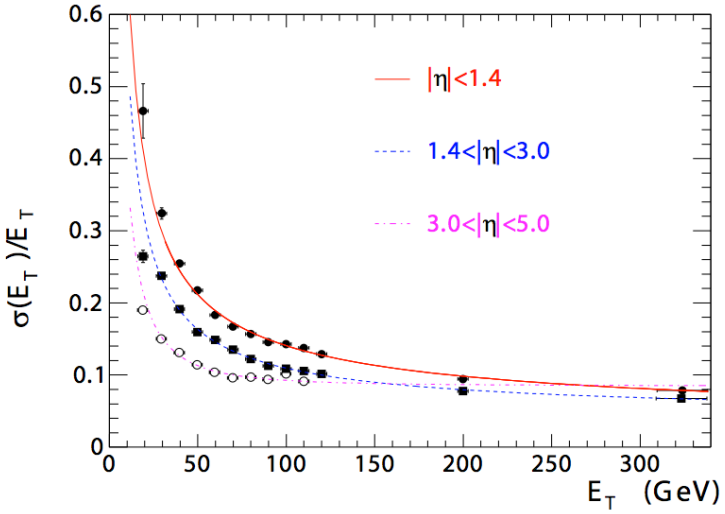

Figure 5.6.: The jet transverse-energy resolution as a function of the jet transverse energy for barrel jets ($|\eta| < 1.4$), endcap jets ($1.4 < |\eta| < 3.0$), and forward jets ($3.0 < |\eta| < 5.0$). The jets are reconstructed with an iterative cone algorithm (R = 0.5). [67]

radius of $R = 0.5$ is used to reconstruct the jet objects. At low energies the resolution is only about 30-50% but it improves with increasing energy to $\approx 10\%$. [67]

5.4. Muon chambers

Although the muon system is not actually used in this work, a precise and robust muon detection is crucial for the main CMS physics program, hence its name. The detection of muons is indeed ideal to identify signatures of interesting processes over the high background.

The muon system provides three functions: muon identification, muon momentum measurement and muon triggering. Good momentum resolutions and trigger performance are enabled by the presence of the 3.8 T solenoid field. To measure the particles, CMS uses 3 types of gaseous particle detectors that, when all their information is combined, fully reconstruct the muon tracks in r, ϕ and z coordinates, as well as the muon time to know to which LHC bunch crossing it belongs. The design consists of a cylindrical barrel section, and 2 planar endcap regions. In total 25 000 m^2 of detection planes is used. [67]

In the central barrel region where the muon rate is low, together with the neutron background, drift tubes (DT) are used. They cover the pseudorapidity range $|\eta| < 1.2$ and are organised into 4 stations. In the two endcaps, where the muon flux and background levels are high, cathode strip chambers (CSC) are used. They cover the pseudorapidity region of $0.9 < |\eta| < 2.4$ and provide muon identification with a fast response time,

fine segmentation and adequate radiation hardness. In each endcap 4 stations of CSC's yield precise measurements in the $r - \phi$ bending plane. The DT and CSC sub-systems have the crucial ability to trigger on the p_T of the muons with very good efficiency and high background rejection. To secure an excellent performance of the muon triggers, a complementary dedicated trigger system built out of resistive plate chambers (RPC) is added in the barrel and endcap regions. They provide an independent and fast trigger over the pseudorapidity range $|\eta| < 1.6$, provide a good time resolution, but a more crude position resolution than the DT and CSC detectors. [67]

A full pseudorapidity interval of $|\eta| < 2.4$ is thus covered, which corresponds to polar angles of $10° < \theta < 170°$. The performance of the muon system is illustrated in figure 5.7. Once again the transverse-momentum, p_T, resolutions are shown as a benchmark for the pseudorapidity regions $|\eta| < 0.8$ (left) and $1.2 < |\eta| < 2.4$ (right). Each plot shows 3 curves corresponding to the usage of the muon system only, the inner tracking system only and both systems together. One can see that the muon systems provide a resolution of about 9% for small η values and transverse momenta up to 200 GeV while it varies between 15% and 40% at energies of 1 TeV. When the inner tracking system is included in the measurement, the transverse-momentum resolution improves by an order of magnitude. [67]

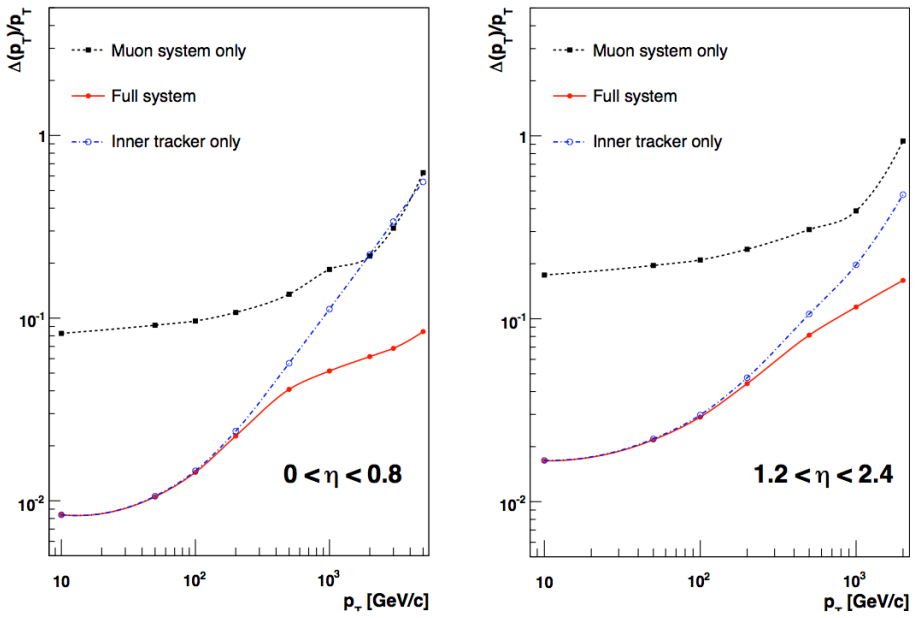

Figure 5.7.: The muon transverse-momentum (p_T) resolution as a function of p_T using the muon system only, the inner tracking only, and both, for pseudorapidity regions $|\eta| < 0.8$ (left) and $1.2 < |\eta| < 2.4$ (right).[67]

5.5. Hadronic Forward calorimeter

The Hadronic Forward (HF) calorimeter is the first so called *forward* detector described. It extends the CMS calorimeter pseudorapidity range from $|\eta| < 3.0$ to $|\eta| < 5.2$ by providing additional energy measurements between $2.9 < |\eta| < 5.2$. It operates very close to the beampipe and thus at small polar angles θ. In this phase space region the charged hadron flux will be extremely high so the design of the HF detector is mainly driven by the necessity to survive these harsh conditions. This lead to the use of steel absorber plates and embedded quartz fibres as the active medium. The light inside the fibres is generated by the Čerenkov mechanism and collected through air-core light guides by photomultipliers. The fused-silica core of the fibres measures 600 ± 10 μm in diameter and in total over 1000 km of fibres is used in HF. [67]

The steel absorber structure is composed of 5 mm thick grooved plates in which the fibres are inserted. A subdivision in two longitudinal segments is available: half of the fibres are embedded through the full depth of the calorimeter while the other half start at a depth of 22 cm from the front face. The former ones are referred to as long fibres and the latter as short fibres. This construction enables one to separate showers generated from hadrons to those generated by electrons and photons, which deposit most of their energy in the first 22 cm of the calorimeter. [67]

A full depth of 165 cm or $10\lambda_I$ is used by the absorber material, which is contained inside a cylindrical structure with an outer radius of 130 cm and an inner radius of 12.5 cm. The front of the calorimeter is located at $z = \pm 11.2$ m from the interaction point and its fibres run parallel to the beam line. They are bundled to form $0.175\Delta\eta \times 0.175\Delta\phi$ towers except for the rings at the edges, where the $\Delta\eta$ equals 0.111 and 0.3 at $|\eta| = 2.9$ and $|\eta| = 5.2$ respectively. The HF calorimeter is housed inside a shielding that consists of 40 cm thick steel and 40 cm thick concrete layers that protect the photomultipliers and read-out electronics from the high radiation levels. [67]

To illustrate the performance of HF, one can refer back to figure 5.6. In addition to the pseudorapidity ranges of the central HCAL calorimeter, it also shows the jet transverse-energy resolution in the pseudorapidity range of HF (indicated $3.0 < |\eta| < 5.0$). In comparison one can see that HF has the same performance at higher energies while it has a better resolution at lower energies, resulting in a jet transverse-energy resolution that is below 20% at all energies and converges to less than 10% at energies above 200 GeV. [67]

5.6. Trigger and Data Acquisition system

The LHC provides collisions at high interaction rates, with beam crossing intervals of 25 ns corresponding to a crossing frequency of 40 MHz at its design settings. Depending on the instantaneous luminosity, multiple simultaneous proton-proton collisions arise what leads to high detector occupancies. Since it is impossible to read out millions

of channels and store the huge amount of data produced at this frequency, a drastic reduction of the rate has to be achieved. This is done in CMS by using a trigger system that is basically the start of the physics event selection process. The system consists of two components. The first stage is the *Level-1* (L1) trigger that reduces the rate to about 100 kHz. It is constructed with custom designed, largely programmable electronics and uses coarsely segmented data from the calorimeters and the muon detectors while holding high-resolution data in pipelined memories in the front-end electronics on all the sub-systems. To keep the L1 trigger flexible, the hardware is implemented using Field Programmable Gate Array (FPGA) technology, Application Specific Integrated Circuit (ASIC) technology and programmable memory Lookup Tables (LUT). The second stage consists of the *High-Level-Trigger* (HLT), which is a software system implemented in a filter farm that uses generic CPU cores to digest the data. It has access to the complete read-out data of CMS and can therefore perform complex calculations similar to those made in the offline analysis. These algorithms can be programmed to look for particular interesting event shapes that correspond to e.g. Higgs decay processes. The HLT reduces the rate with a factor 1000, leading to a combined L1 and HLT reduction of the order of 10^6. Data will then be read out and stored at a rate of the order of 10^2 Hz. [67]

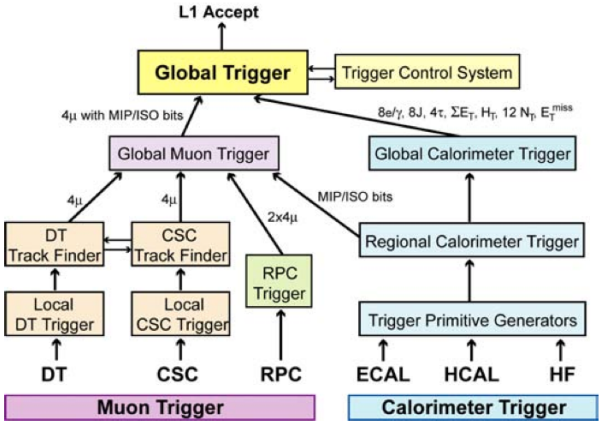

Figure 5.8.: Architecture of the L1 trigger. [67]

The architecture of the CMS L1 trigger is shown in figure 5.8. It consists of several components that are referred to as local, regional and global triggers. First the local triggers, also called Trigger Primitive Generators, use energy deposits in calorimeter towers from ECAL, HCAL or HF and track or hit patterns in the muon chambers from the DT, CSC and RPC systems. The Regional trigger can combine their information and use pattern logic to determine objects such as electron or muon candidates. The global muon and calorimeter triggers can use information from the entire CMS detector to search for muon or calorimeter objects such as jets. At the top of the system, the Global Trigger (GT) finally takes the decision whether or not to keep an event for further evaluation by the HLT. The result of the GT is communicated to all the sub-detectors through the Timing, Trigger and Control (TTC) system. If the event is accepted, all channels from all sub-detectors are read out. [67]

Since the L1 trigger is the very first selection stage, it has to analyse every LHC bunch crossing. The processing however introduces a latency between the actual bunch crossing and the distribution of the trigger decision to the front-end electronics. This delay is 3.2 μs and hence the data processing has to be pipelined in order to minimise the dead-time between two registered events. The L1 trigger hardware is partly housed on the detector itself, and partly in the underground control room located next to the detector, at a distance of approximately 90 m. [67]

The CMS trigger is completely embedded in the data acquisition (DAQ) system, whose general layout is illustrated in figure 5.9. The purpose of the CMS DAQ is to read out the information available in all detector channels, taking into account the trigger decision, and to construct a complete event out of it that represents an LHC bunch crossing. It must sustain a maximum input rate of 100 kHz, which corresponds to a data flow of $\approx$ 100 GB/s coming from approximately 650 data sources. [67]

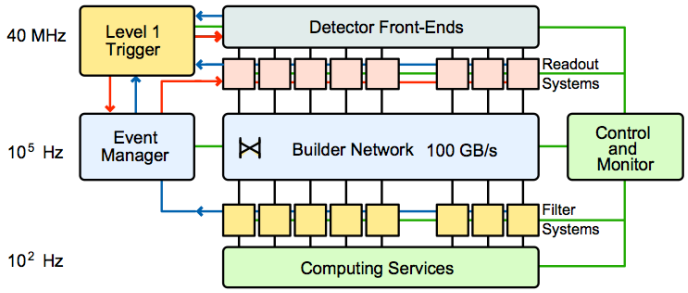

Figure 5.9.: Architecture of the CMS DAQ system. [67]

The various sub-detector front-end systems store their data continuously in 40 MHz pipelined buffers, then upon arrival of a synchronous L1 trigger through the TTC system, the corresponding data are extracted from the front-end buffers and pushed into the DAQ system by the Front-End Drivers (FED). Next, the event builder network assembles all fragments belonging to the same L1 trigger decision from all FED's into a complete event and transmits it to the filter farm (Computing Services) for further processing. The event builder is also in charge of transporting the data from the underground electronics to the surface building, where the HLT filter farm is located. The LHC conditions require these CMS computing services to be very powerful: HLT algorithms will demand a mean processing time of around 50 ms on a 3 GHz Xeon CPU core. This implies that for a DAQ system running at a 50 kHz rate, an equivalent of about 2500 such CPU cores must be deployed. [67]

During operation, trigger thresholds and pre-scales can be optimised in order to fully exploit the available DAQ and HLT capacity. However, CMS has defined a *luminosity section* (LS) as a fixed period of time set to 93 s, corresponding to 2^{20} LHC orbits, during which trigger thresholds and pre-scales can not be changed. [67]

5.7. Beam and Radiation Monitoring systems

The Beam and Radiation Monitoring systems (BRM) are introduced to both monitor and protect CMS with respect to LHC beam conditions and radiation doses near the experiment. To achieve this, multiple systems have been installed where some have the capability to initiate LHC beam aborts and/or CMS detector control. However next to the protective and monitoring function of these systems, two of them can also be used for trigger purposes since they have time resolutions below the 25 ns LHC bunch crossing level. [67]

A first system that can be used as such, are the *Beam Scintillator Counters* (BSC) [79] that are a series of scintillator tiles designed to provide hit and coincidence rates. There are two BSC detectors installed at each side of the CMS interaction point. The BSC1 is located in front of the HF calorimeter and consists of two types of tiles. Closest to the beampipe it uses disks that are segmented into 8 independent slices in ϕ and have an inner(outer) radius of 22(45) cm. The main objective of these disks is to provide rate information corresponding to the beam conditions. In addition, there are 4 large area paddles between a radial distance of approximately 55 cm and 80 cm, which provide beam coincidence information. The BSC1 detector has an average detection efficiency of 96.3% for minimum-ionising particles and a time resolution of 3 ns. The pseudorapidity range covered by BSC1 equals $3.23 < |\eta| < 4.65$. The second detector, BSC2, is located behind the TOTEM T2 [71] tracker and consists of two tiles on each side of the interaction point with a minimum inner radius of 5 cm and a maximum outer radius of 29 cm. The primary function of the BSC2 is to distinguish between ingoing and outgoing particles along the beam line. [67]

The second system is called *Beam Pickup Timing for the experiments* (BPTX) [80], which are beam pickup devices constructed at all LHC experiments. They are installed for CMS at $\pm$ 175 m from the interaction point and will provide accurate information on the timing, phase and intensity of each LHC bunch with a precision better than 200 ps. This design will allow the interaction point z-position to be calculated from the relative phases of the BPTX measurements. In addition, signals from the BPTX will also be sent as trigger inputs to the CMS global trigger. This will provide 3 flags on each bunch crossing as to whether the bunch in beam 1 is occupied, the bunch in beam 2 is occupied or both beams are occupied. The latter flag, where both beams are occupied, is very useful trigger information since it's indicative of whether collisions can occur in this particular LHC bunch crossing. [67]

Chapter 6.

The CASTOR calorimeter

In this chapter we will examine the Centauro And Strange Object Research (CASTOR) detector in more detail. Introduced in chapter 5 as one of the CMS forward calorimeters, it actually covers a pseudorapidity range of $-6.6 < \eta < -5.2$ and is only installed on one side of the interaction point. It is originally designed to search for Centauro events and Strangelet particles [81] but can also contribute significantly to small-x and forward QCD physics. The ability to measure energies at angles very close to the beampipe enables us to [82] a) study QCD dynamics, e.g. DGLAP versus BFKL type evolution equations, at high parton densities, b) study (hard) diffraction, c) contribute to quark-gluon plasma studies, and d), as done in this work, examine the underlying event structure and study the multi-parton interaction phenomenology.

6.1. Introduction to calorimetry

Before describing the CASTOR specifications and performance it is interesting to summarise the general concept of calorimetry in high energy physics. In the following we briefly explain the different detection mechanism, their designs and how the interaction of particles with matter results in energy measurements. For a more detailed description we refer to [83] and [84].

6.1.1. Detection mechanisms and design

Even though the terminology originates from thermodynamics, calorimetry is widely used within the field of high energy physics as a method to measure the energy of elementary particles. This energy measurement is destructive: while the particle traverses the material of the detector, it interacts with the atoms or molecules and hence loses its energy. A small fraction of the energy is released through heat dissipation, but the largest part is converted to light, via scintillation or Čerenkov processes, or to charge via ionisation. [84]

The concept of calorimetry can be implemented in two major types of design: *homogenous* and *sampling* calorimeters [84]. Homogenous detectors exist out of one type of material that has a high density, to absorb the particles, and at the same time propagates the scintillation or Čerenkov light. One such example is the CMS ECAL calorimeter: its lead tungstate ($PbWO_4$) crystals have a high density (8.28 g/cm^3) and propagate the scintillation light to the rear of the crystal where it is collected by photodetectors. Sampling calorimeters on the other hand, consist out of *active* and *passive* material. The passive material takes care of the absorption of the incoming particles. It needs to have a high density and thus materials such as Fe, Cu, Pb and W are typically used. The active materials produce and propagate the signals that can be collected. They have a lower density and good transparency. Two examples of the sampling calorimeter type are the central CMS HCAL and HF detectors. The former one combines brass absorber plates interleaved with plastic scintillator tiles as active material, while the latter uses steel absorber plates with embedded quartz fibres to propagate Čerenkov light.

When a charged particle traverses matter it loses energy through electromagnetic interactions that excite the atoms or molecules in the material. These unstable excitations then decay back to their ground state by releasing photons. If these photons have a wavelength that is inside the visible light spectrum, the aforementioned process is called *scintillation* or *fluorescence*. The time scale ranges from 10^{-12} to 10^{-6} seconds depending on excitation energy and type of atom or molecule. The main advantages of scintillation are: a good energy and position resolution, and a high light production. [84]

An another important process that is widely used in calorimetry, as in the CMS HF and CASTOR detectors, is the *Čerenkov* mechanism. When the velocity v of a highly energetic charged particle inside a dielectric medium with a refractive index n becomes bigger than the speed of light c/n in this medium, the particle will produce electromagnetic radiation, called Čerenkov radiation. The charged particle polarises the atoms or molecules along its path, creating electrical dipoles. These are symmetric when the velocity of the particle is smaller than the speed of light $v < c/n$, but when $v > c/n$ this symmetry is broken and a net dipole moment rises. This is illustrated in figure 6.1a. Thereafter the disrupted atoms or molecules restore themselves to their equilibrium during which they emit photons. Since the charged particle travels faster than the speed of light through the medium, the photons constructively interfere and intensify the observed radiation producing a coherent wavefront at a fixed angle. A common analogy is the sonic boom of a supersonic aircraft or bullet. [85] [1] [86]

The angle θ_c between the trajectory of the charged particle and the emitted photons can be calculated by using the relations indicated in figure 6.1b. The particle travels a distance AB $= t\beta c$ and the photon traverses a distance AC $= t(c/n)$, which results in the following relationship: $\cos\theta_c = 1/n\beta$. Hence the Čerenkov angle depends on the velocity of the charged particle and the refractive index of the medium it traverses. [85]

In principle all materials can produce Čerenkov radiation: one can use solids (e.g. acrylic glass $n \approx 1.5$), fluids (e.g. water $n \approx 1.33$) or gasses (e.g. isobutane with $n \approx 1.001$). One of the main disadvantages is the low light yield, the production of

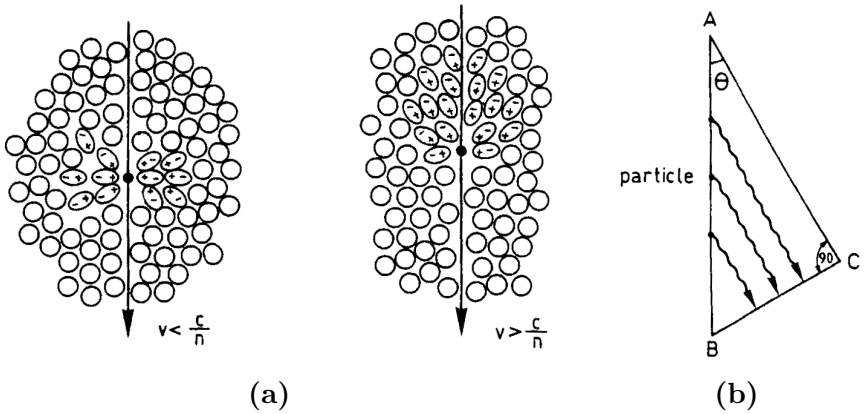

Figure 6.1.: (a) Dipole creation by the passage of relativistic charged particles in a dielectric medium. (b) Derivation of the Čerenkov angle. [85]

scintillation light is 100 times more intensive, but the generation of Čerenkov radiation is however much faster than the scintillation process. Čerenkov signals are always generated within nanoseconds, while scintillation usually takes up to the order of 10^2 ns. [84]

6.1.2. Particle showers

Calorimeters measure energy by absorbing the incoming particles that interact with the material in a destructive way. Due to this, secondary particles are created that in turn create additional particles. This process goes on and results in an avalanche of particles inside the material until all the energy is dissipated. As these *particle showers* progress, more particles are created each with less energy until their energy is too low to induce additional interactions. Understanding the dynamics and properties of such particle showers is important to interpret the measured calorimeter signals and crucial for the detector design.

It is important to state that particle absorption inside matter is a stochastic process. Individual showers can look quite different from event to event and thus the measured output exhibits significant fluctuations. This means that one can only measure *average* particle shower quantities. Its stochastic property has an exceptional advantage however: the concept of particle showering implies that more particles are produced if the impinging particle energy increases, hence the statistics improves and the shower fluctuations become less pronounced. As a consequence better resolutions are obtained for higher particle energies. There are 2 types of particle showers: a) *electromagnetic showers* that originate from impinging particles such as electrons, positrons or photons that exclusively interact through electromagnetic processes, and b) *hadronic showers* that are generated by incoming hadrons, which also trigger strong interactions in the material. [84]

All the interactions that arise in *electromagnetic showers* can be well described with QED and produce in turn electrons, positrons and photons. Ionisation is the

most significant process at low energies, but when the initial particle energy increases, radiative processes such as: Bremsstrahlung, pair production, Compton scattering, Coulomb scattering, and electron-positron annihilation, become more important. In fact, pair production and Bremsstrahlung are the most important ones at high energies: above 100 MeV, Bremsstrahlung is already the dominating process for electrons and positrons. [84]

An important quantity in calorimetry is the *radiation length* X_0. This is the length in which a high energy ($E > 1$ GeV) electron or positron loses 63.2% of its energy via the Bremsstrahlung process. Since this is material dependent, each one has its own specific radiation length, which makes it possible to have material independent statements in X_0 units: e.g. electrons will lose the same amount of energy in 18 cm of water and 2.8 mm Pb, for both lengths are $0.5X_0$. Hence the unit X_0 is commonly used in calorimetry to indicate the available stopping power of a specific design. [84]

The shape and dynamics of electromagnetic showers can be well described and they are much smaller than hadronic showers in both their longitudinal and lateral profile. The shower properties depend on material type and initial particle energy, which is illustrated in figure 6.2 that shows the electron energy deposit as a function of depth, plotted for different energies and materials. [84]

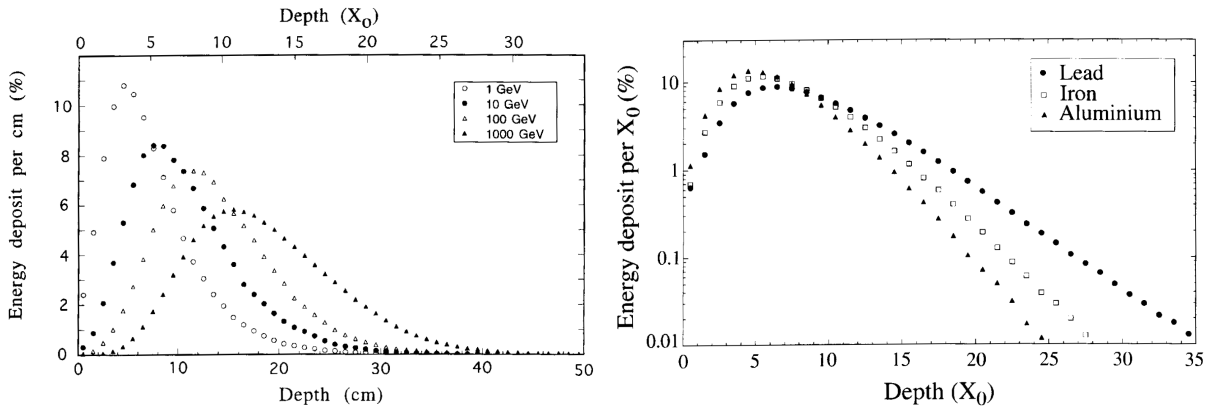

Figure 6.2.: (a) Electron energy deposit per cm in Cu as a function of depth, shown for different initial energies. (b) 10 GeV electron energy deposit per X_0 as a function of depth, for different materials (Al, Fe and Pb). [84]

Muons too generate electromagnetic showers, but this will only happen at much higher energies. This can be seen in figure 6.3, which shows the different contributions to the muon energy loss (stopping power) in Cu as a function of the muon momentum. While radiative processes are already dominant for 1 GeV electrons, it is certainly not the case for muons. At this energy, the main contribution is still ionisation, and the muon will only lose a small fraction of its energy. This is why muons are typically called *minimum ionising particles* (MIP) in this energy region, and only at energies of 1 TeV the loss is dominated by radiative processes. Muons, with energies of the order of GeV,

are therefore ideal particles to study and calibrate calorimeters, since they will deposit a rather constant ionisation signal in the detector material. [84] [87]

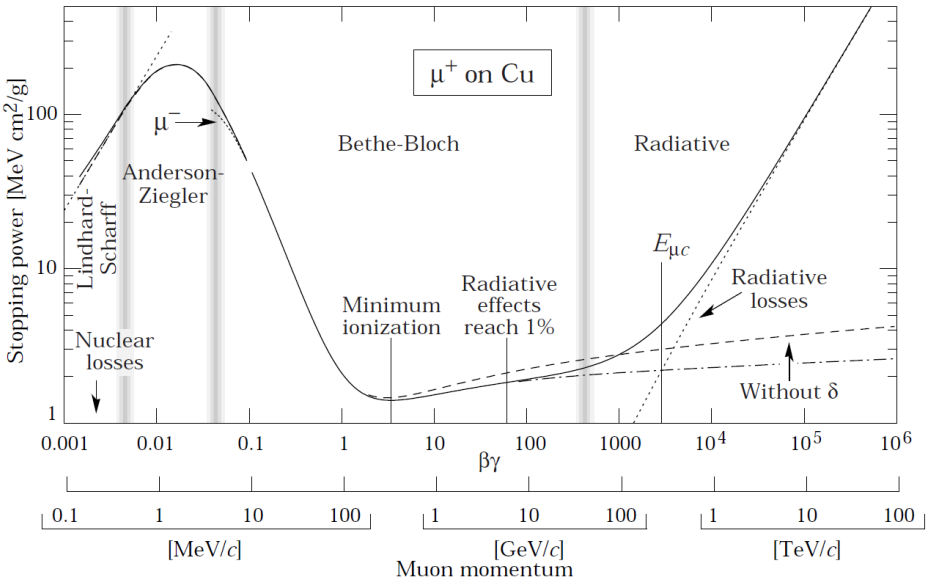

Figure 6.3.: Average stopping power ($-\langle dE/dx \rangle$) in Cu as a function of muon momentum. The different processes that contribute to the total loss at a specific energy range are indicated. [87]

The concept of *hadronic shower* development is analog to the one in electromagnetic showers, the significant difference however is that in case of hadrons, one has to take the strong interactions into account. This results in a much more complex shower development due to the additional possible nuclear interactions with the material. As such, one of the main differences with electromagnetic showers is that not all energy loss in hadronic showers can be measured. This fraction of invisible energy loss has the consequence that the average energy measurement of a hadron with a certain energy will be lower than the measurement of an electron with the same energy. It is caused by the appearance of nuclear spallation reactions: when an incident high energy hadron scatters on a nucleus it induces a disintegration of the latter into smaller nuclei. It is this energy, lost through the process to free the nucleons, which becomes invisible and can reach fractions up to 30-40% of the non-electromagnetic energy loss. [84]

Hadronic showers always have an electromagnetic component, where the main contribution originates from the π^0 particle that decays into 2 photons, but are typically much bigger than electromagnetic showers, both in longitudinal and lateral profile. The additional nuclear interactions induce larger fluctuations in the hadronic shower shapes, which makes them much harder to describe. These fluctuations are also the reason why hadronic showers result in a worse energy resolution. To describe the much longer hadronic showers one uses the *nuclear interaction length*, λ_I, which is defined as the average distance a high energy hadron traverses between two nuclear interactions. As

with the radiation length, it is a commonly used quantity to express the available matter to absorb the particles in a calorimeter. [84]

Due to the different nature and composition of electromagnetic and hadronic showers, it is essential to map the response of a calorimeter to different types of particles. One crucial variable to measure is the π/e ratio, it represents the response of a charged pion (π^+ or π^-) with a certain initial energy, relative to that of an electron with the same initial energy. The response of calorimeters to electrons is well known and exhibits a linear behaviour, but this is not true for hadrons, due to the fraction of invisible energy in the showering and due to an increasing electromagnetic fraction in the hadron showers respectively. The latter property leads to a π/e ratio that can converge to 1 at higher energies. The mapping of this response ratio is important to characterise the calorimeter performance since it can be used to recalculate the correct initial hadron energy. Calorimeters that have a π/e ratio < 1 are called *non-compensating*. [84]

Finally it is also relevant to note that only relativistic charged particles generate Čerenkov radiation, and hence only following shower particles contribute to the signal: electrons and positrons with $E > 700$ keV, charged pions with $E > 190$ MeV and protons with energy $E > 1.3$ GeV. This means that calorimeters designed to detect the generated Čerenkov signal are mostly sensitive to the electromagnetic fraction of all particle showers. Hence the hadron response is very small with respect to electrons, these calorimeters are therefore called extreme non-compensating and usually have low π/e ratios (≈ 0.5). [84]

6.2. CASTOR specifications

In accordance to the introduced calorimetry physics on the previous pages, we can specify CASTOR as a non-compensating cylindrical Čerenkov calorimeter. It is installed at the CMS experiment around the beampipe and covers the forward pseudorapidity range of $-6.6 < \eta < -5.2$. In contrast to many other sub-detectors, it is only present at the minus z-side from the interaction point, at -14.38 m. The position of CASTOR with respect to the other central CMS sub-systems is indicated in figure 6.4. Conditions in the forward region of CMS require a compact detector design, radiation hard materials, a fast response and acceptable operation in a magnetic field. This lead to the usage of a sampling calorimeter design, existing out of tungsten (W) plates to absorb the particles, with active quartz (SiO_2) plates in-between to generate the Čerenkov radiation. The light is guided through air-core light guides and collected with photomultiplier tubes (PMT), placed on the top of the plates. [88] [89]

The general layout of the detector is drawn, from different point of views, in figure 6.5 with the key structures and components indicated. It has a longitudinal segmentation of 14 *modules* along z, where the first two represent the electromagnetic (EM) section. The remaining 12 modules behind represent the hadronic (HAD) section of CASTOR. In the azimuthal plane a ϕ segmentation of 16 *sectors* used. This granularity results in $14 \times 16 = 224$ channels in the $z-\phi$ phase space. Note that it does not have any segmentation in η,

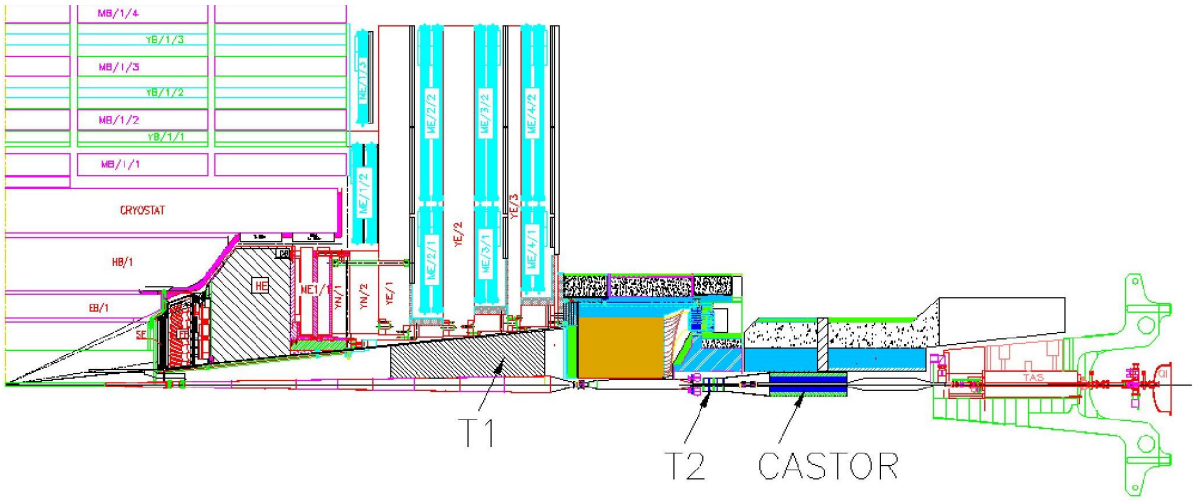

Figure 6.4.: Location of the forward CASTOR calorimeter in the CMS experiment. It is indicated together with the T1 and T2 Totem [71] detectors. The central CMS sub-systems are also shown, such as ECAL (EE), HCAL (HB, HE) and the muon detectors (MB, ME).

so every channel represents an energy measurement in the aforementioned pseudorapidity range. However, since the detector is aligned parallel to the beam along z, the η coordinates are slightly different for the first and last channels. The inner radius of the plates equals $r = 3.7$ cm, and outer radius $r = 14$ cm. If one includes the light guides and PMT housings, a total radius of 30 cm is reached. [89]

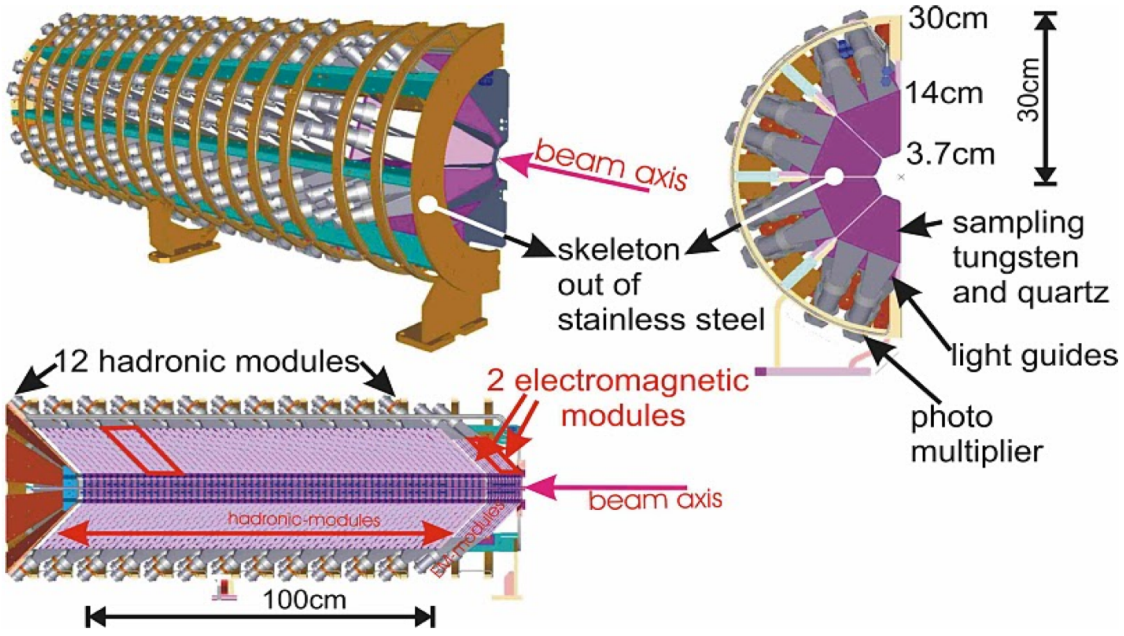

Figure 6.5.: Drawings of the CASTOR calorimeter design indicating the key components. [89]

From a mechanical point of view it is constructed in two halves that are separately commissioned and transported. During installation they are then placed to each other enclosing the beampipe. After that, extensive shielding material is closed to protect the PMT's and read-out electronics from the radiation and magnetic field. A skeleton out of stainless steel supports all the absorber plates and read-out components. This mechanical design actually implies that the calorimeter is structured into 8 azimuthal wedges, called octants, which hold one tungsten plate interleaved with segmented quartz plates that provide two read-out channels (two ϕ sectors). This is reflected in the trapezoid design illustrated in figure 6.5. [89]

Figure 6.6 shows a description of the CASTOR geometry with respect to the CMS coordinate system. Here the module configuration along z is clearly indicated, with the first module closest to the CMS interaction point. The ordering of the sectors in the azimuthal, or $x-y$, plane is based on the ϕ angle definition: sector 1 starts at $\phi = 0°$ and sector 16 ends at $\phi = 360°$. This implies that the left mechanical half contains the ϕ sectors 5-12, and the right half ϕ sectors 1-4 and 13-16. [89]

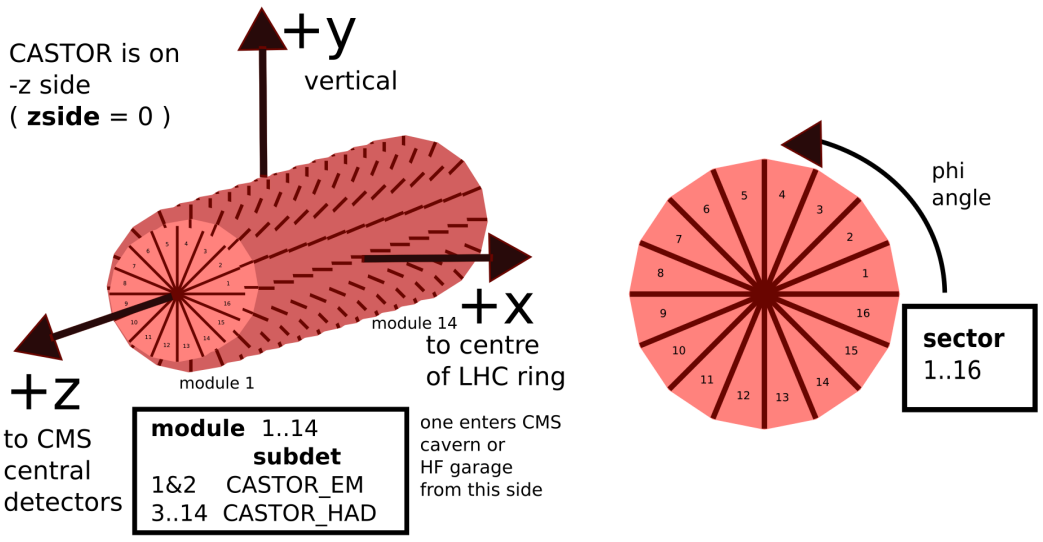

Figure 6.6.: Geometrical definitions of the CASTOR calorimeter with respect to the CMS coordinate system.

Each PMT read-out channel, or *Reading Unit* (RU), consists out of 5 *Sampling Units* (SU). One SU represents 1 tungsten plate followed by 1 quartz plate. All plates are inclined by 45° with respect to the horizontal axis to maximise the Čerenkov light collection. The quartz refractive index ranges from 1.46 to 1.55 for wavelengths λ of 600 nm and 200 nm respectively. Hence to generate Čerenkov radiation one needs a minimal velocity of $\beta = 1/n = 0.65 - 0.69$, which leads to angles θ_c of $46° - 50°$. [88]

The tungsten and quartz plates in the *EM section* have a thickness of 5 mm and 2 mm respectively. However since they have an inclination of 45° the effective length becomes 7.07 mm ($1.988X_0$) and 2.83 mm ($2.4 \times 10^{-2}X_0$). One SU then measures 9.9 mm and one RU has a length of 49.5 mm. The EM section consists out of 2 RU per sector and

thus has a total depth of 99 mm or $20.12X_0$. The tungsten and quartz plates in the *HAD section* have a thickness of 10 mm and 4 mm respectively, which due to the 45° inclination have an effective length of 14.14 mm ($0.1414\lambda_I$) and 5.66 mm ($1.32 \times 10^{-2}\lambda_I$). One SU measures 19.8 mm and one RU thus 99 mm or $0.77\lambda_I$. The total HAD section contains 12 RU (or modules) per sector and has a total depth of 1.188 m or $9.24\lambda_I$. When all the material in the EM and HAD sections is added, a total length of $10\lambda_I$ is available to absorb the particle showers. [88]

In an octant, the plates have a trapezoid shape in the $x - y$ plane, illustrated in the right drawing on figure 6.5. They have a height of $\approx$ 100 mm in the EM section, and $\approx$ 140 mm in the HAD section. At the inner radius an octant has a width of $\approx$ 30 mm that increases to $\approx$ 120 mm and $\approx$ 150 mm for the EM and HAD sections respectively. The air-core light guides are glued on top of the absorber plates. They have a three-dimensional trapezoid shape and are covered with a reflective foil on the inside to maximise the Čerenkov photon guidance to the PMT's, which are in turn mounted at the end of the light guides. The latter ones detect the photons and convert them to an electrical current that can be read-out. They need to have a good quantum efficiency, be radiation hard, and should be able to operate within magnetic fields. Therefore fine-mesh Hamamatsu R5505 PMT's were chosen. [88] [89]

6.3. Prototype performance

Before a final calorimeter design is fully constructed for installation, they are subject to *beam tests*. These are experimental setups of prototype designs and are commonly used to study basic calorimeter properties. This is done by shooting beams of particles (e.g. electrons, pions, muons) with known energy and position onto the surface of the calorimeter. With this advantage one can completely map the response of the prototype and measure properties such as the energy scale, resolution, linearity, π/e ratios, etc. These basic measurements can then be used to improve the design, for software validation and calibration purposes.

The CASTOR calorimeter underwent several beam tests before the final design was installed at the CMS detector. The first two, in 2003 and 2004, had the main purpose to test and compare different design and read-out choices, while the ones in 2007 and 2008 were more advanced and had the goal to completely map the calorimeter properties. They were conducted at the H2 beam line at the CERN SPS accelerator that can deliver electrons, pions and muons at various energies. The 2007 beam test [88] was the first to feature a prototype construction of a full-depth octant. It consisted out of a steel support structure, mounted on a horizontal and vertical moveable table, which contained tungsten and quartz plates along the full design depth ($10\lambda_I$). For each RU, a light guide and PMT was installed on top to read out the signal. The octant, which represents 2 ϕ sectors, thus had 14×2 channels in $z - \phi$. [88]

First the response to electrons was studied by measuring the linearity and resolution of the prototype. This was done by shooting electron beams with energies from 30 GeV to 200 GeV at a central point on the calorimeter. The measured signal distribution was then fitted by a Gaussian function at each energy. Figure 6.7a shows the response (ADC/GeV) linearity to electrons. It is fitted with a zero degree polynomial and found to be linear within $\approx 4\%$. This measurement also gives us the energy scale of the calorimeter to electrons: from the fit it is clear that the read-out electronics yield a constant 41 ADC counts per GeV incident energy. The electron energy resolution is shown in figure 6.7b. Here the normalised width of the Gaussian signal distributions is shown with respect to the beam energy. The result can be fitted with the functional form $\sigma/E = p_0 \oplus p_1/\sqrt{E}$, which contains two general terms that contribute to the energy resolution of the calorimeter. The constant term, p_0, is related to imperfections of the detector, signal generation and collection non-uniformity, calibration errors and fluctuations in energy leakage, which limit the resolution at high energies. The stochastic term, p_1, is due to the intrinsic shower statistics and characterises the fluctuations in the signal generating process. The latter one thus reflects the stochastic process of the particle shower development as introduced in this chapter, and figure 6.7b indeed confirms that the resolution improves at higher energies. The prototype has an electron energy resolution of 9% at low energies (30 GeV), which improves to $\approx 5\%$ at high energies (> 200 GeV). [88]

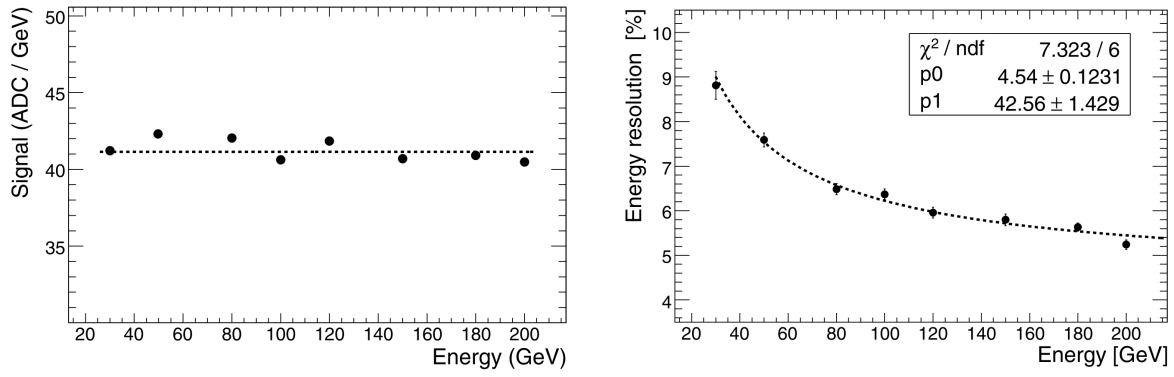

(a) **(b)**

Figure 6.7.: (a) Response (ADC/GeV) of the calorimeter to electrons. The data points were fitted with a zero degree polynomial. (b) Energy resolution of the calorimeter for electrons. The fit parameters shown are from the fit function $\sigma/E = p_0 \oplus p_1/\sqrt{E}$ and represent the constant (p_0) and stochastic (p_1) contributions. [88]

The same measurements were repeated for pions, with energies from 20 GeV to 300 GeV. Figure 6.8a shows the linearity of the CASTOR prototype to incident pions, obtained by plotting the normalised mean value of the signal distribution (ADC/GeV) at different beam energies. The non-linear behaviour at low energies reflects the non-compensating nature of the detector. Above 100 GeV, the mean signal becomes constant within 5% and the calorimeter response then corresponds to 20 ADC counts per GeV incident energy. The response to pions is thus maximum half the response to electrons,

and the previous introduced π/e ratio equals $20/41 = 0.49$ at these energies, which confirms the extreme non-compensating character of Čerenkov calorimeters. In addition the pion energy resolution is measured and shown in figure 6.8b. The same procedure is followed as with the electron resolution and the data points are fitted with the same function to indicate the constant and stochastic contributions. The resolution starts at $\approx 47\%$ at low energies and improves to $\approx 21\%$ at high energies. It exhibits the same behaviour as a function of energy, but compared to the electron resolution it is much worse, which is mainly due to larger hadronic shower fluctuations. [88]

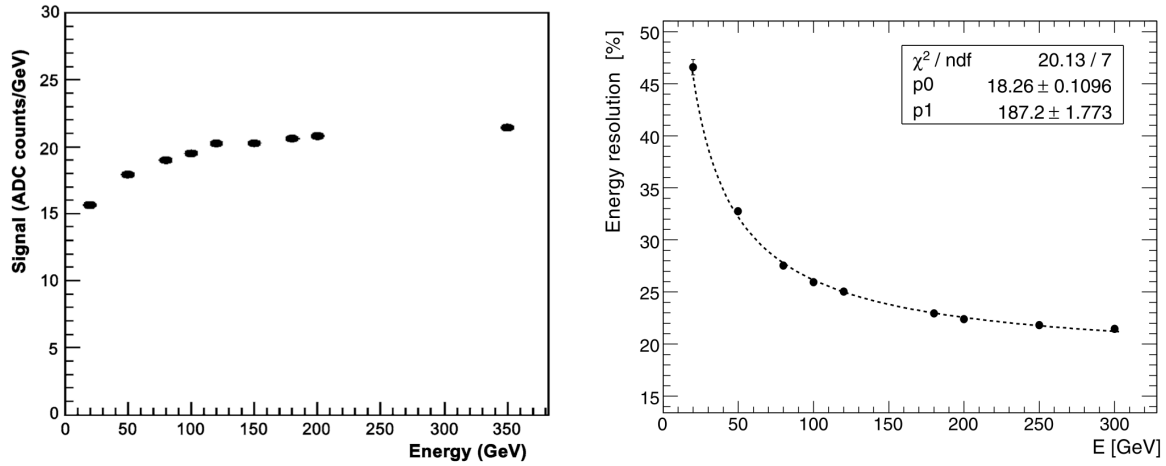

(a) **(b)**

Figure 6.8.: (a) Response (ADC/GeV) of the calorimeter to pions. (b) Energy resolution of the calorimeter for pions. The fit parameters shown in the inset are from the fit function $\sigma/E = p_0 \oplus p_1/\sqrt{E}$ and represent the constant (p_0) and stochastic (p_1) contributions. [88]

Another measurement conducted during the 2007 CASTOR prototype beam tests aimed to study the longitudinal shower development of pions for different energies. The results are shown in figure 6.9 for energies ranging from 20 GeV to 350 GeV. Here the mean response of the calorimeter in each z module is plotted as a function of the nuclear interaction length, and the total response is normalised to the beam energy in order to compare the different shapes. One can see that a depth of $10\lambda_I$ is sufficient to absorb almost all hadronic showers, with only a leakage of the order of 0.1%. The shower shapes exhibit a maximum that shifts slowly to the back with increasing energy. After that the showers die out, resulting in an exponential shape of the tail. [88]

The results shown in this section only represent a small fraction of all the conducted beam test measurements with the 2007 prototype, but illustrate the basic response and performance quite well. These measurements, together with the ones conducted in 2008 with an updated prototype, are crucial for further detector development and operation, and will e.g. be used in the next chapter to validate the available software simulations.

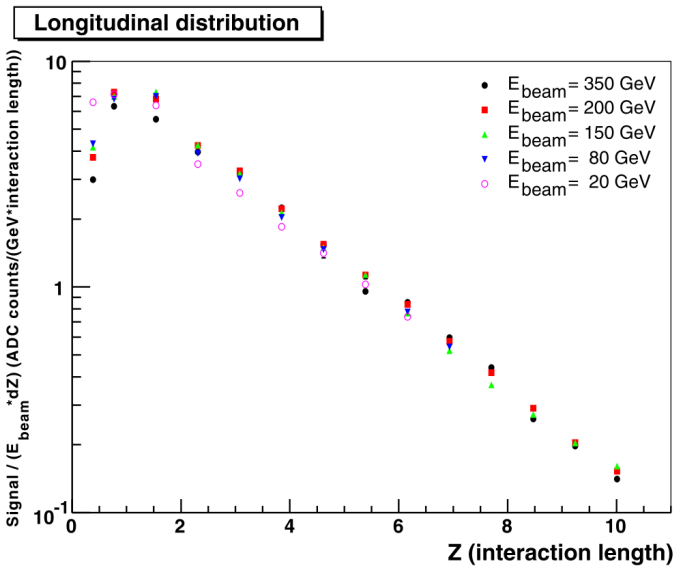

Figure 6.9.: Longitudinal profiles for pions of different energies. The mean response of the calorimeter was normalised to the beam energies. [88]

Chapter 7.

Software framework

7.1. Introduction

In this chapter we will describe the software that is used to process and store the data that survive the L1 and HLT trigger conditions. The front end read-out electronics and L1 trigger logic consists of specifically programmed firmware that is directly implemented in the detector hardware, but this is not the case anymore once the data reach the HLT level. At this point commercial CPU units are used to process the data, and hence the usage of distributable software is possible. This software package is then also available to conduct the offline analysis and to store the data on a worldwide computing network.

Given that CMS is a completely custom built detector, no plug and play software packages are available to handle the output of the hardware. Hence in addition to design and construct the detector itself, the CMS collaboration developed a custom software framework, called *CMS SoftWare* (CMSSW), which is capable to reconstruct and store all data produced by the read-out electronics. It is a framework programmed in the C++ computing language and combines an extensive collection of classes and objects that each serve a specific purpose. Every sub-system has its own set of software packages to process their specific data and execute custom functions. Everything is linked and combined together through Python based configuration modules that can execute a full software cycle. The CMSSW framework is heavily interfaced with the ROOT[90] software, which is a C++ based analysis package commonly used in experimental high energy physics to statistically analyse and plot all results. All CMS data are thus completely processed through the CMSSW framework and stored in ROOT compatible objects, which enables one to directly read the data and develop the analysis code needed for the measurement. Additional interfaces for other relevant software packages are also available, such as for MC generators (e.g. Pythia), Geant4, Rivet and Professor. The complete CMSSW software package can be compiled and installed on x86 (32 or 64 bit) and osx architectures making it executable on any UNIX distribution or Mac OS X version. Despite this advantage it is usually operated on powerful computing centres that have direct access to LHC data, spread around different storage elements all over the world given the huge file sizes involved. Once a first ROOT compatible dataset is created and suitable for analysis it can be copied to a local machine to further conduct

the analysis offline. The network that distributes the data to all available computing centres is called the *Worldwide LHC Computing Grid* and consists of three layers or Tiers, which are made up of computer centres that each contribute to different aspects. All LHC data first pass the Tier-0. This is one centre based at CERN and provides on-site prompt data reconstruction and storage. This centre also distributes the data to the next layer: Tier-1 sites. These are large computing centres at different locations and provide data storage and reprocessing power. The final layer consists out of many Tier-2 centres that receive datasets from Tier-1 storage, and provide CPU power to the end user. The analysis presented in his work used the available Belgian Tier-2 centre located in Brussels to access and process the LHC data.

The main purpose of the CMSSW framework is to transform the basic digital detector signals, registered by the read-out electronics as plain binary data, into physical objects such as electrons, muons and jets that can be used in measurements. This transformation consists out of many steps and takes information from all sub-systems into account. In the end, a complete picture of a bunch crossing is reconstructed, stored as a collection of ROOT compatible classes that represent all kinds of physics objects, trigger information, and auxiliary information such as current data taking conditions (detector alignment, calibration, etc.). The reconstruction of particles, including their trajectories, momentum and energy, is achieved by running advanced algorithms that combine information from different CMS detector layers. This is where the onion-like design of CMS contributes to a powerful particle identification: following the signals from the interaction point through the tracker, ECAL, HCAL and muon detectors one can identify all particles and calculate their properties.

This procedure should be transparent for data and MC models, and hence the output of such MC generators should be transformed into the same binary data structure as it would come directly from the real read-out electronics. Most MC model generators produce a collection of four-momenta that describe the final state, this is however an ideal theoretical outcome, and thus a *detector simulation* has to be performed. At this stage the complete design and geometry of the detector is implemented, the program then takes the four-momenta as input and propagates all particles through the material of the virtual detector, simulating all possible physical interactions. The output of such simulation programs is then similar as it would be in the real detector, and consists of induced currents or charges in the read-out channels. For calorimeters this involves a simulation of the particle showers, where all interactions that a particle can have in the material are taken into account. The complete CMS detector simulation is handled by the GEANT4 toolkit [91] [92], which is a general purpose program used to simulate the passage of particles through matter.

Describing the complete CMSSW framework and all the available detector algorithms would fall outside the scope of this work, therefore we will only explain the software of the inner tracking system and the forward CASTOR calorimeter in more detail since they are the two main sub-detectors we will use for the measurement conducted in this work.

7.2. CMS tracker software

7.2.1. Simulation

To develop a realistic and precise simulation of the inner tracker system a detailed description of the pixel and silicon strip detector components and materials in GEANT4 is needed. This involves a complete implementation of the entire lay-out as described in section 5.2, based on engineering's drawings. This results in a very complex geometry in which all pixels and strip sensors are modelled and available to GEANT4. A three-dimensional visualisation of the implemented geometry of one layer of the tracker outer barrel is shown in figure 7.1a as an example. Due to the large number of read-out channels the tracker requires a substantial amount of passive material that support the electronics, cooling and power systems. These materials will however create additional effects such as multiple scattering, electron bremsstrahlung and photon conversion that can alter the sensor response. Hence an accurate knowledge of both active and passive materials is needed. This can be expressed in terms of material budget, which represents the amount of material, usually expressed in radiation lengths, a particle has to travel to pass the detector. Figure 7.1b shows the available material budget (x/X_0) implemented in the tracker simulation as a function of the pseudorapidity η for different detector components. It confirms that the implemented geometry allows GEANT4 to take these effects correctly into account. [93]

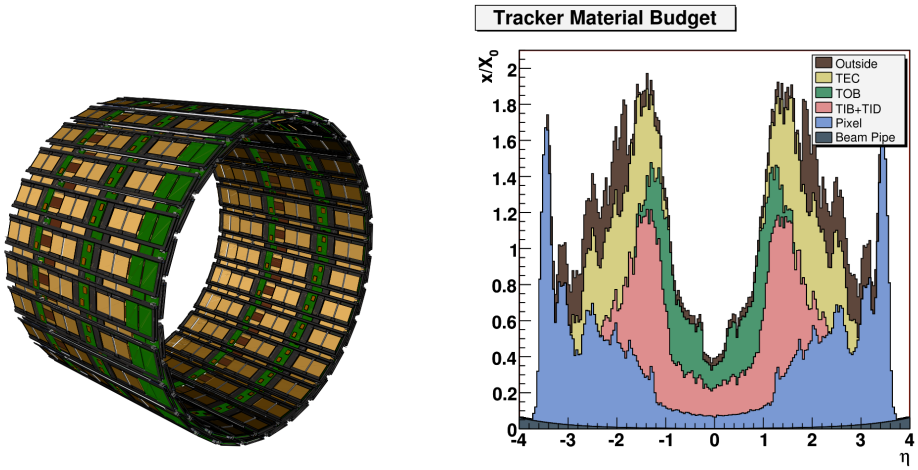

(a) (b)

Figure 7.1.: (a) Visualisation of one layer of the tracker outer barrel (TOB) as implemented in the GEANT4 simulation. (b) Material budget profile of the tracker simulation. The fraction of radiation length (x/X_0) is shown as a function of η for the different tracker components and support structures. [93]

The simulation toolkit then propagates all particles through the tracker geometry and calculates the deposited charge in all the active sensor volumes taking into account several additional effects such as the Lorentz drift in the 3.8 T magnetic field. The

collected charge distributions are then mapped to the tracker geometry and a list of hit channels is stored. After that the read-out electronics is simulated during which the Analog-to-Digital Conversion (ADC) is done. In this digitisation step the properties of the hardware are taken into account and corresponding gain and threshold factors are set. After all calculations, the output is registered as a DIGI object that represents a certain amount of ADC counts as a function of a fixed number of 25 ns time slices. This information is then stored in the same way as real data coming from the detector hardware, which is referred to as RAW data. [93]

7.2.2. Reconstruction

From this point onwards, the RAW datasets, whether they come from MC simulations or from actual LHC data, are processed by the same common reconstruction code that calculates the objects one will eventually use. The most important objects that can be reconstructed with the inner tracking system are: a) the charged particle trajectories (tracks) themselves, b) interaction vertices, and c) the beamspot. A brief description on how these are calculated is provided in this section.

The reconstructed tracks of charged particles are among the most fundamental objects that are used in any physics analysis and hence precise and robust algorithms are mandatory, together with a thorough validation of the reconstruction performance. A CMS track object is defined by its 5 basic parameters:

- The transverse momentum p_T.
- The angle θ, related to the pseudorapidity by $\eta = -\ln\tan(\theta/2)$, of the momentum vector.
- The azimuthal angle ϕ of the momentum vector.
- The transverse impact parameter d_0 with respect to the nominal interaction point, located at the centre of CMS.
- The longitudinal impact parameter d_z with respect to the nominal interaction point, located at the centre of CMS.

The *track reconstruction* starts from the generation of seeds. These give a first constraint to the track parameters and are the basis for the linear fitting algorithm that is executed in the next step. They are built in the innermost layers of the tracker and the reconstruction of the charged particle trajectories then further proceeds from the inner to the outer regions. Two types of seeds can be used: pixel hit pairs and triplets. Pixel hit pairs provide the minimal information needed, and in order to constrain the momentum of the track an additional assumption has to be made on the reconstructed location of the interaction point. Triplet seeds are better defined and less numerous, which results in higher purities at the expense of lower efficiencies however.

Once the seeds are available, the pattern recognition is initiated. It is based on a combinatorial Kalman filter [94] [95] method and is called the Combinatorial Track Finder (CTF) algorithm. Here the seed track is extrapolated towards successive detector layers taking into account the previous track parameter estimations. This extrapolation is calculated using the equations of motion of a charged particle in a constant magnetic field. In addition, multiple scattering and energy loss in the material is taken into account. Each time a hit in the tracker is found compatible with the extrapolation, a new trajectory candidate is calculated accordingly. At each detector layer the Kalman filter then updates the track parameters with the additional information that is provided by the hits added to the track collection. This procedure is iterated until the outermost layer is reached, or a certain stop condition is triggered.

During the track finding it can happen that a track is reconstructed starting from different seeds, or that a given seed results in multiple trajectory candidates. To avoid such double counting a resolution criterium is introduced, based on the fraction of hits shared between the two tracks. To further improve the track reconstruction, a trajectory refitting is done after the last hit is added to the track collection to avoid any bias possibly induced by the constraints used during the seeding stage.

The complete track reconstruction is optimised by repeating the CTF algorithm several times, with each iteration having a smaller subset of input hits since all the hits attached to a track reconstructed in the previous iterations are removed. Accordingly at each step the CTF algorithm is applied with updated parameters tuned to maximise the performance. In addition the track collection is cleaned by checking the compatibility of the trajectories with the interaction point. The first two iterations are sufficient to reconstruct the majority of high-p_T tracks, while the remaining steps are mainly executed to find low-p_T tracks.

On top of the improvements embedded in the reconstruction algorithm itself, extra quality cuts are applied on the resulting track collection. These provide a strong reduction of the track fake rate while keeping the reconstruction efficiency as high as possible. The quality cut variables are based on the basic track parameters, and following are available: the track p_T, η, d_0, d_z, the track χ^2 per degree of freedom and the transverse (longitudinal) compatibility, defined as d_0/δ_{d_0} (d_z/δ_{d_z}), with the interaction point region. The optimal cuts depend on the number of crossed layers in the tracker, and if a track passes all such cuts, it is called a *high purity track*. These are the ones that are commonly used in physics analyses. The specific cuts for the datasets used for the measurement in this work will be defined in the analysis part.

Interaction vertex reconstruction calculates the primary and secondary vertices from a given set of reconstructed tracks. A primary vertex is the location of the actual proton-proton interaction, and its determination is very important since it improves the track reconstruction and selection. It is even more crucial for the offline event selection given that the presence of at least one good primary vertex is a mandatory requirement to trigger on proton-proton interactions in the detector. Secondary vertices are created by primary particles, originating from the proton-proton interaction, which decay or

interact and produce in turn secondary particles. A first measurement of the primary vertex is based on a set of tracks selected by using the transverse impact parameter (d_0) significance, the number of hits in the tracker, and the normalised track χ^2. These are then clustered using their z coordinates at the point of closest approach to the beamspot. Next, vertex candidates are formed by asking for track separations in z that are less than 1 cm. The final parameters are then estimated by fitting the vertex candidates with at least 2 tracks using the adaptive vertex fitter technique [96].

The beamspot is defined as the three dimensional profile of the collision luminous region. Its measurement enters the event reconstruction at various levels and is e.g. used in the track and vertex calculations introduced above. In addition, the monitoring of the beamspot is used as prompt feedback by the LHC operators to adjust the beam parameters. The position of the beamspot can be calculated in two ways:

- Since the primary vertices represent the exact collision locations one can perform a likelihood fit to their three dimensional distribution to determine the mean (x, y, z) position of the beamspot.
- One can use the correlation between the track transverse impact parameter d_0 and its azimuthal angle ϕ_0, which exists when the beamspot is displaced from the nominal interaction position. An iterative fitting procedure can then exploit this $d_0 - \phi_0$ correlation and as such determine the beamspot position. With a sample of 1000 tracks a statistical precision of ≈ 5 μm is possible.

More detailed information about track, vertex and beamspot reconstruction can be found in references [96, 97, 98, 99].

7.2.3. Basic validation

The CMS inner tracking system has been extensively validated throughout its design, commissioning and data taking phases. The measurement of basic track parameter distributions, reconstruction efficiencies and detector resolutions are crucial to understand the detector and to validate the implemented simulation and track reconstruction algorithms. A thorough verification was done during the so called Cosmic Runs At Four Tesla (CRAFT) measurements. During this commissioning phase the CMS detector ramped its superconducting solenoid to the 3.8 T value and took data with the purpose to measure the trajectories of cosmic muons that happen to traverse the detector and leave their traces in the pixel and silicon strip systems. This allowed an extensive validation of the CMS tracking system that is documented in [100, 101, 102].

In addition the system has also already been thoroughly validated with LHC Minimum Bias data at $\sqrt{s} = 7$ TeV taken in 2010 during the first proton-proton collisions. One such analysis is documented in [103], which tested the performance of the track reconstruction by comparing LHC data with simulated models. Figures 7.2 and 7.3 represent the basic results achieved. Figure 7.2 shows the track transverse momentum p_T (a), track pseudorapidity η (b) and track impact parameter (c,d) distributions. The data are

shown as black dots and compared to a simulation of the Pythia8 Tune 1 model (blue histogram). Figure 7.3 illustrates the performance in terms of transverse and longitudinal impact parameter resolutions, as a function of track p_T (a,b) and pseudorapidity η (c,d). The resolutions versus track p_T are measured with central tracks only ($|\eta| < 0.4$). The impact parameter resolutions as a function of η are shown for different values of track p_T (1, 3 and 8 GeV). From these plots one can clearly see that the basic behaviour of the inner tracking system and its reconstruction software is well understood and exhibits an excellent performance. In all cases a good agreement between the data and MC models is achieved.

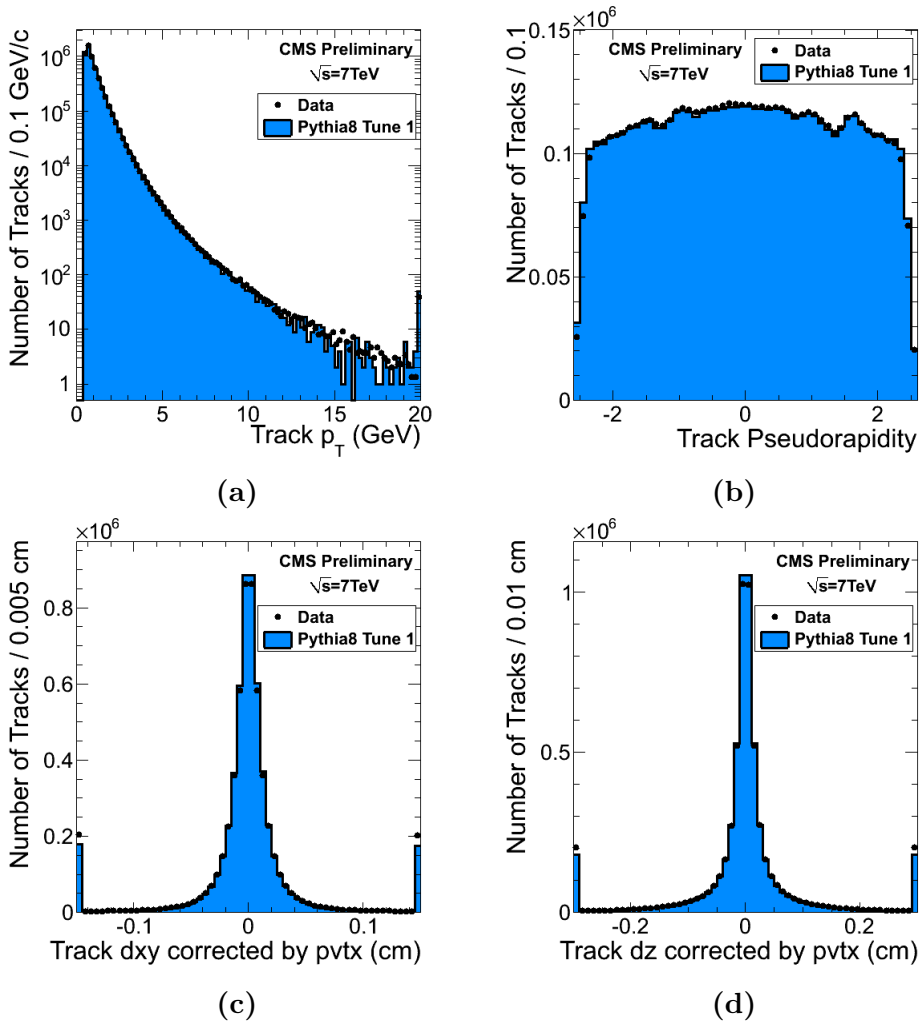

Figure 7.2.: Basic track distributions from analysis of collected Minimum Bias data at $\sqrt{s} = 7$ TeV (black dots) compared to the implemented detector simulation (blue histogram). (a) Track transverse momentum p_T (b) Track pseudorapidity η (c) track transverse impact parameter d_{xy} (d) track longitudinal impact parameter d_z. [103]

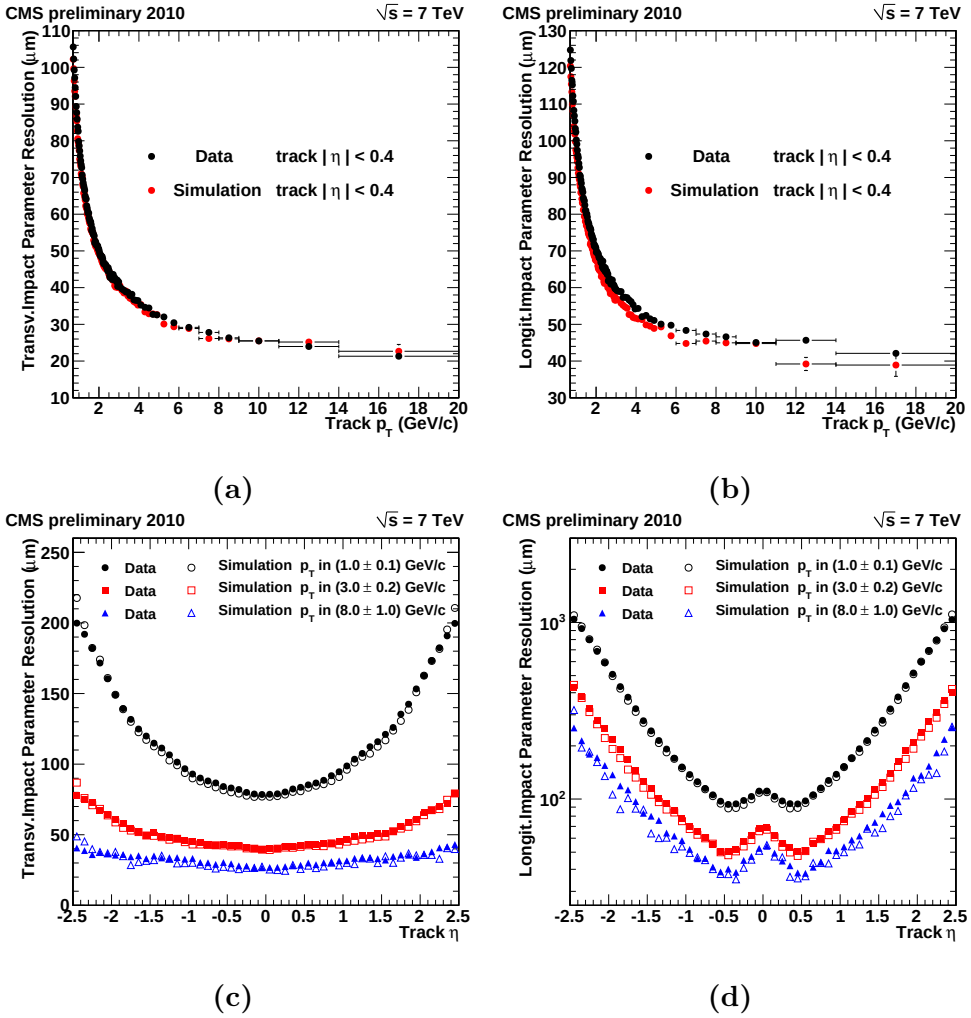

Figure 7.3.: Track resolution distributions from analysis of collected Minimum Bias data at $\sqrt{s} = 7$ TeV compared to implemented detector simulations. For the transverse (a,c) and longitudinal (b,d) impact parameters as a function of track p_T and track η. Figures (a) and (b) show the resolution for central tracks with $|\eta| < 0.4$, and in (c) and (d) different track p_T values are illustrated. [103]

7.3. CASTOR calorimeter software

7.3.1. Simulation

As with the tracker software, a precise and correct implementation of the CASTOR geometry is crucial to have a simulation that can be validated with data. Especially the configuration of the materials, the tungsten absorber and active quartz plates, is important since it has a significant effect on the shower development. The GEANT4 toolkit will then completely simulate the passage of particles through all the available materials in the implemented geometry. This implies that, as in reality, a complete particle shower develops. Here the choice of the best GEANT4 *physics list* becomes

important. Such list defines all possible interactions a particle can potentially have during the simulation. Most common for particle showers are e.g. ionisation, electron Bremmstrahlung and pair production as introduced in the previous chapter. Different lists can thus result in particle showers with a varying composition, shape and energy deposit. Hence for all calorimeters it is mandatory to compare such different physics list simulations with test-beam data, to determine the one that agrees best with the hardware. The current default physics list chosen by CMS carries the abbreviation QGSP_FTFP_BERT_EML, and combines a quark gluon string model [104], a high energy hadronic collisions model [105] and the Bertini cascade model [106]. Another important physics list in high energy calorimetry is LHEP, which uses parametrized models to describe the interactions of hadrons [107].

During the simulation of the particle showers, the code calculates the number of Čerenkov photons that can be emitted in the quartz plates by using the equations introduced in [85]. This is the first step of the simulation chain, which is illustrated in figure 7.4. The next step in the process is the conversion of those Čerenkov photons into a number of photo-electrons that are produced inside the photo-multiplier tubes when the former hit the cathode. In between are several factors that need to be accounted for:

- Quartz survival probability: when the number of Čerenkov photons is calculated, one still has to take into account their propagation towards the entrance of the light guides on top of the quartz plates. The probability to reach the light guides then depends on the angle of the emitted photons and the reflections inside the quartz.
- Light guide efficiency: the air-core light guides are covered with a reflective foil on the inside and designed to guide all the photons to the surface of the PMT. A fraction of the photons however gets lost due to imperfections.
- PMT quantum efficiency: this is the efficiency at which the PMT can actually produce photo-electrons from incident Čerenkov photons.

The resulting number of photo-electrons in the PMT then produce a current that is read-out by the electronics. This is simulated in the software by producing a charge (in units of fC) distribution utilising the PMT gain factor. At the same time, the code also reproduces the pulse shape and stores the collected charge in time slices of 25 ns. The last step in the simulation chain then converts this analog signal into a discretized digital one according to the properties of the read-out electronics. The resulting ADC counts distribution (still in 25 ns time slices) can then be stored into the RAW data format.

Due to the fact that the GEANT4 toolkit simulates a full particle shower, and thus has to calculate thousands of interactions inside the material, the CPU time needed to calculate one event is very high. It is shown that a simulation of electrons (pions) between 100 - 250 GeV takes on average 8.84 (9.53) s/evt. To speed up this process a *Shower Library* (SL) has been developed. This method uses pre-recorded results of particle showers, obtained with a full GEANT4 simulation, of electrons and pions in a broad energy and $\eta - \phi$ range. If one then simulates a random event, the collection of particles that enter the front of the calorimeter is checked and electrons or pions that

satisfy the necessary conditions (on energy, position and direction) are replaced with the pre-recorded shower from the library, instead of simulating the complete particle shower from scratch. If we apply the SL code on the example mentioned above, the CPU times significantly reduce to 1.34 (1.22) s/evt for electron (pions).

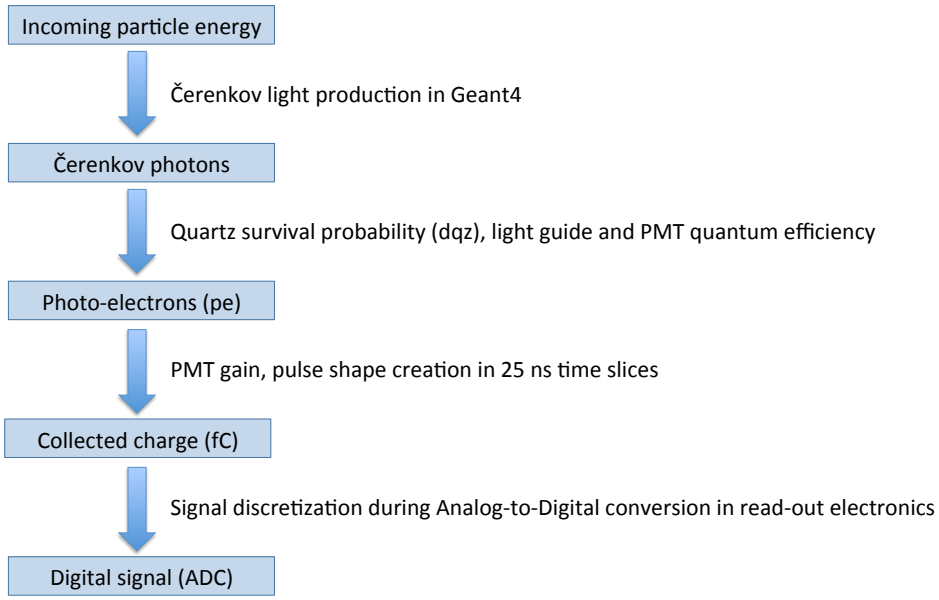

Figure 7.4.: A schematic representation of the CASTOR simulation chain.

7.3.2. Reconstruction

Once the RAW dataset is available, one can initiate the reconstruction code that is common for both data and MC. The different steps and objects produced during this stage are shown in figure 7.5. First reconstructed hits, which represent an amount of deposited energy in GeV units in one read-out channel, are produced in a two step conversion process:

1. The RAW data are read out and converted to an analog signal (charge distribution in fC) using a DAC (Digital to Analog Converter) in the read-out electronics.
2. The average noise contribution is subtracted from the resulting charge distribution and the signal is integrated over a fixed number of time slices. Finally the absolute calibration factor, which can be derived from the determined electron response in beam tests, is applied to convert the integrated current into an energy deposit in GeV units.

At this stage a collection of reconstructed hits is available that represent energy deposits in all available channels. In the next step, one adds all the channels in one ϕ sector to construct a tower. This object contains the energy sum of all modules in that sector, and

has additional variables that characterise the tower. One such variable is $f_{em} = E_{em}/E_{tot}$, the fraction of energy deposited in the EM section divided by the total energy in the tower (EM+HAD sections). During this step, only channels that have an energy above a certain noise threshold are kept and channels that are designated as bad (i.e. channels with no or a false signal) are thrown away. The determination of the noise threshold is studied in detail and will be described in the analysis part.

The last step produces the final jet objects, which are constructed out of the tower collection by using the Anti-k_T jet algorithm with a radius R = 0.7. A jet in this case is then a combination of calorimeter towers in ϕ that represent a clustered energy deposit in the $\phi - z$ phase space. It is this physical object that resembles a particle shower in the calorimeter produced by one or more particles coming from the interaction point. To identify whether the jets originate from electromagnetic interacting particles (e.g. electrons) or from hadrons (e.g. pions), following cut variables are available:

- Energy: total energy of the jet E_{jet}, energy deposited in EM section E_{em}, energy deposited in HAD section E_{had}.
- Position: available in (η, ϕ) and (x, y) coordinates.
- f_{em}: fraction of energy deposited in the EM section E_{em}/E_{jet}.
- f_{hot}: the ratio between the energy in the hottest channel in the jet and the total energy of the jet.
- Depth: the energy weighted average of the z coordinate of all channels in the jet: $< z >= (\Sigma_{ch} z_{ch} E_{ch})/E_{jet}$.
- Width: characterises the spread in ϕ and is defined as: $\Delta R_{jet} = \sqrt{\Sigma_{tower}(\phi_{tower} - \phi_{jet})^2 E_{tower}/E_{jet}}$.
- σ_z: this variable represents the spread on the calculated depth of the jet object. It can thus help to characterise the shape of the shower development. It is defined as: $\sigma_z^2 = \Sigma_{ch}(z_{ch} - < z >)^2 E_{ch}/E_{jet}$.
- The number of towers that are merged in the jet.

7.3.3. Basic validation

In this section we will summarise the extensive validation of the CASTOR calorimeter simulation software. This is done by comparing simulated results with test-beam measurements, as described in section 6.3. To achieve this the experimental test-beam setup is configured in the simulation and accordingly beams of electrons, pions and muons are shot into the calorimeter. As such one can directly compare the test-beam data with the outcome of different GEANT4 physics list simulations, determine the most appropriate physics list and validate the implemented geometry.

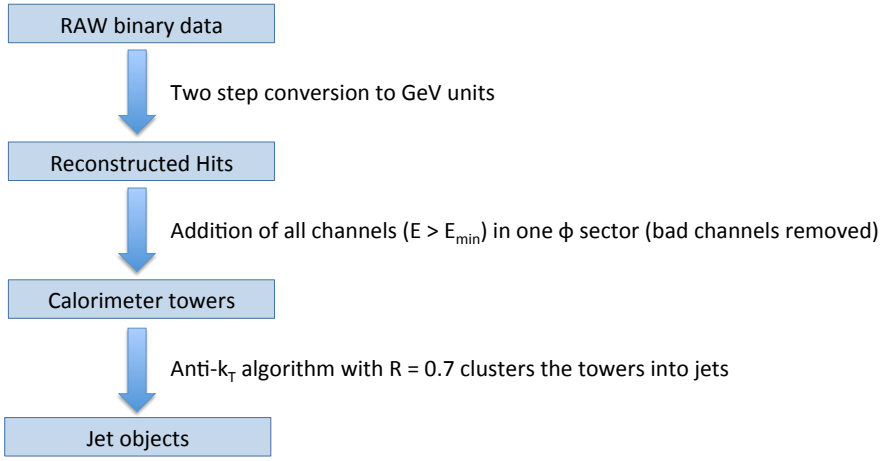

Figure 7.5.: A schematic representation of the CASTOR reconstruction software.

To start one can check the energy resolution of the calorimeter. Figure 7.6 shows this for electrons (a) and pions (b) as a function of the initial particle energy. Both for electrons and pions the test-beam data of a 2008 prototype is compared to a GEANT4 simulation with the QGSP_FTFP_BERT_EML physics list, while for the pion energy resolution an additional simulation with the LHEP list is shown for comparison. The points are fitted with a similar function as defined in section (6.3), however an extra parameter p_2 is added to the existing stochastic (p_1) and constant (p_0) contributions: $\sigma/E = p_0 \oplus p_1/\sqrt{E} \oplus p_2/E$. This last term is added to take the noise of the read-out electronics into account. The resulting fit parameters are shown in the legend. For electrons one can see that the noise and stochastic behaviour can be well reproduced by the simulation, while the constant contribution is underestimated. This is somewhat different for the pion energy resolution: the contribution of the noise is well described, but the stochastic and constant parameters are challenging. Here the QGSP_FTFP_BERT_EML physics list seems to describe the data better. For both electrons and pions the discrepancies in the constant term can be explained by the missing non-uniformity in the simulation: in reality the absorbing performance of the tungsten plates is not uniform but changes with position, and this feature is currently not implemented in the simulation.

The normalised longitudinal shape of the particle showers is shown in figure 7.7 for 100 GeV electrons (a) and pions (b). The fraction of energy (%) is drawn for each z-module in the calorimeter. Test-beam data points are compared to GEANT4 simulations with two physics lists, and the uncertainty on the inter-calibration applied on the prototype is indicated by the coloured band. The electron showers only penetrate until the third module and their shape can be well described by both physics lists. The pion showers go on until the end of the calorimeter, their shape is well described by QGSP_FTFP_BERT_EML, but not by LHEP.

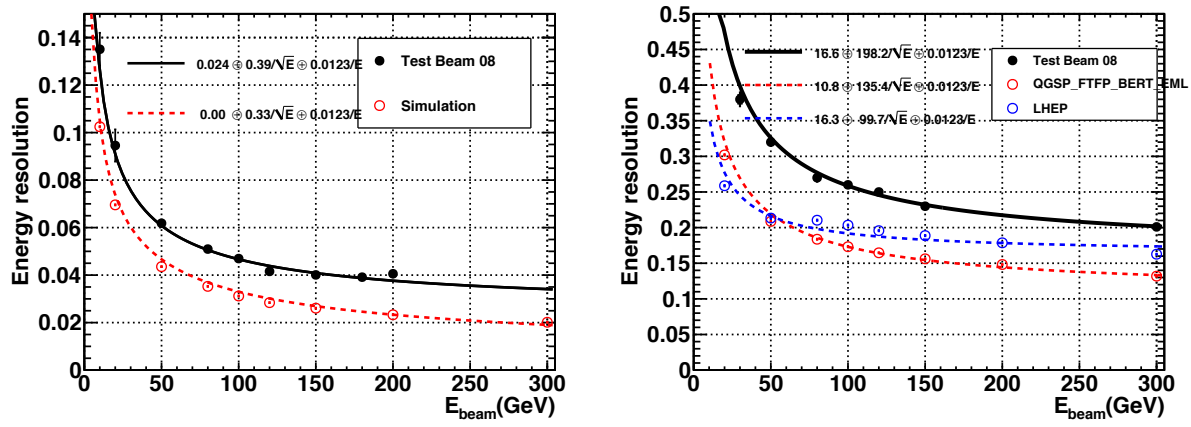

(a) (b)

Figure 7.6.: Electron (a) and pion (b) energy resolution as a function of the initial energy E_{beam}. The test-beam results are compared to the QGSP_FTFP_BERT_EML physics list simulation. For the pion energy resolution an additional simulation with the LHEP physics list is available. The points are fitted with the function described in the text, its parameters are shown in the legend.

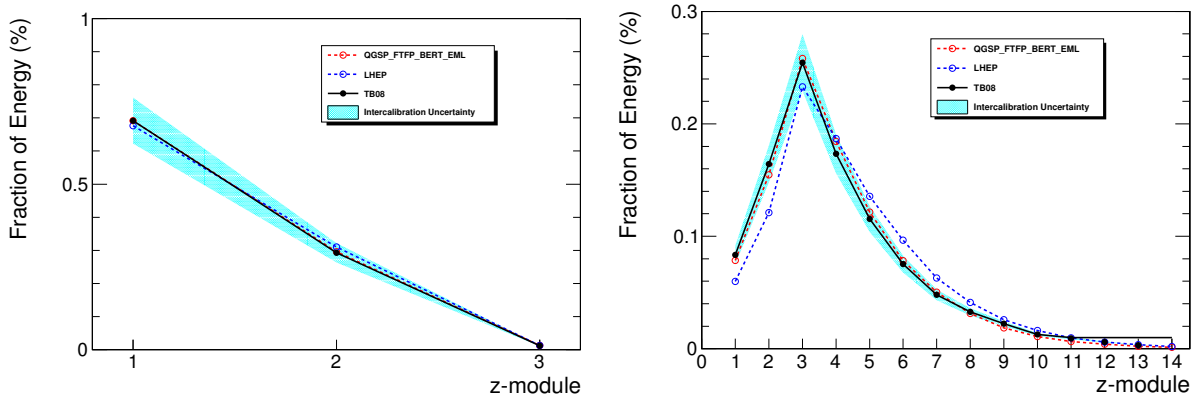

(a) (b)

Figure 7.7.: Normalised longitudinal shower profile of 100 GeV electrons (a) and pions (b) shown as a function of module number. Test-beam results are compared to two GEANT4 physics list configurations and the uncertainty on the test-beam channel inter-calibration is indicated by the coloured band.

One important property to study is the π/e ratio of the calorimeter that characterises its non-compensating and non-linear behaviour. Figure 7.8 shows this ratio measured from the test-beam and compares it to two GEANT4 simulations. As explained in the previous chapter, non-compensating Čerenkov calorimeters have a much lower response to hadrons than to electrons. This is also the case for CASTOR and is reflected in a π/e ratio that has an average value of ≈ 0.5. It changes with energy however due to

the non-linearity of the calorimeter. None of the simulations can correctly describe this ratio, both physics lists fail to reproduce the non-compensation, although the non-linear behaviour of QGSP_FTFP_BERT_EML is in a slightly better agreement with the test-beam data.

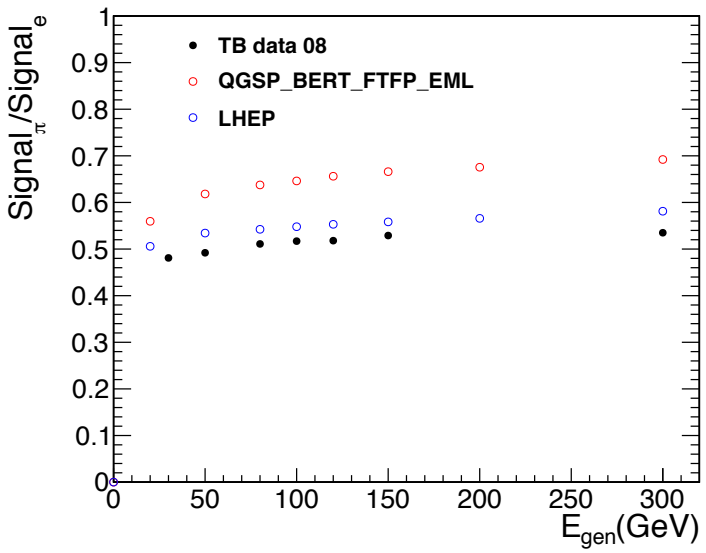

Figure 7.8.: The measured π/e ratio of the test-beam, as a function of the initial particle energy E_{gen}, compared to two GEANT4 physics list configurations.

Taking into account all the results shown above, the QGSP_FTFP_BERT_EML physics list provides a better description of the available test-beam data, especially the longitudinal shower profile of hadrons. In addition, the behaviour with energy of all quantities is in better agreement although the normalisation can be improved. One significant discrepancy is in the non-compensation, seen in figure 7.8. It is clear that the response to hadrons is too high in the simulation. To correct for this, we introduce a *non-compensation correction factor* that is the double ratio: data/simulation. We then scale the response of hadrons with this factor to put the GEANT4 result on the test-beam data. This correction can only be applied with the SL method.

All the above results are simulated without the usage of the pre-recorded SL in order to reach the highest precision for validation purposes. However when simulating different MC models in general for physics analysis, the SL is used by default in order to save CPU time. Hence a validation of this method is also needed, since one can expect to introduce errors when a particle is replaced with a pre-recorded shower. Figure 7.9 shows a comparison of the calorimeter energy resolutions, simulated with the two methods. It is clear that the SL code is able to reproduce the full GEANT4 simulation. The successful description of particle showers and their energy response is validated with a simulated Minimum Bias sample at $\sqrt{s} = 7$ TeV. The results of the full simulation and SL code are compared in figure 7.10, which shows the longitudinal profile (top left), the azimuthal distribution (top right), the cumulative energy as a function of depth (bottom left) and

the cumulative FS/SL ratio as a function of depth (bottom right). All distributions show a good agreement between the full GEANT4 simulation and the pre-recorded SL method.

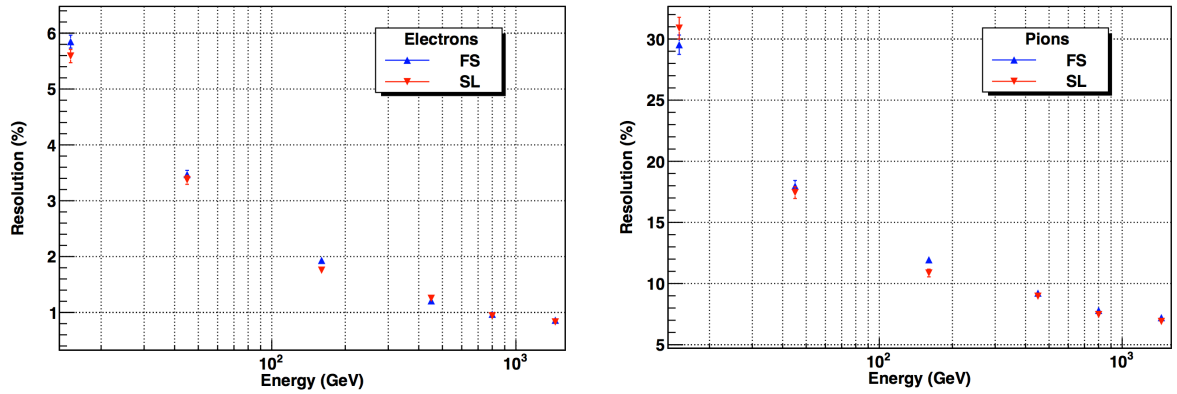

(a) (b)

Figure 7.9.: Electron (a) and pion (b) energy resolution for the full GEANT4 simulation (FS) compared to the shower library method (SL). [108]

From this section we can conclude that the basic response and behaviour of the CASTOR calorimeter is well understood and described by the implemented geometry and simulation software. Specifically the test-beam results can be reproduced by a simulation that has an implementation of the nominal calorimeter design. The performance of the calorimeter and its software during the LHC data taking is validated in the next part of the thesis, given the importance for the conducted measurements.

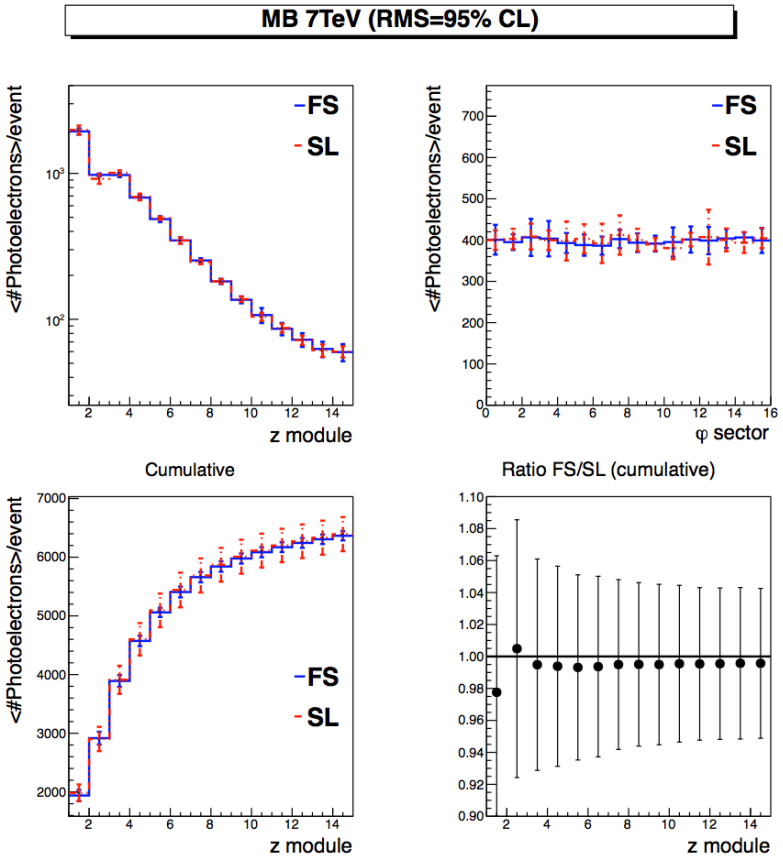

Figure 7.10.: Comparison of a full GEANT4 simulation (FS) with a pre-recorded shower library simulation (SL), for a Minimum Bias sample at $\sqrt{s} = 7$ TeV. The longitudinal profile (top left), the azimuthal distribution (top right), the cumulative energy versus depth (bottom left) and the cumulative ratio FS/SL versus depth (bottom right) are shown. [108]

Part III.

Study of the underlying event in pp collisions at the LHC

Chapter 8.

State of the art: available experimental data from the LHC

Before we start with the description of the analysis performed in this thesis, it is interesting to review the existing measurements that are done to study the underlying event. It will then become more clear how our analysis is complementary and novel with respect to the existing ones. Although the underlying event is being studied for a long time, at many different accelerators (for a comprehensive overview of the studies done at the Tevatron accelerator we refer to [109]), we will only highlight a selection of the latest measurements conducted with proton-proton collisions at the LHC accelerator, with the ALICE, ATLAS, CMS and LHCb experiments.

To study the underlying event structure of hadronic collisions one usually analyses a so called *minimum bias*, or *inclusive*, data sample. Such datasets contain events that are selected with the minimum possible selection bias, to ensure that the sample of hadronic collisions is as inclusive as possible. The term minimum bias is an experimental term, and mostly corresponds to a set of basic detector selection cuts that make sure one really selects hadronic collisions. These selection cuts can be e.g. interaction vertex requirements, hit coincidence triggers, bunch crossing triggers, minimal detector activity, etc. The term inclusive is more often used to denote an equivalent sample on particle or parton level in theoretical contexts. With such samples one can then look e.g. at particle multiplicity or transverse momentum distributions to study the underlying event behaviour. This can be done with or without the presence of a *hard scale* in the event, which is the observable that characterises the scale (e.g. p_T) of the hard parton scatter in the collision. Especially the measurement of the underlying event activity as a function of such hard scales yields important information on the behaviour of MPI.

8.1. Underlying event measurements at central rapidity

To measure the underlying activity as a function of the hard scale of the event, one needs to make sure that the former is well separated from the latter. This is certainly important for studies performed at central rapidities, where the result of the hard scatter

lies in the same rapidity range as the underlying event activity. To take this into account, the azimuthal plane is divided into the *toward*, *transverse* and *away* regions. This is illustrated in figure 8.1 (left). The toward region is defined as the space in ϕ that contains the object (e.g. a jet) that comes from the hard scatter, and the away region is defined as the space that contains the recoil system of that interaction. The transverse region in ϕ is then dominated by the underlying event activity. This behaviour is confirmed with measurements as shown in figure 8.1 (right). This plot shows the average scalar sum of transverse momenta ($\sum p_T$) of charged particles with $p_T > 0.5$ GeV/c and $|\eta| < 2$, plotted as a function of the azimuthal angle difference $\Delta\phi$ relative to the leading track, which is required to have $|\eta| < 2$ and $p_T > 2$ GeV/c. Here, the leading track is defined as the hard scale of the event. In the toward region ($\Delta\phi < 60°$) a peak in the scalar sum $\sum p_T$ is visible that originates from the leading track, and a similar peak structure is seen in the away region ($\Delta\phi > 120°$), although it is broader and less pronounced. The transverse region ($60° < \Delta\phi < 120°$) shows the lowest activity, which indicates that this part of phase space is indeed dominated by the associated underlying activity.

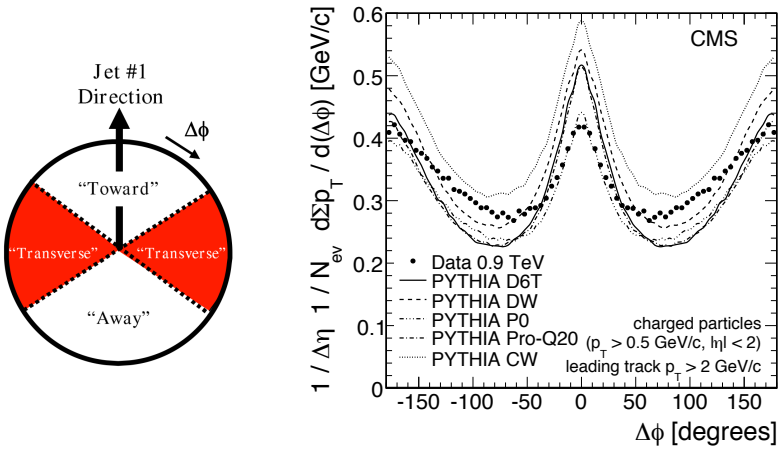

Figure 8.1.: (left) Definition of the azimuthal regions with respect to the direction of the leading track or jet. The angle $\Delta\phi$ is the relative azimuthal angle between the measured UE observables and the direction of the hard scattered object. [109] (right) Average scalar sum of transverse momenta of charged particles with $p_T > 0.5$ GeV/c and $|\eta| < 2$ for $\sqrt{s} = 0.9$ TeV minimum bias data and several PYTHIA6 tunes, plotted as a function of the azimuthal angle difference $\Delta\phi$ relative to the leading track, which is required to have $|\eta| < 2$ and $p_T > 2$ GeV/c. [110]

8.1.1. The UE activity with leading tracks and jets

The first measurements of the underlying event activity, performed at the LHC with the ATLAS and CMS experiments are reported in [110, 111, 112, 113]. They studied the UE activity at central rapidities, $|\eta| < 2$ in CMS and $|\eta| < 2.5$ in ATLAS, by looking at the charged particle multiplicity and average scalar sum $\sum p_T$ distributions as a function of the p_T of the leading track (ATLAS) or track-jet (CMS). The leading track is defined as

the track in the event with the highest p_T, and is required to have $p_T > 1$ GeV/c and $|\eta| < 2.5$ in the ATLAS detector. The leading track-jet in CMS is a jet constructed out of several tracks, with $|\eta| < 2.5$ and $p_T > 0.5$ GeV/c, combined with a jet algorithm (SISCone, R = 0.5) and is required to have $p_T > 1$ GeV/c and $|\eta| < 2$. Both experiments studied such distributions in minimum bias data at $\sqrt{s} = 0.9$ and 7 TeV.

Figure 8.2 then shows the results obtained by the CMS experiment. It shows the average charged particle multiplicities (left plots) and average scalar sums of the transverse momenta $\sum p_T$ (right plots) in the transverse region, for particles with $p_T > 0.5$ GeV/c and $|\eta| < 2$, as a function of the leading track-jet p_T. The bottom plots show the ratio of the average values at 7 TeV to the average values at 0.9 TeV. One can clearly see that the distributions quickly rise at low values of leading track-jet p_T, to then enter some kind of plateau region. This can be understood from the impact parameter picture of MPI: at low values of leading track-jet p_T, the collisions are peripheral and only few parton interactions can happen, resulting in a low UE activity, but when the p_T increases, the collisions get more central and more additional parton interactions can happen, which leads to an increased UE activity (pedestal effect). This goes on until the collisions are completely centralised at a certain value of p_T, the additional UE activity then saturates and the distributions in figure 8.2 enter their plateau region. The Pythia6 Z1 tune can describe the data quite well, while it is seen that the Pythia8 4C model underestimates the amount of UE activity. The ratio plots between the two centre-of-mass energies show that the older Pythia6 D6T tune can not describe the latest data, and predicts too much MPI.

Figure 8.3 shows the results of the ATLAS experiment. It shows the average scalar sum $\sum p_T$ distributions of charged particles with $p_T > 0.5$ GeV/c and $|\eta| < 2.5$ as a function of the leading track p_T in the transverse region (top), toward (middle) and away (bottom) regions for 0.9 TeV (left) and 7 TeV (right) minimum bias data. The UE activity in the transverse region shows a similar behaviour as observed in CMS. Here the data are compared to various Pythia6 models, Herwig and Phojet, which all seem to underestimate the UE activity. In addition to the transverse region, ATLAS also looked at the toward and away regions, which show a higher, more linear, increase of the average scalar sum $\sum p_T$. This indicates again that these regions are dominated by the hard scatter and its recoil. Similar measurements were performed with the ALICE experiment [114].

In addition, a measurement at $\sqrt{s} = 7$ TeV has been performed at the CMS experiment [115], where the production of primary K^0_S mesons and $\Lambda + \overline{\Lambda}$ baryons in the transverse region was studied at central rapidities, as a function of the leading track-jet p_T (with $p_T > 1$ GeV/c and $|\eta| < 2$). The measured K^0_S mesons and $\Lambda + \overline{\Lambda}$ baryons are required to have $p_T^{K^0_S} > 0.6$ GeV/c, $p_T^{\Lambda,\overline{\Lambda}} > 1.5$ GeV/c and $|\eta| < 2$. One can then study the average primary strange particle multiplicity, shown in figure 8.4, as a function of the hard scale (leading track-jet p_T). The behaviour is very similar to what is observed in the charged particle distributions shown in figure 8.2. However, all recent Pythia tunes significantly underestimate the production of K^0_S mesons and $\Lambda + \overline{\Lambda}$ baryons in the transverse region.

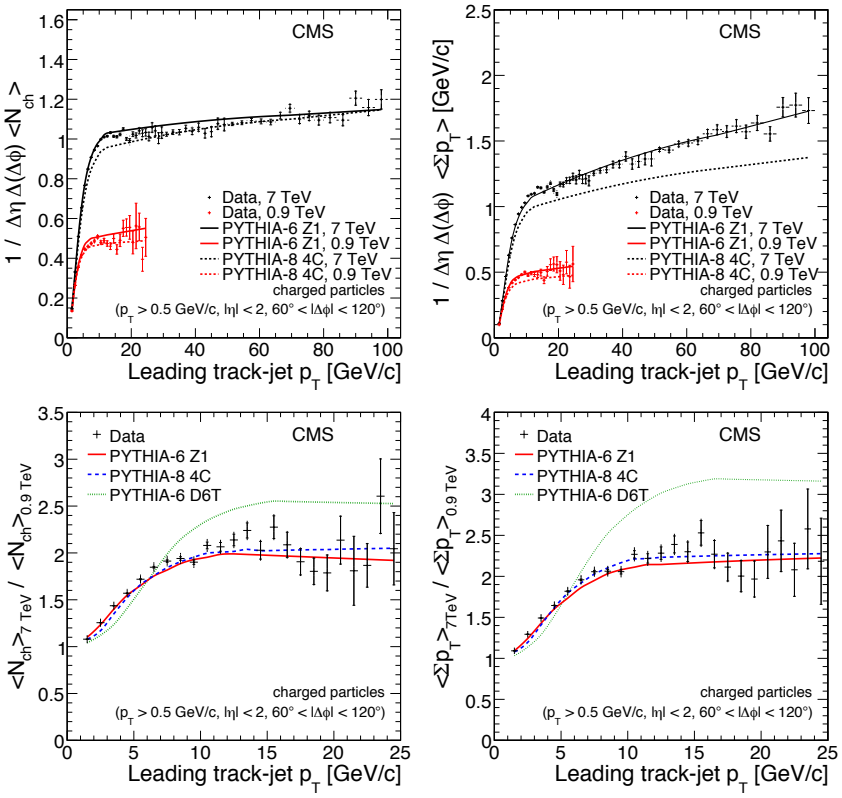

Figure 8.2.: Average charged particle multiplicities and average scalar sum of transverse momenta, in the transverse region $60° < |\Delta\phi| < 120°$, for minimum bias data at $\sqrt{s} = 0.9$ and 7 TeV recorded with the CMS experiment, as a function of the leading track-jet p_T. The bottom plots show the ratio of the average values at 7 TeV to the average values at 0.9 TeV. [111]

8.1.2. The UE activity in the Drell-Yan process

One possibility is to study the UE activity using the experimentally clean Drell-Yan interaction. This is a complementary approach to the previous studies and has the additional advantages of providing a clean separation of the hard interaction from the soft components, the absence of FSR and a low probability of photon brehmsstrahlung from the muons. The analysis strategy presented here is to measure the charged particle - and energy densities ($p_T > 0.5$ GeV/c, $|\eta| < 2$, muons from DY excluded) as a function of the di-muon p_T and the di-muon mass in the different geometrical toward, transverse and away regions with respect to the di-muon pair ($81\ \text{GeV}/c^2 < M_{\mu\mu} < 101\ \text{GeV}/c^2$). Analysing the di-muon p_T dependence enables us to probe the ISR spectrum while studying the di-muon mass behaviour verifies the MPI saturation. The away region is dominated by the hardest ISR that balances the di-muon system while the toward and transverse regions are sensitive to soft emissions due to MPI. Figure 8.5 shows the results of the energy densities (average scalar sum $\sum p_T$) as a function of the di-muon p_T. In the toward and transverse regions a slow growth of the densities is observed with increasing di-muon p_T. The leading order matrix element generator MADGRAPH (with tune Z2)

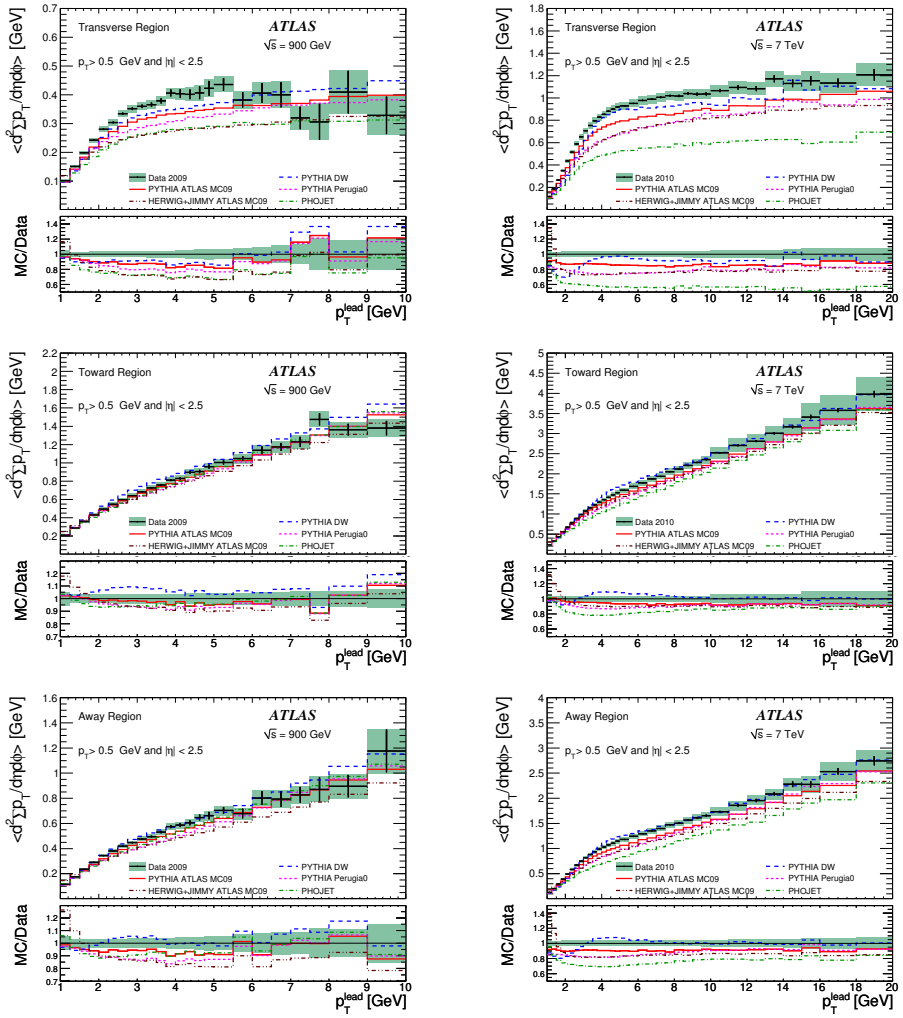

Figure 8.3.: Average scalar sum of transverse momenta, shown in the transverse, toward and away regions, for minimum bias data at $\sqrt{s} = 0.9$ and 7 TeV recorded with the ATLAS experiment, as a function of the leading track p_T. [112]

describes the data well, while the POWHEG Z2, PYTHIA8 4C and HERWIG models, which do not generate the multiple hard emissions with sufficient accuracy, underestimate the energy density. The away region, sensitive to the spectrum of the hardest emission, is equally well described by all models and tunes. [116]

8.1.3. Jet area/median approach

This analysis [117] uses an alternative approach to study the UE activity at central rapidity. The soft hadronic activity in the event is measured by calculating the ratio of the jet p_T and the area covered by this jet in the (η, ϕ) plane for all jets in the event.

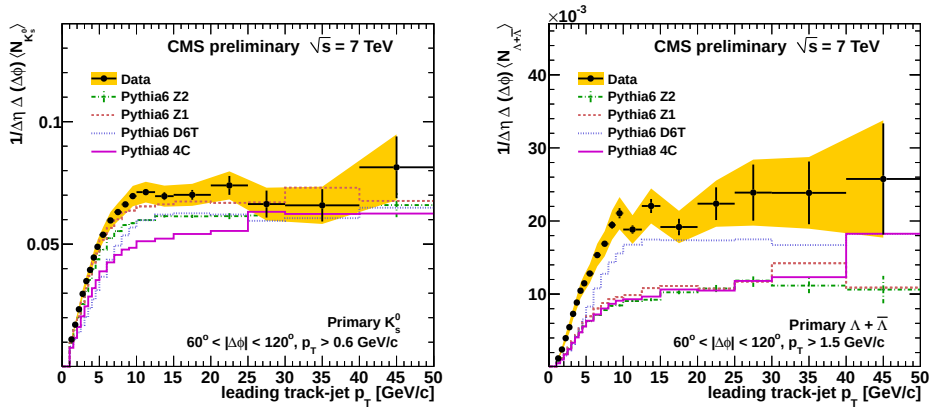

Figure 8.4.: The average primary strange particle multiplicity in the transverse region, as a function of the leading track-jet p_T, in $\sqrt{s} = 7$ TeV minimum bias data. Shown for both K^0_S meson (left) and $\Lambda + \overline{\Lambda}$ baryon (right) production. [115]

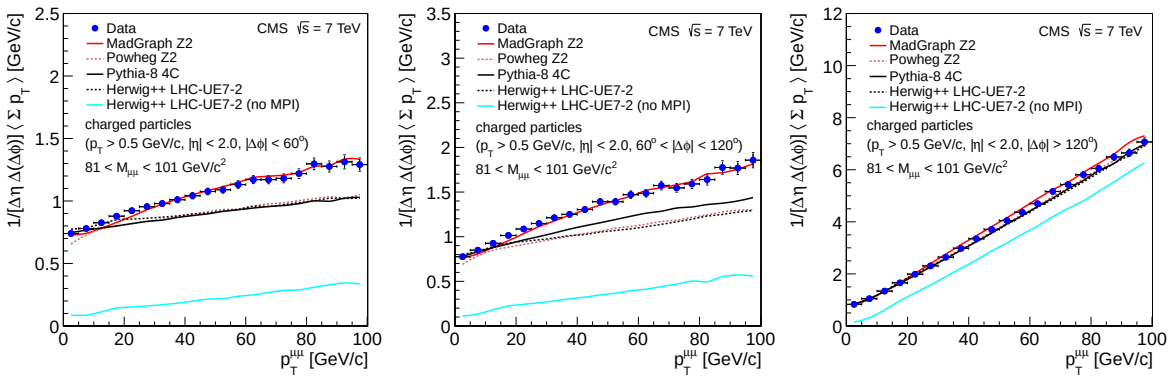

Figure 8.5.: The energy density (average scalar sum $\sum p_T$) in the towards (left), transverse (middle), and away (right) regions as a function of $p_T^{\mu\mu}$ for events satisfying 81 $< M_{\mu\mu} <$101 GeV/c^2. Predictions of MADGRAPH Z2, POWHEG Z2, PYTHIA8 4C, and HERWIG++ LHC-UE7-2 (with and without MPI's) are superimposed. [116]

To quantify this we introduce the event variable:

$$\rho = \underset{j \in \text{jets}}{\text{median}} \left[\left\{ \frac{p_{T,j}}{A_j} \right\} \right]. \tag{8.1}$$

This variable naturally isolates the UE contributions assuming that the majority of the event is dominated by soft interactions and has the additional advantage that no geometrical slicing of the phase space, in toward, transverse and away regions, is needed. The usage of the median in the definition makes it robust to outliers in the distributions that can be hard interactions. To avoid problems with limited detector acceptance, an adjusted observable ρ' is introduced that uses only jets containing at least one physical particle [117]. The jets to then calculate ρ' are track-jets reconstructed with the k_T algorithm (R = 0.6) within $|\eta| < 1.8$. The input tracks to the jets have $p_T > 0.3$ GeV/c

and $|\eta| < 2.3$. One can then study the jet area/median behaviour as a function of the leading jet found in the event. Figure 8.6 shows the results for $\sqrt{s} = 0.9$ and 7 TeV. Tunes Z1, Z2 and 4C of PYTHIA are too low at 7 TeV and one can generally see that the amount of events with very high activity is underestimated by the current models.

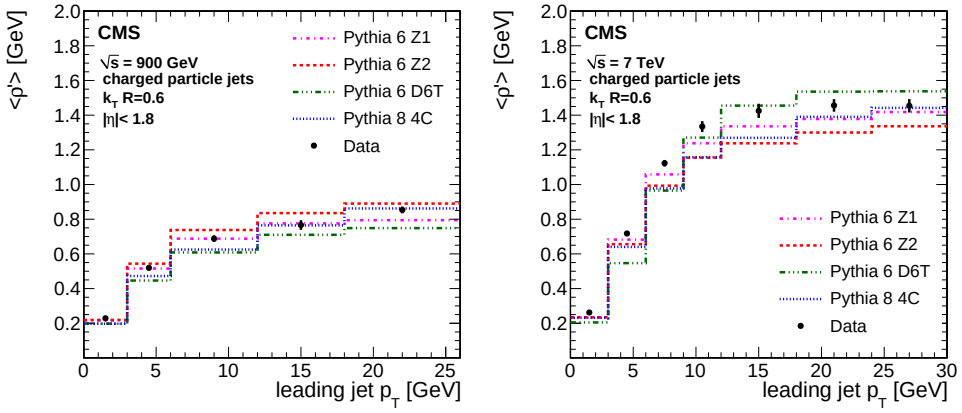

Figure 8.6.: Mean values of the corrected ρ' distributions versus leading jet p_T at $\sqrt{s} = 0.9$ TeV (left) and $\sqrt{s} = 7$ TeV (right) in comparison to the predictions by the different generator tunes. [117]

8.2. Energy density measurements at forward rapidity

Other fundamental studies that yield interesting results in the context of UE activity are energy density measurements at forward rapidities. Such studies were performed at the CMS [118] and LHCb [119] experiments. In the paper of CMS they measured the energy density, at $\sqrt{s} = 0.9$ and 7 TeV, in the pseudorapidity range $3.15 < |\eta| < 4.9$ for two classes of events: minimum bias and so called dijet events. In this case a dijet event is defined as an event that contains a hard scatter that produced two hard jets ($p_T > 8$ GeV/c at 0.9 TeV and $p_T > 20$ GeV/c at 7 TeV) at central rapidity ($|\eta| < 2.5$) that are back-to-back ($|\Delta\phi(\text{jet}_1, \text{jet}_2) - \pi| < 1.0$). The results for $\sqrt{s} = 7$ TeV are shown in figure 8.7 and are compared to different MC models. As the presence of a hard scatter in the event centralises the collision and enhances the probability to have multiple parton interactions, the dijet sample has a higher energy density than the minimum bias sample. Models that include MPI are close to the data, while models without MPI (PYTHIA6 D6T - no MPI and CASCADE) significantly underestimate the data. This confirms again that it is mandatory to include MPI in the models to account for all the UE activity. None of the PYTHIA6 tunes can describe the energy flow measurements equally well, and in general they predict a flatter distribution in minimum bias events. The predictions from HERWIG and DIPSY are in agreement with the data, as well as the cosmic ray event generators. Although they are not tuned to LHC data they give a reasonable well description of the measured energy flow.

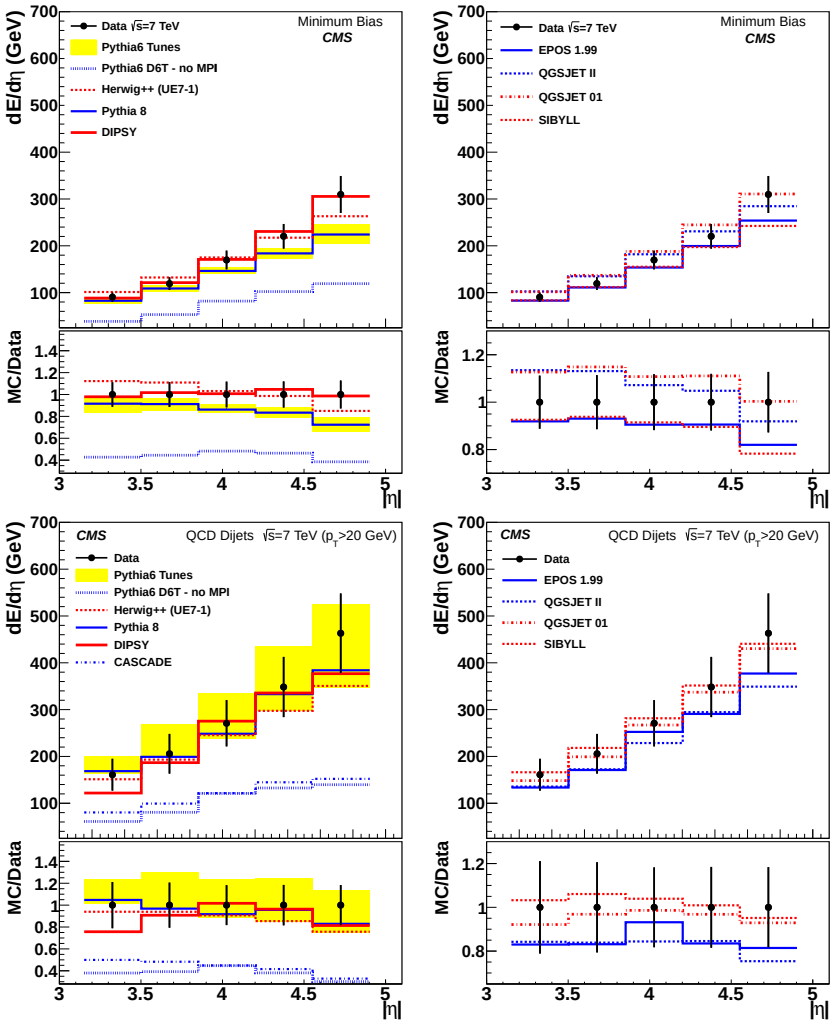

Figure 8.7.: The measured energy density at forward rapidity, at $\sqrt{s} = 7$ TeV, for minimum bias events (top plots) and dijet events (bottom plots). Data are compared to different MC models: (left) PYTHIA, HERWIG, DIPSY, CASCADE and (right) cosmic ray event generators EPOS, QGSJET, SIBYLL. [118]

The analysis performed at the LHCb experiment [119] looked at the energy density in the pseudorapidity range $1.9 < |\eta| < 4.9$ at $\sqrt{s} = 7$ TeV for four classes of event samples. Here we will only illustrate the results of the minimum bias and hard scattering type events. The primary measurement is the energy flow carried by charged particles (charged energy flow) that are reconstructed by tracks with $p_T > 2$ GeV/c in the above mentioned η region. A hard scattering event is then defined as an event with at least one track with $p_T > 3$ GeV/c within $1.9 < |\eta| < 4.9$. The results are shown in figure 8.8 for minimum bias events (top) and hard scattering events (bottom). One can see that the charged energy flow in data rises more steeply with η than predicted by most PYTHIA models. Only the PYTHIA8 model overestimates the data in the hard scattering event sample. The cosmic ray event generators EPOS and SIBYLL are able to describe the rise of the charged energy flow with η very well in minimum bias events, while the

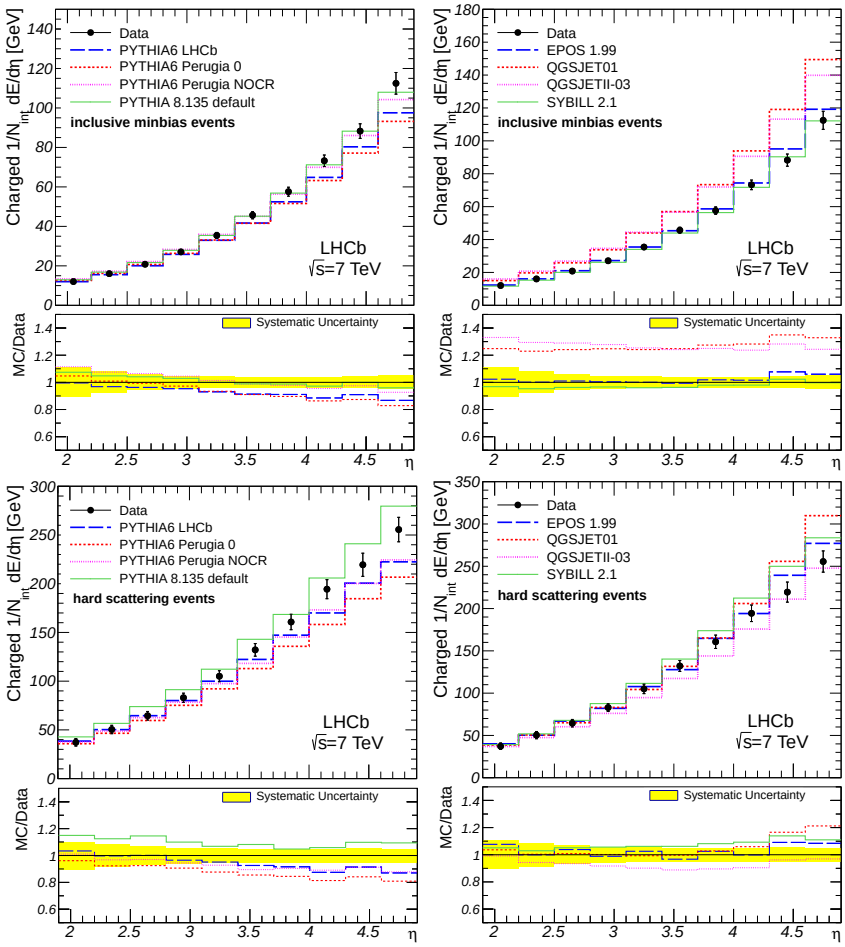

Figure 8.8.: The charged energy flow, at $\sqrt{s} = 7$ TeV, measured in the pseudorapidity range $1.9 < |\eta| < 4.9$, for minimum bias events (top) and hard scattering events (bottom). Data are compared with various PYTHIA models (left) and generators used in cosmic ray physics (right). [119]

response of the QGSJET models is too high. The description of the cosmic ray event generators in the hard scattering samples is again rather good, although they are not able to describe the charged energy flow evolution equally well over the whole η range.

Chapter 9.

Measurement of the underlying event at forward rapidity

9.1. Analysis strategy

As seen in the preceding chapter, previous studies [110, 112, 113, 111, 114, 116] typically study the underlying event at central rapidities and therefore have to separate hadronic activity due to the underlying event, from activity resulting from the hard scattering by dividing the azimuthal plane into the so-called toward, transverse, and away regions with respect to the direction of the highest-p_T jet. The hadronic activity in the transverse region is then assumed to be dominated by the underlying event, while the toward and away regions are mainly populated by the jets from the hard scatter. A complementary method, followed in this thesis, consists of studying the hadronic activity in a region far away in rapidity from the hard-scattering products. The toward, transverse, and away regions are then all dominated by the underlying event, which is well separated from the hard scattering.

In this work we will study the underlying event activity in proton-proton collisions at forward pseudorapidity ($-6.6 < \eta < -5.2$) in a novel way by measuring the *ratio* of the forward energy density per unit of pseudorapidity ($dE/d\eta$) for events with a charged-particle jet produced at central pseudorapidity ($|\eta^{\text{jet}}| < 2$) to the forward energy density for inclusive, dominantly nondiffractive, events. This energy density ratio is measured as a function of the jet transverse momentum (p_T) at three different centre-of-mass energies ($\sqrt{s} = 0.9$, 2.76, and 7 TeV). In addition, the *relative* increase of the forward energy density as a function of centre-of-mass energy is presented for inclusive events and for events with a central charged-particle jet. The measurement is conducted with the CMS detector (chapter 5) at the CERN LHC accelerator (chapter 4) and the forward energy density ratio's in the region $-6.6 < \eta < -5.2$ are measured with the CASTOR calorimeter (chapter 6). This extends the study of the forward energy density in pseudorapidity ranges $|\eta| < 5$ ([118, 119]) to a previously unexplored region.

As seen in the previous conducted measurements, a crucial component needed to describe the underlying event activity is the MPI model (introduced in section 3.3), which takes into account that multiple parton interactions can occur in addition to the

primary hard scattering. These additional interactions, which are still perturbatively calculable, are however softer than the primary one, which makes it difficult to describe them. Furthermore, the lack of a universal theoretical framework led to the usage of phenomenological models that have free parameters. The requirement of jets in the final state selects, on average, collisions with a smaller impact parameter [47, 48]. In the MPI model as implemented in PYTHIA (section 3.3), this correlation is realised by a suppression of low-p_T parton interactions at small impact parameter. Such central collisions then have a larger overlap of the matter distributions of the colliding hadrons and are therefore more likely to have many parton interactions. The comparison of particle and energy densities between events with hard jets in the final state and inclusive events thus yields information on underlying events with many parton interactions relative to those with few of them. This relative information, provided by the ratio measurement proposed above, will then enable us to test the different MPI model implementations in available Monte Carlo event generators.

Figure 9.1 shows the result of a Monte Carlo generator study based on the D6T underlying event tune [109] of the PYTHIA6 generator. Although this is not the best tune to describe early measurements of the underlying event activity at the LHC, it is used here because it yields a large number of MPI, which results in an enhanced effect on the forward energy density. Other tunes show a similar, but somewhat reduced, behaviour. Figure 9.1a shows the energy density, $dE/d\eta$, in the range $-6.6 < \eta < -5.2$, as a function of $\sqrt{s}$ for inclusive events. Figure 9.1b shows the energy density, in the same pseudorapidity range, for events with a central ($|\eta| < 2$) hard parton interaction with transverse momentum transfer, $\hat{p}_{\mathrm{T}}$, above 10 or 25 GeV/c, and finally, figure 9.1c shows the ratio of these two distributions, henceforward called the "*hard-to-inclusive forward energy ratio*".

One can see that the energy density in inclusive events is only slightly affected by the presence of MPI, which is not the case in events with a hard parton interaction at large $\sqrt{s}$, where a large increase of the energy density is predicted when including MPI. In addition, this increase is roughly independent of $\hat{p}_{\mathrm{T}}$, indicating that the collisions are already central for $\hat{p}_{\mathrm{T}} > 10$ GeV/c. Finally, the hard-to-inclusive forward energy ratio would be close to unity in the absence of MPI. But with MPI however, the ratio is significantly higher than 1 at large $\sqrt{s}$, while it drops below 1 at small $\sqrt{s}$. This last observation points to a depletion of the energy of the proton remnant in events with hard central jets. Indeed, at $\sqrt{s} = 0.9$ TeV, the proton remnant has a rapidity $y = \ln(\sqrt{s}/m_p) \approx 7$ with m_p the proton rest mass. Hence, at this centre-of-mass energy, the energy density in the considered pseudorapidity range is sensitive to the details of the beam remnant fragmentation.

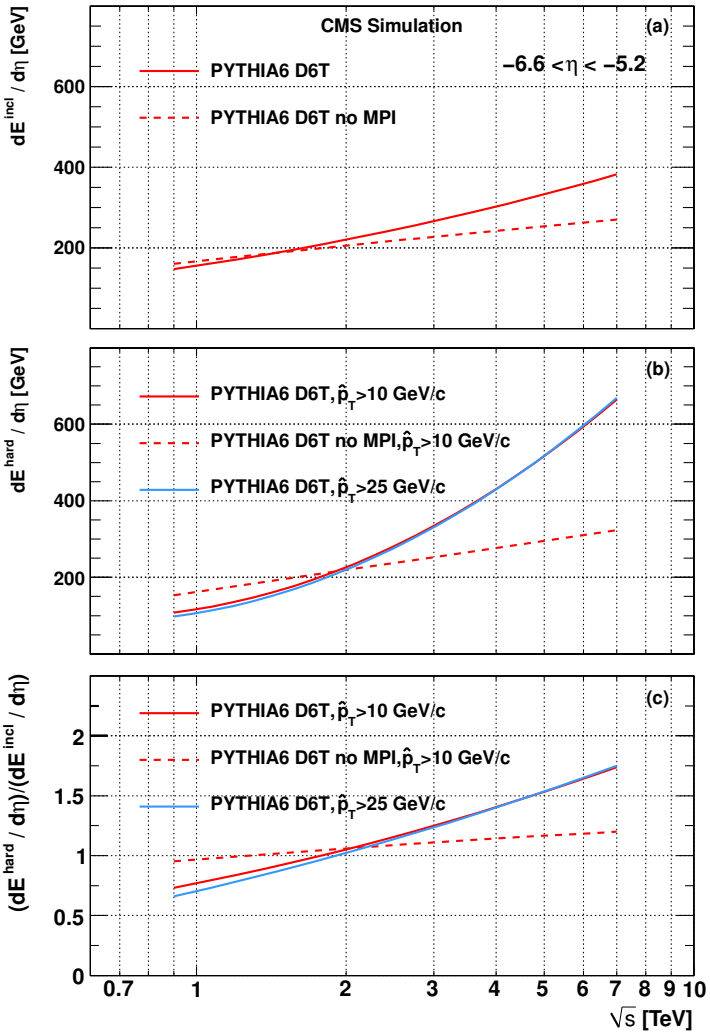

Figure 9.1.: The energy density $dE/d\eta$ in the pseudorapidity region $-6.6 < \eta < -5.2$, obtained with PYTHIA6 D6T model, is plotted as a function of $\sqrt{s}$, for inclusive, nondiffractive events (a) and for events with a central ($|\eta| < 2$) hard parton interaction with transverse momentum transfer, $\hat{p}_{\mathrm{T}}$, above a given threshold (b). The ratios of the plots in (a) and (b) are shown in (c).

9.2. Monte Carlo models

In this section, we list the specific Monte Carlo (MC) models used in the analysis for correction and comparison of data, and briefly repeat their implementation and tuning of the underlying event, which was already introduced in more detail in section 3.4.

Several tunes of the PYTHIA6 (version 6.424) [42] and PYTHIA8 (version 8.145) [50] event generators are used, each one providing a different description of the underlying event in nondiffractive interactions: D6T [109], Z1, Z2 [111], Z2*, the central Perugia 2011 tune (P11) [120] and the ATLAS minimum bias tune 1 (AMBT1) [121] for PYTHIA6 and tune 4C [122] for PYTHIA8. These tunes differ in the choice of flavour, fragmentation

and underlying event parameters. The latter set of parameters, which are expected to be important for these measurements, includes parameters for the parton showers, cut-off values for MPI sequences, parameters determining the geometrical overlap between the incoming protons, and probabilities for colour reconnection. Some of the tunes have common flavour and fragmentation parameters, which have been determined using data from LEP. An overview of the tunes can be found in [120].

The parameter settings in D6T were determined from the Tevatron data, while the other tunes were determined from the LHC data on inclusive and underlying event properties at central pseudorapidity. The more recent PYTHIA6 Z2 and Z2* tunes, as well as PYTHIA8, use a new model [123] where multiple parton interactions are interleaved with parton showering (section 3.3.4). The Z2 and Z2* tunes are derived from the Z1 tune [124], which uses the CTEQ5L [125] parton distribution set, whereas Z2 and Z2* adopt CTEQ6L [126]. The Z2* tune is the result of retuning the PYTHIA6 parameters PARP(82) and PARP(90) by means of the automated PROFESSOR tool [127], yielding PARP(82)=1.921 and PARP(90)=0.227. The former parameter represents the $p_{T,0}$ cut-off of the MPI model, while the latter represents its $\sqrt{s}$ dependence ϵ (section 3.3, eq. (3.10) and (3.11)). The results of the study in this thesis are also compared to predictions obtained with PYTHIA6, tune Z2*, with MPI switched off. PYTHIA8 is used with tune 4C, based on the early LHC data. Parton showers in PYTHIA are modelled according to the DGLAP evolution equations and the hadronisation is based on the Lund string fragmentation model [41].

The HERWIG++ (version 2.5) [51] MC event generator, with a recent tune to LHC data (UE-EE-3C [128]), is used for comparison to data. The evolution of the parton distribution functions with momentum scale in HERWIG++ is also driven by the DGLAP evolution equations. However, HERWIG++ features angular-ordered parton showers and uses a cluster fragmentation model for the hadronisation.

In contrast to PYTHIA and HERWIG++, CASCADE [54, 53] is based on the CCFM evolution equation for the initial-state cascade, supplemented with off-shell matrix elements for the hard scattering. Multiple parton interactions are not implemented in CASCADE.

The DIPSY generator [55] is based on a dipole picture of BFKL evolution. It includes multiple dipole interactions, with parameters tuned as described in [55], and is suitable to predict nondiffractive final states. In the present implementation, however, quarks are not included in the parton evolution. Hence the treatment of the proton remnant and valence quark structure is therefore rather simplistic, and predictions for the structure of the final state in the very forward region are somewhat uncertain.

Finally, data are also compared to the predictions of Monte Carlo *pp* event generators used in cosmic ray physics [129]. Here the generators EPOS1.99 [60], QGSJETII [59] and SYBILL 2.1 [61] are considered. These models describe the soft component in terms of the exchange of virtual quasi-particle states, within Gribov's reggeon field theory (section 2.4.2), with multi-pomeron exchanges accounting for MPI effects. At higher energies and scales, the interaction is described by perturbative QCD with the DGLAP evolution

equations. These models also include non-linear parton effects, either by including pomeron-pomeron interactions, as in QGSJET and EPOS, or by means of a parton saturation approach, as in SYBILL. These cosmic ray models were not tuned to LHC data.

9.3. Performance of the CASTOR calorimeter

9.3.1. Data taking conditions

The performance of the CASTOR calorimeter was extensively studied in a test beam environment (section 6.3) and accordingly simulation software was developed and tested to it (section 7.3). However, as we shall see, understanding the performance of the CASTOR calorimeter in an *in situ* environment is not as trivial as it was in ideal test beam setups.

The main challenge in the operation of the CASTOR calorimeter is its location: at $z = -14.38$ m from the interaction point, close to the beampipe and surrounded by massive shields, a very compact form of the detector is required. One of the consequences is that the 224 PMT's are mounted directly on the detector, less than 30 cm away from the LHC beam, and as such they are exposed to high radiation levels and strong fringe magnetic fields. The collected light is therefore detected using fine-mesh Hamamatsu R5505 PMT's, which should allow an operation in magnetic fields up to 0.5 T, if the field direction is within $\pm 45°$ with respect to the PMT axis [130]. In addition, one should take the exposure to high radiation levels into account since it can induce a slow darkening of the currently used borosilicate PMT's, leading to a slow degradation of the overall performance. Fortunately, this is not a problem for the present study, since all data used in this analysis were taken before the high-luminosity operation of the LHC in 2011.

The complicated magnetic field configuration at the location of CASTOR is caused by the fact that in the centre of CASTOR (around module 7) the massive protective shields meet, producing an air gap of 40 mm between them. The absolute value of the magnetic field flux measured at this region does not exceed 0.2 T, but unfortunately the direction of the field varies strongly. This results in totally suppressed responses of the PMT's located around the gap in the shielding, as illustrated in figure 9.2. Therefore, with modules 6 to 8 suffering from the magnetic field and modules 9 to 14 collecting only a small fraction of hadronic showers, the present analysis is restricted to the modules 1 to 5. Although this corresponds to a reduction of the calorimeter depth from 10.5 to 3.2 hadronic interaction lengths (λ_I), it has been checked with simulation studies that about 80% of the energy deposited in CASTOR in inclusive events is contained within the first 5 modules. This fraction is rather insensitive to the centre-of-mass energy. Furthermore, the reduction in depth does not affect the range of acceptance in pseudorapidity.

Another consequence of the strong remnant fields in the forward region of the CMS detector is that the CASTOR calorimeter slightly shifts in the (x, y) plane when the CMS

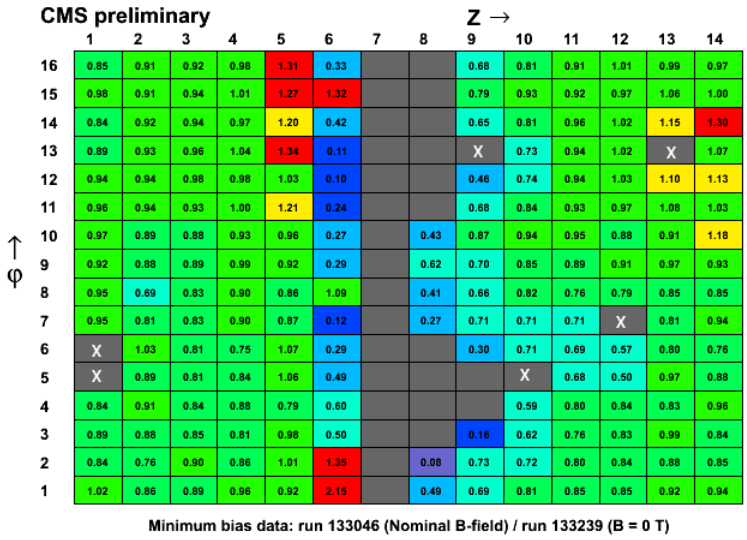

Figure 9.2.: A map (ϕ vs. z) of the ratio $\langle S_i(B = 3.8\text{ T})\rangle / \langle S_i(B = 0\text{ T})\rangle$ of the average response of all channels i of CASTOR with and without magnetic field. The colour code indicates how much the signal ratios deviate from 1. Blue colours indicate a reduction in signal with increasing magnetic field strength, while yellow and red colours indicate an increase in signal strength. Green channels yield similar signals with and without magnetic field. Channels with no observed signal in the presence of the nominal magnetic field are grey (with the crossed channels being dead regardless of the magnetic field).

solenoid is switched on. This is illustrated in figure 9.3, which shows the location of the two CASTOR halves as measured by position sensors that serve to monitor movements that may harm the beampipe. During the 2010 data taking period (figure 9.3 left plot) it appears that the two halves move separate, both away from the beampipe, although the left half moves significantly further than the right one. The same effect is seen during 2011 data taking (figure 9.3 right plot), but the position slightly changed with respect to the 2010 position. This is probably due to the fact that between the two run periods, the CMS solenoid was switched off and on, during which CASTOR goes back to its nominal position and shifts again to a new offset respectively. The sensor measurements indicate a position of the left CASTOR half at (-11.5 mm,-1.8 mm) in 2010 and (-14.6 mm,-0.5 mm) in 2011, while the right half is shifted to (3.1 mm,-3.8 mm) in 2010 and (2.4 mm,-1.7 mm) in 2011. The error on the measurements is of the order of 2 mm. The largest shift is thus found to be between approximately 12-14 mm away from the beampipe. This results in some ϕ sectors to move to more central rapidity, covering the range between $-6.3 < \eta < -5.13$, while others go more forward. It is obvious that such displacements in position give rise to important changes in performance and energy deposit, certainly in the forward region in which the energy densities are strongly varying with η. Therefore a lot of effort has been put in understanding this effect, and to address a systematic uncertainty to it, which will be explained in a later section.

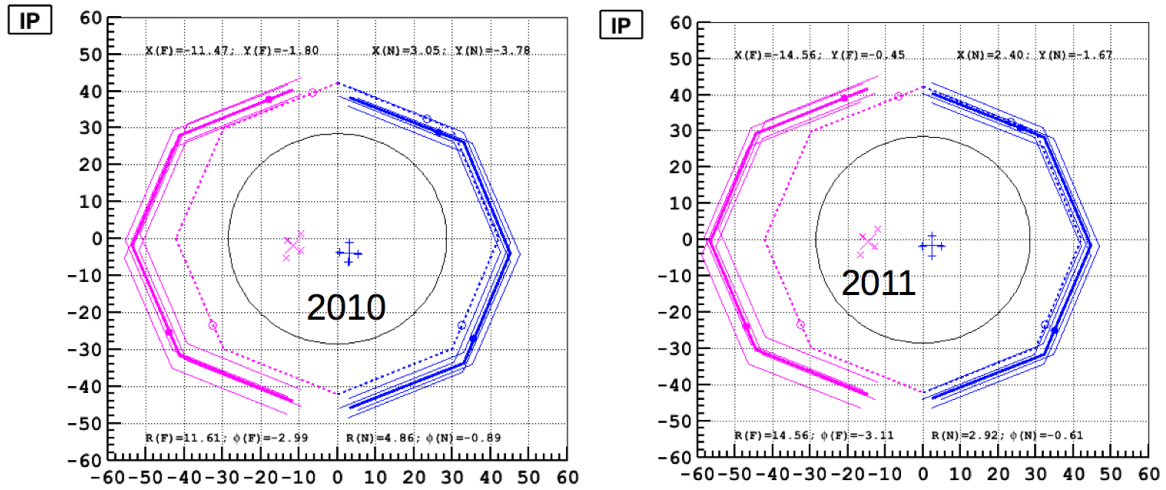

Figure 9.3.: Position in the (x, y) plane of the CASTOR half detectors (at $B = 3.8$ T) during the 2010 LHC run period (left) and during 2011 data taking (right). Both plots show the position of the front (IP) side of the detector. The beampipe is represented by the black circle and the dashed line indicates the nominal position of the CASTOR detector. The axis units are in mm.

9.3.2. Alignment

In order to understand the effects, and to confirm the position of the CASTOR detector, an attempt was made to tune the detector simulation software to the measured data. This simulation, as explained in section 7.3, contains an ideal implementation of the CASTOR geometry, placed at its nominal position. A naive comparison of such simulation results with in situ data of a displaced detector then leads to a disagreement, which is most notably seen in the ϕ sector profiles of the calorimeter. This can explained as follows. In a collinear collision of two protons, with opposite incoming momenta, the total transverse momentum p_T is zero. Hence, due to momentum conservation, the total transverse momentum of the final state must be zero too. As a consequence, one expects, on average, a flat response of the detectors as a function of the azimuthal angle ϕ, if the collision happens exactly at the nominal (0,0) position in the detector. In reality however, this is not the case, and the collisions happen at a certain offset, which is called the beamspot (section 7.2). As such, the ϕ profiles in the detectors will show a sinusoidal behaviour that is determined by this offset. Then, if the detector itself is displaced, the additional translation with respect to the beamspot will result in a different sinusoidal behaviour then expected. It is this effect that can be exploited to tune the simulation to measured data, and to extract a displacement of the detector.

To tune the simulation we made use of the convenient Professor package [127]. This program is a general tuning tool for MC event generators that parameterises a generator's response to changes in defined steering parameters. A set of generated input samples, with each sample having a different value of the steering parameters, is then

used for the interpolation of the generator's response. With this information available, an observable distribution can then be tuned to data by performing a minimisation, which yields new parameter values. In our specific case, the steering parameters are defined as the x and y coordinates of the left and right half positions. Each position then leads to a different ϕ profile. We then construct a grid of (x, y) points, in which each point corresponds to a simulated minimum bias sample of the CASTOR detector that is displaced to the position of those points. PROFESSOR then combines all this information and parameterises the behaviour of the ϕ profile as function of the steering parameters x and y. An example of the grid that is used to tune the $\sqrt{s} = 0.9$ TeV data taken during the 2010 run period is shown in figure 9.4, in which the sensor positions (from figure 9.3) are included for comparison. A similar grid is constructed to tune the $\sqrt{s} = 2.76$ TeV data taken in 2011.

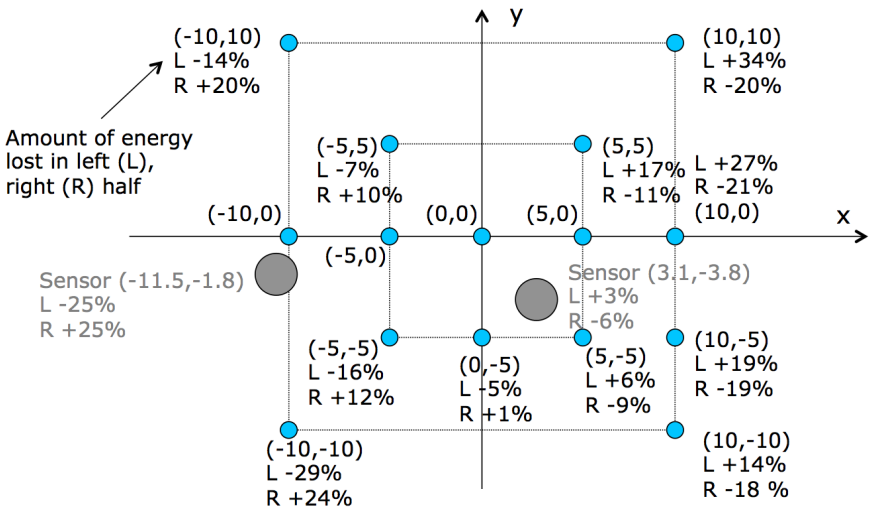

Figure 9.4.: A grid of (x, y) positions used to tune the simulation to data with $\sqrt{s} = 0.9$ TeV. The sensor measurements are shown for comparison. At most points, an indication is given of the relative energy change that is expected due to the shift. If the detector is shifted towards the (-10,10) position, the energy in the left (L) half will decrease with 14%, while the energy deposited in the right (R) half will increase with 20%. The axis units are in mm.

With such grids available, the response of the ϕ profile can be interpolated, and tuned to the data through minimisation. This yields new values of x and y needed to produce the tuned ϕ profile. The results for 2010 and 2011 run periods are shown in figure 9.5. Here, the ϕ profile is defined as the average detector response in modules 1 to 5, as a function of sector number, in minimum bias data. It is clear that the tuned results (blue dashed lines) describe the data (black) much better than the nominal simulations (red dashed lines) as expected. The tuned positions of the left and right halves in the $\sqrt{s} = 0.9$ TeV 2010 data are $(-10 \pm 1.5, 2.2 \pm 1.9)$ mm and $(3.1 \pm 1.4, 2.2 \pm 1.3)$ mm

respectively, the results for $\sqrt{s} = 2.76$ TeV 2011 data are $(-7.1 \pm 1.3, 5 \pm 1.7)$ mm and $(-0.8 \pm 1.1, 3.7 \pm 1.1)$ mm.

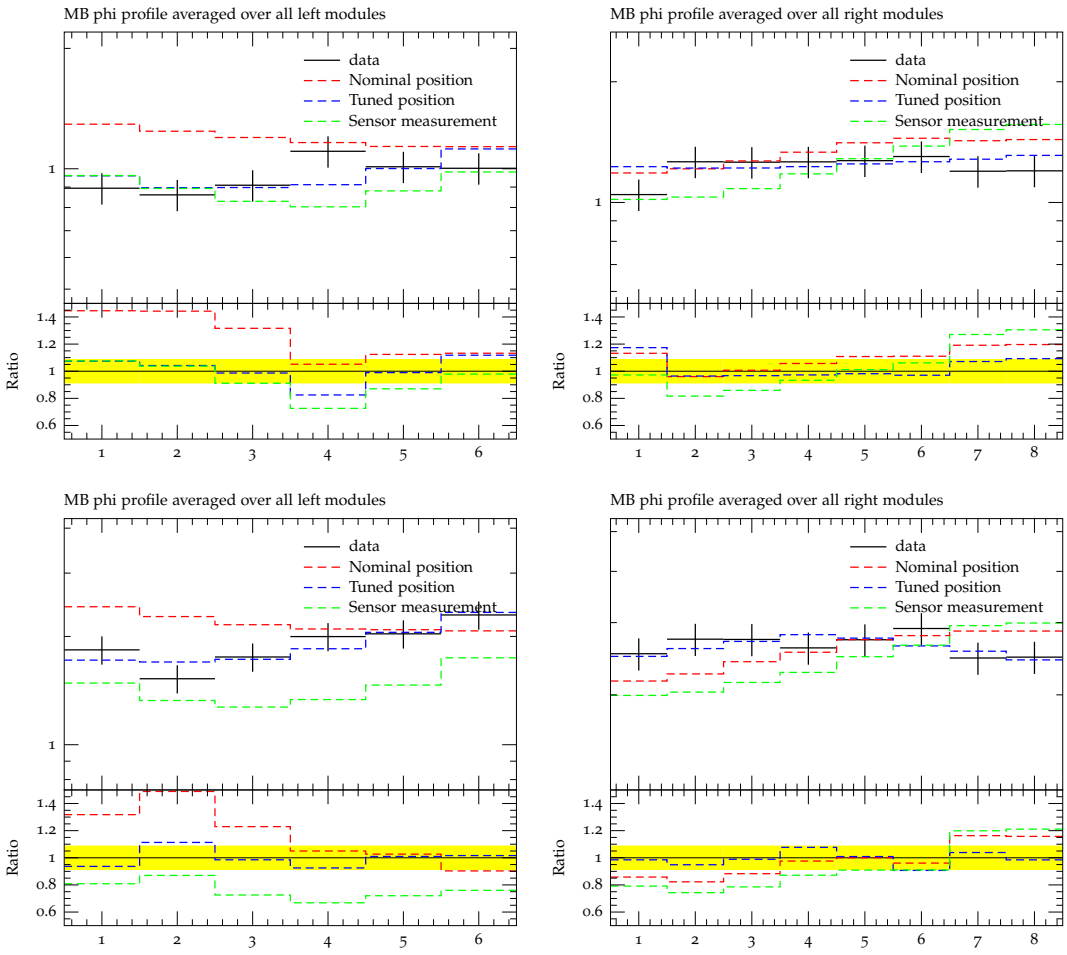

Figure 9.5.: The CASTOR detector ϕ profiles, as a function of sector number, shown for minimum bias data at $\sqrt{s} = 0.9$ TeV (top row) and $\sqrt{s} = 2.76$ TeV (bottom row). The response of the left and right halves are shown on the left and right side accordingly. The measured data are shown in black, nominal simulation in red dashed, the sensor measurement in green dashed, and the tuned result in blue dashed lines. The left side is only plotted for 6 sectors, due to the missing channels 5 and 6 (cf. figure 9.2). The logarithmic y axis is shown in units of GeV.

One can however also see that the tuned results do not completely agree with the profile from the sensor positions (green dashed lines). As can be seen in figure 9.6, this discrepancy is more pronounced at $\sqrt{s} = 2.76$ TeV then at $\sqrt{s} = 0.9$ TeV, which shows a reasonable agreement of the x coordinate, within errors, but seem to indicate a swap of the y coordinate sign. Until now, the exact reasons for such discrepancies are not yet understood, and more studies are needed to disentangle all possible effects. Preliminary studies, including a tuning of the data at $\sqrt{s} = 7$ TeV taken during the same run period in 2010, have shown that the non-compensation correction and energy

reweighting procedures of the simulated detector response can have significant effects. The main ambiguity is that PROFESSOR just performs a minimisation to improve the agreement between simulation and data, it doesn't take any physics into account, it only knows that the energy deposit will decrease as the detector moves to more central rapidities. Thus, e.g., if a MC model generated at the nominal position has a too high energy response with respect to data, PROFESSOR will simply fix this by moving the detector to central rapidities, while the too high response may be partly due to the physics of the underlying model. These effects are difficult to disentangle, but crucial for the tuning procedure. In addition, studies of the response of the backward modules (10-14), which are currently not used in this analysis, have shown that the response in data is much higher than what can be achieved with displaced simulations, within physical boundaries. This can be an indication of possible tilts, such that the backward modules are closer to the beampipe, and can receive more direct hits due to the angle of the detector.

Nevertheless, from this first tuning attempts it is clear that the description of the ϕ profile can be improved if the CASTOR halves effectively move away from the beampipe, and that the magnitude of the translation is found to be compatible with sensor measurements. Furthermore, an independent study done in [131], confirms our first preliminary results. As such we will use this basic information on the magnitude and direction of the translation to address a conservative systematic uncertainty on the measurement conducted in this analysis.

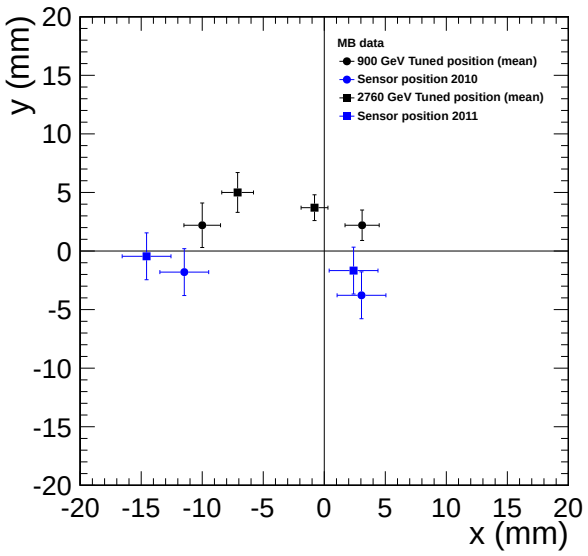

Figure 9.6.: A combined plot showing the results of the tuning attempts (black) at $\sqrt{s} =$ 0.9 TeV and 2.76 TeV, together with the known sensor measurements (blue).

9.3.3. (Inter-)calibration

The in situ inter-calibration of the CASTOR calorimeter, i.e. the equalisation of the response of individual CASTOR channels, was performed with samples of beam halo muon events taken in 2010 [132, 133]. As seen in chapter 6, muons deposit a rather constant signal in calorimeters, which allows an equalisation of the individual channel response of the detector. These beam halo muons can be detected in-between LHC collision runs, when the beams are simply circulating, as they originate from proton interactions with surrounding accelerator facilities such as collimator material, or from present beam gas. During such data taking one only expects clean events containing collinear muons, which can be detected in CASTOR by triggering on the requirement that multiple channels in a particular sector have a signal above noise. An example of a muon signal spectrum is shown in figure 9.7 (left), and the result of the inter-calibration procedure for, e.g. sector 1, is shown in figure 9.7 (right).

In addition, a preliminary absolute calibration factor of 0.015 GeV/fC, with an uncertainty of $\pm 22\%$, is obtained from a Monte Carlo based extrapolation of the η dependence of the energy density per unit of pseudorapidity measured in the HF calorimeter to the CASTOR acceptance [131]. This factor is found to be consistent with test beam measurements [88]. Note however that the energy ratios presented in this analysis do not depend on the absolute calibration and are only marginally affected by the relative inter-calibration of channels, as will be shown later.

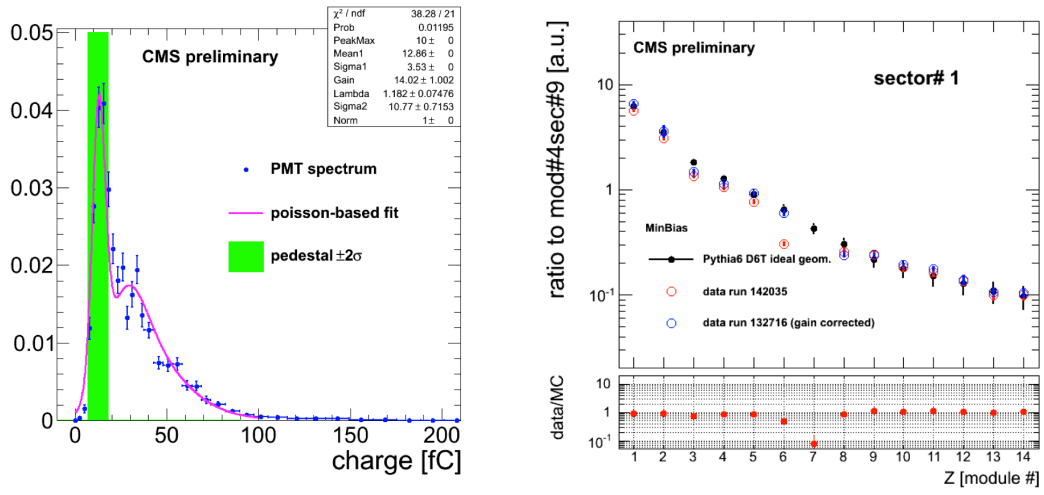

Figure 9.7.: (left) Example of a muon spectrum obtained with a 25 ns signal integration time (blue) fitted to a convolution of Gaussian and Poisson distributions (magenta). The green band indicates the pedestal position. (right) Average inter-calibrated minimum bias shower profile in sector 1 compared to a corresponding Monte Carlo prediction (black), of the PYTHIA6 D6T generator with CASTOR at its nominal position (ideal geometry). Data taken with two different PMT gain settings are shown in red and blue. [133]

9.3.4. Control plots

In this analysis, the total charge (fC) collected by the PMT's of the 5 front-most z-modules of the CASTOR calorimeter is used to measure the energy deposited in the CASTOR η range. No zero-suppression is applied, although pedestal values are subtracted channel-wise. As indicated before (figure 9.2), channels 5 and 6 of module 1 were found to be unstable and are thus rejected from the analysis. Figure 9.8 shows the longitudinal and azimuthal shower profiles as well as the total energy distribution for data and MC models, including a version of the PYTHIA6 Z2 model that has been reweighted as a function of the total energy distribution in order to improve the description of the observed data. To calculate this weight, the ratio between the data and PYTHIA6 Z2 (data/PYTHIA6 Z2) is determined as a function of the total energy measured in CASTOR, and then parametrized with a quartic polynomial. The resulting function from the fit procedure is then evaluated with the total generated energy at stable particle level, in the range $-6.6 < \eta < -5.2$, in order to define the weight that is applied to the event. The control plots are obtained with an ideal geometry setup, and the ϕ distributions are thus affected by tilts and shifts of the CASTOR detector, as stated before. The z profile and the energy distribution, on the other hand, are affected by the physics of the underlying model: the energy evolution with $\sqrt{s}$ is not well described, and also the fraction of electromagnetic and hadronic particles in the forward shower varies a lot between models.

9.4. Event selection and reconstruction

The analysis is based on data collected by the CMS detector in 2010 and 2011 at $\sqrt{s} = 0.9, 2.76$ and 7 TeV, corresponding to integrated luminosities (L) of, respectively, 0.19 nb^{-1}, 0.30 nb^{-1} and 0.12 nb^{-1}. Runs are selected by requiring that the relevant components of the CMS detector were fully functional, in particular, the CASTOR forward calorimeter. The average number of collisions per bunch crossing, inferred from the instantaneous luminosity and the total inelastic cross section, in the runs considered for this analysis are 0.017, 0.22 and 0.12 at $\sqrt{s} = 0.9$, 2.76 and 7 TeV, respectively.

The data samples and runs used in this analysis are:

- For $\sqrt{s} = 0.9$ TeV: runs 134721 and 134725
  Dataset: `/MinimumBias/Commissioning10-07JunReReco_900GeV/RECO`
- For $\sqrt{s} = 2.76$ TeV: runs 161366, 161396, 161404, 161439, 161445, 161450, 161454, 161473 and 161474
  Dataset: `/AllPhysics2760/Run2011A-16Jul2011-v1/RECO`
- For $\sqrt{s} = 7$ TeV: runs 135059, 135521, 135523, 135525, 135528, 135535, 135573 and 135575
  Dataset: `/MinimumBias/Commissioning10-May19ReReco-v1/RECO`

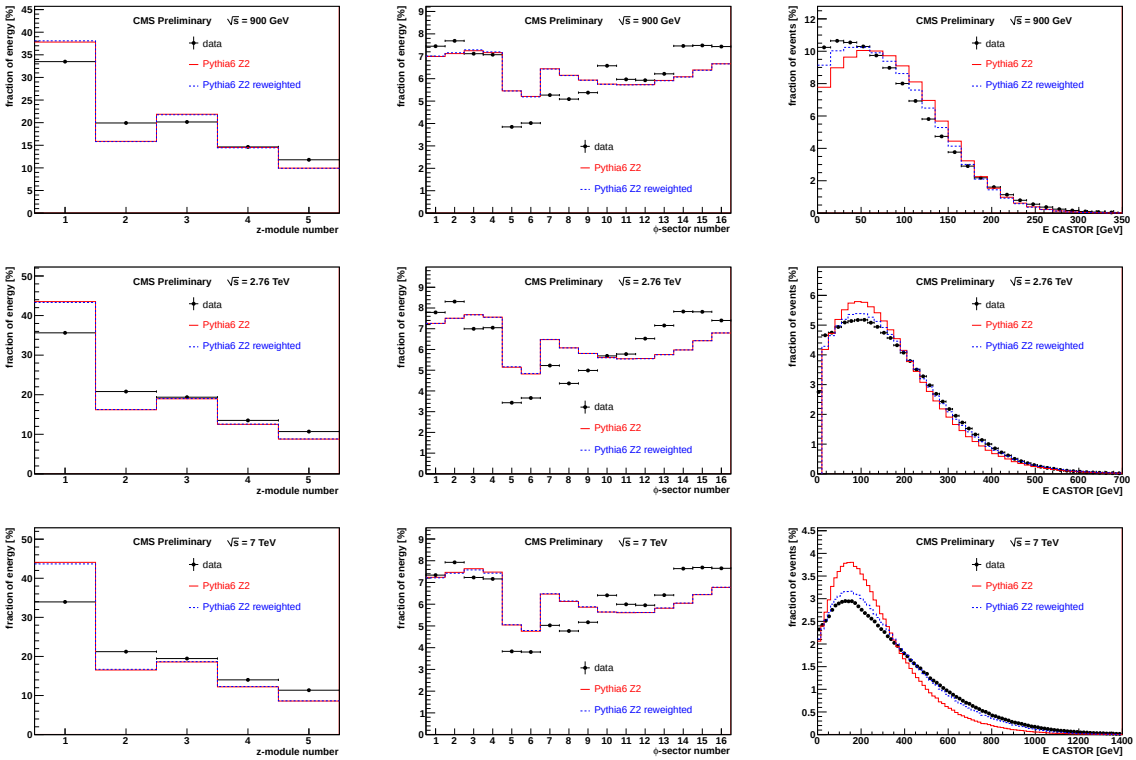

Figure 9.8.: Longitudinal (left) and azimuthal (middle) shower profiles and total energy distribution (right) at $\sqrt{s}$ = 0.9 (top), 2.76 (middle) and 7 TeV (bottom) measured in minimum bias data and obtained from Monte Carlo simulations. Note that the first two modules have half the absorber thickness of the next three modules. The dip in the ϕ profiles at sectors 5 and 6 is caused by the missing channels 5 and 6 in module 1.

All the data are processed with CMSSW release 4_2_3 and corresponding Global Tag `FT_R_42_V13A`.

The CMS trigger system (section 5.6) is used to select the data, with in particular information from the CMS detector monitoring system, containing the BSC and BPTX devices (section 5.7). The CMS data acquisition was then triggered by the minimum bias requirement of having hits in both BSC1 detectors (for the 0.9 and 7 TeV data sample) or having hits in any of the BSC1 detectors (for the 2.76 TeV data sample). In addition, standard CMS cleaning algorithms to remove beam halo and scraping events are applied. The final L1 trigger decision is then based on the coincidence of following technical (TT) and physical (PT) trigger bits:

- A valid bunch crossing based on the BPTX: `TT[0]`
- A veto on the presence of beam halo muons:
  `!(TT[36] or TT[37] or TT[38] or TT[39])`
- At 0.9 and 7 TeV: hits in both BSC1 detectors: `TT[40] or TT[41]`

- At 2.76 TeV: hits in any BSC1 detector: `PT[126]`

No further trigger conditions are applied at HLT level. Events are further selected by, a) requiring the "physics declared bit" of CMS to be on, b) by rejecting events with invalid CASTOR HTR data (faulty electronics behaviour), and c) by rejecting beam scraping events, i.e. 25% of the measured tracks in events with more than 10 tracks must be of high purity (see section 7.2). Events need to have at least one primary vertex reconstructed and selected by requiring $|z| < 15$ cm, $\rho \leq 2$ cm and NDF (number of degrees of freedom) ≥ 4.

"*Minimum bias*", or inclusive events, are then selected more precisely offline by requiring exactly one primary vertex, at least one HF tower with an energy larger than 4 GeV in the pseudorapidity range of each BSC1 detector, and at least one CASTOR tower (defined as the sum of the 5 front-most modules in a sector) with an energy above 1.5 GeV. These cuts effectively remove events triggered by noise in the BSC1 detectors. The final numbers of selected minimum bias events are then 4.7, 9.8, and 4.6 million at $\sqrt{s} = 0.9, 2.76$ and 7 TeV, respectively.

The above introduced threshold applied to CASTOR towers is obtained from a dedicated study of so called "zero-bias" events. An almost pure noise sample is then obtained by first removing events with CASTOR invalid HTR data or beam scraping events, and then requiring no signal in either BSC1 detectors and no reconstructed vertex. The read-out electronics of the CASTOR calorimeter yield a mean noise per channel of 1 ADC count, which corresponds to a current of 2.6 fC. Using the absolute calibration factor of 0.015 GeV/fC, this would then lead to a mean noise signal per channel of $\sim$60 MeV, when the signal is integrated over two time slices (50 ns), as used to reconstruct the signal. However, after applying the channel inter-calibration constants, which both equalise the channel responses and compensate for changes in the high voltage settings, the average pedestal width increases to $60 - 300$ MeV at 0.9 and 7 TeV, and $40 - 100$ MeV at 2.76 TeV (for which a different high voltage setting was applied to the PMT's). The mean noise per CASTOR tower, which contains 5 channels, is then found to be 364 MeV at 0.9 and 7 TeV and 124 MeV at 2.76 TeV.

The effect on zero-bias data, of requiring a tower signal of at least n times the mean noise level is shown in table 9.1. One can see that with an increasing threshold, the fraction of empty CASTOR events surviving the cut decreases, while the energy measured by CASTOR for those events that do survive the cut increases. The final threshold that will be applied uniformly to data at all centre-of-mass energies is the one corresponding to the 4σ-cut at $\sqrt{s} = 7$ TeV, yielding a value of 1.5 GeV. Figure 9.9 then shows the low end of the energy spectrum measured in CASTOR, for events obtained at different centre-of-mass energies, before and after the 1.5 GeV CASTOR tower cut. The peak around zero originates from events with no energy deposited in CASTOR and is well described by the noise distribution as obtained from the zero bias data, and scaled to fit the lower edge of the pedestal peak of the non-suppressed distribution. It is clear that, after applying the CASTOR tower selection, the empty CASTOR events are effectively removed and do not affect the distribution at higher energies.

cut	$\sqrt{s} = 0.9$ TeV			$\sqrt{s} = 2.76$ TeV			$\sqrt{s} = 7$ TeV		
	E_{cut} (GeV)	f_{noise}	$\langle E_{\text{noise}} \rangle$ (GeV)	E_{cut} (GeV)	f_{noise}	$\langle E_{\text{noise}} \rangle$ (GeV)	E_{cut} (GeV)	f_{noise}	$\langle E_{\text{noise}} \rangle$ (GeV)
no cut	0	100%	0.015	0	100%	0.38	0	100%	0.017
1σ	0.36	93%	0.14	0.12	93%	0.082	0.36	93%	0.14
2σ	0.73	35%	0.86	0.25	38%	0.35	0.73	35%	0.86
3σ	1.10	5.0%	1.41	0.37	7.6%	0.55	1.10	5.7%	1.42
4σ	1.46	0.6%	1.83	0.50	2.2%	0.68	1.46	1.4%	1.91

Table 9.1.: The effect of asking at least one CASTOR tower above a given threshold was studied using samples of zero bias data, obtained at different centre-of-mass energies. The table lists the cut value (E_{cut}), the fraction of noise events surviving the cut (f_{noise}) and the mean energy of those noise events ($\langle E_{\text{noise}} \rangle$).

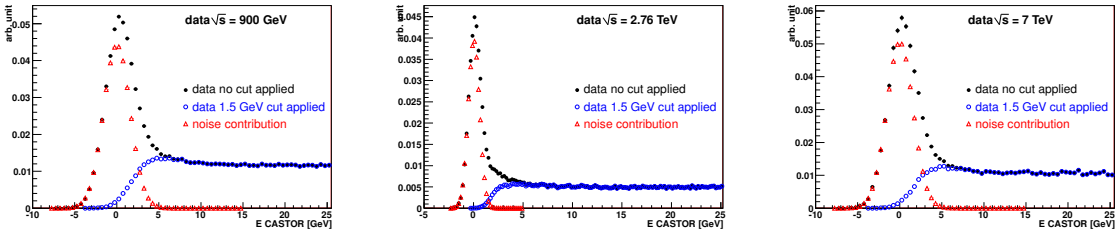

Figure 9.9.: The low end of the energy spectrum measured in CASTOR, for events obtained at $\sqrt{s} = 0.9$, 2.76 and 7 TeV is shown before (black) and after (blue) requiring at least one CASTOR tower above 1.5 GeV. The noise distribution as obtained from zero bias data, scaled to fit the lower edge of the pedestal peak of the non-suppressed distribution, is also shown (red).

9.5. Track-jet reconstruction

As stated in the introduction, the analysis strategy is to measure the ratio of the forward energy density per unit of pseudorapidity ($dE/d\eta$) for events with a charged-particle jet produced at central pseudorapidity ($|\eta^{\text{jet}}| < 2$) to the forward energy density for inclusive, dominantly nondiffractive, events. The latter, inclusive, sample is defined by the minimum bias selection cuts and reconstruction described in the previous section, while the former sample is a subset of the minimum bias data and will be described in this section.

In this analysis, the charged-particle jets produced at central pseudorapidity ($|\eta^{\text{jet}}| < 2$) are reconstructed in the detector as *track-jet* objects in the same pseudorapidity range. These track-jets are reconstructed using the anti-k_T jet algorithm (section 3.2.3) with

$R = \sqrt{(\Delta\eta)^2 + (\Delta\phi)^2} = 0.5$ that takes a collection of reconstructed tracks as input, which are fitted to a primary vertex and have a reconstructed transverse momentum, p_T, of at least 300 MeV/c. The leading track-jet in the event with $p_T > 1$ GeV/c and $|\eta^{\text{jet}}| < 2$ then defines the *hard scale* of the event, as its p_T represents the scale of the hard scatter. An advantage of using track-jets is that they are experimentally well-defined objects. Therefore, no attempt is made to refer to the corresponding parton-level objects, as this would result in additional model uncertainties. Moreover, track-jets are much better correlated in energy and direction to partons than the highest-p_T track. Finally, in the few GeV/c region, the p_T of a track-jet is better determined than the p_T of calorimeter based jets, which suffer from a poor energy resolution at low p_T.

In summary, the tracks selected for input to the anti-k_T jet algorithm have to fulfil the following criteria:

- All tracks need to pass the high purity selection cuts (section 7.2)
- Tracks need to be associated to the primary vertex: $d_0/\sigma_{d_0} < 3\%$ and $d_z/\sigma_{d_z} < 3\%$
- All tracks need to have a good transverse momentum resolution: $\sigma_{p_T}/p_T < 5\%$

Control plots are presented in figures 9.10 to 9.12, which show basic track-jet distributions obtained from data, and PYTHIA6 Z2 and PYTHIA8 4C Monte Carlo simulations. In general one can see that the simulated distributions describe the detector level data very well. However, the track-jet p_T distributions in figure 9.11 show a systematic discrepancy that increases with momentum. Therefore, an extra weight factor, in addition to the CASTOR energy reweighting (section 9.3.4), will be applied to the MC to improve the description of the data. First, the ratio between the data and PYTHIA6 Z2 (data/PYTHIA6 Z2) is determined as a function of track-jet p_T from figure 9.11. The weight that is applied to the event is then obtained by evaluating this ratio distribution as a function of stable particle level charged-particle jet p_T. Both the CASTOR energy and track-jet p_T weights are finally included in the PYTHIA6 Z2 *Reweighted* distribution.

9.6. Uncorrected detector-level results

We can now measure the energy density ($dE/d\eta$) in CASTOR separately in minimum bias events and in events with a central leading track-jet. The ratio of the energy in events with a leading jet, with respect to minimum bias events is then plotted in bins of leading track-jet p_T. The results at detector level for the three centre-of-mass energies are shown in figure 9.13 and compared to the available detector-level MC predictions. In addition, the energy density at $\sqrt{s} = 0.9$ and 7 TeV, relative to the energy density at $\sqrt{s} = 2.76$ TeV is calculated for both minimum bias events, and for events with a central leading track-jet that has a p_T above 10 GeV/c. This relative energy density measurement at detector level is plotted as a function of $\sqrt{s}$, and again compared to detector level MC predictions. This is shown in figure 9.14, which, for illustration, also shows the absolute energy density measurements.

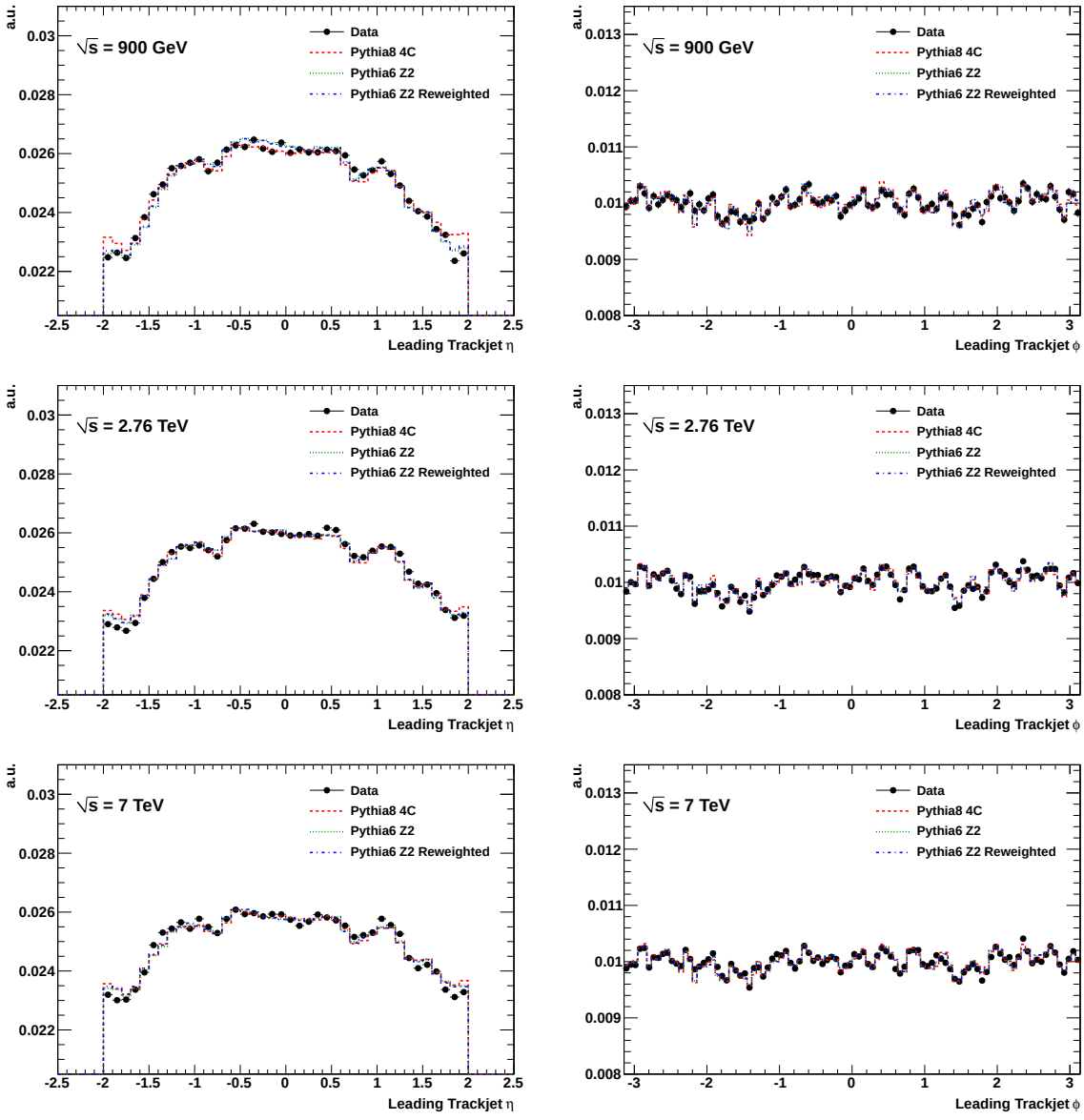

Figure 9.10.: Basic η and ϕ distributions for track-jets at $\sqrt{s}$ = 0.9, 2.76 and 7 TeV as obtained from data and Monte Carlo simulation.

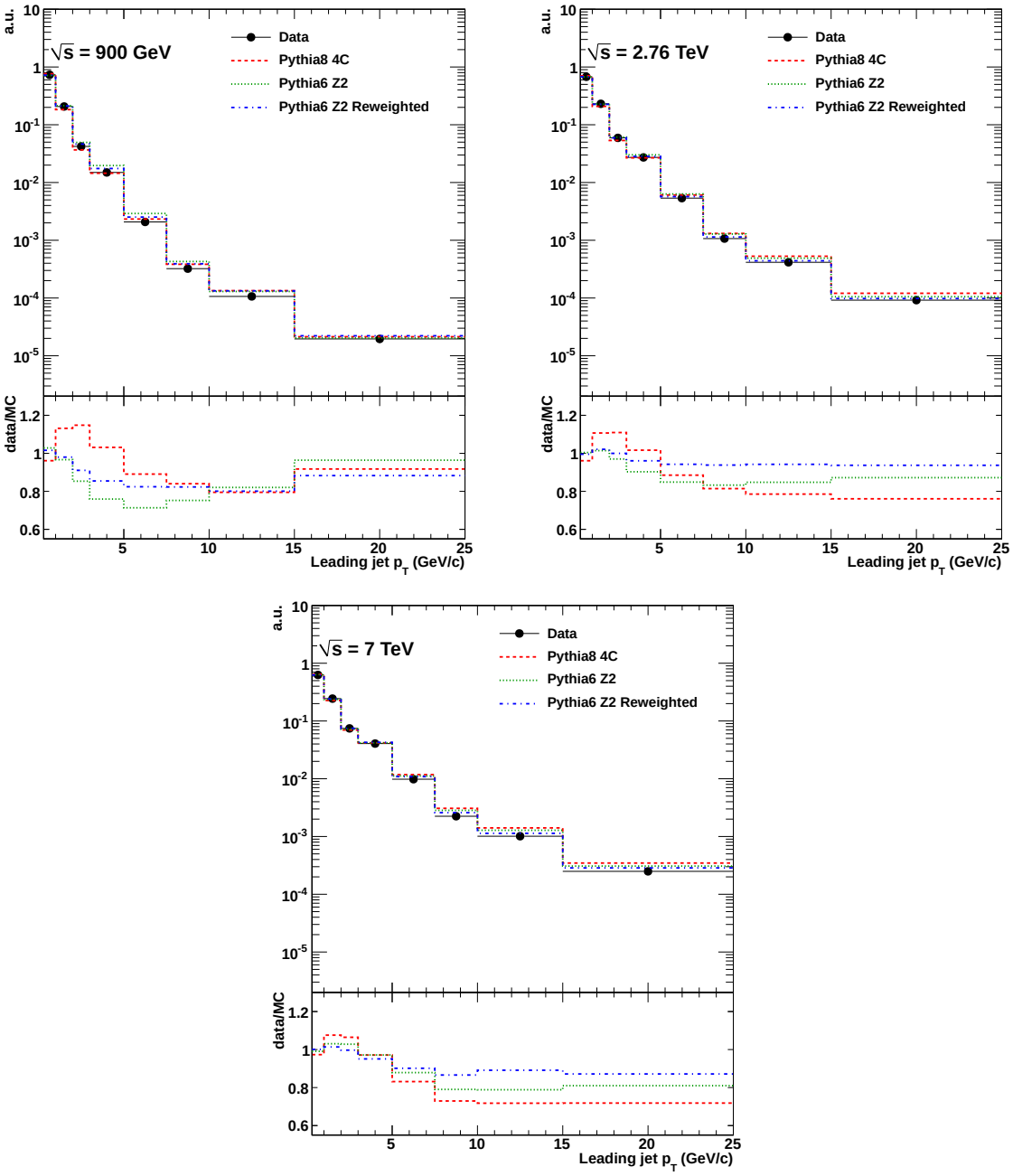

Figure 9.11.: Basic p_T distributions for track-jets at $\sqrt{s} = 0.9$, 2.76 and 7 TeV as obtained from data and Monte Carlo simulation.

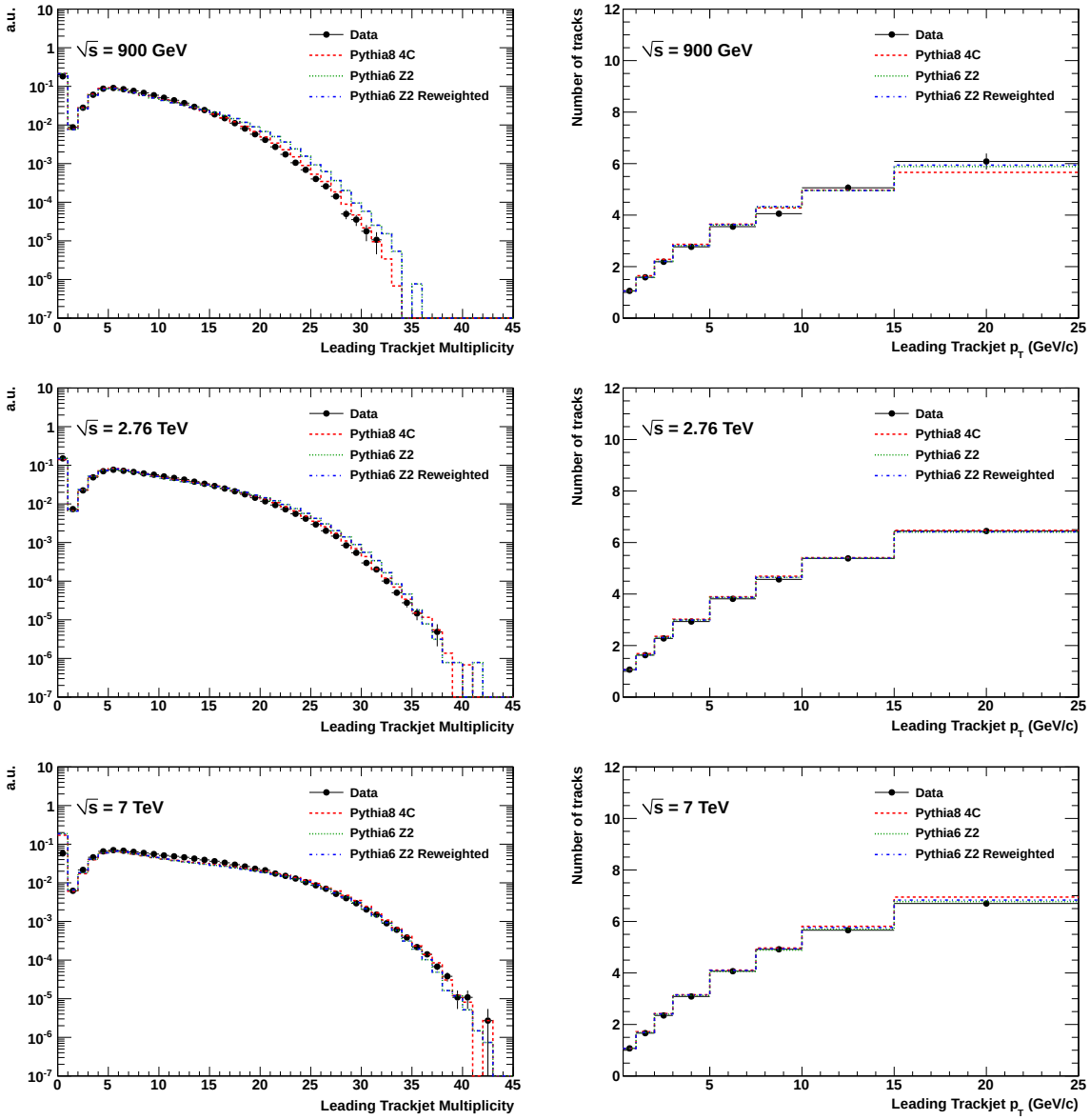

Figure 9.12.: Track-jet multiplicity distributions (left) and track multiplicity per track-jet vs. track-jet p_T (right) at $\sqrt{s} = 0.9$, 2.76 and 7 TeV as obtained from data and Monte Carlo simulation.

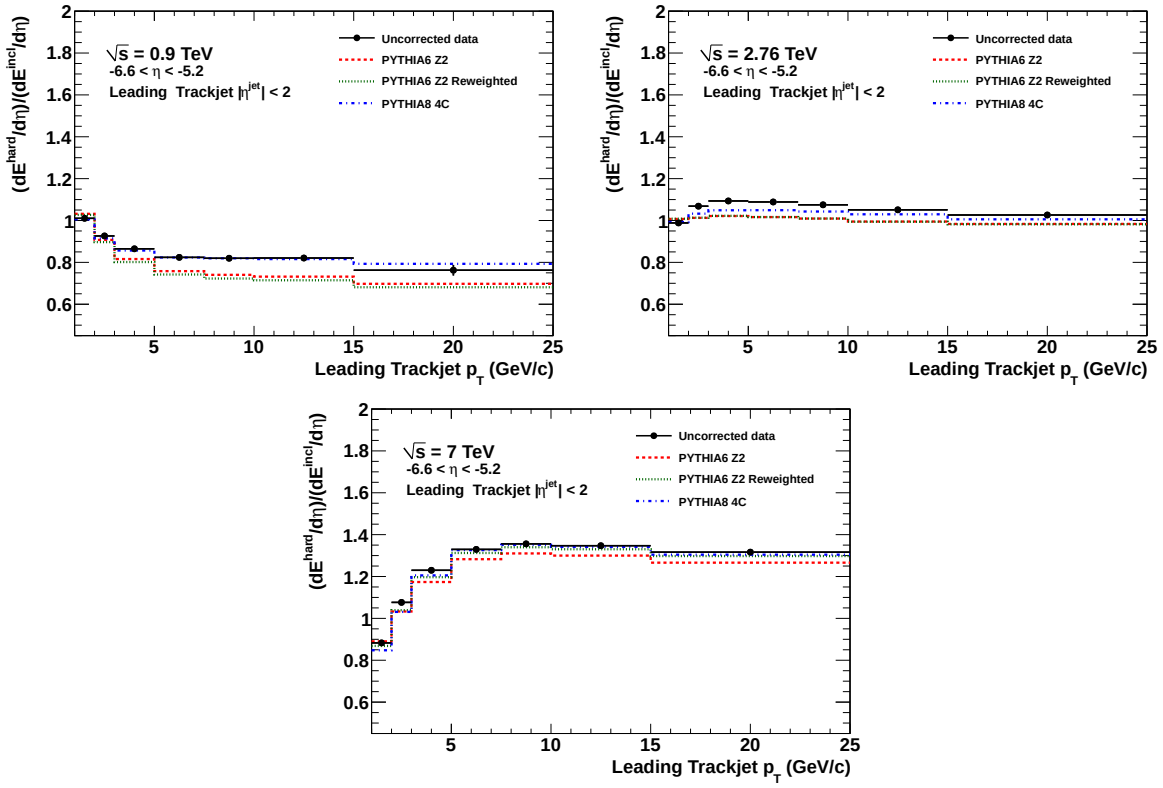

Figure 9.13.: Detector level ratio of $dE/d\eta$ in CASTOR in events with a central leading track-jet, with respect to the energy density in minimum bias events, as a function of the leading track-jet p_T.

In addition to the hard-to-inclusive forward energy ratio, and the relative energy density versus $\sqrt{s}$ presented above we can also look at the relative $\Delta\phi$ profiles of the detector level hard-to-inclusive forward energy ratio, in bins of leading track-jet p_T. We encountered such plots for the first time in section 8.1 (figure 8.1) [110], where they showed the average scalar sum of the transverse momenta of charged particles at central pseudorapidity, plotted as a function of the azimuthal angle difference $\Delta\phi$ relative to the leading track. Here we can construct a similar type of plot, by decomposing the hard-to-inclusive forward energy ratio as a function of the $\Delta\phi$ relative to the central leading track-jet. Figure 9.15 shows such profiles for data and MC, at $\sqrt{s} = 7$ TeV, for each track-jet p_T bin. Since we are looking at detector level quantities, the $\Delta\phi$ is expressed in sector units. With CASTOR having a 16-fold segmentation in ϕ, one sector unit represents 22.5°. If we compare figure 9.15 with figure 8.1 we clearly see that our $\Delta\phi$ profile is much more flat, which implies that the azimuthal plane is indeed completely dominated by the underlying event as expected. The central peak in the toward region that originates from the hard scatter is clearly not present, which is expected since the leading jet is asked to be within $|\eta| < 2$. The away region does have a slightly higher response, which indicates that the recoil products of the hard scatter can enter the CASTOR pseudorapidity range in a small fraction of the events. Furthermore, the data (black) can be described quite well by the PYTHIA6 Z2 Reweighted (red) simulation. It

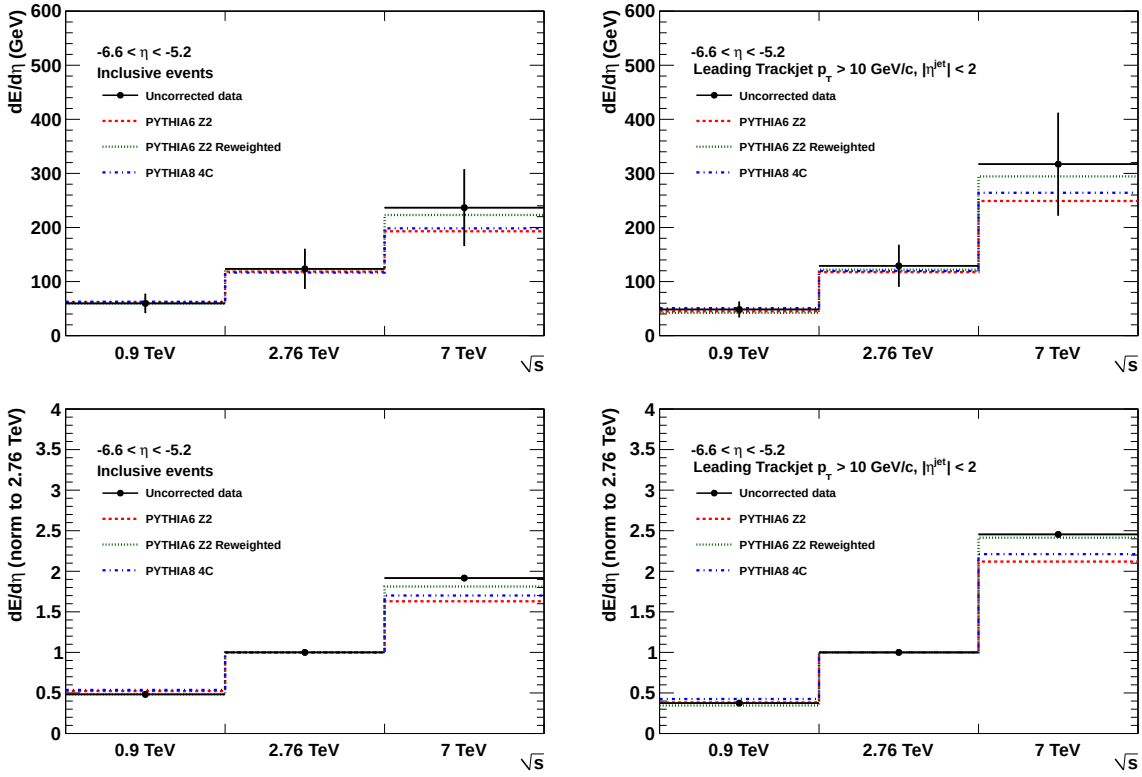

Figure 9.14.: Detector level $dE/d\eta$ in CASTOR in minimum bias events (left) and in events with a central leading track-jet $p_T > 10$ GeV/c (right) as a function of $\sqrt{s}$. The absolute energy density (top) and normalised, at $\sqrt{s} = 2.76$ TeV, energy density (bottom) are shown.

is interesting to note that, in data, at high values of leading track-jet p_T, the depletion in the toward region gets less pronounced, with even a small hint at an increase of the ratio at the leading track-jet position in bin $15 < p_T < 25$ GeV/c that is not visible in the MC model. However, the statistical errors are unfortunately too high to conclude and therefore we will not consider this set of plots onwards for further corrections.

9.7. Data correction

We will now correct the results for various detector effects, including trigger efficiency, event selection, energy reconstruction in CASTOR and migrations in track-jet p_T. Except for the trigger efficiency correction, which is extracted directly from data, corrected results are obtained using a simulation of the CMS detector based on the GEANT4 toolkit. For the CASTOR simulation in particular, a shower library is used that contains a set of pre-simulated showers for a wide range in energy, from which the CASTOR response is retrieved by interpolation (see section 7.3).

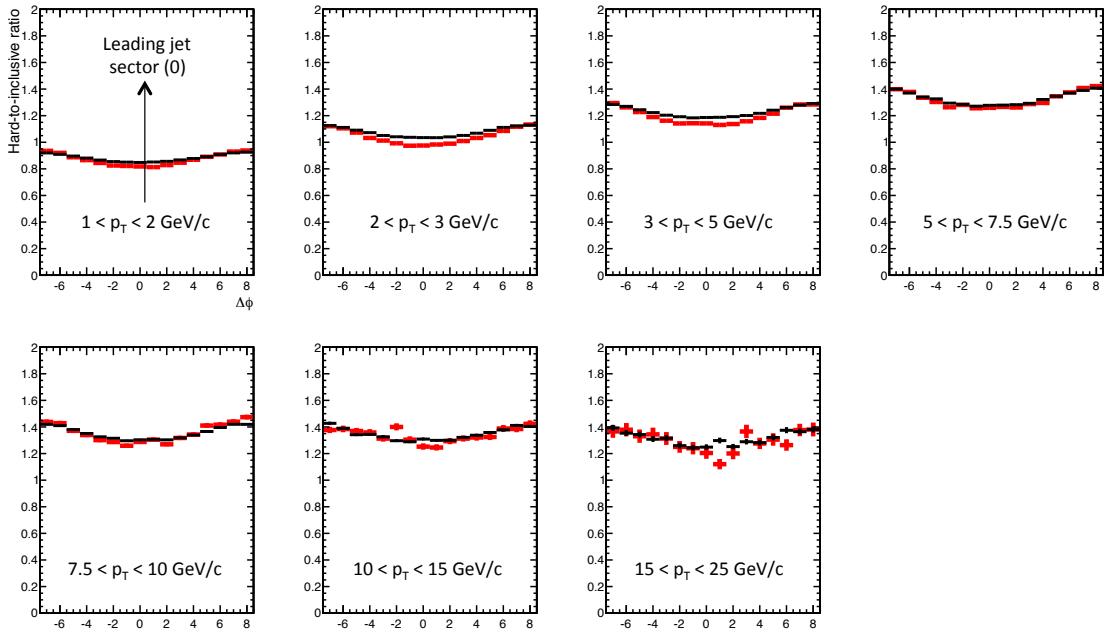

Figure 9.15.: Detector level hard-to-inclusive forward energy ratio at $\sqrt{s} = 7$ TeV plotted as a function of the azimuthal angle difference $\Delta\phi$ relative to the leading track-jet. The $\Delta\phi$ profiles are shown for all leading track-jet p_T bins. The data are shown in black, and compared to a PYTHIA6 Z2 Reweighted simulation in red. The azimuthal angle difference is expressed in sector units (22.5°).

9.7.1. Particle level definition

The trigger conditions and event selection criteria outlined in section 9.4 are chosen such that a sample dominated by nondiffractive events is obtained. Some high-mass diffractive dissociation events, covering the full detector but having a large rapidity gap outside the acceptance, will however remain in the data sample and a precise definition of the hadron level phase space for which corrected results are presented is needed and obtained as follows.

The collection of stable ($\tau > 10^{-12}$ s) final state particles is divided into two systems, X and Y, using the mean rapidity of the two particles separated by the largest rapidity gap in the event. All particles to the negative side of the largest gap are assigned to the system X, while the particles at the positive side are assigned to the system Y [134]. The invariant mass, $M_{\mathrm{X,Y}}$, of each system is then calculated using the four-momenta of the individual particles and their ratio to the total centre-of-mass energy, ξ_{X}, ξ_{Y} and ξ_{DD}, is then defined as follows:

$$\xi_{\mathrm{X}} = \frac{M_{\mathrm{X}}^2}{s}, \qquad \xi_{\mathrm{Y}} = \frac{M_{\mathrm{Y}}^2}{s}, \qquad \xi_{\mathrm{DD}} = \frac{M_{\mathrm{X}}^2 M_{\mathrm{Y}}^2}{m_p^2\, s}, \tag{9.1}$$

$\sqrt{s}$ (TeV)	$\xi_{\mathrm{X}}^{\mathrm{min}}$	$\xi_{\mathrm{Y}}^{\mathrm{min}}$	$\xi_{\mathrm{DD}}^{\mathrm{min}}$	ϵ	$f_{\{\xi<\xi^{\mathrm{min}}\}}$	ϵ_{max}
0.9	0.1	0.4	0.5	76%	10.4%	80−90%
2.76	0.07	0.2	0.5	85%	7.7%	94%
7	0.04	0.1	0.5	87%	5.5%	95%

Table 9.2.: Acceptance limits on ξ_{X}, ξ_{Y} and ξ_{DD} used to define the phase space domain for which corrected results are presented. These limits at the particle level correspond to the phase space selected by detector level conditions. The efficiency ϵ, i.e. the fraction of events fulfilling the particle level condition that are selected at the detector level, and $f_{\{\xi<\xi^{\mathrm{min}}\}}$, defined as the fraction of events selected at detector level that do *not* fulfil the particle level condition, are also given. Finally, ϵ_{max} is the maximal selection efficiency reached at high ξ.

with m_p the proton rest mass. These variables are well-defined for any type of events, and in the case of large rapidity gap events, they are related the size of the rapidity gap via $\Delta\eta = \ln 1/\xi$. The phase space that remains for events with a large rapidity gap, after applying the detector cuts, can then be quantified at the particle level by setting proper limits on ξ_{X}, ξ_{Y} and ξ_{DD}. These acceptance limits are obtained from a dedicated study using fully simulated events generated by Pythia6 Z2 and are summarised in table 9.2. An event is then selected at the particle level if *any* of ξ_{X}, ξ_{Y} or ξ_{DD} is larger than the respective limit:

$$\text{event selected at particle level} \quad \Longleftrightarrow \quad \xi_{\mathrm{X}} > \xi_{\mathrm{X}}^{\mathrm{min}} \ \vee \ \xi_{\mathrm{Y}} > \xi_{\mathrm{Y}}^{\mathrm{min}} \ \vee \ \xi_{\mathrm{DD}} > \xi_{\mathrm{DD}}^{\mathrm{min}}. \quad (9.2)$$

Because the detector acceptance changes with centre-of-mass energy, different thresholds are used at $\sqrt{s} = 0.9$ TeV, 2.76 TeV and 7 TeV. At all energies however, the selected phase space domain ensures that there are no large gaps inside the detector acceptance. Furthermore, adapting the selected phase space dynamically to the detector acceptance results in a smaller correction of the data, and thus also in a smaller model dependence of the correction factors. Using a ξ selection optimised for $\sqrt{s} = 7$ TeV, at $\sqrt{s} = 0.9$ TeV is equivalent to a mismatch in η of about 1 to 1.5 units. This would result in an increase of the correction factors by $\sim$3%, and a decrease in the efficiency and fake rate of $\sim$5%. Finally, using Pythia8 4C to determine the ideal ξ selection does not yield any significant difference in the cut values.

Figure 9.16 shows a scatter plot of ξ_{X} versus ξ_{Y} at particle level for all events, and for events selected at detector level, for all centre-of-mass energies. It can be seen that only events with high values of ξ_{X}, ξ_{Y} or ξ_{DD} are selected by the detector cuts. The lines in the figures indicate the position of the particle level ξ cuts, which correspond to the detector acceptance. In order to estimate these cut values, the event sample was in fact split in three subsamples. First, two distinct samples were constructed: one with the centre of the largest gap outside the negative side of the detector acceptance ($\eta_{\mathrm{gap}} < -6.6$), and one with the gap centre outside the positive side ($\eta_{\mathrm{gap}} > 5$). These samples were then

used to determine $\xi_{\mathrm{Y}}^{\mathrm{min}}$ and $\xi_{\mathrm{X}}^{\mathrm{min}}$, respectively, by requiring:

$$\epsilon_{\mathrm{max}} \times \int_{\xi_{\mathrm{X,Y}}^{\mathrm{min}}}^{1} N_{\mathrm{evt}}^{\mathrm{all}}(\xi_{\mathrm{X,Y}})\, d\xi_{\mathrm{X,Y}} = \int_{0}^{1} N_{\mathrm{evt}}^{\mathrm{sel}}(\xi_{\mathrm{X,Y}})\, d\xi_{\mathrm{X,Y}}, \tag{9.3}$$

with ϵ_{max} the maximal selection efficiency reached at high $\xi_{\mathrm{X,Y}}$, $N_{\mathrm{evt}}^{\mathrm{all}}(\xi_{\mathrm{X,Y}})$ the total number of events in a $\xi_{\mathrm{X,Y}}$ bin, and $N_{\mathrm{evt}}^{\mathrm{sel}}(\xi_{\mathrm{X,Y}})$ the number of events in a $\xi_{\mathrm{X,Y}}$ bin that passed the detector selection criteria. The resulting thresholds for ξ_{X} and ξ_{Y} are asymmetric because the CMS detector does not cover the same range in pseudorapidity on the positive and negative side. Finally, the sample of events that do not fulfil the ξ_{X} or ξ_{Y} criteria is used to determine the threshold $\xi_{\mathrm{DD}}^{\mathrm{min}}$ by following the same procedure as for $\xi_{\mathrm{X}}^{\mathrm{min}}$ and $\xi_{\mathrm{Y}}^{\mathrm{min}}$.

The top rows of figures 9.17, 9.18 and 9.19 show the ξ distributions, for all and selected events for the 3 subsamples mentioned above, for the 3 different centre-of-mass energies. The middle rows show the selection efficiency as a function of ξ, obtained as the ratio of selected to all event distributions shown in the top-row histograms. The left columns present the event samples with the largest gap to the positive side of the detector acceptance. In this sample, the system X has to extend over the full detector, including HF+, in order to be selected at detector level. The efficiency is therefore large at large M_{X} and thus large ξ_{X}. The middle columns present the event sample with the gap to the minus side of the detector acceptance. Now, the Y system has to extend over the full detector, including CASTOR, and thus a high efficiency is again reached for large M_{Y} and ξ_{Y}. Finally, the right columns show the events that are not kept by the already obtained ξ_{X} and ξ_{Y} criteria. These have a rapidity gap with the centre inside the detector acceptance. Since the detector level requirement to have activity in the tracker, HF calorimeters and CASTOR calorimeter, does not allow large gaps, a high efficiency is reached for large ξ_{DD}. Indeed, this variable is related to the gap size as $\Delta y \sim \ln 1/\xi_{\mathrm{DD}}$. The bottom rows of figures 9.17, 9.18 and 9.19 show the left hand side of equation 9.3 as a function of ξ^{min}, together with the number of selected events at detector level, integrated over all ξ. The cut values are then determined by looking at which ξ^{min} the cumulative number of events becomes equal to the number of selected events at detector level, indicated by the yellow lines.

With the above introduced ξ cuts we can thus translate the detector level minimum bias selection to a particle level inclusive event selection. The one item that remains to be translated, is the definition of the central leading track-jet. This is fortunately rather straight forward: similarly to reconstructed track-jets, jets at particle level are obtained by running an anti-k_T jet algorithm with $R = 0.5$ on stable ($\tau > 10^{-12}s$) charged particles with a $p_T > 300$ MeV/c and $|\eta| < 2.5$. The leading charged-particle level jets are then selected by requiring $p_T^{\mathrm{jet}} > 1$ GeV/c and $|\eta^{\mathrm{jet}}| < 2$.

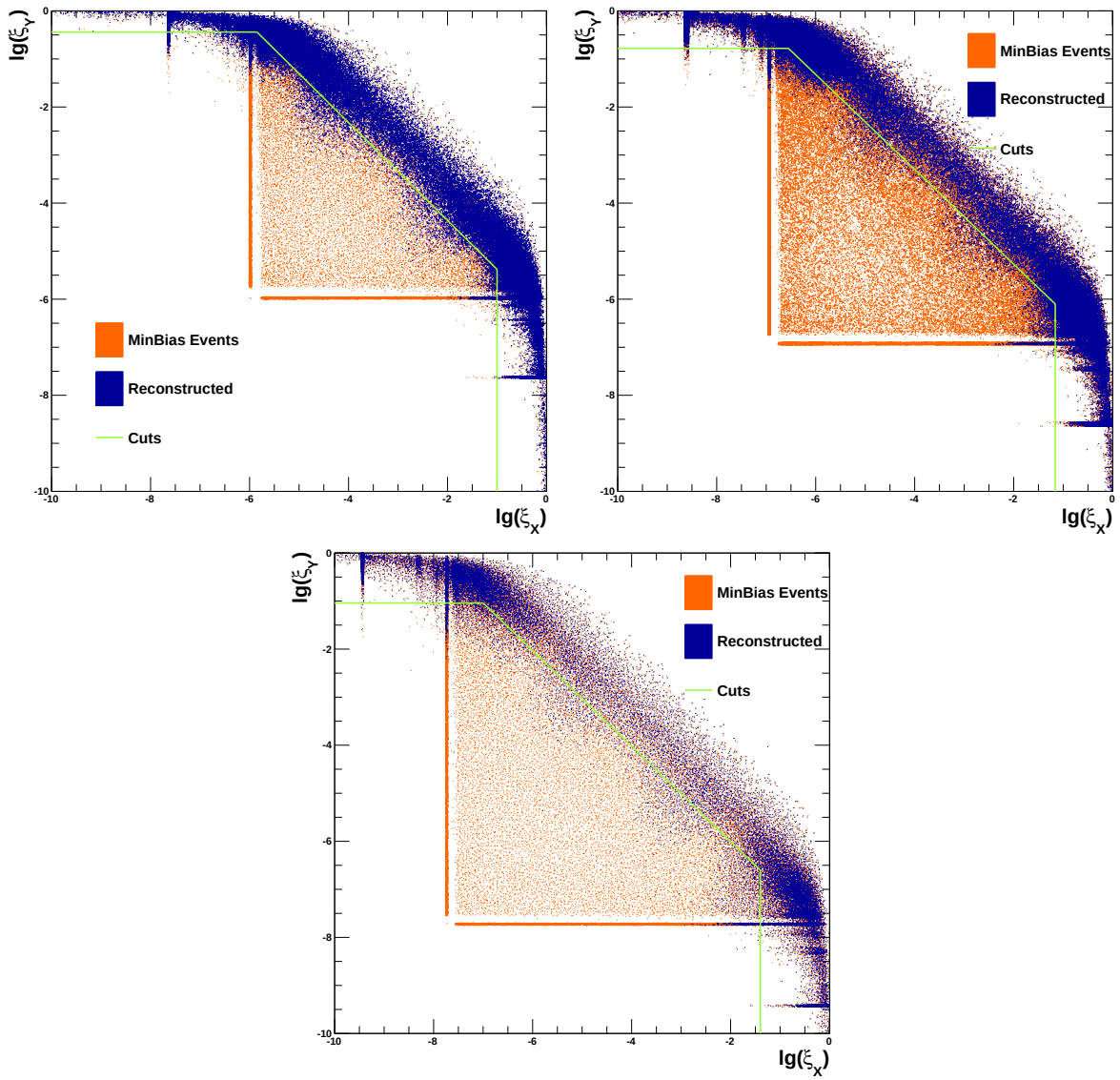

Figure 9.16.: Scatter plots of $\log_{10}(\xi_{\mathrm{Y}})$ vs. $\log_{10}(\xi_{\mathrm{X}})$ for all generated events (orange) and for generated events selected at detector level (blue) for $\sqrt{s} = 0.9$ (left), 2.76 (right) and 7 TeV (bottom). Single diffractive dissociation events have a ξ_{X} or ξ_{Y} value equal to m_p^2/s ($\approx 10^{-7.7}$ at $\sqrt{s} = 7$ TeV), while double diffractive dissociation and nondiffractive events have ξ_{X} and ξ_{Y} values ranging from 0 to 1. The green lines indicate the particle level cuts listed in table 9.2. At the particle level, all events to the top and to the right of the green lines are selected.

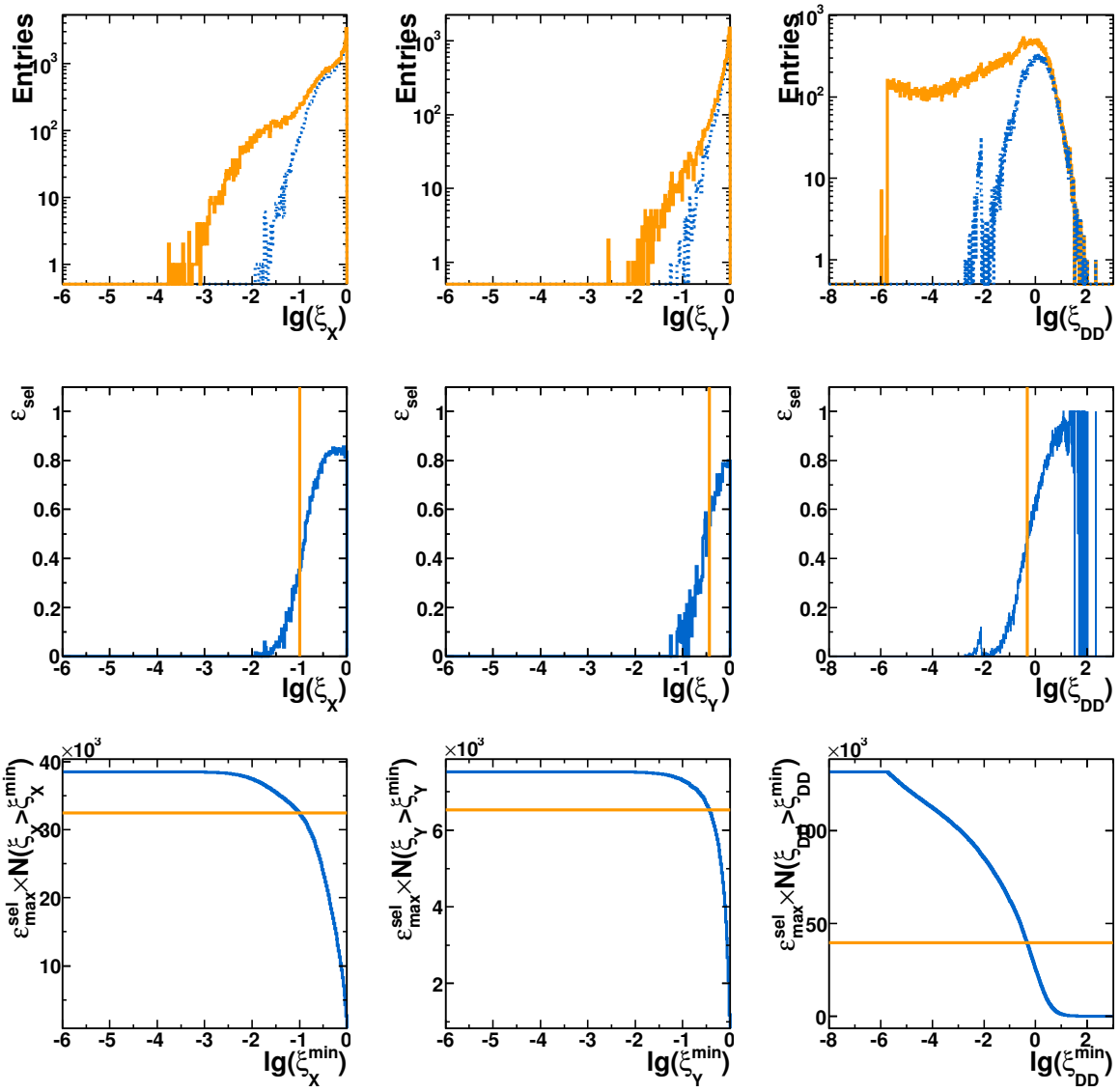

Figure 9.17.: The ξ acceptance study at $\sqrt{s} = 0.9$ TeV. Top row: ξ_{X}, ξ_{Y} and ξ_{DD} distributions, for all events (orange) and selected events that pass the offline reconstruction cuts (blue dashed), in each of the 3 subsamples defined in the text. Middle row: selection efficiencies as a function of ξ. The orange line shows the position of the cut. Bottom row: cumulative ξ distributions. In this case, the orange line indicate the total number of events selected at detector level.

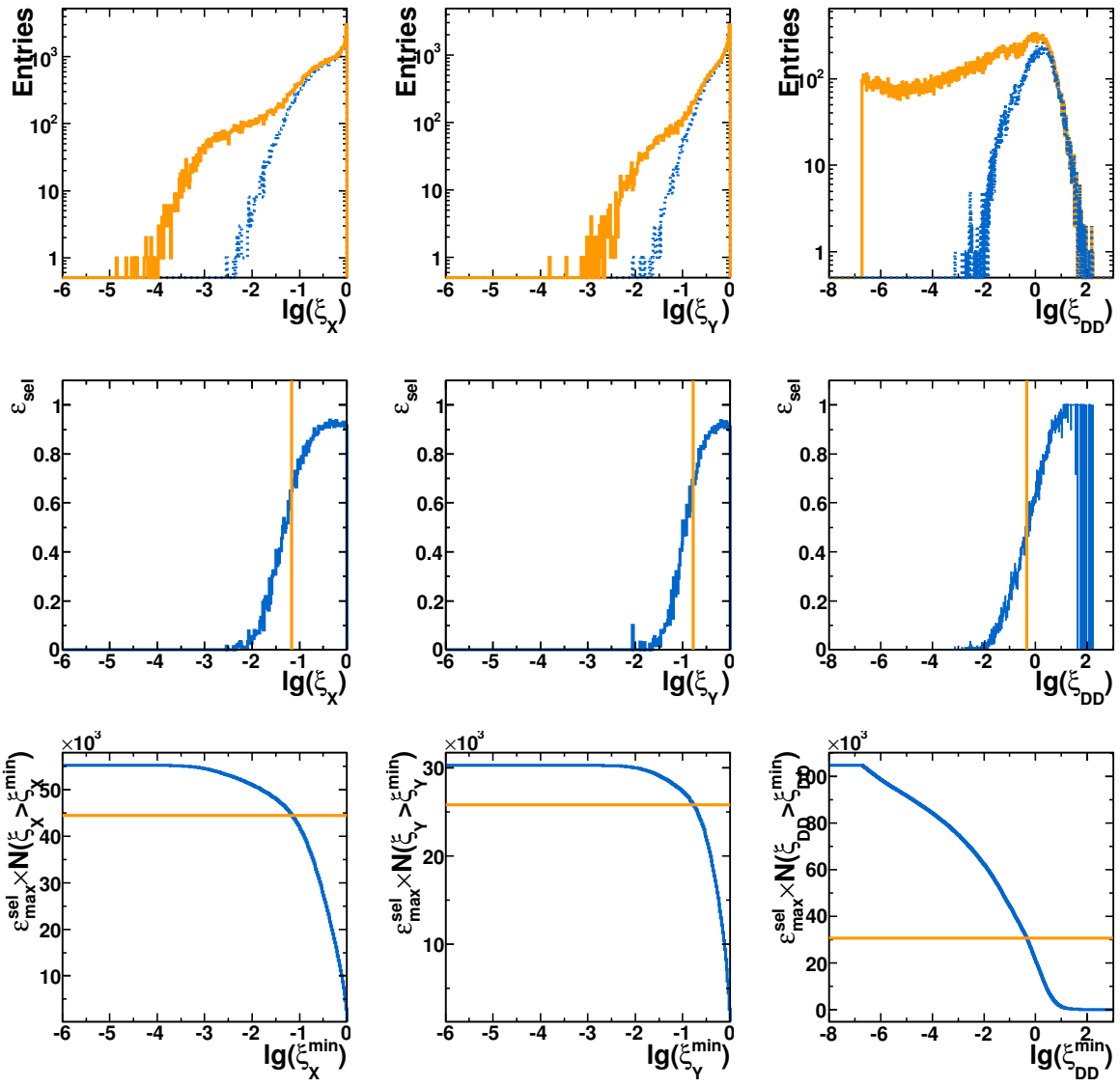

Figure 9.18.: The ξ acceptance study at $\sqrt{s} = 2.76$ TeV. Similar plots are shown as in figure 9.17.

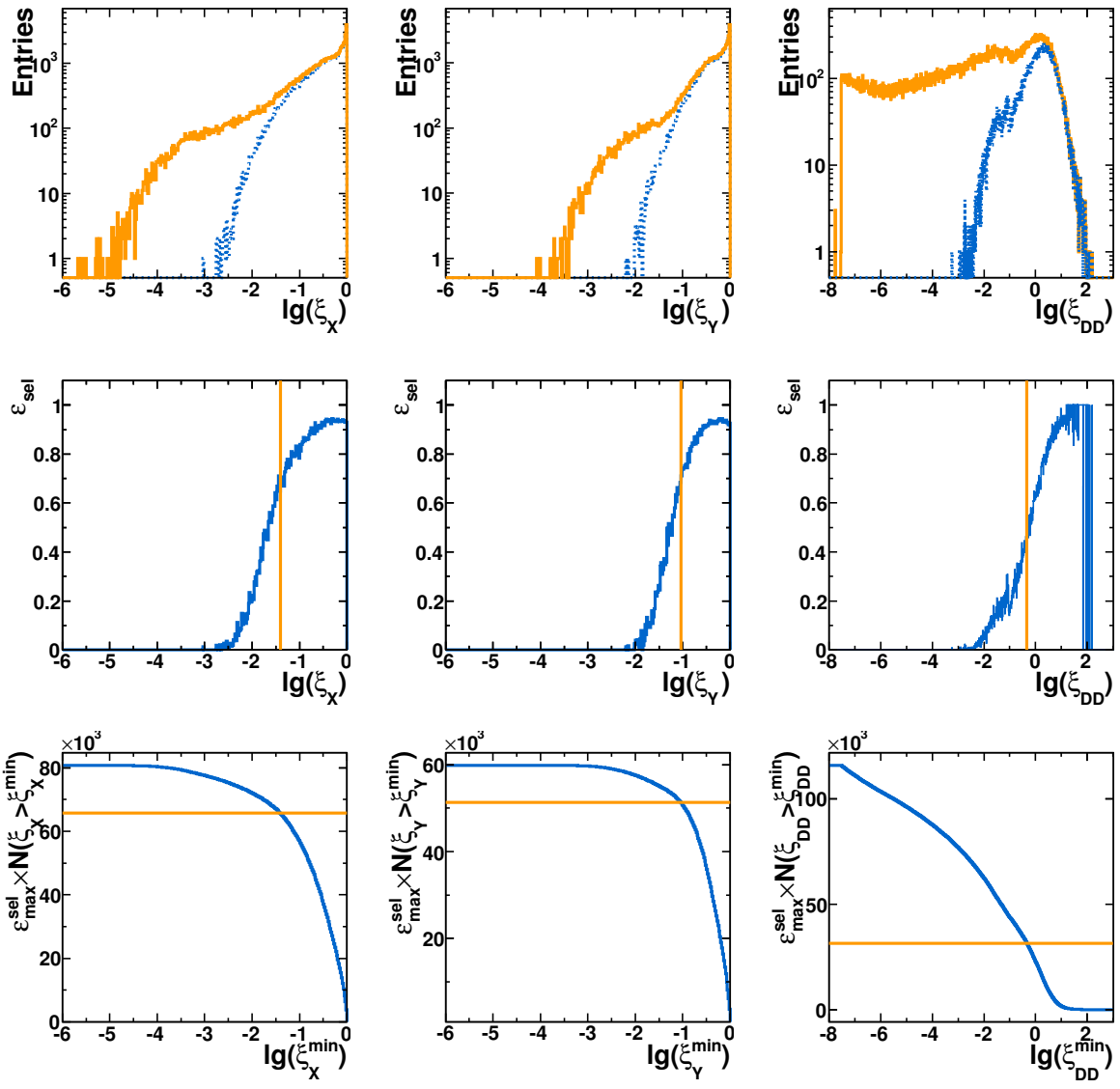

Figure 9.19.: The ξ acceptance study at $\sqrt{s} = 7$ TeV. Similar plots are shown as in figure 9.17.

9.7.2. Trigger efficiency

The trigger efficiency has been analysed using the zero-bias samples, where the data are triggered by the sole requirement of having filled bunches crossing each other in the CMS interaction point. The efficiency of the trigger is then determined as the fraction of offline selected zero-bias events that have also been triggered. As such, the overall efficiency for triggering on the coincidence of a hit in both BSC1 detectors is found to be 96.5% (98.4%) at $\sqrt{s} = 0.9$ (7) TeV. For $\sqrt{s} = 2.76$ TeV, where a trigger based on a hit in *any* BSC is used, the overall trigger efficiency is found to be 99.9%, and thus no further correction is applied.

To take the inefficiencies at $\sqrt{s} = 0.9$ and 7 TeV into account a correction is derived as follows. First the evolution of the trigger efficiency is plotted as a function of the energy product measured by the HF calorimeters in the pseudorapidity range of BSC1, as this quantity corresponds to the notion of a simultaneous hit in both BSC's. This is shown in figure 9.20. It is clear that the minimum bias trigger is almost fully efficient, except for low HF energy deposits where a correction is needed. We then fit the trigger efficiencies with a Fermi function ($a/(\exp(\frac{x-b}{c})+1)$, with a, b and c the fit parameters) to parametrize their behaviour. This information is then used to compute a weight, equal to the inverse of this parametrized efficiency, which is applied to each observed event in the data sample. The results of this reweighting procedure are presented in figure 9.21, which shows the trigger efficiency as a function of leading track-jet p_T and as a function of the energy reconstructed in CASTOR. Similar trigger inefficiencies as observed in figure 9.20 are present at low energies in CASTOR and low track-jet p_T before the reweighting is applied (black). However, after the application of the reweighting procedure (red) the trigger efficiencies are compatible with 100%, which implies that the derived weights are able to fully correct the trigger efficiency. This is possible due to the existing correlation between the energy in HF, and the energy in CASTOR or track-jet p_T. The overall effect of the correction for trigger efficiency on the final results is however smaller than the statistical uncertainty on the data.

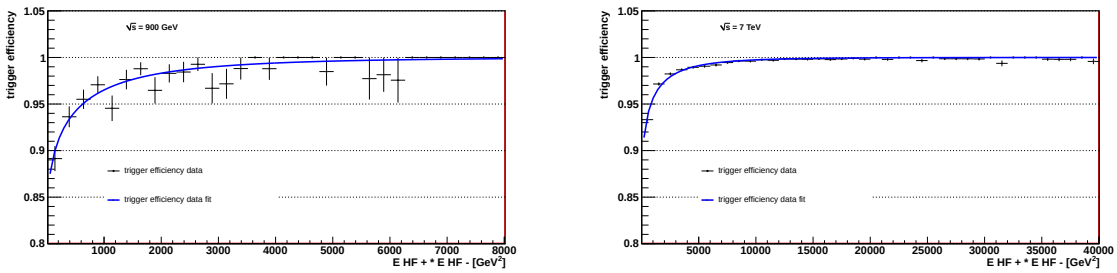

Figure 9.20.: The trigger efficiency as obtained from zero-bias data samples at $\sqrt{s} = 0.9$ (left) and 7 TeV (right). The efficiency is plotted as a function of the product of the energy measured by the HF calorimeters ($E_{HF+} * E_{HF-}$), and fitted with a Fermi function (see text).

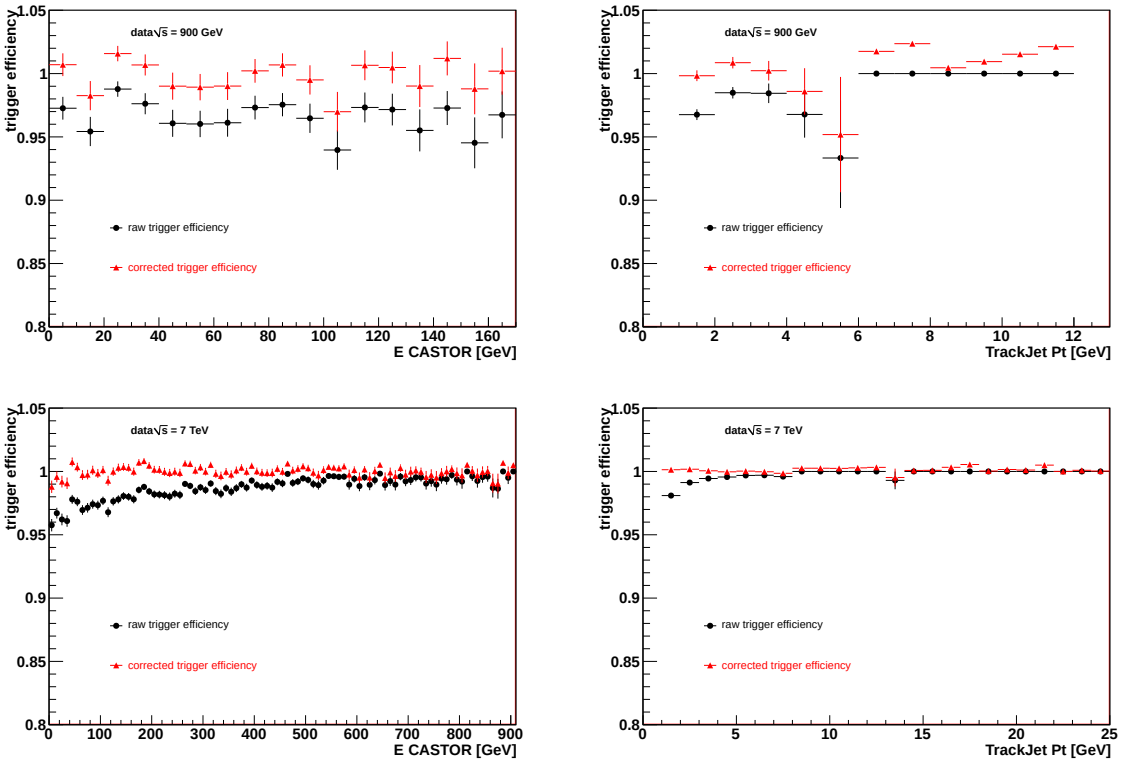

Figure 9.21.: The trigger efficiency, before (black) and after (red) the reweighting procedure. As a function of the energy measured in CASTOR (left), and as a function of leading track-jet p_T (right).

9.7.3. Correction of the CASTOR energy measurement

The final correction factors that will be used to correct the detector level results to particle level are shown in figure 9.22 for the hard-to-inclusive forward energy ratio versus leading track-jet p_T, and in figure 9.23 for the relative energy densities versus $\sqrt{s}$. The correction factors for the hard-to-inclusive ratio versus track-jet p_T can be decomposed into a "CASTOR correction factor", and a "track-jet p_T correction factor". The former takes care of the non-compensating behaviour of the CASTOR calorimeter, while the latter is mostly due to track-jet p_T migrations. This correction will be discussed in the next section.

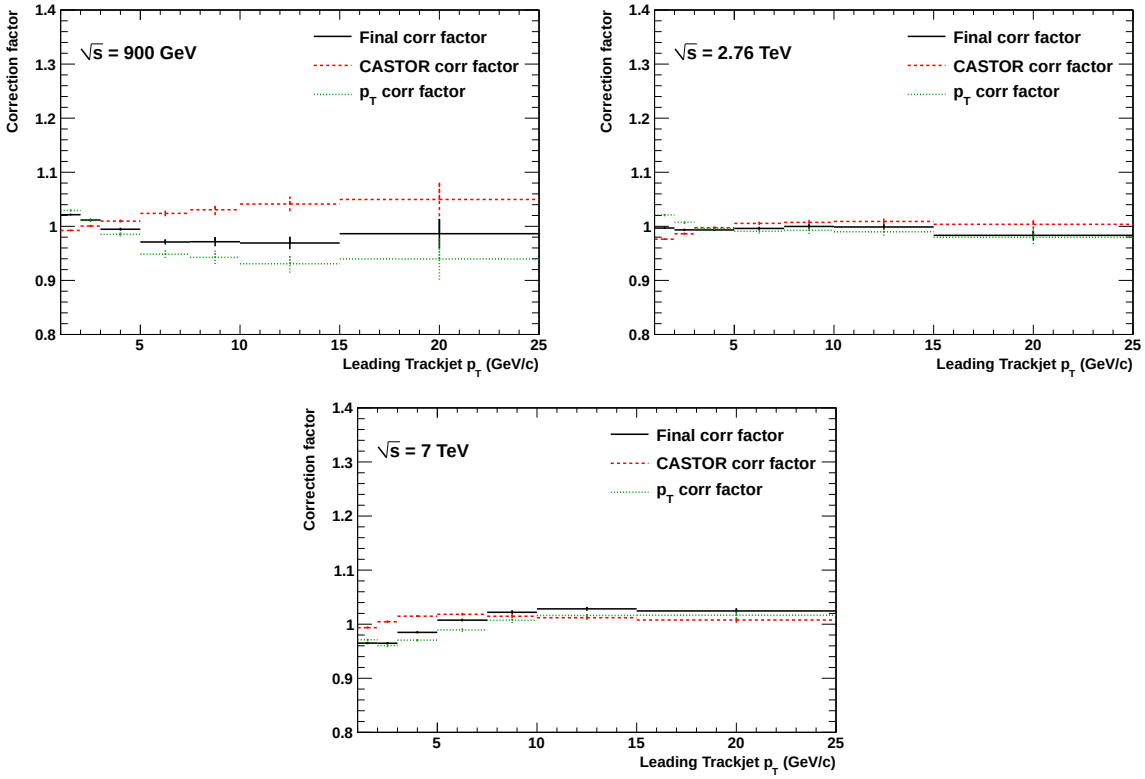

Figure 9.22.: Correction factors applied to the hard-to-inclusive forward energy ratios as a function of central leading track-jet p_T. The final correction factors are shown, as well as the decomposition in correction factors for the CASTOR energy ratio measurement and correction factors for track-jet p_T migrations.

The results presented in this analysis are all based on *relative* measurements of energy reconstructed in CASTOR, and by measuring such energy *ratios*, many systematic uncertainties, in particular the absolute calibration uncertainty, cancel. However, due to the non-compensating nature of the CASTOR calorimeter, the response may vary with changing particle composition and energy spectrum. The measured energy ratio is therefore corrected by a factor that depends on the measured central leading track-jet p_T. This CASTOR correction factor is obtained from a simulation of the PYTHIA6 Z2 MC model, which is reweighted as a function of charged-particle jet p_T and as a function of

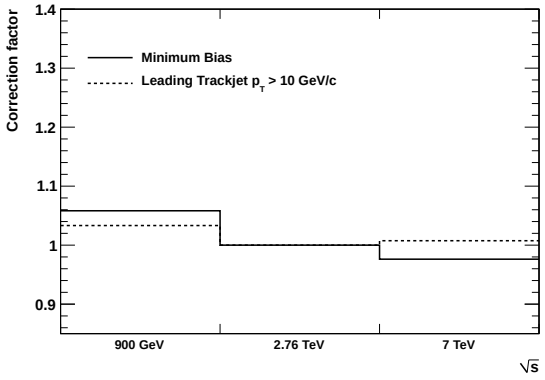

Figure 9.23.: The final correction factors applied to the relative energy density measurements as a function of $\sqrt{s}$, normalised to $\sqrt{s} = 2.76$ TeV

the total energy in CASTOR in order to obtain a better description of the track-jet p_T evolution and the CASTOR total energy distribution observed in data. The correction is indeed driven by the non-compensating nature of the calorimeter: e.g. at $\sqrt{s} = 7$ TeV, the energy fraction carried by electromagnetic particles ($e^{\pm}$, γ) decreases from 28% to 24% when increasing the track-jet p_T from zero (minimum bias) to 20 GeV/c, while the total energy increases from 512 GeV to 650 GeV. Using a π/e factor of ≈ 0.5 as measured in the test beam setup [88], this results in corrections of the order of $\sim 3\%$ at high track-jet p_T, as seen in figure 9.22.

Figure 9.24 shows the correlation between the detector and hadron level hard-to-inclusive energy ratios per central leading track-jet p_T bin, for the three different centre-of-mass energies. From this information we can then obtain the p_T-dependent CASTOR correction factors of figure 9.22 by calculating the double ratio of the mean detector level and hadron level ratios, defined as:

$$CF_{\mathrm{CASTOR}} = \frac{\langle E^{\mathrm{had}}_{\mathrm{CASTOR}}(p_T^{\mathrm{det}})\rangle / \langle E^{\mathrm{had}}_{\mathrm{CASTOR}}(all)\rangle}{\langle E^{\mathrm{det}}_{\mathrm{CASTOR}}(p_T^{\mathrm{det}})\rangle / \langle E^{\mathrm{det}}_{\mathrm{CASTOR}}(all)\rangle}, \tag{9.4}$$

with $E^{\mathrm{had}}_{\mathrm{CASTOR}}(p_T^{\mathrm{det}})$ ($E^{\mathrm{det}}_{\mathrm{CASTOR}}(p_T^{\mathrm{det}})$) the energy measured in CASTOR at particle (detector) level for events with a central leading track-jet with reconstructed transverse momentum p_T^{det}, and $E^{\mathrm{had}}_{\mathrm{CASTOR}}(all)$ ($E^{\mathrm{det}}_{\mathrm{CASTOR}}(all)$) the particle (detector) level energy in CASTOR for inclusive events.

9.7.4. Correction for migrations in track-jet p_T

A further bin-by-bin correction is applied to account for possible migrations in track-jet p_T. These are the track-jet p_T correction factors we mentioned before, and are shown in

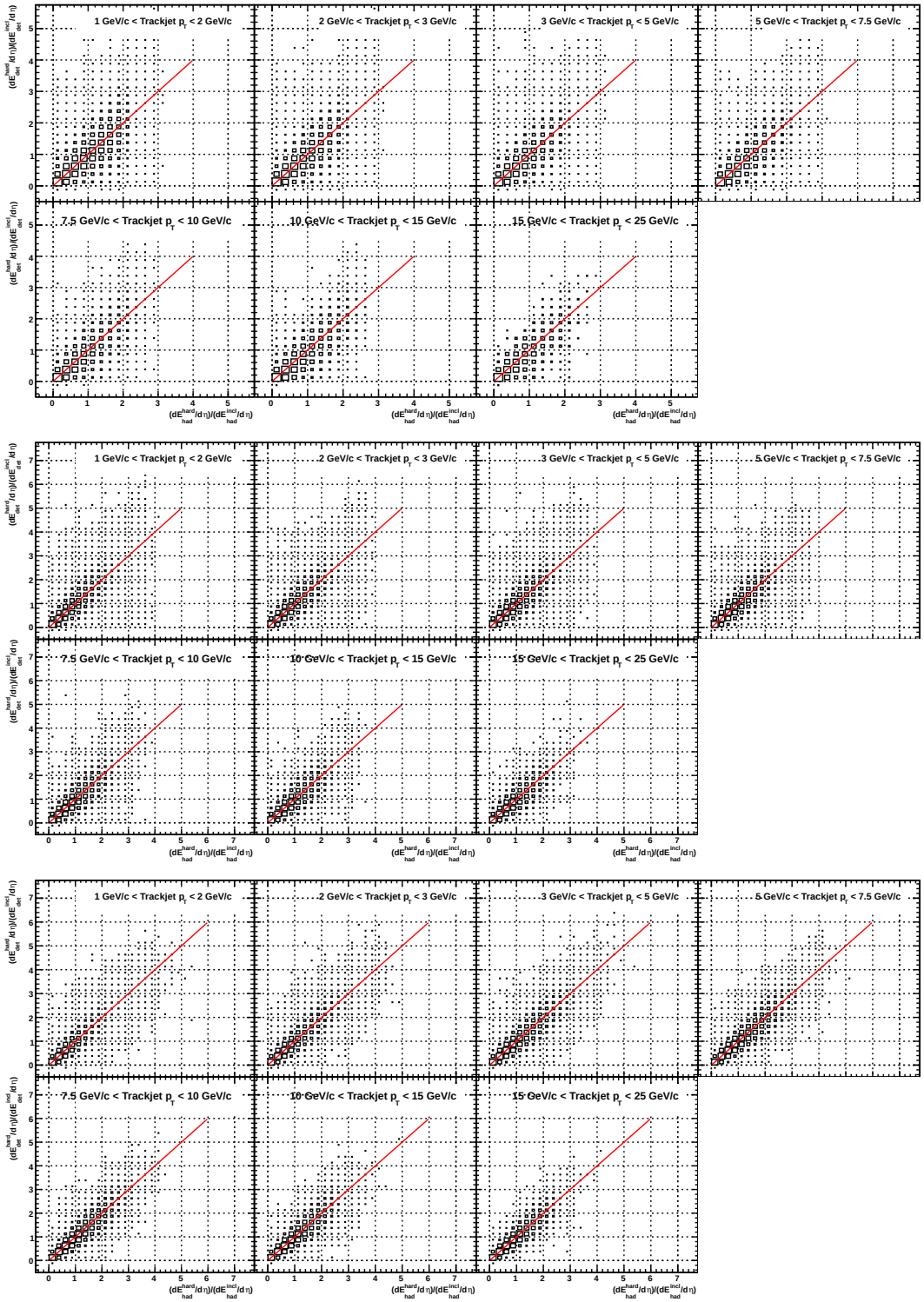

Figure 9.24.: Detector versus particle level hard-to-inclusive forward energy ratio in leading track-jet p_T bins at $\sqrt{s} = 0.9$ (top), 2.76 (middle) and 7 TeV (bottom).

figure 9.22. They are calculated as follows:

$$CF_{\text{track-jet}} = \frac{\langle E^{\text{had}}_{\text{CASTOR}}(p_T^{\text{had}})\rangle / \langle E^{\text{had}}_{\text{CASTOR}}(all)\rangle}{\langle E^{\text{had}}_{\text{CASTOR}}(p_T^{\text{det}})\rangle / \langle E^{\text{had}}_{\text{CASTOR}}(all)\rangle}, \tag{9.5}$$

with $E^{\text{had}}_{\text{CASTOR}}(p_T^{\text{had}})$ the particle level energy deposited in CASTOR for events with a central charged-particle jet with transverse momentum p_T^{had}. These correction factors are due to the limited track-jet reconstruction performance of the detector, which is illustrated in figure 9.25 that shows the distribution of the ratio of detector to charged-particle level jet p_T. The distributions peak at unity, showing that track-jets are well calibrated, but the presence of tails indicates a limitation in reconstruction and resolution. Indeed, it can happen that a charged-particle level jet is not fully reconstructed because a fraction of the tracks can be missed by the reconstruction or jet algorithms, yielding a lower track-jet p_T than the true charged-particle jet p_T. These tails increase for smaller values of p_T and are responsible for migrations in track-jet p_T.

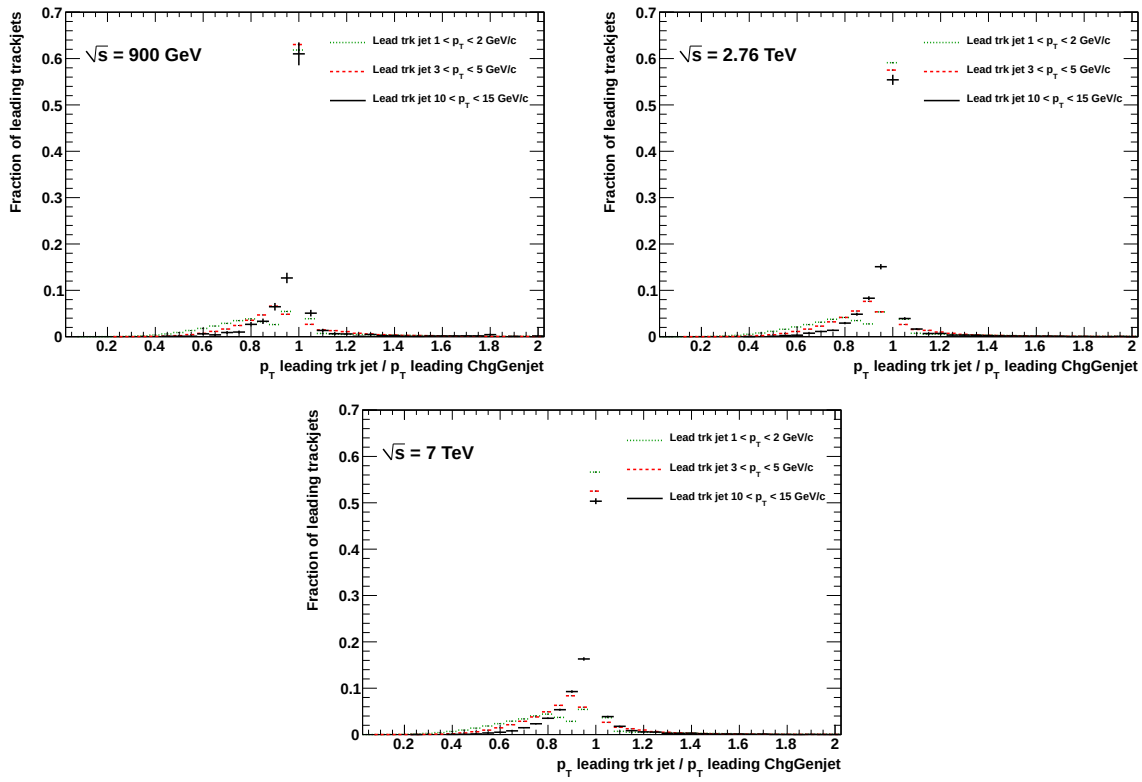

Figure 9.25.: The distribution of the ratio of the leading track-jet p_T to the leading charged-particle jet p_T is plotted for different ranges of leading track-jet p_T, for all centre-of-mass energies.

The performance of the reconstruction and matching of leading track-jets and leading charged-particle jets can be further examined by a study of acceptance, background, stability and purity for leading track-jets and charged particle jets. These variables are defined as follows:

- Acceptance: the fraction of events with a leading charged-particle jet within a p_T bin for which a reconstructed track-jet with a $p_T > 300$ MeV is found.
- Background: the fraction of events with a leading track-jet within a p_T bin for which *no* leading charged-particle jet with $p_T > 300$ MeV is found.
- Stability: the fraction of events with a leading charged-particle jet within a p_T bin for which a reconstructed track-jet in the same p_T bin is found.
- Purity: the fraction of events with a leading track-jet within a p_T bin for which a leading charged-particle jet in the same p_T bin is found.

and are shown in figures 9.26, 9.27 and 9.28 for the three centre-of-mass energies. The values are everywhere above 60% for acceptance, purity and stability, while the background is compatible with zero. This demonstrates in general the rather good reconstruction and matching performance of the anti-k_T algorithm that is used to construct the track-jet objects. In addition, figure 9.29 shows a good geometrical matching performance: it shows the fraction of leading detector level (particle level) jets that can be matched in (η, ϕ) phase space ($\Delta R < 0.5$) with a leading particle level (detector level) jet. Nevertheless, the p_T bin corresponding to 300 MeV/c $< p_T <$1 GeV/c is dropped from the analysis because of the significantly lower acceptance compared to the other bins.

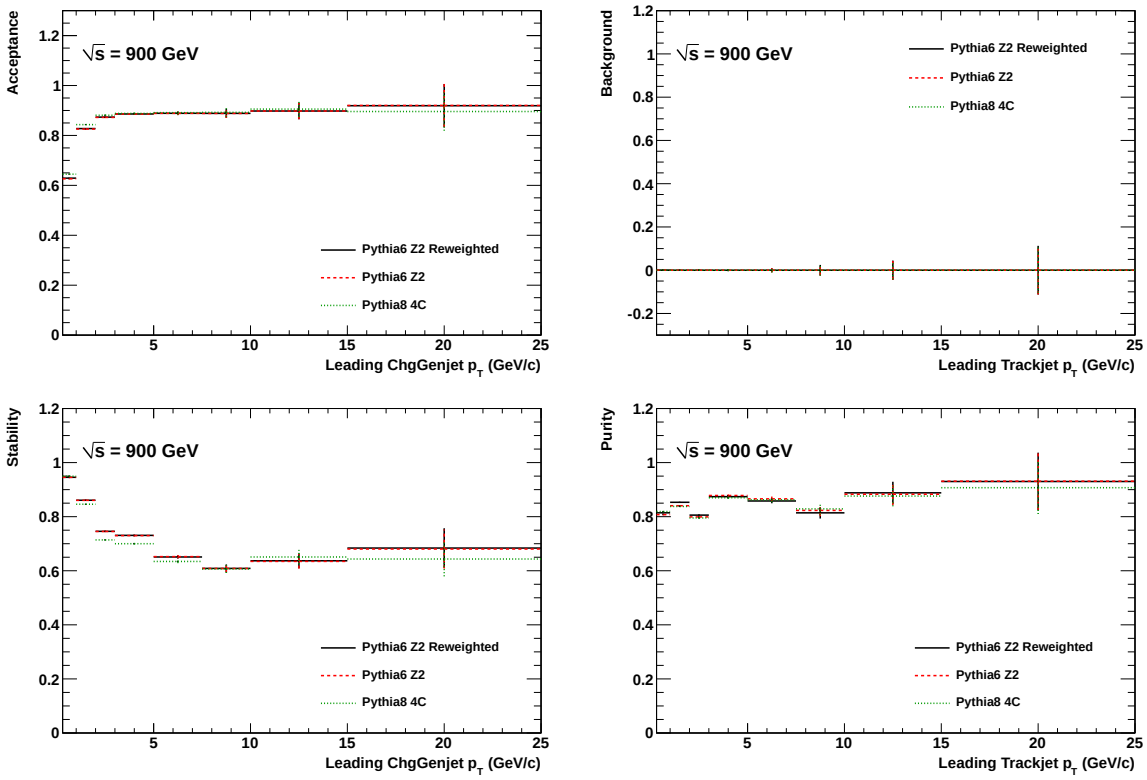

Figure 9.26.: Acceptance, background, stability and purity for leading track-jets and charged-particle jets at $\sqrt{s} = 0.9$ TeV

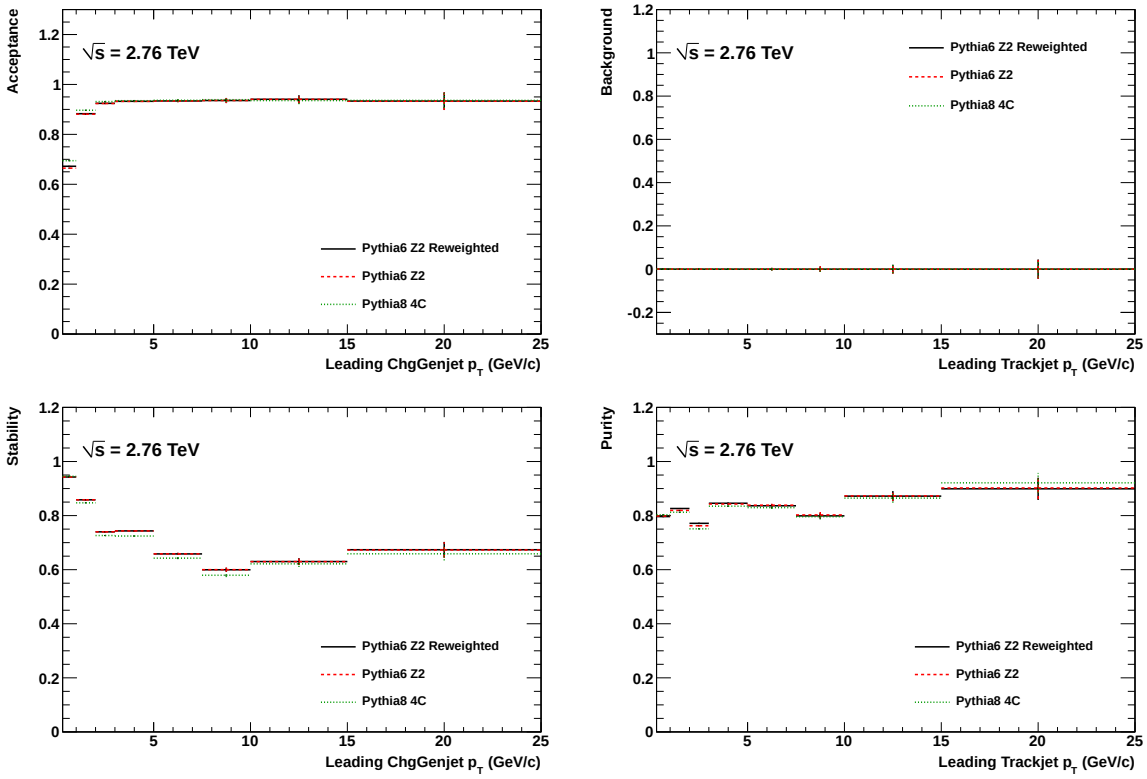

Figure 9.27.: Acceptance, background, stability and purity for leading track-jets and charged-particle jets at $\sqrt{s} = 2.76$ TeV

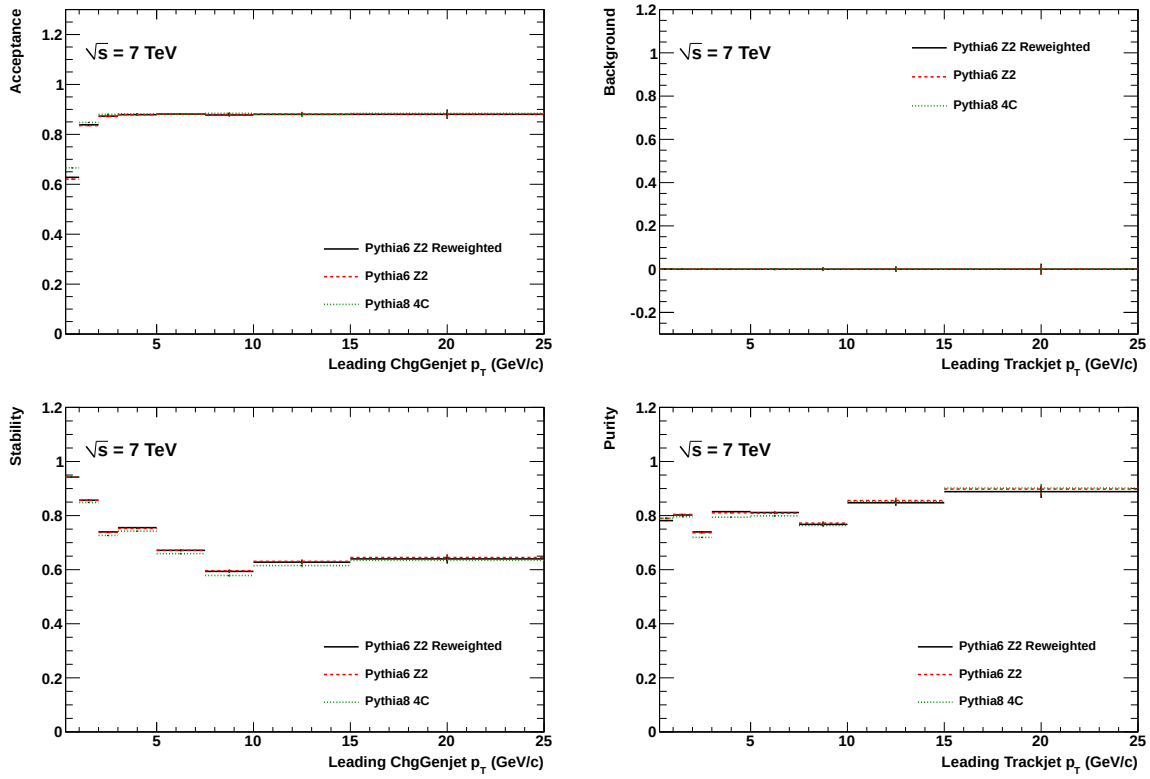

Figure 9.28.: Acceptance, background, stability and purity for leading track-jets and charged-particle jets at $\sqrt{s} = 7$ TeV

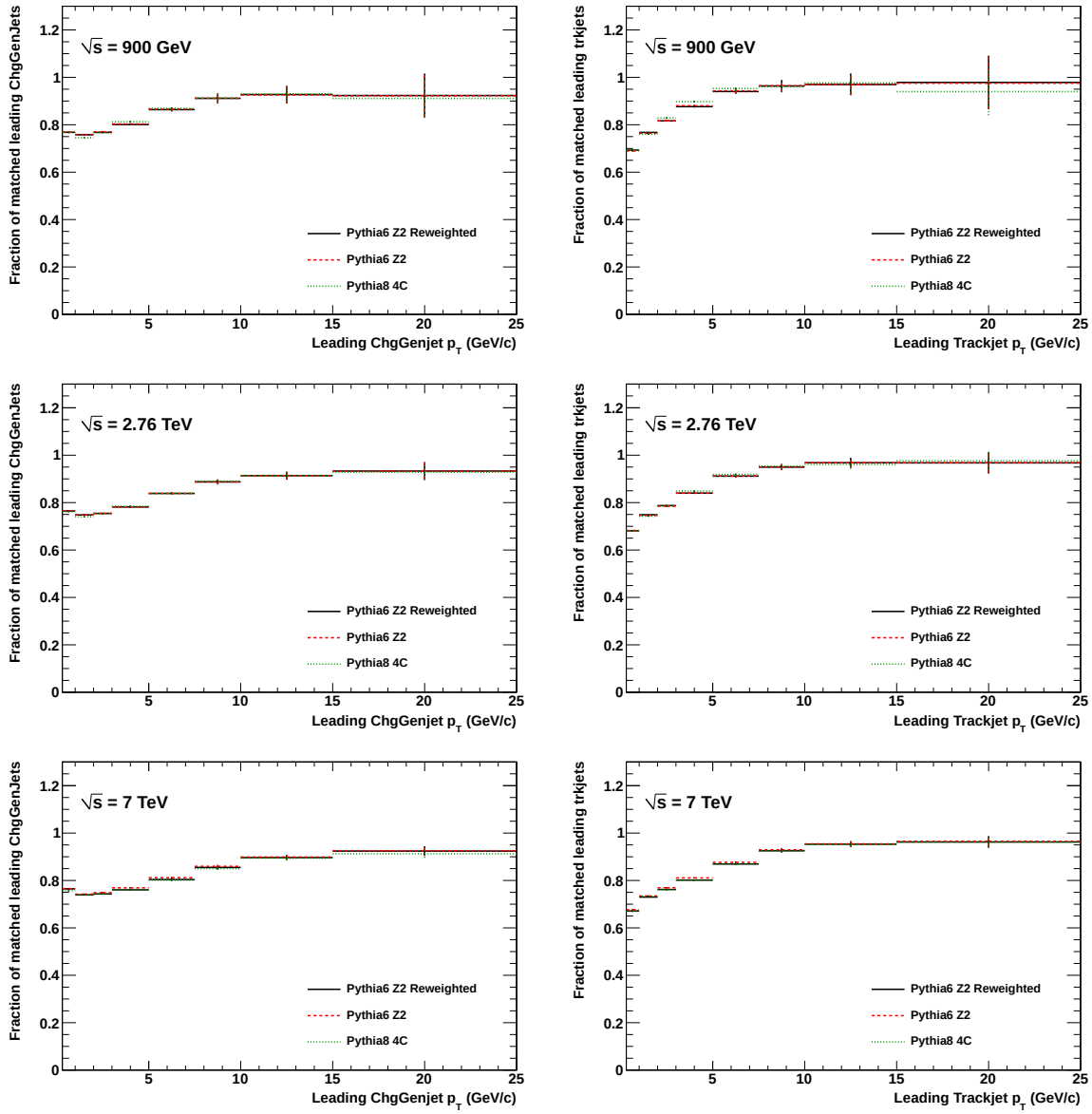

Figure 9.29.: The fractions of leading detector level (particle level) jets that can be matched in (η, ϕ) phase space ($\Delta R < 0.5$) with a leading particle level (detector level) jet.

In the end, the final correction factor applied to the data, shown in figure 9.22, is the product of the two above-mentioned factors, equations 9.4 and 9.5.

9.8. Systematic uncertainties

All sources of systematic uncertainties that can have a significant effect on the final results were investigated and are summarised in this section. To calculate each systematic effect, the full analysis is repeated and the differences in the final data points are added in quadrature to obtain the total systematic error. The following sources of uncertainty, summarised in tables 9.3 and 9.4, were found to have significant effects on the corrected results:

- *CASTOR detector alignment:* As extensively discussed and studied in section 9.3, position sensors monitoring the movement of the CASTOR calorimeter indicate that the detector moves by ~ 1 cm in the transverse plane when switching the CMS solenoid on or off. As a result of this, some ϕ sectors move towards more central pseudorapidity, so that the range they cover changes to approximately $-6.3 < \eta < -5.13$, while corrected results are presented for the range $-6.6 < \eta < -5.2$. A new correction factor is obtained by assuming a shift between the pseudorapidity range at the detector and the stable-particle level in the MC simulation, equal to the displacement of the most affected sectors in the data. The default corrected results are then obtained as the average between the correction factors based on the nominal and the shifted position of CASTOR, with half the difference taken as systematic uncertainty. In addition, for the measurement of the relative energy density as a function of centre-of-mass energy, a second systematic uncertainty needs to be added, to take possible shifts in the CASTOR position between runs at different $\sqrt{s}$ into account. Figure 9.3 indeed showed that sensor measurements indicate a different position during the 2010 ($\sqrt{s} = 0.9$ and 7 TeV) and 2011 ($\sqrt{s} = 2.76$ TeV) data taking. Since the relative energy density measurement is normalised to $\sqrt{s} = 2.76$ TeV, this difference has to be taken into account. This additional uncertainty is calculated by comparing the nominal relative energy densities, where CASTOR is not displaced, with relative energy densities extracted from simulations in which the CASTOR calorimeter is placed at the appropriate sensor position measurements. Although such displacements give rise to a big change in absolute energy, as expected, they lead to acceptable systematics on the relative energy measurements. The uncertainty is found to be 4.8% for the $\sqrt{s} = 0.9$ TeV bin, and only 1.8% for the $\sqrt{s} = 7$ TeV bin. These values are added in quadrature to the first introduced uncertainty, and the total is presented in table 9.4.

- *Non-compensation:* The non-compensating nature of the CASTOR calorimeter has been described in sections 6.2 and 7.3. Measurements using a test beam setup have shown (recall figure 7.8) that the response to pions relative to the response to electrons is $\sim 50\%$, and that this ratio slowly increases with the incoming particle energy. This result was then used to correct the MC simulation with a "non-

compensation correction factor" in order to reproduce the measured test beam response. However an error of $\pm 5\%$ is present on the non-compensation factor obtained from the test beam measurement, to take this uncertainty into account, we scaled the response to hadronic showers in the simulation up and down with $\pm 5\%$ in dedicated simulated samples and repeated the analysis with it.

- *Model dependence:* The correction factors described in the previous sections are obtained from Monte Carlo simulations, and thus they are model dependent. The correction of the CASTOR energy ratio in particular is sensitive to the charged to neutral pion ratio used in the model. Therefore we did not only calculate the correction factors with the default PYTHIA6 Z2 Reweighted sample, but in addition obtained correction factors from the unweighted PYTHIA6 Z2 sample and from a fully simulated PYTHIA8 4C sample. The differences in corrections factors are then taken as systematic uncertainty and added in quadrature. Figures 9.30 and 9.31 show the correction factors obtained with the available simulated MC samples.

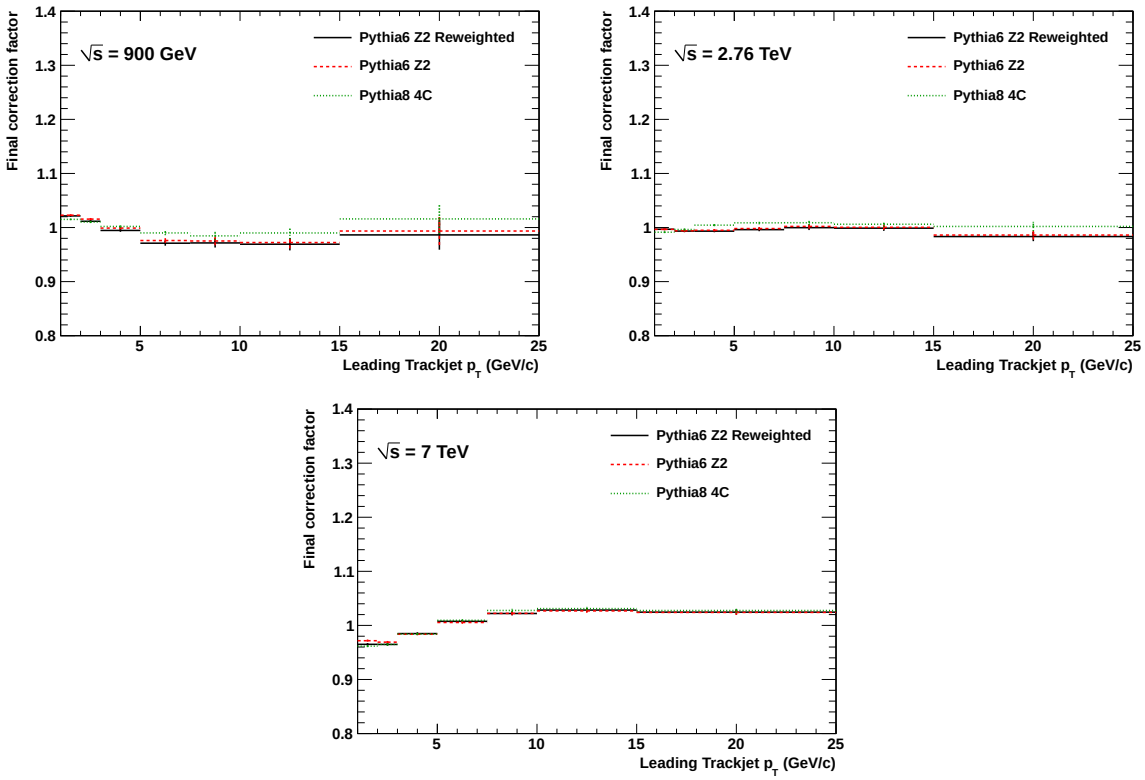

Figure 9.30.: Model dependence of the total correction factors for the hard-to-inclusive forward energy ratio versus leading track-jet p_T at $\sqrt{s} = 0.9$, 2.76 and 7 TeV.

In addition, an extra systematic uncertainty on the model dependence is taken into account, by not looking only at PYTHIA. This was done with a dedicated study that analysed and compared the response factors of different models (EPOS, QGSJET, HERWIG, PYTHIA) on generator level. Here a response factor is defined as the sum of the electromagnetic energy and 50% of the hadronic energy, divided by the total

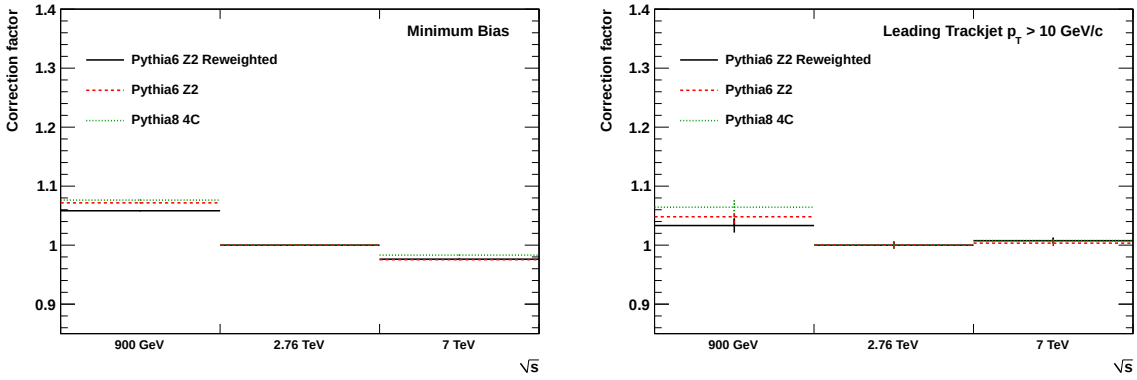

Figure 9.31.: Model dependence of the correction factors for the relative energy density vs. $\sqrt{s}$ for minimum bias events (left) and for events with a leading track-jet with $p_T > 10$ GeV/c (right).

Source of uncertainty	$\sqrt{s} = 0.9$ TeV	$\sqrt{s} = 2.76$ TeV	$\sqrt{s} = 7$ TeV
CASTOR alignment	1.5%	2.9%	3.1%
Noncompensation	1.1%	0.4%	0.6%
Model dependence	3.0%	2.3%	1.3%
Shower containment	1.2%	1.4%	1.0%
Noise suppression	0.3%	0.2%	0.2%
Total uncertainty	3.7%	4.0%	3.6%

Table 9.3.: Systematic uncertainties on the hard-to-inclusive forward energy ratio for track jet $p_T > 10$ GeV/c at different centre-of-mass energies.

energy deposited in CASTOR. The largest relative variation in the response factors is then taken as a systematic uncertainty on the correction factor, and added in quadrature with the above determined model uncertainty from PYTHIA6 Z2 and PYTHIA8 4C.

- *Shower containment:* In this analysis only the 5 front modules of the CASTOR calorimeter are used. In order to assess the systematic uncertainty due to the partial containment of the hadronic shower, the difference in the observed energy ratios obtained from simulations based on all 14 modules and those based on only the front 5 modules is taken as a contribution to the systematic uncertainty.

- *Noise suppression:* The noise threshold applied to CASTOR towers is varied by $\pm 20\%$, reflecting the uncertainty in the absolute calibration factor.

We also examined the following sources of possible systematic uncertainties, which were fortunately found to be negligible and are not included in the summary tables:

Source of uncertainty	0.9 TeV (incl.)	0.9 TeV (hard)	7 TeV (incl.)	7 TeV (hard)
CASTOR alignment	8.0%	7.0%	2.5%	2.7%
Non-compensation	0.5%	1.1%	0.1%	1.0%
Model dependence	2.4%	3.6%	2.0%	2.2%
Shower containment	1.2%	1.0%	1.3%	0.9%
Noise suppression	0.6%	0.8%	0.6%	1.0%
Total uncertainty	8.5%	8.0%	3.5%	3.9%

Table 9.4.: Systematic uncertainties on the relative energy density vs. $\sqrt{s}$ in inclusive events (incl.) and in events with a central charged-particle jet with $p_T > 10$ GeV/c (hard).

- The detector simulation code (section 7.3) based on GEANT4 uses a detailed description of the forward geometry of the CMS detector, which includes a stainless steel disk partially covering the CASTOR acceptance in pseudorapidity. In order to assess the sensitivity of the simulation to the amount of material in front of the CASTOR calorimeter, the density of this material was modified by changing it to air and to tungsten. A comparison of the different simulations showed that the absolute energy density changed significantly, but the energy ratio was found to be stable.

- It can happen that particles directly hit the CASTOR PMT windows and as a consequence produce anomalous signals. The PMT window itself is a source of Čerenkov radiation, and thus a single fast charged particle may produce a signal equivalent to a $\sim$1.4 GeV energy deposit when traversing the window. It should however be noted that the CASTOR PMT's are in principle shielded by HF. To study the effect in a GEANT simulation, the geometry of the PMT volumes was modified to accurately describe the PMT windows. Then, 100 000 minimum bias events generated by the PYTHIA6 D6T model were fully simulated in this new setup. In this sample it was found that PMT hits were produced in only 536 events. The fraction of such events is thus very low and figure 9.32, which shows the longitudinal shower profile in CASTOR, confirms the small contribution of PMT hits to the total measured energy. Only in the last modules the contribution rises to $5 - 15\%$, but since the measurement in this analysis is only based on the energy deposits in the 5 front-most modules, we are unaffected by PMT hits.

- The effect of pile-up was investigated by measuring the energy deposited in CASTOR as a function of the instantaneous LHC bunch luminosity, shown in figure 9.33. Using a linear fit, the energy is extrapolated to zero bunch luminosity, yielding a pile-up correction to the energy in inclusive events of -0.5%, -0.9% and $+0.2\%$ at $\sqrt{s} = 0.9$, 2.76 and 7 TeV, respectively. The pile-up correction to the energy in events with a central leading track-jet is expected to be of the same order. The correction on the ratio is therefore estimated to be smaller than 0.1% and as such not included in the systematic uncertainties.

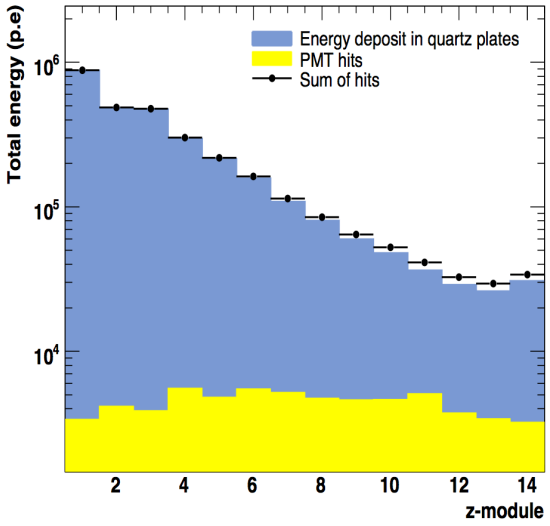

Figure 9.32.: The longitudinal shower profile in CASTOR for minimum bias events in a simulation including signals from particles directly hitting the PMT windows.

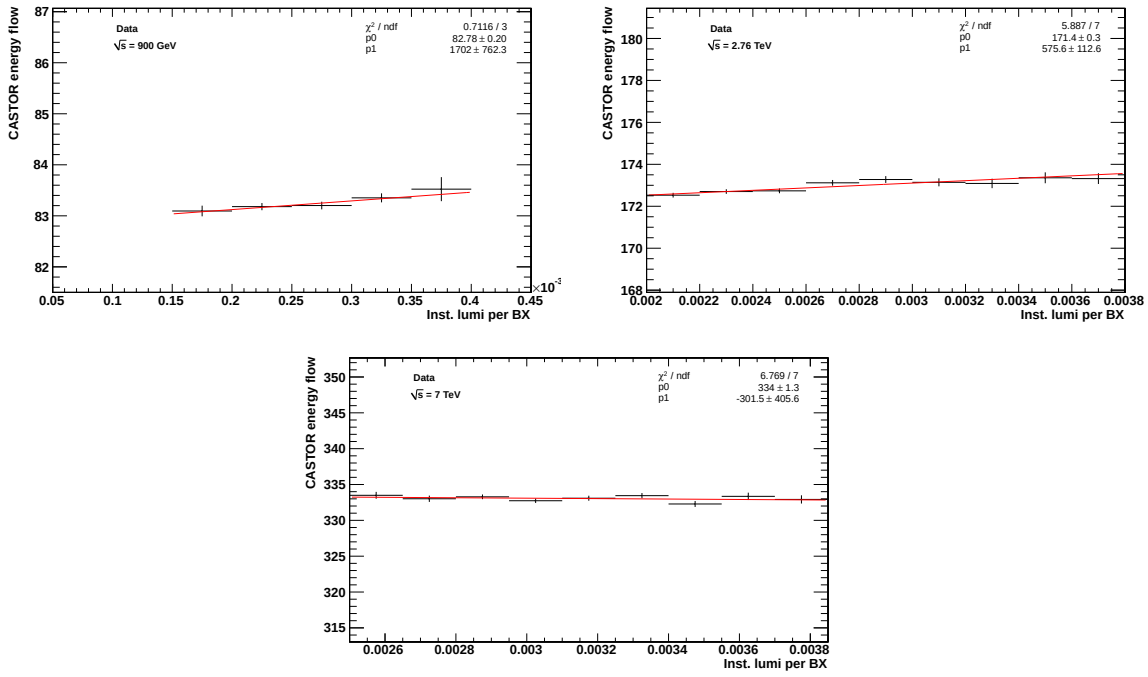

Figure 9.33.: The energy measured in CASTOR as a function of LHC bunch luminosity for inclusive events at $\sqrt{s} = 0.9$, 2.76 and 7 TeV.

- Track-jets are reconstructed with an anti-k_T clustering algorithm that takes reconstructed tracks with $p_T > 300$ MeV/c as input. At low values of track-jet p_T however, the p_T resolution is affected by tracks missed by the reconstruction or jet clustering algorithm. This effect is automatically absorbed in the factor used to

correct for migrations in track-jet p_T, but in order to estimate its magnitude, the p_T threshold on the tracks was increased to 500 MeV/c in a MC sample, while it remained unchanged in the data. The different response with respect to the default track-jet reconstruction was found to be negligible.

- The inter-calibration procedure, introduced in section 9.3.3, which was used to equalise the response from individual CASTOR channels, yields an error of $\sim 20\%$ on the inter-calibration constants. To estimate the possible systematic uncertainty due to this error on the inter-calibration, a simulated sample was produced in which the response of each channel in MC was rescaled to describe the response observed in real data, but the resulting uncertainty with respect to the default response was found to be negligible. In addition, figure 9.34 shows the CASTOR energy ratio of events with a leading track-jet with $p_T > 10$ GeV/c with respect to minimum bias events *per channel* for data and a simulated PYTHIA6 Z2 sample. It shows that despite a possible remaining uncertainty in the inter-calibration of channels, the energy ratio is constant within errors.

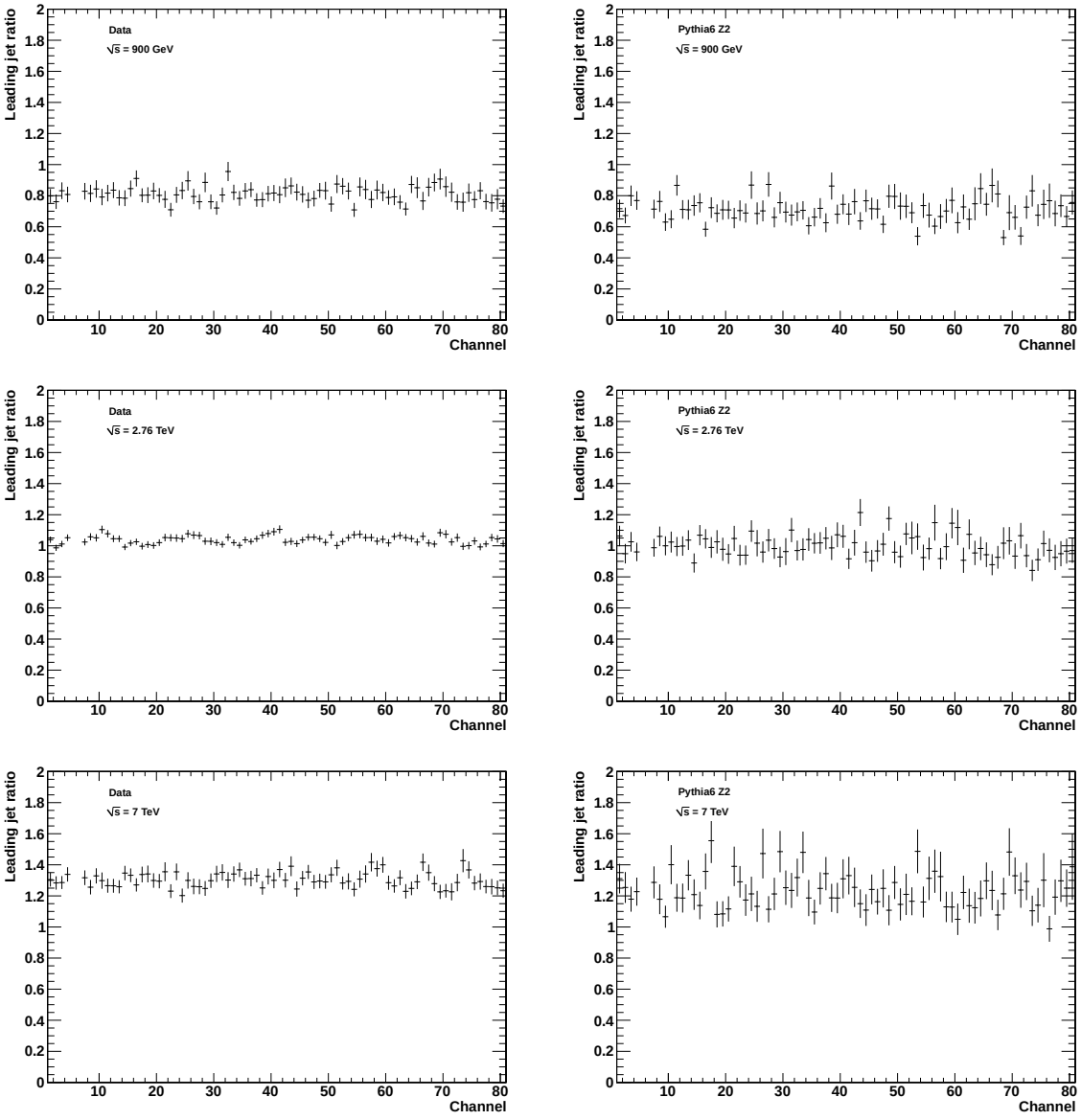

Figure 9.34.: The CASTOR energy ratio, per channel, in events with a leading track-jet with $p_T > 10$ GeV/c with respect to minimum bias events, at $\sqrt{s} = 0.9$, 2.76 and 7 TeV for data (left) and PYTHIA6 Z2 (right).

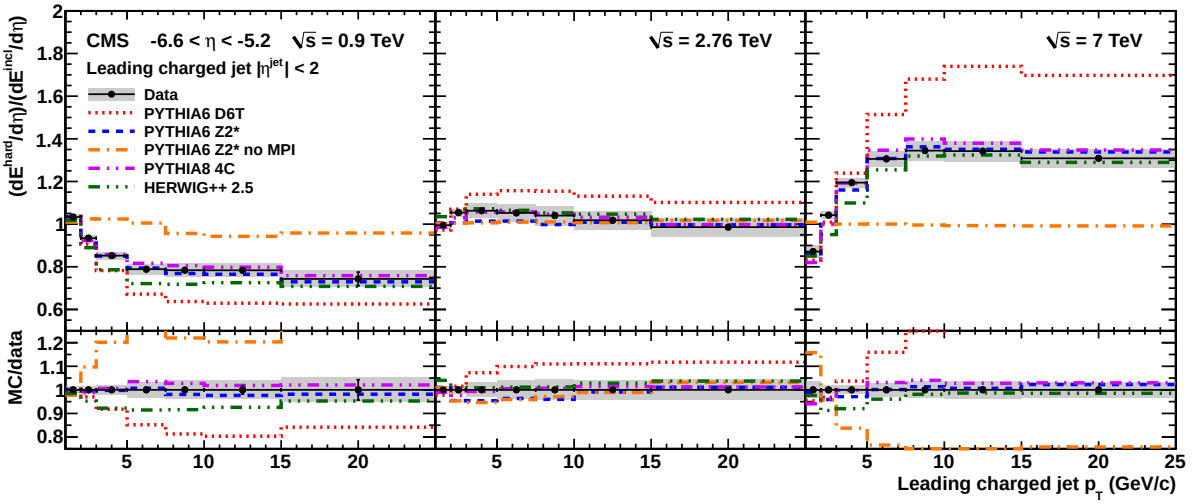

Figure 9.35.: Ratio of the energy deposited in the pseudorapidity range $-6.6 < \eta < -5.2$ for events with a charged-particle jet with $|\eta^{\text{jet}}| < 2$ with respect to the energy in inclusive events, as a function of the jet transverse momentum p_T for $\sqrt{s} =$ 0.9 (left), 2.76 (middle), and 7 TeV (right). Corrected results are compared to the PYTHIA and HERWIG++ MC models. Error bars indicate the statistical uncertainty on the data points, while the grey band represents the statistical and systematic uncertainties added in quadrature.

9.9. Results

We are now able to show the final results that are fully corrected for detector effects as described in section 9.7, and have associated systematic uncertainties determined in section 9.8. As described in section 9.4, these results are obtained for a sample of events dominated by nondiffractive collisions so that the energy density ratios are not biased by rapidity gaps in the CASTOR pseudorapidity range.

Figures 9.35, 9.36 and 9.37 show the hard-to-inclusive forward energy ratios, defined as the energy deposited in the pseudorapidity range $-6.6 < \eta < -5.2$ in events with a charged-particle jet with $|\eta^{\text{jet}}| < 2$ divided by the energy deposited in inclusive, dominantly nondiffractive events, as a function of the jet transverse momentum p_T. All three figures show the same data points, but compared to different models.

At $\sqrt{s} = 7$ TeV, a fast increase is seen at low p_T followed by a plateau above $p_T = 8$ GeV/c. In the framework of the MPI model for the underlying event (section 3.3), this can be understood from the relation between the impact parameter b and the scale of the event, quantified by p_T. As p_T increases, the collisions become more central and the number of parton interactions increases. Above $p_T = 10$ GeV/c, the collision is central and the underlying event activity saturates. The pre-LHC PYTHIA6 tune D6T fails to describe the data, while the PYTHIA6 and PYTHIA8 tunes fitted to LHC data on the underlying event at central rapidity agree with the data at forward rapidity within $\pm 5\%$. In addition, the Perugia P11 tune, which is not tuned to LHC data, gives a remarkable

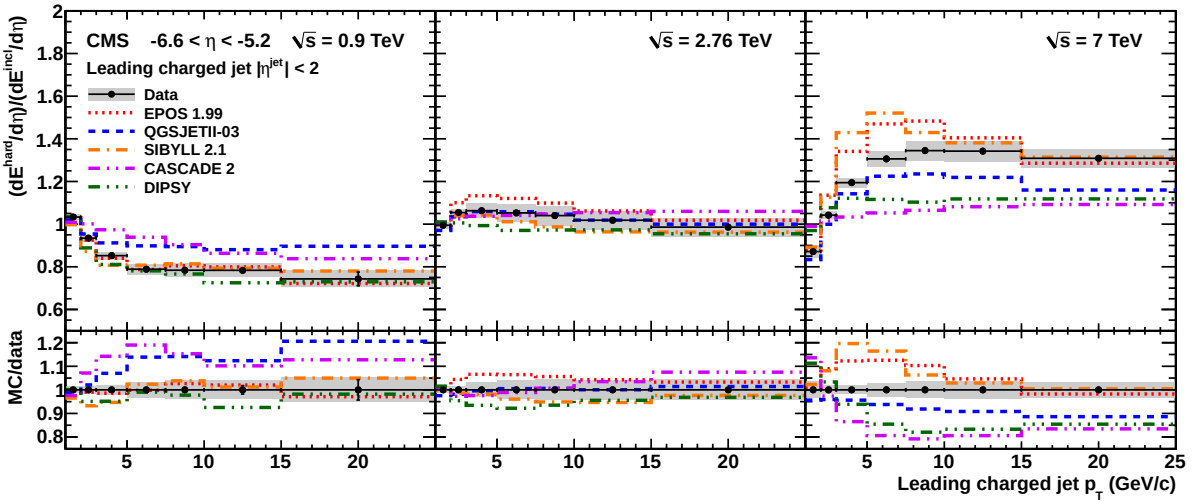

Figure 9.36.: Ratio of the energy deposited in the pseudorapidity range $-6.6 < \eta < -5.2$ for events with a charged-particle jet with $|\eta^{\text{jet}}| < 2$ with respect to the energy in inclusive events, as a function of the jet transverse momentum p_T for $\sqrt{s} =$ 0.9 (left), 2.76 (middle), and 7 TeV (right). Corrected results are compared to MC models used in cosmic ray physics and to CASCADE and DIPSY. Error bars indicate the statistical uncertainty on the data points, while the grey band represents the statistical and systematic uncertainties added in quadrature.

good agreement. The Atlas AMBT1 tune, which is determined from central charged particle multiplicity measurements, yields a little too low MPI. As expected, when MPI are switched off, PYTHIA predicts a forward energy density that is independent of the central jet p_T. The HERWIG++ 2.5 simulation with tune UE-EE-3C gives a slightly worse description of the data in the turn-on region, but is still within $\pm 10\%$ of the measured points. It is a big improvement on the older HERWIG++ 2.4 version. The CASCADE model, which does not simulate multiple parton interactions, does not describe the data and the discrepancy shows that the features observed in the data cannot be explained by the CCFM parton dynamics as implemented in this model. The DIPSY model, based on the BFKL dipole picture, and supplemented with multiple interactions between dipoles, however, also fails to describe the data. However models used in cosmic ray physics, which incorporate MPI through multi-pomeron exchanges, do describe the increase of the energy ratio as a function of p_T reasonably well. The QGSJETII-03 generator yields a ratio that is too low in the plateau region, while SIBYLL 2.1, and EPOS 1.99 overestimate the turn-on but converge on a very good description at large p_T.

At $\sqrt{s} = 2.76$ TeV, the increase of the energy ratio with p_T is much reduced. This tendency is consistent with the result at $\sqrt{s} = 0.9$ TeV, where the ratio becomes less than unity. Here, the energy density in events with a central jet is thus lower than the energy density in inclusive events. As discussed in section 9.1, this can be understood as a kinematic effect: the production of central hard jets, accompanied by a higher underlying event activity, depletes the energy of the proton remnant, which at $\sqrt{s} =$ 0.9 TeV fragments within the pseudorapidity region covered by CASTOR. This feature

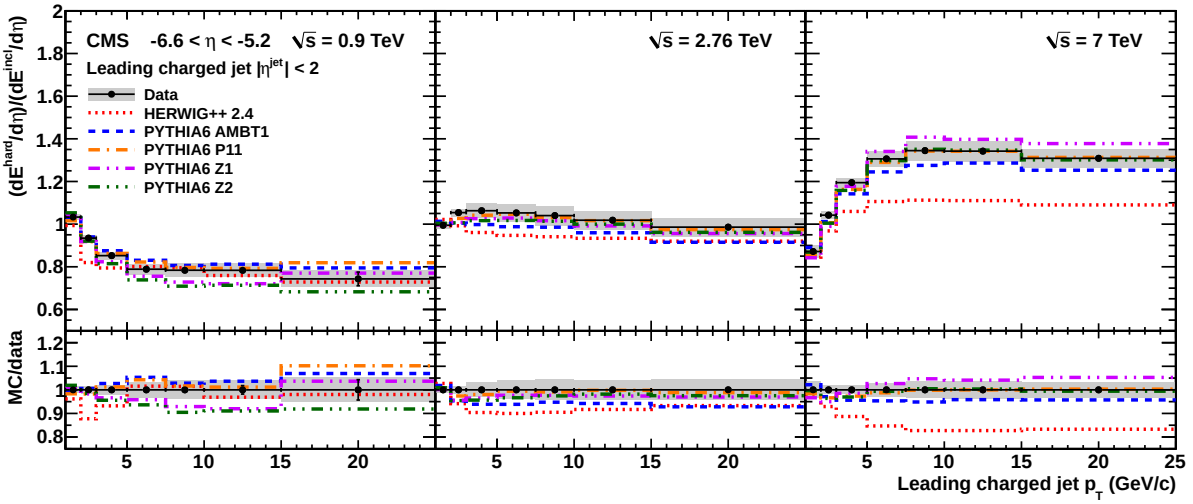

Figure 9.37.: Ratio of the energy deposited in the pseudorapidity range $-6.6 < \eta < -5.2$ for events with a charged-particle jet with $|\eta^{\text{jet}}| < 2$ with respect to the energy in inclusive events, as a function of the jet transverse momentum p_T for $\sqrt{s} =$ 0.9 (left), 2.76 (middle), and 7 TeV (right). Corrected results are compared to additional PYTHIA models and an older version of HERWIG++. Error bars indicate the statistical uncertainty on the data points, while the grey band represents the statistical and systematic uncertainties added in quadrature.

is roughly described by the models. Again, the PYTHIA6 D6T tune exhibits too strong an underlying event activity, even at $\sqrt{s} = 0.9$ TeV where it is below the data as the high amount of MPI takes too much energy from the beam remnant. Other PYTHIA tunes describe the data at $\sqrt{s} = 2.76$ TeV and 0.9 TeV rather well. The HERWIG++ 2.5 predictions lie slightly below the data at $\sqrt{s} = 0.9$ TeV, which also indicates a too strong underlying event activity. The CASCADE generator does not reproduce the data, while DIPSY yields a reasonable description at these lower centre-of-mass energies. Most of the cosmic ray models describe the data well, with QGSJETII-03 again yielding a slightly too low underlying event activity.

Overall, in this study, the PYTHIA6 Z2*, PYTHIA6 P11 and PYTHIA8 4C tunes give a good description of all the data. This is however in contrast with studies of the underlying event in the central region [111], where PYTHIA6 Z2* gives an excellent description of the underlying event activity in the region transverse to the jet in azimuth (to which it was tuned), while PYTHIA8 4C is too low.

Figures 9.38, 9.39 and 9.40 present the increase of the energy density deposited in the range $-6.6 < \eta < -5.2$ as a function of $\sqrt{s}$, normalised to the energy density at $\sqrt{s} = 2.76$ TeV, for both inclusive events and for events with a central charged-particle jet. The $\sqrt{s} = 2.76$ TeV data are taken as a normalisation point because this minimises the statistical and systematic uncertainties. The p_T threshold for jets is 10 GeV/c at all centre-of-mass energies. Since this is well within the plateau region, the energy density

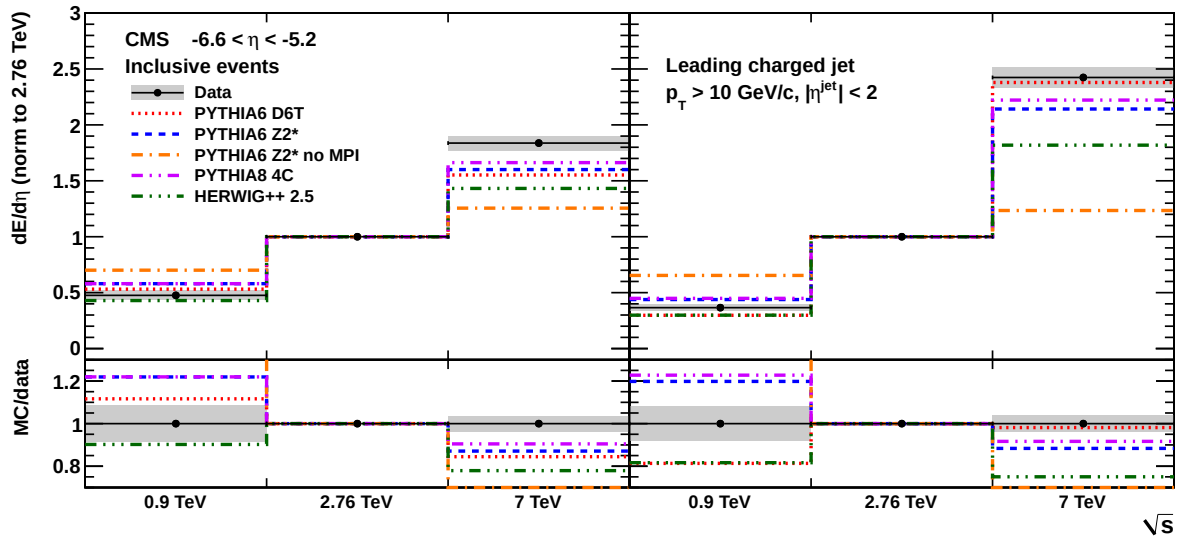

Figure 9.38.: Energy density in the pseudorapidity range $-6.6 < \eta < -5.2$ in inclusive events (left) and in events with a charged-particle jet in the range $|\eta^{\text{jet}}| < 2$ (right) as a function of $\sqrt{s}$, normalised to the energy density at $\sqrt{s} = 2.76$ TeV. The p_T threshold used for jets is 10 GeV/c at all centre-of-mass energies. Corrected results are compared to the PYTHIA and HERWIG++ MC models. Statistical uncertainties are smaller than the marker size, while the grey band represents the statistical and systematic uncertainties added in quadrature.

does not change significantly as a function of the actual value of the threshold. All three figures again show the same data points, but compared to different models.

None of the PYTHIA or HERWIG++ models describe the increase with $\sqrt{s}$ seen in the data. For inclusive events the predictions differ little and they all underestimate the increase from $\sqrt{s} = 2.76$ to 7 TeV (by up to $\sim$20% for HERWIG++ 2.5). In this event class, the contribution of the underlying event is expected to be small. For events with central charged-particle jets, the predictions vary more widely. Indeed, for this event class the description of the underlying event in various tunes is expected to differ. None of the tunes give a satisfactory description, with PYTHIA6 D6T and PYTHIA8 4C being closest to the data and HERWIG++ 2.5 underestimating the increase from 2.76 to 7 TeV by $\sim$25%. The CASCADE and DIPSY generators also show a slower increase of the forward energy density with $\sqrt{s}$ than observed in the data. Of the cosmic ray models, QGSJETII-03 gives a good description of the data. The EPOS and SYBILL generators yield an increase with centre-of-mass energy that is lower than that in the data by $10 - 15$%.

The results presented in this paper show that the MPI model, as implemented in PYTHIA (described in section 3.3), and tuned to central inclusive and underlying event data, is capable of describing the p_T dependence of the forward energy density. This is an important consistency check of the MPI model. Models inspired by BFKL or CCFM parton dynamics do not describe the p_T dependence of the data. Hence, contributions

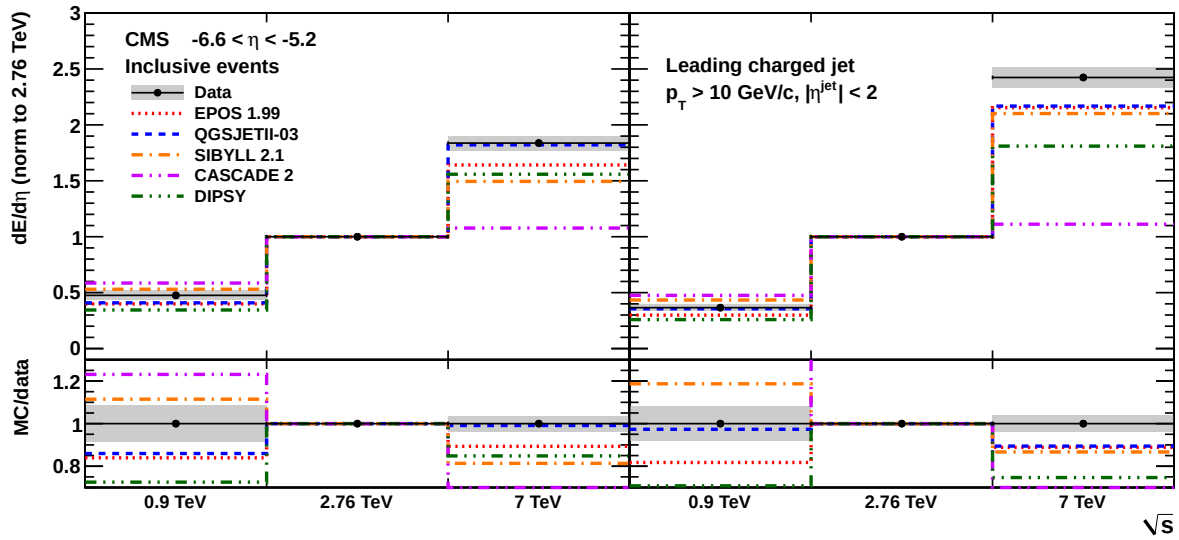

Figure 9.39.: Energy density in the pseudorapidity range $-6.6 < \eta < -5.2$ in inclusive events (left) and in events with a charged-particle jet in the range $|\eta^{\text{jet}}| < 2$ (right) as a function of $\sqrt{s}$, normalised to the energy density at $\sqrt{s} = 2.76$ TeV. The p_T threshold used for jets is 10 GeV/c at all centre-of-mass energies. Corrected results are compared to MC models used in cosmic ray physics and to CASCADE and DIPSY. Statistical uncertainties are smaller than the marker size, while the grey band represents the statistical and systematic uncertainties added in quadrature.

that go beyond what is presently implemented in those models seem to be mandatory. Models used for cosmic rays studies, which include MPI and saturation effects via multi-pomeron interactions work well. The PYTHIA6 model with tune D6T describes the $\sqrt{s}$ dependence well, but only by invoking too large an amount of MPI, as can be concluded from the p_T dependence.

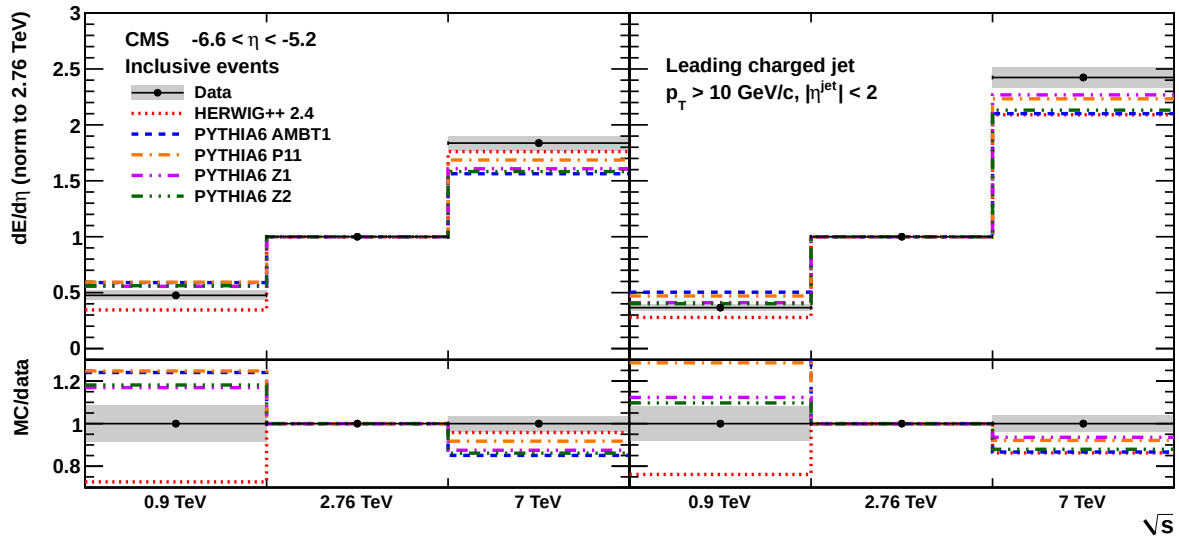

Figure 9.40.: Energy density in the pseudorapidity range $-6.6 < \eta < -5.2$ in inclusive events (left) and in events with a charged-particle jet in the range $|\eta^{\text{jet}}| < 2$ (right) as a function of $\sqrt{s}$, normalised to the energy density at $\sqrt{s} = 2.76$ TeV. The p_T threshold used for jets is 10 GeV/c at all centre-of-mass energies. Corrected results are compared to additional models of PYTHIA and an older version of HERWIG++. Statistical uncertainties are smaller than the marker size, while the grey band represents the statistical and systematic uncertainties added in quadrature.

Chapter 10.

Summary

In the Standard Model of particle physics, Quantum Chromodynamics (QCD) is the theory of strong interactions between hadrons. It is a relativistic quantum field theory, of which the non-abelian nature leads to the properties of asymptotic freedom and confinement. Short distance processes have a small coupling, which makes perturbative calculations possible, while long distance processes at a low energy scale have a large coupling, the reason why quarks can not be detected separately, but are confined in colour neutral hadrons.

With the help of deep inelastic scattering processes, hadrons were found to be built out of partons, quarks and gluons, and their interactions are then described as the interactions between the constituent partons. The cross section of hadron collisions is then factorised into a non-perturbative long distance part, the parton distribution functions ($f_i(x, \mu^2)$, which describe the probability to find a parton i, inside the hadron, with a longitudinal momentum fraction x at an energy scale μ), convoluted with the perturbatively calculable partonic cross section, which represents the high energy short distance interaction. This is called collinear factorisation. The parton distributions can not be calculated from first principles, but their evolution with μ can be calculated perturbatively with the DGLAP evolution equations. The strength of the factorisation ansatz is that the parton distribution functions are independent of the hard scattering. Once they are measured for a specific hadron, they can be used to calculate any process involving this type of hadron.

One important limitation of collinear factorisation is that it does not take possible multiple parton interactions (MPI) at hadron-hadron collisions into account. This appears to be a crucial component of the underlying event, which is defined as everything except the hard scattering. This includes parton showers from initial and final state radiation, beam remnants and the aforementioned MPI. These additional parton interactions are mostly soft or semi-hard, but can alter the colour flow and total scattered energy of the event significantly. The lack of a universal theoretical framework to describe such effects led to the introduction of phenomenological models. A longstanding and successful model that implements MPI, is based on an impact parameter picture of particle collisions. However, such models rely on free parameters that need to be tuned to experimental data.

Therefore, a lot of measurements are currently conducted to study the underlying event. In particular with the experiments at the CERN LHC accelerator, where it is extensively studied in proton-proton collisions. In such measurements, one usually studies the underlying activity at central rapidities as a function of the scale of the hard scatter in the event. This can either be the leading track(jet) or a Drell-Yan lepton pair. The underlying activity itself can then be measured in terms of particle multiplicities, transverse momentum sums, strangeness production or jet area/medians. In addition, energy density measurements at forward rapidity are also performed. All these measurements confirm that multiple parton interactions are mandatory to account for all the underlying event activity, and that the MPI models developed in the impact parameter picture are able to describe the data if their parameters are tuned accordingly.

This thesis presents a complementary underlying event measurement at forward rapidity, conducted at the CMS experiment. The CMS detector is a general purpose detector that completely surrounds the interaction point. Its onion like structure consists out of a tracker system, calorimeters, a 4 T solenoid and muon detectors. This design makes it possible to completely reconstruct the final state of LHC proton-proton collisions. In particular, the high performant tracking system is ideal to detect central leading tracks or track-jets that originate from charged particles from the hard scatter.

A crucial component of the CMS detector for our analysis is the forward CASTOR calorimeter. It covers the pseudorapidity range $-6.6 < \eta < -5.2$, and is located at $z = -14.38$ m from the interaction point. It uses tungsten plates as absorber material, and quartz plates to generate Čerenkov signals. It thus has the ability to measure the energy of electromagnetic and hadronic particles in the very forward region of the CMS detector. CASTOR has 14 segmentations in z (a total length of $10\lambda_I$), a 16 fold segmentation in the azimuthal plane, but no segmentation in η. The analysis presented in this thesis is the first ever to use data recorded with the CASTOR calorimeter, therefore a significant part of the research was devoted to the commissioning and validation of the detector. Contributions were made to a) the study of prototypes in test beam environments, b) simulation and reconstruction software development and validation, and c) understand the in situ detector operation, in particular the alignment of the calorimeter. The operation during LHC data taking was found to be challenging, but sufficiently understood for the purpose of this analysis.

A study of the underlying event at forward pseudorapidity ($-6.6 < \eta < -5.2$) is then presented with a novel observable. The energy density per unit of pseudorapidity has been measured at three different centre-of-mass energies, $\sqrt{s} = 0.9$, 2.76, and 7 TeV, for events with a central charged-particle jet, relative to the energy density for inclusive events. This hard-to-inclusive forward energy ratio has been studied as a function of the jet transverse momentum p_T. In addition, the relative increase of the energy density as a function of the centre-of-mass energy has been measured for both inclusive events and events with a central charged-particle jet. All results have been corrected to stable-particle level.

These results complement those obtained from studies of the underlying event at central rapidity [110, 112, 113, 111, 114] because the large η separation from the central

hard scattering system yields a different sensitivity to the relative contributions of parton showers and multiple-parton interactions. The data can thus be used to tune the underlying event parameters in a way that is complementary to that possible with central-rapidity data.

The data exhibit the typical underlying event behaviour characterised by a rapid change of the energy density at small charged-particle jet p_T, followed by a plateau at larger p_T. At $\sqrt{s} = 7$ TeV, the relative energy density increases with jet p_T, while at $\sqrt{s} = 0.9$ TeV, the energy density decreases with increasing jet p_T. At this centre-of-mass energy, the hard-to-inclusive forward energy ratio drops below 1, which suggests that the energy of the proton remnant is depleted in events with a central charged-particle jet. Data at $\sqrt{s} = 2.76$ TeV exhibit an intermediate behaviour and are characterised by an approximately constant energy density as a function of the jet p_T.

Models that include multiple-parton interactions suggest that they only make a limited contribution to the forward energy density in inclusive events. In contrast, collisions with a small impact parameter, characterised by the presence of a charged-particle jet, appear to give rise to a significant number of multiple-parton interactions. Above $p_T = 8$ GeV/c, the hard-to-inclusive forward energy ratio is roughly independent of p_T, indicating that the collisions are already central for this value of the jet p_T. Some Monte Carlo models are able to describe the hard-to-inclusive forward energy ratio as a function of p_T, however, all models fail to reproduce the dependence on the centre-of-mass energy simultaneously for inclusive events and for events with a central charged-particle jet.

Acknowledgements

The most difficult part of writing a PhD thesis, is probably the part where one wants to thank all the people that helped him along the way. Simply because for some of those people it is impossible to actually translate the real gratitude into a few lines of text, and second, because there are *really a lot of people* that I should thank. Certainly in the field of experimental particle physics, where thousands of people collaborate to extend the frontier of science. So, I hereby want to thank *everybody* that I got to meet during the course of my PhD and helped me in one way or another!

It is clear however that certain persons deserve a special thanks. This thesis and the results in it would not be possible without them.

First and foremost I like to thank my supervisor, Pierre Van Mechelen, to give me the chance do a PhD, to always support me, to always be available for questions, to help me find my way in CERN, for the experience, for the interesting discussions and the friendly atmosphere. Thanks for everything!

I would like to thank Benoît Roland and Silvia Ochesanu for being *the* office mates all these years. For all the help, support, discussions, fun and friendship, for everything, thanks! Furthermore, Silvia was so kind to provide me a few CASTOR software plots from her thesis draft.

In addition I would also like to thank Karel Černý and Zlatka Staykova. They joined and left our office team along these years, but even in those short periods they helped me a lot with many things and provided good times.

I would also like to give a special thanks to all the members of the particle physics group at the University of Antwerp, the CMS CASTOR group and the CMS small-x QCD physics group. They provided me a nice work environment and helped me with many things.

Finally I would like to thank my family and friends, to support me all these years. Especially my parents, who gave me the chance to study physics and always supported me in everything.

To all of you, thank you very much!

Samenvatting

Studie van de Underlying Event activiteit bij voorwaartse rapiditeit in pp botsingen met $\sqrt{s}$ = 0.9, 2.76 en 7 TeV

Het doel van de deeltjesfysica is om de fundamentele bouwstenen van het heelal te bestuderen. Dit houdt in dat men wil begrijpen welke elementaire deeltjes en interacties nodig zijn om alle materie en alle processen waargenomen in de natuur te verklaren. Onze huidige kennis is samengevat in het Standaardmodel, dat een verenigde beschrijving van de interacties (met uitzondering van de zwaartekracht) bevat die de dynamica van de gekende elementaire deeltjes verklaart. Ondanks het succes in het verklaren van experimentele resultaten met een hoge precisie, moeten veel details nog volledig begrepen worden en is de puzzel van de natuur nog niet compleet.

Deeltjesversnellers bieden de ideale omgeving om dit verder te bestuderen. Deze machines versnellen deeltjes tot zeer hoge energieën om ze dan te laten botsen. Uit het puin van deze botsingen kan men dan vervolgens het gedrag en de eigenschappen bestuderen van de betrokken deeltjes en wisselwerkingen. De nieuwe energiedomeinen die kunnen worden onderzocht met dergelijke versnellers stellen ons in staat om de geldigheid van het Standaardmodel te bevestigen, en te zoeken naar de ontbrekende puzzelstukken, bijv. nieuwe deeltjes en wisselwerkingen. De nieuwste en krachtigste deeltjesversneller momenteel beschikbaar is de Large Hadron Collider (LHC) te CERN (Genève). Deze machine biedt proton-proton, en zware-ionen, botsingen aan in energie domeinen die nooit eerder bereikbaar waren.

De LHC is een ware ontdekkingsmachine, de hoog energetische proton-proton botsingen bieden de ideale condities voor de productie van deeltjes zoals het beroemde Higgs boson, maar het is ook de ideale machine om de proton-proton botsingen zelf te bestuderen. De theorie die de sterke interacties tussen protonen beschrijft is de Quantum Chromodynamica (QCD), en is het onderwerp van dit proefschrift. Hoewel het deel uitmaakt van het Standaardmodel, is de beschrijving van proton-proton botsingen, of meer algemeen hadron-hadron botsingen, verre van triviaal en nog steeds onderworpen aan veel onderzoek, aangezien vele aspecten nog niet volledig begrepen worden. Het verbeteren van onze kennis over QCD is niet alleen belangrijk voor het uitvoeren van nauwkeurige metingen om het Standaardmodel te testen, maar ook voor het zoeken naar nieuwe fysica. Hoe kan men anders precieze ontdekkingen maken als de standaard (achtergrond) processen van proton-proton botsingen niet volledig begrepen zijn?

De Quantum Chromodynamica is een relativistische kwantumveldentheorie, waarvan de niet-abelse symmetrie leidt tot de eigenschappen van "asymptotische vrijheid" en "opsluiting". Processen over een korte afstand (hoge energie) hebben een kleine koppeling, die perturbatieve berekeningen mogelijk maakt, terwijl processen over een lange afstand een lage energie en grote koppeling hebben, wat de reden is waarom quarks niet afzonderlijk gedetecteerd kunnen worden, maar worden opgesloten in kleur neutrale hadronen.

Met de hulp van diep inelastische verstrooiingsprocessen, werd het duidelijk dat hadronen opgebouwd zijn uit partonen (quarks en gluonen), en hun interacties vervolgens beschreven worden als de interacties tussen de interagerende partonen. De werkzame doorsnede van hadron botsingen wordt vervolgens opgesplitst in een niet-perturbatief deel, de parton distributie functies ($f_i(x, \mu^2)$, die de waarschijnlijkheid geven dat een parton i, met een longitudinale impuls fractie x, in het hadron aanwezig is bij een energie-schaal μ), en een perturbatief berekenbare partonische werkzame doorsnede, die de harde verstrooiing van de hoog energetische parton interactie vertegenwoordigt. Deze methode noemt men collineaire factorisatie. De parton distributies kunnen niet analytisch berekend worden, maar hun evolutie met μ kan perturbatief berekend worden met de DGLAP evolutie vergelijkingen. De sterkte van deze methode is dat de parton distributie functies onafhankelijk zijn van de harde verstrooiing.

Een belangrijke beperking van de collineaire factorisatie methode is dat het niet mogelijk is om meerdere parton interacties (MPI) bij hadron-hadron botsingen in rekening te nemen. Dit is echter een essentieel element van de *Underlying Event* activiteit, die wordt gedefinieerd als alles behalve de harde parton-parton verstrooiing. Dit omvat cascades van uitgestraalde partonen in de begin- en eindtoestanden, restanten van de inkomende hadronen en de eerder genoemde MPI. Deze extra parton interacties zijn meestal zacht of semi-hard, maar kunnen de stroom van kleurladingen en de totale verspreide energie tijdens de botsing aanzienlijk veranderen. Het ontbreken van een universeel theoretisch kader om dergelijke effecten te beschrijven leidde tot de invoering van fenomenologische modellen. Een langdurig en succesvol model dat MPI implementeert, is gebaseerd op een impact parameter beeld van botsingen tussen deeltjes. Deze modellen maken echter gebruik van parameters die moeten worden afgestemd op experimentele data.

Daarom worden er momenteel veel metingen uitgevoerd om deze Underlying Event activiteit te bestuderen. In het bijzonder met de experimenten bij de CERN LHC versneller, waarbij het grotendeels wordt bestudeerd in proton-proton botsingen. In dergelijke metingen bestudeert men meestal de Underlying Event activiteit bij centrale rapiditeit[1] als functie van de energie-schaal van de harde verstrooiing. Dit kan zowel de transversale impuls van de leidende jet of een Drell-Yan lepton paar zijn. De Underlying Event activiteit zelf kan dan worden gemeten in termen van deeltjes multipliciteiten, totale transversale impuls sommen, de vreemdheid-productie, of de jet oppervlakte/mediaan. Daarnaast werden ook metingen van de energiedichtheid uitgevoerd bij voorwaartse

[1]Gedefinieerd als $y = \frac{1}{2} \ln \frac{E+p_z}{E-p_z}$, met E de energie van het deeltje en p_z de longitudinale impuls. Bij hoge energieën kan men de massa m van het deeltje verwaarlozen en de (pseudo)rapiditeit definiëren als $\eta \equiv y|_{m=0} = -\ln \tan \frac{\theta}{2}$, met θ de polaire hoek tussen het deeltje en de bundelpijp.

rapiditeit. Al deze metingen bevestigen dat meerdere parton interacties verplicht zijn om alle Underlying Event activiteit te verklaren, en dat de MPI modellen ontwikkeld in het impact parameter beeld in staat zijn om de gegevens te beschrijven als hun parameters dienovereenkomstig worden afgestemd naar de data.

Dit proefschrift presenteert een nieuwe en complementaire meting van de Underlying Event activiteit bij een voorwaartse rapiditeit, uitgevoerd aan het CMS experiment, dat bestaat uit een algemene detector die het interactie punt volledig omringt. Zijn ui-achtige structuur bestaat uit sporendetectoren, calorimeters, een 4 T magneetveld en muondetectoren. Dit ontwerp maakt het mogelijk om de eindtoestand van LHC proton-proton botsingen volledig te reconstrueren. Met name de zeer efficiënte centrale sporendetector is ideaal voor het reconstrueren van sporen of spoor-jets die afkomstig zijn van geladen deeltjes van de harde verstrooiing.

Een cruciaal onderdeel van de CMS detector voor onze analyse is de voorwaartse CASTOR calorimeter. Het systeem bevindt zich in een rapiditeitsinterval van -6.6 $< \eta < -5.2$, en is gelegen op $z = -14.38$ m van het interactie punt. Het maakt gebruik van wolfraam platen als absorptiemateriaal, en kwarts platen om Čerenkov signalen te genereren. Het heeft dus de mogelijkheid om de energie van elektromagnetische en hadronische deeltjes te meten in het voorste gebied van de CMS detector. CASTOR heeft 14 segmentaties in z (een totale lengte van $10\lambda_I$), een 16-voudige segmentatie in het azimuthale vlak, maar geen segmentatie in η. Het is de allereerste keer dat data van deze detector gebruikt wordt in een analyse, en daarom werd een groot deel van het onderzoek tijdens het doctoraat gewijd aan de inbedrijfstelling en validatie van de CASTOR calorimeter. Zo werden bijdragen geleverd aan a) de studie van prototypes in ideale laboratorium omgevingen, b) simulatie en reconstructie software ontwikkeling en validatie, en c) het begrijpen van de detector in een in-situ omgeving, voornamelijk de positie van de calorimeter. Het gebruik van de detector in een in-situ omgeving tijdens het nemen van LHC data was zeer uitdagend, maar voldoende begrepen voor het doel van deze analyse.

Vervolgens werd dan een studie van de Underlying Event activiteit in het voorwaartse rapiditeitsinterval (-6.6 $< \eta < -5.2$) met een nieuwe observabele gepresenteerd. De energiedichtheid per rapiditeitseenheid werd gemeten bij massamiddelpuntsenergieën van $\sqrt{s} = 0.9$, 2.76 en 7 TeV, voor botsingen met een centrale geladen deeltjes jet ten opzichte van de energiedichtheid voor inclusieve botsingen. Deze *hard-to-inclusive* voorwaartse energieverhouding is dan bestudeerd als functie van de transversale impuls (p_T) van de jet. Verder is de relatieve toename van de energiedichtheid als functie van de massamiddelpuntsenergie gemeten voor zowel inclusieve botsingen, en botsingen met een centrale geladen deeltjes jet.

Deze resultaten vullen de vorige studies aan die bij een centrale rapiditeit zijn uitgevoerd [110, 112, 113, 111, 114] omdat de grote η scheiding van de centrale harde verstrooiing tot een andere gevoeligheid leidt voor de relatieve bijdragen van parton lawines en meerdere parton interacties. Deze gegevens kunnen dus worden gebruikt om

de Underlying Event parameters af te stemmen op een wijze die complementair is aan die met data genomen bij een centrale rapiditeit.

De data vertonen een typisch gedrag van de Underlying Event activiteit gekenmerkt door een snelle verandering van de energiedichtheid bij kleine jet p_T, gevolgd door een plateau bij grotere p_T waarden. Bij $\sqrt{s} = 7$ TeV, zien we dat de relatieve energiedichtheid toeneemt met jet p_T, terwijl bij $\sqrt{s} = 0.9$ TeV de energiedichtheid afneemt met toenemende jet p_T. Bij deze massamiddelpuntsenergie is de hard-to-inclusive voorwaartse energieverhouding kleiner dan 1, hetgeen suggereert dat de energie van de proton restanten opgebruikt wordt door de productie van centrale geladen deeltjes jets. Data bij $\sqrt{s} = 2.76$ TeV vertonen een tussenliggend gedrag en worden gekenmerkt door een nagenoeg constante energiedichtheid als functie van de jet p_T.

Modellen die meerdere parton interacties omvatten suggereren dat zij slechts voor een beperkte bijdrage zorgen aan de voorwaartse energiedichtheid in inclusieve botsingen. Botsingen met een kleine impact parameter daarentegen, gekenmerkt door de aanwezigheid van een geladen deeltjes jet, blijken wel aanleiding te geven tot een groot aantal verschillende parton interacties. Boven $p_T = 8$ GeV/c, is de hard-to-inclusive voorwaartse energieverhouding ruwweg onafhankelijk van p_T, wat aangeeft dat de botsingen al centraal zijn voor deze waarden. Sommige Monte Carlo modellen kunnen de hard-to-inclusive voorwaartse energieverhouding beschrijven als functie van p_T, maar geen enkel model kan de massamiddelpuntsenergie afhankelijkheid van de voorwaartse energiedichtheid gelijktijdig reproduceren voor inclusieve botsingen en voor botsingen met een centrale geladen deeltjes jet.

Bibliography

[1] D. Perkins, *Introduction to High Energy Physics*. Cambridge University Press, 2000.

[2] S. Glashow, *Partial-symmetries of weak interactions*, *Nucl.Phys.* **22** (Feb., 1961) 579–588.

[3] S. Weinberg, *A Model of Leptons*, *Phys. Rev. Lett.* **19** (Nov, 1967) 1264–1266.

[4] A. Salam, *Weak and electromagnetic interactions*, *Elementary Particle Theory, Stockholm, Almquist and Wiksell* (1968) page 367.

[5] F. Englert and R. Brout, *Broken Symmetry and the Mass of Gauge Vector Mesons*, *Phys. Rev. Lett.* **13** (Aug, 1964) 321–323.

[6] P. W. Higgs, *Broken Symmetries and the Masses of Gauge Bosons*, *Phys. Rev. Lett.* **13** (Oct, 1964) 508–509.

[7] G. S. Guralnik, C. R. Hagen, and T. W. B. Kibble, *Global Conservation Laws and Massless Particles*, *Phys. Rev. Lett.* **13** (Nov, 1964) 585–587.

[8] **ATLAS** Collaboration, G. Aad et al., *Observation of a new particle in the search for the Standard Model Higgs boson with the ATLAS detector at the LHC*, *Phys.Lett.* **B716** (2012) 1–29, [arXiv:1207.7214].

[9] **CMS** Collaboration, S. Chatrchyan et al., *Observation of a new boson at a mass of 125 GeV with the CMS experiment at the LHC*, *Phys.Lett.* **B716** (2012) 30–61, [arXiv:1207.7235].

[10] J. Collins, *Foundations of perturbative QCD*. Cambridge monographs on particle physics, nuclear physics, and cosmology. Cambridge Univ. Press, New York, 2011.

[11] R. K. Ellis, W. J. Stirling, and B. R. Webber, *QCD and Collider Physics*. Cambridge monographs on particle physics, nuclear physics, and cosmology. Cambridge Univ. Press, Cambridge, 2003. Photography by S. Vascotto.

[12] F. Halzen and A. D. Martin, *Quarks and leptons: an introductory course in modern particle physics*. Wiley, New York, NY, 1984.

[13] **CMS** Collaboration, S. Chatrchyan et al., *Measurement of the ratio of the inclusive 3-jet to 2-jet cross-sections in pp collisions at 7 TeV and first determination of the strong coupling at transverse momenta in the TeV range*,

Tech. Rep. CMS-PAS-QCD-11-003, CERN, Geneva, 2011.

[14] V. Barone and E. Predazzi, *High-Energy Particle Diffraction*. Springer, 2002.

[15] A. Buckley, J. Butterworth, S. Gieseke, D. Grellscheid, S. Hoche, et al., *General-purpose event generators for LHC physics*, *Phys.Rept.* **504** (2011) 145–233, [arXiv:1101.2599].

[16] **H1 and ZEUS** Collaboration, F. Aaron et al., *Combined Measurement and QCD Analysis of the Inclusive e+- p Scattering Cross Sections at HERA*, *JHEP* **1001** (2010) 109, [arXiv:0911.0884].

[17] H. Jung, "QCD and Monte Carlo." Lecture notes of QCD course at University of Antwerp and DESY, 2013.

[18] M. Kuhlen, *QCD and the hadronic final state in deep inelastic scattering at HERA*, hep-ph/9712505.

[19] J. C. Collins, D. E. Soper, and G. F. Sterman, *Factorization of Hard Processes in QCD*, *Adv.Ser.Direct.High Energy Phys.* **5** (1988) 1–91, [hep-ph/0409313].

[20] **CTEQ** Collaboration, R. Brock et al., *Handbook of perturbative QCD: Version 1.0*, *Rev.Mod.Phys.* **67** (1995) 157–248.

[21] S. Catani, M. Ciafaloni, and F. Hautmann, *High energy factorization and small-x heavy flavour production*, *Nuclear Physics B* **366** (1991), no. 1 135 – 188.

[22] E. Kuraev, L. Lipatov, and V. S. Fadin, *The Pomeranchuk Singularity in Nonabelian Gauge Theories*, *Sov.Phys.JETP* **45** (1977) 199–204.

[23] I. Balitsky and L. Lipatov, *The Pomeranchuk Singularity in Quantum Chromodynamics*, *Sov.J.Nucl.Phys.* **28** (1978) 822–829.

[24] M. Ciafaloni, *Coherence effects in initial jets at small Q2/s*, *Nuclear Physics B* **296** (1988), no. 1 49 – 74.

[25] S. Catani, F. Fiorani, and G. Marchesini, *Small-x behaviour of initial state radiation in perturbative QCD*, *Nuclear Physics B* **336** (1990), no. 1 18 – 85.

[26] S. Catani, F. Fiorani, and G. Marchesini, *QCD coherence in initial state radiation*, *Physics Letters B* **234** (1990), no. 3 339 – 345.

[27] K. Kutak, *On High Energy Factorization: Theoretical Basics and Phenomenological Applications*, *Acta Phys.Polon.* **B42** (2011) 1487–1496, [arXiv:1105.0096].

[28] **H1** Collaboration, C. Adloff et al., *Forward jet and particle production at HERA*, *Nucl.Phys.* **B538** (1999) 3–22, [hep-ex/9809028].

[29] **ZEUS** Collaboration, J. Breitweg et al., *Forward jet production in deep inelastic scattering at HERA*, *Eur.Phys.J.* **C6** (1999) 239–252, [hep-ex/9805016].

[30] F. Hautmann and H. Jung, *Angular correlations in multi-jet final states from k_T-dependent parton showers*, *JHEP* **0810** (2008) 113, [arXiv:0805.1049].

[31] J. Collins and J.-W. Qiu, *k_T factorization is violated in production of high-transverse-momentum particles in hadron-hadron collisions*, *Phys.Rev.* **D75** (2007) 114014, [arXiv:0705.2141].

[32] T. Regge, *Introduction to complex orbital momenta*, *Nuovo Cim.* **14** (1959) 951.

[33] O. Nachtmann, *Pomeron physics and QCD*, hep-ph/0312279.

[34] A. Donnachie and P. Landshoff, *Small x: Two pomerons!*, *Phys.Lett.* **B437** (1998) 408–416, [hep-ph/9806344].

[35] F. Low, *A Model of the Bare Pomeron*, *Phys.Rev.* **D12** (1975) 163–173.

[36] S. Nussinov, *Colored Quark Version of Some Hadronic Puzzles*, *Phys.Rev.Lett.* **34** (1975) 1286–1289.

[37] V. Gribov, *The Theory of Complex Angular Momenta: Gribov Lectures on Theoretical Physics*. Cambridge Monographs on Mathematical Physics. Cambridge University Press, 2003.

[38] V. Gribov, *A Reggeon Diagram Technique*, *Sov.Phys.JETP* **26** (1968) 414–422.

[39] **AFS** Collaboration, T. Akesson et al., *Double Parton Scattering in pp Collisions at $\sqrt{s}$ = 63 GeV*, *Z.Phys.* **C34** (1987) 163.

[40] **CDF** Collaboration, F. Abe et al., *Double parton scattering in $\bar{p}p$ collisions at $\sqrt{s} = 1.8\,TeV$*, *Phys.Rev.* **D56** (1997) 3811–3832.

[41] B. Andersson, G. Gustafson, G. Ingelman, and T. Sjostrand, *Parton fragmentation and string dynamics*, *Physics Reports* **97** (1983) 31 – 145.

[42] T. Sjostrand, S. Mrenna, and P. Z. Skands, *PYTHIA 6.4 Physics and Manual*, *JHEP* **0605** (2006) 026, [hep-ph/0603175].

[43] T. Sjostrand and P. Z. Skands, *Transverse-momentum-ordered showers and interleaved multiple interactions*, *Eur.Phys.J.* **C39** (2005) 129–154, [hep-ph/0408302].

[44] T. Sjostrand and P. Z. Skands, *Multiple interactions and the structure of beam remnants*, *JHEP* **0403** (2004) 053, [hep-ph/0402078].

[45] G. P. Salam and G. Soyez, *A Practical Seedless Infrared-Safe Cone jet algorithm*, *JHEP* **0705** (2007) 086, [arXiv:0704.0292].

[46] M. Cacciari, G. P. Salam, and G. Soyez, *The Anti-k(t) jet clustering algorithm*, *JHEP* **0804** (2008) 063, [arXiv:0802.1189].

[47] T. Sjostrand and M. V. Zijl, *Multiple parton-parton interactions in an impact parameter picture*, *Physics Letters B* **188** (1987), no. 1 149 – 154.

[48] L. Frankfurt, M. Strikman, and C. Weiss, *Transverse nucleon structure and diagnostics of hard parton-parton processes at LHC*, *Phys.Rev.* **D83** (2011) 054012, [arXiv:1009.2559].

[49] G. Fishman, *Monte Carlo: Concepts, Algorithms, and Applications*. Springer series in operational research. Springer, 1996.

[50] T. Sjostrand, S. Mrenna, and P. Z. Skands, *A Brief Introduction to PYTHIA 8.1*, *Comput.Phys.Commun.* **178** (2008) 852–867, [arXiv:0710.3820].

[51] M. Bahr, S. Gieseke, M. Gigg, D. Grellscheid, K. Hamilton, et al., *Herwig++ Physics and Manual*, *Eur.Phys.J.* **C58** (2008) 639–707, [arXiv:0803.0883].

[52] M. Bahr, S. Gieseke, and M. H. Seymour, *Simulation of multiple partonic interactions in Herwig++*, *JHEP* **0807** (2008) 076, [arXiv:0803.3633].

[53] H. Jung, S. Baranov, M. Deak, A. Grebenyuk, F. Hautmann, et al., *The CCFM Monte Carlo generator CASCADE version 2.2.03*, *Eur.Phys.J.* **C70** (2010) 1237–1249, [arXiv:1008.0152].

[54] H. Jung and G. Salam, *Hadronic final state predictions from CCFM: The Hadron level Monte Carlo generator CASCADE*, *Eur.Phys.J.* **C19** (2001) 351–360, [hep-ph/0012143].

[55] C. Flensburg, G. Gustafson, and L. Lonnblad, *Inclusive and Exclusive Observables from Dipoles in High Energy Collisions*, *JHEP* **1108** (2011) 103, [arXiv:1103.4321].

[56] A. H. Mueller, *Soft gluons in the infinite momentum wave function and the BFKL pomeron*, *Nucl.Phys.* **B415** (1994) 373–385.

[57] A. H. Mueller and B. Patel, *Single and double BFKL pomeron exchange and a dipole picture of high-energy hard processes*, *Nucl.Phys.* **B425** (1994) 471–488, [hep-ph/9403256].

[58] A. H. Mueller, *Unitarity and the BFKL pomeron*, *Nucl.Phys.* **B437** (1995) 107–126, [hep-ph/9408245].

[59] S. Ostapchenko, *Monte Carlo treatment of hadronic interactions in enhanced Pomeron scheme: I. QGSJET-II model*, *Phys.Rev.* **D83** (2011) 014018, [arXiv:1010.1869].

[60] K. Werner, F.-M. Liu, and T. Pierog, *Parton ladder splitting and the rapidity dependence of transverse momentum spectra in deuteron-gold collisions at RHIC*, *Phys.Rev.* **C74** (2006) 044902, [hep-ph/0506232].

[61] E.-J. Ahn, R. Engel, T. K. Gaisser, P. Lipari, and T. Stanev, *Cosmic ray interaction event generator SIBYLL 2.1*, *Phys.Rev.* **D80** (2009) 094003, [arXiv:0906.4113].

[62] S. Ostapchenko, *High Energy Cosmic Ray Interactions: An Overview*, *J.Phys.Conf.Ser.* **60** (2007) 167–170, [astro-ph/0610788].

[63] H. Schopper, *LEP: a historical introduction*, *Philos. Trans. R. Soc. Lond., A* **336** (1991) 179–189. Discussion: C H Llewellyn Smith.

[64] L. R. Evans and P. Bryant, *LHC Machine*, *J. Instrum.* **3** (2008) S08001. 164 p. This report is an abridged version of the LHC Design Report (CERN-2004-003).

[65] P. Collier and B. Goddard, *The SPS as LHC Injector*, *Conf.Proc.* **C0106181** (2001) 3150–3152.

[66] **ATLAS** Collaboration, G. Aad et al., *The ATLAS Experiment at the CERN Large Hadron Collider*, *JINST* **3** (2008) S08003.

[67] **CMS** Collaboration, S. Chatrchyan et al., *The CMS experiment at the CERN LHC*, *JINST* **3** (2008) S08004.

[68] O. S. Bruning and P. Collier, *Building a behemoth*, *Nature* **448** (2007) 285–289.

[69] **LHCb** Collaboration, J. Alves, A. Augusto et al., *The LHCb Detector at the LHC*, *JINST* **3** (2008) S08005.

[70] **ALICE** Collaboration, K. Aamodt et al., *The ALICE experiment at the CERN LHC*, *JINST* **3** (2008) S08002.

[71] G. Antchev, P. Aspell, I. Atanassov, V. Avati, V. Berardi, et al., *The TOTEM Detector at LHC*, *Nucl.Instrum.Meth.* **617** (2010) 62–66.

[72] **LHCf** Collaboration, O. Adriani et al., *The LHCf detector at the CERN Large Hadron Collider*, *JINST* **3** (2008) S08006.

[73] M. Church, *Tevatron Run II Performance and Plans*, . 8th European Particle Accelerator Conference, Paris, France, 3 - 7 Jun 2002.

[74] M. Ferro-Luzzi, *LHC Operation - as viewed from the Experiments*, . Chamonix 2011 Workshop on LHC Performance, Chamonix, France, 24 - 28 Jan 2011.

[75] M. Ferro-Luzzi, *Review of 2011 LHC run from the experiments perspective*, . Chamonix 2012 Workshop on LHC Performance, Chamonix, France, 6 - 10 Feb 2012.

[76] **CMS** Collaboration, O. A. Grachov et al., *Status of zero degree calorimeter for CMS experiment*, *AIP Conf.Proc.* **867** (2006) 258–265, [nucl-ex/0608052].

[77] A. J. Bell, D. d'Enterria, R. Hall-Wilton, G. Veres, V. Khoze, et al., *Physics and Beam Monitoring with Forward Shower Counters (FSC) in CMS*, .

[78] A. Holzner, *78 reconstructed vertices in event from high-pileup run 198609*, tech. rep., CMS Collaboration, Sep, 2012.

[79] A. J. Bell, *The design and construction of the beam scintillation counter for CMS*,

Master's thesis, University of Canterbury, 2008.

[80] T. Aumeyr, *Beam Phase and Intensity Monitoring for the Compact Muon Solenoid Experiment*, Master's thesis, Vienna University of Technology, 2008.

[81] E. Norbeck, E. Gladysz-Dziadus, P. Katsas, Y. Onel, and A. D. Panagiotou, *Exotic Physics at the LHC with CASTOR in CMS*, *Int. J. Mod. Phys. E* **16** (Apr, 2007) 2451–2456. 5 p.

[82] B. Roland, *Forward Physics Capabilities of CMS with the CASTOR and ZDC detectors*, Tech. Rep. arXiv:1008.0592, Universiteit Antwerpen, Aug, 2010. Comments: 5 pages - 6 figures - DIS 2009 proceedings.

[83] H. Van Haevermaet, *Ontwikkeling van de CASTOR reconstructie software en elektron/pion separatie analyse*, Master's thesis, Universiteit Antwerpen, 2009.

[84] R. Wigmans, *Calorimetry: Energy Measurement in Particle Physics*. International series of monographs on physics. Clarendon Press, Oxford, 2000.

[85] C. Grupen, B. Shwartz, and H. Spieler, *Particle Detectors*. Cambridge Monographs on Particle Physics, Nuclear Physics and Cosmology. Cambridge University Press, 2008.

[86] R. Feynman, R. Leighton, and M. Sands, *The Feynman Lectures on Physics*. No. v. 1-v. 3 in The Feynman Lectures on Physics. Addison-Wesley, 1964.

[87] **Particle Data Group** Collaboration, J. Beringer et al., *Review of Particle Physics (RPP)*, *Phys.Rev.* **D86** (2012) 010001.

[88] V. Andreev, X. Aslanoglou, A. Azman, M. Bakirci, S. Basegmez, et al., *Performance studies of a full-length prototype for the CASTOR forward calorimeter at the CMS experiment*, *Eur. Phys. J. C* **67** (2010) 601–615. 15 p.

[89] I. Katkov, *Physics with the CMS forward CASTOR calorimeter*, Tech. Rep. CMS-CR-2011-008, CERN, Geneva, Jan, 2011.

[90] R. Brun and F. Rademakers, *ROOT: An object oriented data analysis framework*, *Nucl.Instrum.Meth.* **A389** (1997) 81–86.

[91] **GEANT4** Collaboration, S. Agostinelli et al., *GEANT4: A Simulation toolkit*, *Nucl.Instrum.Meth.* **A506** (2003) 250–303.

[92] J. Allison, K. Amako, J. Apostolakis, H. Araujo, P. Dubois, et al., *Geant4 developments and applications*, *IEEE Trans.Nucl.Sci.* **53** (2006) 270.

[93] M. Biasini and V. Cuplov, *The CMS all silicon Tracker simulation*, Tech. Rep. CMS-CR-2009-338, CERN, Geneva, Nov, 2009.

[94] R. Fruhwirth, *Application of Kalman filtering to track and vertex fitting*, *Nucl.Instrum.Meth.* **A262** (1987) 444–450.

[95] R. E. Kalman, *A New Approach to Linear Filtering and Prediction Problems*, *Transactions of the ASME–Journal of Basic Engineering* **82** (1960), no. Series D 35–45.

[96] R. Fruhwirth, W. Waltenberger, and P. Vanlaer, *Adaptive Vertex Fitting*, Tech. Rep. CMS-NOTE-2007-008, CERN, Geneva, Mar, 2007.

[97] S. Cucciarelli, M. Konecki, D. Kotlinski, and T. Todorov, *Track reconstruction, primary vertex finding and seed generation with the Pixel Detector*, Tech. Rep. CMS-NOTE-2006-026, CERN, Geneva, Jan, 2006.

[98] T. Speer, K. Prokofiev, R. Frühwirth, W. Waltenberger, and P. Vanlaer, *Vertex Fitting in the CMS Tracker*, Tech. Rep. CMS-NOTE-2006-032, CERN, Geneva, Feb, 2006.

[99] T. Miao, N. Leioatts, H. Wenzel, and F. Yumiceva, *Beam Position Determination using Tracks*, Tech. Rep. CMS-NOTE-2007-021, CERN, Geneva, Aug, 2007.

[100] **CMS** Collaboration, S. Chatrchyan et al., *Commissioning of the CMS Experiment and the Cosmic Run at Four Tesla*, *JINST* **5** (2010) T03001, [arXiv:0911.4845].

[101] **CMS** Collaboration, S. Chatrchyan et al., *Commissioning and Performance of the CMS Pixel Tracker with Cosmic Ray Muons*, *JINST* **5** (2010) T03007, [arXiv:0911.5434].

[102] **CMS** Collaboration, S. Chatrchyan et al., *Commissioning and Performance of the CMS Silicon Strip Tracker with Cosmic Ray Muons*, *JINST* **5** (2010) T03008, [arXiv:0911.4996].

[103] **CMS** Collaboration, S. Chatrchyan et al., *Tracking and Primary Vertex Results in First 7 TeV Collisions*, *CMS-PAS-TRK-10-005* (2010).

[104] G. Folger and J. P. Wellisch, *String Parton Models in Geant4*, Tech. Rep. nucl-th/0306007, CERN, Geneva, Jun, 2003.

[105] B. Andersson, G. Gustafson, and H. Pi, *The FRITIOF model for very high energy hadronic collisions*, Tech. Rep. LU-TP-92-20. LUTP-92-20, Lunds Univ. Dept. Theor. Phys., Lund, May, 1992.

[106] A. M. Heikkinen, N. Stepanov, and J. P. Wellisch, *Bertini intra-nuclear cascade implementation in Geant4*, Tech. Rep. nucl-th/0306008, CERN, Geneva, Jun, 2003.

[107] H. S. Fesefeldt, *The simulation of hadronic showers: physics and applications*, Tech. Rep. PITHA-85-02, Aachen TU 3. Inst. Phys., Aachen, Sep, 1985.

[108] W. Carvalho, L. Mundim, M. Pol, and H. Van Haevermaet, *The CASTOR shower library*, internal detector note dn-2012/016, CMS Collaboration, 2012.

[109] R. Field, *Physics at the Tevatron*, *Acta Phys.Polon.* **B39** (2008) 2611–2672.

[110] **CMS** Collaboration, V. Khachatryan et al., *First Measurement of the Underlying*

Event Activity at the LHC with $\sqrt{s} = 0.9$ TeV, *Eur.Phys.J.* **C70** (2010) 555–572, [arXiv:1006.2083].

[111] **CMS** Collaboration, S. Chatrchyan et al., *Measurement of the Underlying Event Activity at the LHC with $\sqrt{s} = 7$ TeV and Comparison with $\sqrt{s} = 0.9$ TeV*, *JHEP* **1109** (2011) 109, [arXiv:1107.0330].

[112] **ATLAS** Collaboration, G. Aad et al., *Measurement of underlying event characteristics using charged particles in pp collisions at $\sqrt{s} = 900GeV$ and 7 TeV with the ATLAS detector*, *Phys.Rev.* **D83** (2011) 112001, [arXiv:1012.0791].

[113] **ATLAS** Collaboration, G. Aad et al., *Measurements of underlying-event properties using neutral and charged particles in pp collisions at 900 GeV and 7 TeV with the ATLAS detector at the LHC*, *Eur.Phys.J.* **C71** (2011) 1636, [arXiv:1103.1816].

[114] **ALICE** Collaboration, B. Abelev et al., *Underlying Event measurements in pp collisions at $\sqrt{s} = 0.9$ and 7 TeV with the ALICE experiment at the LHC*, *JHEP* **1207** (2012) 116, [arXiv:1112.2082].

[115] **CMS** Collaboration, S. Chatrchyan et al., *Measurement of Strange Particle Production in Underlying Events in proton-proton collisions at $\sqrt{s} = 7$ TeV*, *CMS PAS QCD-11-010* (2012).

[116] **CMS** Collaboration, S. Chatrchyan et al., *Measurement of the underlying event in the Drell-Yan process in proton-proton collisions at $\sqrt{s} = 7$ TeV*, *Eur.Phys.J.* **C72** (2012) 2080, [arXiv:1204.1411].

[117] **CMS** Collaboration, S. Chatrchyan et al., *Measurement of the underlying event activity in pp collisions at $\sqrt{s} = 0.9$ and 7 TeV with the novel jet-area/median approach*, *JHEP* **1208** (2012) 130, [arXiv:1207.2392].

[118] **CMS** Collaboration, S. Chatrchyan et al., *Measurement of energy flow at large pseudorapidities in pp collisions at $\sqrt{s} = 0.9$ and 7 TeV*, *JHEP* **1111** (2011) 148, [arXiv:1110.0211].

[119] **LHCb** Collaboration, R. Aaij et al., *Measurement of the forward energy flow in pp collisions at $\sqrt{s} = 7$ TeV*, arXiv:1212.4755.

[120] P. Z. Skands, *Tuning Monte Carlo Generators: The Perugia Tunes*, *Phys.Rev.* **D82** (2010) 074018, [arXiv:1005.3457].

[121] **ATLAS** Collaboration, G. Aad et al., *Charged-particle multiplicities in pp interactions measured with the ATLAS detector at the LHC*, *New J.Phys.* **13** (2011) 053033, [arXiv:1012.5104].

[122] R. Corke and T. Sjostrand, *Interleaved Parton Showers and Tuning Prospects*, *JHEP* **1103** (2011) 032, [arXiv:1011.1759].

[123] P. Z. Skands and D. Wicke, *Non-perturbative QCD effects and the top mass at the*

Tevatron, *Eur.Phys.J.* **C52** (2007) 133–140, [hep-ph/0703081].

[124] R. Field, *Early LHC Underlying Event Data - Findings and Surprises*, arXiv:1010.3558.

[125] **CTEQ** Collaboration, H. Lai et al., *Global QCD analysis of parton structure of the nucleon: CTEQ5 parton distributions*, *Eur.Phys.J.* **C12** (2000) 375–392, [hep-ph/9903282].

[126] J. Pumplin, D. Stump, J. Huston, H. Lai, P. M. Nadolsky, et al., *New generation of parton distributions with uncertainties from global QCD analysis*, *JHEP* **0207** (2002) 012, [hep-ph/0201195].

[127] A. Buckley, H. Hoeth, H. Lacker, H. Schulz, and J. E. von Seggern, *Systematic event generator tuning for the LHC*, *Eur.Phys.J.* **C65** (2010) 331–357, [arXiv:0907.2973].

[128] S. Gieseke, D. Grellscheid, K. Hamilton, A. Papaefstathiou, S. Platzer, et al., *Herwig++ 2.5 Release Note*, arXiv:1102.1672.

[129] D. d'Enterria, R. Engel, T. Pierog, S. Ostapchenko, and K. Werner, *Constraints from the first LHC data on hadronic event generators for ultra-high energy cosmic-ray physics*, *Astropart.Phys.* **35** (2011) 98–113, [arXiv:1101.5596].

[130] **CMS-CASTOR** Collaboration, P. Gottlicher, *Design and test beam studies for the CASTOR calorimeter of the CMS experiment*, *Nucl.Instrum.Meth.* **A623** (2010) 225–227.

[131] **CMS** Collaboration, S. Chatrchyan et al., *Measurement of the pseudorapidity and centrality dependence of the very forward energy density in PbPb collisions at* $\sqrt{s}$ *= 2.76 ATeV*, Tech. Rep. CMS-PAS-HIN-12-006, CERN, Geneva, 2012.

[132] V. Khachatryan et al., *Calibration of CASTOR: Status and Prospects.*, *CERN-CMS-IN-2011-024* (2011).

[133] E. Kuznetsova, *Performance and calibration of CASTOR calorimeter at CMS.*, Tech. Rep. CMS-CR-2011-199, CERN, Geneva, Sep, 2011.

[134] **H1** Collaboration, C. Adloff et al., *Diffraction dissociation in photoproduction at HERA*, *Z.Phys.* **C74** (1997) 221–236, [hep-ex/9702003].